An Investigation of Candidate Protostars

Claire Judith Chandler

Doctor of Philosophy
University of Edinburgh
1990

This thesis is my own composition, except where specifically indicated in the text.

November 1990

Abstract

This thesis examines several regions of star formation selected because they were believed to be the youngest of their type. The sources studied are examples of low, medium and high–mass star formation, namely B335, NGC 2024 and DR21(OH).

High–resolution mapping of the thermal dust emission from B335 shows it to contain a dense core elongated in a direction perpendicular to the orientation of the bipolar outflow. The core is sufficiently gravitationally bound to be able to collimate an initially isotropic wind into the observed bipolar structure. The presence of an evolved outflow from a source of such low luminosity and high extinction means that it does not appear to fit the currently popular models for protostellar evolution.

CS and $C^{34}S$ $J = 7 - 6$ molecular line observations show that most of the six dense cores, FIR1–6, in NGC 2024 are too warm to be protostellar condensations. Significant CS $7 - 6$ emission with excitation temperatures of 20 to 60 K has been found to be associated with all of the cores. Revised mass estimates lie between 2 and 11 $M_\odot$, and the corresponding luminosities require the presence of embedded heating sources. FIR4 contains a highly reddened 2 μm source and a possible reflection nebula, and FIR6 has a very wide CS $7 - 6$ line that is probably the result of the interaction between a very young outflow and the surrounding dense core.

A chain of dense cores situated in the DR21 cloud has been mapped in 1.3 mm thermal dust emission and the $2 - 1$ and $1 - 0$ transitions of CS and $C^{34}S$. The sources detected have sufficiently high luminosities that the cores must contain embedded young stars. To account for the location of the masers near the brightest source it seems likely that there is a single 15 $M_\odot$ star. The CS spectra indicate the presence of infalling gas along the line–of–sight, and all the spectra are relatively wide with high–velocity emission present towards the east. They have been fitted by a two component model, with warm background gas and cooler foreground gas, and the results indicate that the two components are physically associated. The mass of the cloud core is about 2000 $M_\odot$, obtained from both the dust emission and the CS data, which together with the CS linewidths indicates that the cloud is approximately in virial equilibrium.

All three sources are found to be quite young, although it seems likely that they have already begun nuclear burning and so none is a "true protostar." Suggestions for future observations of these sources and for the identification of further candidate protostars are also described.

Acknowledgements

The work presented here is the culmination of three years of learning that would not have been possible without the help and guidance of my supervisor Walter Gear; I also acknowledge the university supervision of David Emerson. I have come into contact with many enthusiastic people who have inspired me through discussing my work with them, and who have made my trips observing so enjoyable. The staff of the Joint Astronomy Centre, Hilo, Hawaii have made me feel particularly welcome on all of my visits, and I especially thank Saeko Hayashi for looking after me, although everyone I have met in Spain, Japan and Hawaii deserve to be mentioned. I also appreciate the efficiency and humour with which Liz Gibson keeps the staff and students of the Department of Astronomy under control. I acknowledge the SERC for providing the financial means to carry out my research, and STARLINK for the use of their facilities.

During my time in Edinburgh the friends who have put up with more than their fair share of my ranting and raving about the anomalies of star formation, and who I forced much against their will to read parts of this work, include Lance Miller, Bill Dent and Matt Mountain. Specific people have been acknowledged within the text for helping to take some of the data presented here, but I especially thank Toby Moore, whose patience and fondness for cocktails I respect immensely. I also thank Anneila Sargent, Nick Scoville and Harley Thronson for their help and encouragement in the last twelve months.

The people who have experienced, and suffered from, my most non–linear moments are Keith, Penny and Steve; there are others too numerous to mention who had to put up with a rather wildly inaccurate bowling technique of mine during a game of cricket one summer. Chris has played a major role in helping me to understand the philosophical aspects of direct access files, and Alan has provided me with a large number of unrepeatable phrases and an unhealthy attitude towards cosmologists. I particularly value the friendship of Kathryn and John, and I thank Patrick and Anna for giving me the best banana daiquiris in times of need.

It remains for me to dedicate this work to my parents, who have had the wisdom of letting me make my own mistakes for the last 25 years, and have supported me in everything I have done.

Contents

1 Introduction **1**

1.1 Current observations of star formation 1

1.2 Current theory of star formation 5

1.3 Thermal dust emission 10

1.4 Molecular line emission 13

2 B335 **19**

2.1 Introduction 19

2.2 Observations 20

2.3 Results 21

2.4 Discussion 25

2.4.1 The submillimetre source 25

2.4.2 The collimation of the outflow 29

2.5 Conclusions 34

3 NGC 2024 **35**

3.1 Introduction 35

3.2 Existing continuum data 38

3.3 CS emission 41

3.3.1 Observations 42

3.3.2 Results 43

3.3.3 Discussion 44

3.3.3.1 Morphology and LTE analysis 44

3.3.3.2 Individual cores 49

3.4 Near–infrared imaging 51

3.4.1 Observations 51

3.4.2 Results . . . 52
3.4.3 Discussion . . . 57
3.5 Conclusions . . . 61

4 DR21(OH) 63

4.1 Introduction . . . 63
4.2 Dust Continuum Emission . . . 65
4.2.1 Observations . . . 65
4.2.2 Results . . . 66
4.2.3 Individual sources . . . 69
4.2.3.1 DR21(OH)M . . . 69
4.2.3.2 DR21(OH)S and DR21(OH)W . . . 71
4.2.3.3 DR21(OH)N1 and DR21(OH)N2 . . . 71
4.2.3.4 FIR1(H_2O) . . . 72
4.2.3.5 FIR2 and FIR3(H_2O) . . . 74
4.2.4 Discussion . . . 74
4.2.4.1 Evolutionary state of the sources . . . 74
4.3 CS emission . . . 79
4.3.1 Observations . . . 80
4.3.2 Results . . . 80
4.3.3 Discussion . . . 81
4.3.3.1 Morphology . . . 81
4.3.3.2 CS spectra . . . 96
4.3.3.3 LTE modelling . . . 97
4.3.3.4 Applicability of the model . . . 107
4.3.3.5 Cloud equilibrium . . . 110
4.4 Conclusions . . . 111

5 Conclusions 113

5.1 Low–mass star formation: B335 . . . 113
5.2 Intermediate–mass star formation: NGC 2024 . . . 115
5.3 High–mass star formation: DR21(OH) . . . 117
5.4 Future observations of protostars . . . 119

References 121

Appendices:

A The stellar content of DR21(OH) 129

B Published papers 131

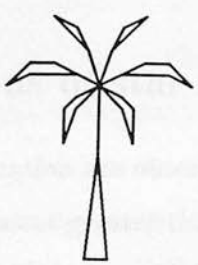

Chapter 1

Introduction

In the last ten years a relatively clear overall picture has begun to emerge concerning the environments of regions undergoing star formation. However as the resolution and sensitivity of observations increase, so does the apparent complexity of the star formation process, so that to build up a self–consistent model to account for all the observed phenomena involves the detailed study of a large number of sources at different stages of evolution. Emission from cool molecular gas and dust at far–infrared and millimetre wavelengths is of extreme importance as a probe of the physical conditions present around young stars and the effect that they have on their surroundings, especially with the high resolution now obtainable from large single–dish telescopes. Here I present studies, mainly in the millimetre/submillimetre, of three regions of star formation chosen because of their apparent youth. As described below, information about very young sources is limited by observational constraints, leaving the earliest stages of protostellar evolution mainly in the realms of theory. For the remainder of the introduction I give a summary of the current state of the observations and theory of star formation, and then I describe the way in which submillimetre dust continuum emission and the emission from diatomic molecules in local thermodynamic equilibrium (LTE) is used to obtain information about regions of star formation.

1.1 Current observations of star formation

Sites of low and high mass star formation are observed to have different spatial distributions in the Galaxy. Stars with masses greater than about $2\,M_{\odot}$ form predominantly in warm giant molecular clouds (GMCs) situated in the spiral arms, and lower mass

stars form in small, cold clouds found throughout the Galactic disk (Solomon, Sanders & Rivolo 1985; Dame *et al.* 1986). Recent analysis of IRAS data (Scoville & Good 1989) shows that the population of clouds can be separated into those with warm peak 60/100 μm colour temperatures of about 40 K which have high luminosity to mass (L/M) ratios and contain giant radio HII regions, and those with 60/100 μm colour temperatures less than 30 K not associated with HII regions having L/M ratios a factor of ten lower than the warm clouds. Clouds with HII regions tend to have higher mass than those without HII regions (*e.g.* Myers *et al.* 1986). The giant molecular clouds show structure on all scales, being composed of smaller clouds of mass $10^3 - 10^4\,M_\odot$ a few parsecs across. Cold, dense cores with dimensions of about 0.1 pc within these clouds are found on still smaller scales (*e.g.* Myers & Benson 1983; Benson & Myers 1989); the close association of these dense cores with cold IRAS point sources makes them the most likely sites in which to search for protostars (Beichman *et al.* 1986).

The width of molecular lines is frequently supersonic, with velocity dispersions significantly greater than the isothermal sound speed (which is around 0.2 to 0.3 $\mathrm{km\,s^{-1}}$) being common. The observed widths are often that required by virial equilibrium (*e.g.* Linke & Goldsmith 1980). This has been used as evidence of the importance of magnetic fields in supporting cloud cores against collapse (Myers & Goodman 1988), because the Alfvén speed is higher than the sound speed. Since the turbulence is observed to be sub–Alfvénic (but still supersonic), magnetic fields are the only way of sustaining the high velocity dispersion. All other possible forms of support appear to be insufficient, and would result in collapse and a far higher star formation rate than is observed (see Shu, Adams & Lizano 1987). Magnetic fields of 10^{-9} to 10^{-8} T have been found for Galactic sources (*e.g.* Troland & Heiles 1986), sufficient to be dynamically important.

Many dark clouds have extremely low rotation rates with typical velocity gradients less than 1 $\mathrm{km\,s^{-1}\,pc^{-1}}$ (*e.g.* Arquilla & Goldsmith 1986; Casali & Edgar 1987). However for those cores that *are* rotating, the rotation is found to play a significant role in the energetics of the cloud. Much higher rotation rates are seen in regions near HII regions (*e.g.* Harris *et al.* 1983; Zheng *et al.* 1985; Ho & Haschick 1986).

Once all forms of support have dissipated from the cloud core, and a young stellar object (YSO) has formed at the centre, it heats the surrounding dust to produce thermal spectra typically much broader than a single–temperature greybody, due to temperature and density gradients in the surrounding core (*e.g.*, Yorke & Shustov 1981; Adams &

Shu 1985; Wolfire & Cassinelli 1986). The search for cold, dense cloud cores that have *not* yet formed a hydrostatic core at the centre of a collapsing envelope of dust and gas has so far failed to identify any candidates, though six dense cores in NGC 2024 found by Mezger *et al.* (1988) looked promising until their evolutionary state was investigated further (Moore *et al.* 1989; Moore & Chandler 1989; Chapter 3). One reason for this is that high mass protostars evolve on the Kelvin–Helmholtz timescale $t_{\rm KH} = GM_*^2/R_*L_*$ which is shorter than the infall timescale, and by the time the newly–formed star disperses the surrounding cloud and becomes visible, it is already on the main sequence, revealing little information about its past history. Although $t_{\rm KH}$ is longer for low mass protostars they are intrinsically very faint whilst they are very young (Boss & Yorke 1990), making them difficult to detect. There have also been very few sources that have unambiguously been determined to be collapsing on small scales (Menten *et al.* 1987; Terebey, Vogel & Myers 1989), though clouds on large scales are often observed to have asymmetrical self–absorption in their CO profiles that has been interpreted as collapse (Snell & Loren 1977, but see Leung & Brown 1977).

Perhaps the most surprising discovery in the last decade concerning the star formation process is the ubiquity of high–velocity molecular gas signifying an energetic phase of mass loss, through which it seems *all* stars pass (Lada 1985; Shu *et al.* 1987). Most often the outflow manifests itself as high–velocity (10 to 100 $\rm km\,s^{-1}$) line wings seen in CO spectra, with the red–shifted and blue–shifted wings often offset spatially (making it "bipolar"), centred on an infrared or submillimetre source (Snell, Loren & Plambeck 1980; Bally & Lada 1983; Goldsmith *et al.* 1984). The CO emission is usually thought of as originating from ambient molecular material that has attained high velocities through being entrained by a powerful stellar wind. In some cases the wind itself has been detected directly in neutral atomic hydrogen emission (Lizano *et al.* 1988). This interpretation is sometimes challenged however, and there are outflow sources in which emission from CO throughout the region occupied by the driving wind proposed in the former model is required to account for the observed spectra (Cabrit & Bertout 1990). The collimation mechanism is still unknown, though it is now clear that it cannot be the large–scale molecular disks that have been suggested in the past (see the discussion of Shu *et al.* 1987). The "disks" commonly seen in high–density molecular tracers on scales of about 0.1 pc (Kaifu *et al.* 1984; Heyer *et al.* 1986; Dent *et al.* 1989) are more likely to be the remnant cloud cores after the remainder of the material has

been blown away by the stellar wind. Mechanisms for the production and collimation of outflows are described in section 1.2.

Other phenomena are also seen to be related to the outflow phase. Highly collimated optical jets that can be traced back to the exciting star are found to be associated with pre–main–sequence stars (Mundt & Fried 1983; Ray *et al.* 1990), and further away from the source shock–excited clumps, Herbig–Haro objects, are observed to have very high proper motions of 100 to 300 $\mathrm{km\,s^{-1}}$ (*e.g.* Herbig & Jones 1981). Compact, high–velocity H_2O masers are found around newly formed OB stars, and are sometimes found near HH objects, accelerated to similarly high velocities (Reid & Moran 1981). OH masers are often associated with compact HII regions and require molecular hydrogen number densities of 10^{11} to $10^{14}\,\mathrm{m^{-3}}$ for maser amplification. They are never associated with low mass stars or "normal" HII regions (Habing *et al.* 1974) indicating that they are probably associated with a very specific phase of high–mass evolution. Shocked molecular hydrogen emission is also seen from clumps within the outflow, and from the walls of the outflow lobes (Beckwith *et al.* 1978; Lane & Bally 1986).

Outflows have kinetic energies between 10^{36} and 10^{40} J, and mechanical luminosities $0.1 - 100\,\mathrm{L_\odot}$, so that they clearly require a large amount of energy to drive them. An extreme example is that of the massive bipolar outflow associated with the cluster of O stars and compact HII regions, DR21. The outflow has an extent of about 5 pc, more than $10^3\,\mathrm{M_\odot}$ of high velocity molecular gas and a kinetic energy of approximately 3×10^{41} J (Garden *et al.* 1986). It also has bipolar shocked molecular hydrogen emission of comparable extent and is possibly the most massive, most energetic outflow source known (Garden *et al.* 1990). It is therefore striking that just 2 pc to the north of the cluster, in the same cloud, lie several relatively quiescent cores with the only sign of star formation being the presence of far–infrared sources (Harvey *et al.* 1986; Richardson, Sandell & Krisciunas 1989; Chapter 4), and compact masers near one source, DR21(OH) (*e.g.* Norris *et al.* 1982). Nothing is visible at near–infrared or optical wavelengths, and there is no detectable HII region. The presence of DR21(OH) in a cloud actively forming O stars whilst it shows so little sign of being evolved makes it an intriguing source.

Low–mass pre–main–sequence stars, once they have sufficiently dispersed the surrounding cloud perhaps leaving a circumstellar disk (Sargent & Beckwith 1987; Beckwith *et al.* 1990), show infrared and ultraviolet excesses, X–ray emission (*e.g.* Montmerle *et al.* 1983), forbidden lines and hydrogen recombination lines, P Cygni profiles and vari-

ability in spectral shapes and fluxes (see, *e.g.*, Appenzeller & Mundt 1989).

1.2 Current theory of star formation

The different conditions prevalent in regions where low and high mass stars form have led to the idea of bimodal star formation, whereby different mechanisms are invoked to explain the two regimes. Lizano & Shu (1989) propose that the key criterion is whether the mass of the cloud core is sufficient to be supported by the embedded magnetic field. In the "supercritical" regime, the mass of the core is greater than a critical mass $M_{\rm crit}$ (Mouschovias & Spitzer 1976), and the core collapses and fragments further, compressing the ambient magnetic field to the high values observed. Cores can then be heated by frictional drag between the ions and neutrals, which has been found to be particularly effective for cores of high column density (Lizano & Shu 1987). Whatever the initial heating mechanism in GMCs (see the review of Goldsmith & Langer 1978), the high temperature seen in their cores raises their Jeans mass and gives rise to high–mass star formation with high star formation efficiency. For cloud cores with masses less than $M_{\rm crit}$, in the "subcritical" regime, the magnetic field, if frozen to the ions, is sufficient to support the cloud via ion–neutral collisions. Collapse can then only proceed via ambipolar diffusion, in which the neutral particles are allowed to slip relative to the ions and the magnetic field; the magnetic field remains approximately constant throughout the collapse. The ionization rate is crucial in determining the point at which the magnetic field decouples from the gas – until the field is decoupled, the mass of the core continues to be subcritical (McKee 1989). This regime results in the formation of low–mass stars, and because the timescale for such a collapse is about an order of magnitude longer than $t_{\rm KH}$ (nearly 10^7 years), the newly–formed star has ample opportunity to disperse the remaining core, implying that the star formation efficiency is also low. The presence of a magnetic field threading the cloud core is also one of the means by which angular momentum can be transferred away from the cloud core allowing matter to accumulate in the middle, via magnetic breaking (*e.g.* Mouschovias & Paleologou 1986).

Once the inner parts of the cloud core no longer have any means of support, they collapse from the inside outwards, forming a power–law density distribution $\rho \propto r^{-3/2}$ characteristic of free–fall inside the collapsing zone and $\rho \propto r^{-2}$ outside (Shu 1977). The collapse is isothermal while the core remains optically thin to infrared radiation, and the

density increases until an optically thick, hydrostatic core develops at the centre of the collapse flow. If the cloud core is initially rotating, the collapse will be approximately spherically symmetric in the outer regions, but will form an accretion disk at the centre around the protostar (Terebey, Shu & Cassen 1984; Boss 1987). The luminosity at this stage comes entirely from accretion, both directly from the infalling envelope onto the disk and protostar, and from the accretion disk onto the protostar (Adams & Shu 1986). Once the central temperature within the hydrostatic core is high enough for deuterium burning to commence, there will also be a significant contribution to the luminosity from the protostar itself. In low mass protostars, and while high mass protostars are sufficiently young that the mass of the hydrostatic core is less than about $2\,M_{\odot}$, the sudden increase in temperature at the centre results in the onset of convection. The precise time at which this happens depends on the mass accretion rate, since if it is high the higher temperature of the accretion shock will enable the core to remain radiative for longer, and deuterium burning will begin after a correspondingly higher mass has accumulated (Cassen, Shu & Terebey 1985).

Shu & Terebey (1984) suggested that the onset of deuterium burning and convection in low–mass protostars could harness its rotational and magnetic energy to produce intense surface activity, and thereby providing the means of powering a wind. There is some evidence for such activity in low–mass pre–main–sequence stars, and also in intermediate mass Herbig Ae/Be stars (*e.g.* Calvet, Basri & Kuhi 1984; Catala 1989). In the case of the formation of intermediate mass protostars, where the accretion rate is higher than that of low mass, the core continues to gain material and the central temperature increases. This lowers the opacity in the middle, enabling the core to become radiative again, with deuterium burning continuing in a convective outer shell (Palla & Stahler 1990). High–mass protostars do not need to form convective shells and the energy released by deuterium burning can be released by radiative energy transport. This therefore results in a completely different evolutionary track in the Hertzsprung–Russell diagram (*e.g.* Iben 1965; Figure 1.1).

Sources evolve from the right to the left along the tracks shown, ending on the main sequence. During a large portion of the time spent on these evolutionary tracks, the young stellar object is still embedded in the cloud core from which it formed, and will not be visible optically. Yorke & Shustov (1981) and Adams (1990) therefore suggest that the characteristic observable properties of a source of a given age are its luminos-

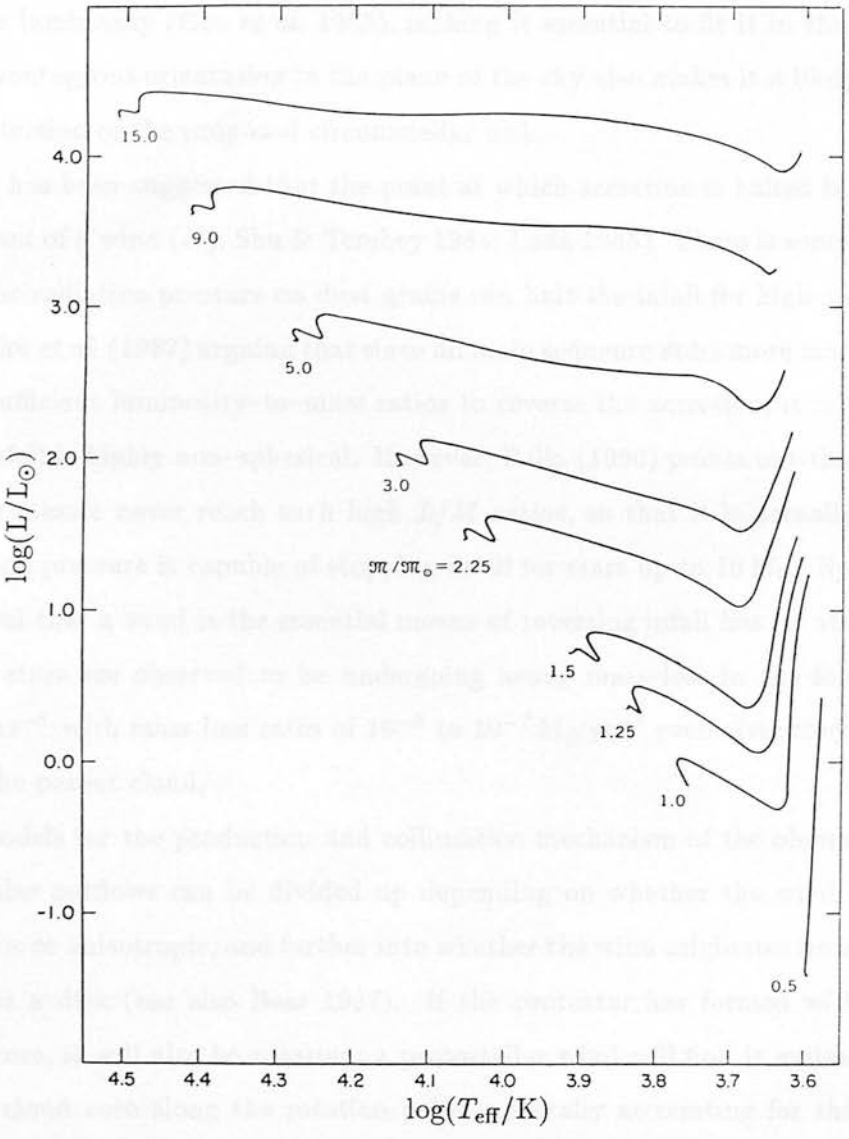

Figure 1.1: Paths in the Hertzsprung–Russell diagram for pre–main sequence evolution (from Iben 1965).

ity (entirely due to accretion until nuclear burning starts) and the remaining column density of material (or equivalently the foreground extinction A_V). In Chapter 2 I use the theoretical tracks calculated by Adams (1990) for protostellar evolution in a luminosity–A_V diagram to examine the evolutionary state of a well–known example of low–mass star formation in the isolated globule B335 (Chandler *et al.* 1990). It had been proposed that the embedded source is a very young protostar with significant accretion luminosity (Gee *et al.* 1985), making it essential to fit it in the above picture. Its advantageous orientation in the plane of the sky also makes it a likely candidate for the detection of the proposed circumstellar disk.

It has been suggested that the point at which accretion is halted is determined by the onset of a wind (*e.g.* Shu & Terebey 1984; Lada 1985). There is some confusion over whether radiation pressure on dust grains can halt the infall for high–mass protostars, with Shu *et al.* (1987) arguing that since all main sequence stars more massive than $7\,M_\odot$ have sufficient luminosity–to–mass ratios to reverse the accretion, it is therefore likely that infall is highly non–spherical. However, Palla (1990) points out that protostars of similar masses never reach such high L/M ratios, so that it is actually unlikely that radiation pressure is capable of stopping infall for stars up to $10\,M_\odot$. Nevertheless, the proposal that a wind is the essential means of reversing infall has its attractions, since young stars are observed to be undergoing heavy mass–loss in the form of winds of $100\,km\,s^{-1}$ with mass loss rates of 10^{-8} to $10^{-7}\,M_\odot\,yr^{-1}$ even after they have emerged from the parent cloud.

Models for the production and collimation mechanism of the observed large–scale molecular outflows can be divided up depending on whether the wind is intrinsically isotropic or anisotropic, and further into whether the wind originates from the protostar itself or a disk (see also Boss 1987). If the protostar has formed within a rotating cloud core, it will also be rotating; a protostellar wind will find it easiest to break out of the cloud core along the rotation poles, naturally accounting for the bipolarity of the observed outflows (Shu *et al.* 1987). The solid angle subtended by the wind then gradually increases until it has dispersed most of the surrounding cloud to reveal a pre–main–sequence star/disk system in the low–mass case. Alternative suggestions for collimating an initially isotropic protostellar wind depend on the density structure of the surrounding cloud; Königl (1982) proposed that de Laval nozzles would form in a wind blowing along a negative pressure gradient, with the ambient magnetic field being

responsible for the flattening of the cloud, and Barral & Cantó (1981) also model the effects of a wind being collimated by a surrounding, flattened disk.

Intrinsically collimated winds can either originate from the protostar or a disk. Protostellar wind models invoke high magnetic fields in a rotating protostar, which if coupled to the magnetic field in the interstellar medium, can result in ambient material being swept up in a magnetic bubble emanating from the protostar (Draine 1983), or can even give rise to a magnetohydrodynamically driven protostellar wind in higher mass protostars (Hartmann & MacGregor 1982). All models for disk winds require that the rotational energy of the disk ultimately be converted into the energy of the wind. Torbett (1984) suggested that the energy liberated at the boundary layer shock of a rotating accretion disk could result in an intrinsically bipolar pressure–driven wind. The last category of disk winds are those in which twisted magnetic field lines thread through a large disk, and the wind is either driven from the surface of the disk centrifugally along the magnetic field lines (Pudritz & Norman 1986) or magnetohydrodynamically (Uchida & Shibata 1985). The problem associated with disk winds is that the massive disks required by the Pudritz & Norman model have very little specific energy and would also result in accretion rates that are too high (Shu *et al* 1987).

An intermediate mechanism is presented by Shu *et al.* (1988), who found that a protostar being spun up to break–up speed at its equator by an accretion disk can result in significant centrifugally–driven mass loss, if its magnetic field is high enough. This can then act as a focussing mechanism for an isotropic protostellar wind. Outflow mechanisms are further discussed in section 2.4.2 with specific reference to B335.

It seems likely that both high and low mass protostars go through a phase of combined infall/outflow, with an accretion disk *and* a bipolar wind. The thermal spectra that emerge from such systems are determined by the temperature and density distributions in the surrounding cloud core, since most of the intrinsic stellar flux will be reprocessed by dust grains further away from the source. Spectra of embedded YSOs have been extensively modelled by Adams & Shu (1985, 1986), Wolfire & Cassinelli (1986) and Wolfire & Churchwell (1987), and for low–mass objects at least, Adams, Lada & Shu (1987) have attempted to classify sources according to their spectral energy distributions. This has been successful to some extent, though the coolest sources that they term "protostars" include rather a large range of evolutionary phases, from sources that are believed to be deriving the majority of their luminosity from accretion

to embedded pre–main–sequence stars such as L1551 IRS5.

Since young stars at almost all stages in their evolution before they reach the main sequence (and high–mass stars at the beginning of their lives on the main–sequence) are surrounded by dust, the properties of interstellar dust grains play an immensely important role in determining the spectral appearance of YSOs. The temperature and density distribution of the gas and dust near forming stars is best traced directly by the characteristic emission from dust and the rotational transitions of molecules; indeed, in order to test the above theories observations of the morphology and velocity structure of dense cores and circumstellar material are *essential* to pin down the nature of the initial collapse process, and the origin of bipolar outflows. The one remaining failing of observational star formation is the lack of "true protostars" that have yet to start nuclear burning within the core, and are still deriving all their luminosity from accretion. Until candidates have been identified, the study of star formation must rely on the results of detailed observations of more evolved sources.

1.3 Thermal dust emission

Not only does dust determine the spectral distribution of YSOs, it can also be used, once its characteristic emission properties are known, to measure cloud masses (Hildebrand 1983). Dust grains in the interstellar medium heated to minimum temperatures of about 10 K radiate strongly in the far–infrared, producing grey–body spectra that peak at around 100 μm. At submillimetre/millimetre wavelengths the emission is almost always optically thin, so that the flux density $F(\nu)$ from a cloud of $N_{\rm tot}$ spherical dust grains with an average radius a, temperature T and emissivity $Q_{\rm em}(\nu)$ at a distance D is

$$F(\nu) = N_{\rm tot} Q_{\rm em}(\nu) B(\nu, T) \frac{\pi a^2}{D^2} \tag{1.1}$$

where $B(\nu, T)$ is the Planck function. This can be related to the mass of dust present, given by

$$M_{\rm dust} = N_{\rm tot} \rho \frac{4}{3} \pi a^3 \tag{1.2}$$

where ρ is the grain density. In order to obtain a total cloud mass (approximately equal to the gas mass), a value for the ratio $M_{\rm gas}/M_{\rm dust}$ must also be assumed. Combining equations 1.1 and 1.2 we obtain $M_{\rm cloud}$ as a function of $F(\nu)$,

$$M_{\rm cloud} = \frac{F(\nu)D^2}{B(\nu,T)}\frac{4\rho a}{3Q_{\rm em}(\nu)}\frac{M_{\rm gas}}{M_{\rm dust}}. \tag{1.3}$$

Fortunately the factor $\frac{4\rho a M_{\rm gas}}{3Q_{\rm em}M_{\rm dust}}$ can be calibrated observationally in the following way (Hildebrand 1983). The cloud mass can also be described by the relation

$$M_{\rm cloud} = \Omega_{\rm source} D^2 N({\rm H_2}) m_{\rm H_2} \mu, \tag{1.4}$$

where $\Omega_{\rm source}$ is the source solid angle, $N({\rm H_2})$ is the molecular hydrogen column density and μ is the mean molecular weight of particles in the interstellar medium, taken to be equal to 1.36. The above equation implicitly assumes that all the hydrogen is molecular. As long as we are using a wavelength that is optically thin, the optical depth of the dust emission is obtained from

$$\tau(\nu) = \frac{F(\nu)}{B(\nu,T)\Omega_{\rm source}}, \tag{1.5}$$

so that substituting for $\Omega_{\rm source}$ in equation 1.4,

$$M_{\rm cloud} = \frac{F(\nu)D^2}{B(\nu,T)}\frac{N({\rm H_2})}{\tau(\nu)} m_{\rm H_2}\mu. \tag{1.6}$$

Comparing this with equation 1.3, it is easy to see that the unknown factor is equivalent to

$$\frac{4\rho a M_{\rm gas}}{3Q_{\rm em}(\nu)M_{\rm dust}} = \frac{N({\rm H_2})m_{\rm H_2}\mu}{\tau(\nu)}.$$

There is now one remaining quantity left to be measured, and that is the ratio $N({\rm H_2})/\tau(\nu)$. The frequency dependence of the optical depth is going to be determined by the frequency dependence of $Q_{\rm em}(\nu)/a$, which for a simple grain model is described below; once that is known, and the ratio $N({\rm H_2})/\tau(\nu)$ has been measured at one frequency, then it can be scaled to obtain its value at other frequencies. By observing a cloud thin enough to measure its A_V, thereby obtaining its molecular hydrogen column density using a suitable reddening law $A_V/E(B-V)$ (Rieke & Lebofsky 1985) and the conversion from $E(B-V)$ to $N({\rm H_2})$ (Bohlin, Savage & Drake 1978), the ratio $N({\rm H_2})/\tau(750\,{\rm GHz})$ has been measured to be $6\times10^{28}\,{\rm molecules\,m^{-2}}$ (see the "1983 Chicago assumptions": Hildebrand 1983).

In order to obtain the behaviour of the emissivity at long wavelengths, consider the interaction of radiation with a grain material that has a complex electric susceptibility $\chi(\nu) = \chi'(\nu) + i\chi''(\nu)$. Sufficiently far away from a resonance, the imaginary part of the complex refractive index of a medium can be approximated by $n'' \simeq \varepsilon_r''/2 = \chi''/2$. This means that the intensity of incident radiation is attenuated by a factor $e^{-2\pi\nu\chi''(\nu)l/c}$ by

passing through a medium of extent l, where c is the speed of light in a vacuum. But this absorption can also be described in terms of the optical depth τ, which is related the extinction efficiency $Q_{\rm ext}$ of the individual dust grains by $\tau(\nu) = \pi a^2 Q_{\rm ext}(\nu) n l$, where n is the grain number density and $Q_{\rm ext}$ is the sum of the grain absorption efficiency $Q_{\rm abs}$ and the scattering efficiency $Q_{\rm sca}$. For far–infrared/submillimetre wavelengths, where $\lambda \gg a$, the scattering efficiency is negligible, and $Q_{\rm ext}$ is dominated by $Q_{\rm abs}$. Therefore,

$$\chi''(\nu) = \frac{a^2 Q_{\rm abs}(\nu) n c}{2\nu}, \tag{1.7}$$

and since Kirchoff's law states that $Q_{\rm abs} = Q_{\rm em}$, $\chi''(\nu)$ can be directly related to $Q_{\rm em}(\nu)$.

For $\nu \rightarrow 0$, the frequency dependence of $Q_{\rm abs}/a$ can be derived by considering a grain model in which χ is determined by the forced oscillation of damped oscillators, namely ions in fixed lattice positions (*e.g.* Andriesse 1977). In this case, χ can be described by

$$\chi(\nu) \propto \frac{n a^3}{\nu_0^2 - \nu^2 + i\gamma\nu}$$

where γ is the damping constant and ν_0 is the last resonance frequency of the material. The imaginary part, which we want to use in equation 1.7, is therefore

$$\chi''(\nu) \propto \frac{\gamma \nu n a^3}{(\nu_0^2 - \nu^2)^2 + \gamma^2 \nu^2},$$

giving, for $\nu \rightarrow 0$,

$$\frac{Q_{\rm abs}}{a} \propto \nu^2.$$

Thus for crystalline grain materials at least, with $Q_{\rm abs}/a \propto \nu^\beta$, $\beta \simeq 2$ is expected. Amorphous materials are also expected to show a similar frequency dependence, $1 \leq \beta \leq 2$, but here the reason is because the absorption depends on the density of phonon states (Tielens & Allamandola 1987), which for isotropic materials is proportional to ν^2, and for layered materials (for example graphite) and small particles is proportional to ν. Mixtures of these structures produce intermediate values of β.

Spectra are generally fitted by functions of the form $\Omega(1 - e^{\tau(\nu)})B(\nu, T)$, with $\tau(\nu) \propto \nu^\beta$, in order to derive the dust temperature T. The cloud mass can then be estimated by inserting the numerical values into equation 1.6 to give

$$M_{\rm cloud} = 0.2 \left(\frac{D}{\rm kpc}\right)^2 \left(\frac{F(\nu)}{\rm Jy}\right) \left(\frac{750\,{\rm GHz}}{\nu}\right)^{3+\beta} \left(e^{h\nu/kT} - 1\right) \quad {\rm M}_\odot. \tag{1.8}$$

The assumption of a single dust temperature can result in severe errors when calculating gas masses from far–infrared emission alone (Draine 1990). However, as equation 1.8 shows, in the Rayleigh–Jeans part of the spectrum, where $h\nu \ll kT_{\rm dust}$, $M_{\rm cloud}$ is only linearly dependent on the dust temperature used; fitting full continuum spectra, including the long–wavelength, optically–thin data, therefore results in a better estimate of the cloud mass than far–infrared colour temperatures obtained from IRAS.

Gaussian geometry is often assumed for both source and beam, so that $F(\nu)$ and $\Omega_{\rm source}$ can be replaced in equation 1.5 by $S(\nu)$, the flux density measured per beam, and Ω, the convolution of the source and beam:

$$\Omega = \Omega_{\rm beam} \otimes \Omega_{\rm source} = \Omega_{\rm beam} + \Omega_{\rm source}. \qquad (1.9)$$

Expressions for the column and space densities, $N(\mathrm{H_2})$ and $n(\mathrm{H_2})$ assuming Gaussian geometry as described above are given by Gear (1988).

Full radiative transfer calculations (*e.g.* Scoville & Kwan 1976) show that in the presence of temperature and density gradients the spectral index of optically–thin emission in the submillimetre never quite reaches the value $S(\nu) \propto \nu^{2+\beta}$. This is mainly because of the presence of cool dust whose emission at submillimetre wavelengths will not be in the Rayleigh–Jeans part of the spectrum, and will therefore enhance the flux at long wavelengths, and have less effect at shorter wavelengths. Emerson (1988) shows how the frequency dependence of the flux can be estimated for given power–law density and temperature distributions. For an optically–thin dust cloud the temperature varies as $T_{\rm dust}(r) \propto r^{-2/(4+\beta)}$, far less significant than the variation in density, which is more likely to be $\rho(r) \propto r^{-1.5}$ to r^{-2}. Since the flux $S(\nu)$ is proportional to the integral along the line of sight of the density times the temperature, it is clear that the density distribution plays the most significant role in determining the flux distribution on the sky (Scoville & Kwan 1976). For this reason optically–thin thermal dust emission is especially good for tracing the morphology of dense cloud cores and disks around young stellar and pre–stellar objects.

1.4 Molecular line emission

One advantage that observations of molecular lines have over dust emission, besides the fact that they reveal the velocity structure of molecular clouds, is that they can be used to probe different excitation conditions within a cloud depending on the line

used, not necessarily just those parts with the highest column density, by virtue of the nature of molecular excitation. The simplest molecules are those that are diatomic, for which the equations relating observed parameters to the excitation conditions under the assumption of LTE are derived below. CS has been used in Chapters 3 and 4 to trace the morphology and kinematics of dense gas in cloud cores, so I have summarised the properties of the molecule that make it such a good probe of dense regions at the end of this section.

Consider a transition between rotation states $J = j \rightarrow i$ with frequency ν_{ji}, where $j = i + 1$. The absorption coefficient $\kappa(\nu_{ji})$ is given by

$$\kappa(\nu_{ji}) = \frac{h\nu_{ji}}{4\pi}(n_i B_{ij} - n_j B_{ji})\phi(\nu_{ji}).$$

where, B_{ij} and B_{ji} are the Einstein B–coefficients for absorption and radiatively–induced emission respectively, $\phi(\nu_{ji})$ is the line profile function and n_j, n_i are the numbers of molecules in the upper and lower states. This can be written as

$$\kappa(\nu_{ji}) = \frac{h\nu_{ji}}{4\pi} n_i B_{ij} \left(1 - \frac{n_j B_{ji}}{n_i B_{ij}}\right) \phi(\nu_{ji}).$$

and since the Einstein B–coefficients are related by the statistical weight of each level, $g_i B_{ij} = g_j B_{ji}$, this is equivalent to

$$\kappa(\nu_{ji}) = \frac{h\nu_{ji}}{4\pi} n_i B_{ij} \left(1 - \frac{n_j g_i}{n_i g_j}\right) \phi(\nu_{ji}). \tag{1.10}$$

If the level populations are thermalised, either because of high density (so that the populations are determined by collisions with gas) or high optical depth (so that the populations of the higher levels are increased by radiative trapping: Leung, 1978), they can be described by a Boltzmann distribution at the gas kinetic temperature $T_{\rm kin}$. Otherwise, an excitation temperature, $T_{\rm ex}$, can be *defined* to be related to the relative populations of the two levels by

$$\frac{n_j}{n_i} = \frac{g_j}{g_i} e^{-h\nu_{ji}/kT_{\rm ex}}. \tag{1.11}$$

The effect of radiative trapping is especially important for abundant molecules such as CO, so that significant emission is possible from molecular gas at densities an order of magnitude lower than would be expected from collisional excitation alone. For this reason CO is the most important molecule for tracing the molecular gas in the Galaxy. However its high optical depth generally makes it unsuitable for use in examining very dense cores of clouds.

It is better to express $\kappa(\nu_{ji})$ in terms of the Einstein A–coefficient for spontaneous emission, which is independent of the incident radiation field, so using the relation

$$B_{ij} = \frac{g_j}{g_i}\frac{c^2}{2h\nu_{ji}^3}A_{ji},$$

and equation 1.11 to substitute for B_{ij} and $\frac{n_j g_i}{n_i g_j}$ in equation 1.10,

$$\kappa(\nu_{ji}) = \frac{c^2}{8\pi}\frac{g_j}{g_i}n_i\frac{A_{ji}}{\nu_{ji}^2}(1 - e^{-h\nu_{ji}/kT_{ex}})\phi_(\nu_{ji}).$$

In order to relate this to the *total* number density of molecules n, n_i has to be expressed in terms of the partition function $\mathcal{U}$:

$$\frac{n_i}{n} = \frac{g_i}{\mathcal{U}}e^{-E_i/kT_{ex}}.$$

The energy above the ground state of level i is $E_i = hBi(i+1)$ where B is the rotation constant of the molecule, and the partition function is defined by

$$\mathcal{U} = \sum_{i=0}^{\infty} g_i e^{-E_i/kT_{ex}}.$$

In general the excitation temperature of a particular level will be different from other levels, and in practice the conditions in molecular clouds will result in a finite number of levels being populated, since the energy level spacing increased with i. The assumption of LTE implies that *all* the levels have the same excitation temperature, equal to the kinetic temperature. For high temperatures $kT_{ex} \gg hB$, the summation can be approximated by an integral, giving

$$\mathcal{U} \simeq \frac{kT_{ex}}{hB}. \tag{1.12}$$

Higher order terms are needed for molecules with high rotation constants like CO under low excitation conditions, so that $\mathcal{U} = \frac{kT_{ex}}{hB} + \frac{1}{3} + ...$ (Townes & Schawlow 1955). However for CS, which has a rotation constant less than half that of CO, the extra terms are negligible for $T_{ex} \gtrsim 10\,\mathrm{K}$, so I have used the expression in equation 1.12 in what follows. So now the absorption coefficient can be expressed in terms of the total molecular number density,

$$\kappa(\nu_{ji}) = \frac{c^2}{8\pi}g_j\frac{hB}{kT_{ex}}e^{-E_i/kT_{ex}}\frac{A_{ji}}{\nu_{ji}^2}(1 - e^{-h\nu_{ji}/kT_{ex}})n\phi(\nu_{ji}).$$

This must now be related to the observed quantity – the line brightness temperature, which is defined by

$$T_R = J(T_{ex})(1 - e^{-\tau(\nu)}) \tag{1.13}$$

where

$$J(T) = \frac{h\nu}{k}\left\{\frac{1}{(e^{h\nu/kT}-1)} - \frac{1}{(e^{h\nu/kT_{\rm bg}}-1)}\right\}, \tag{1.14}$$

and $T_{\rm bg}$ is the temperature of the microwave background, taken to be 2.7 K. It is by making the approximation

$$\begin{aligned}\tau(\nu_{ji}) &= \int \kappa(\nu_{ji})dx \simeq \kappa(\nu_{ji})L \\ &= \frac{c^2}{8\pi}g_j\frac{hB}{kT_{\rm ex}}e^{-E_i/kT_{\rm ex}}\frac{A_{ji}}{\nu_{ji}^2}(1-e^{-h\nu_{ji}/kT_{\rm ex}})N\phi(\nu_{ji}).\end{aligned}$$

for a uniform source, where x is an element along the line of sight, and L is the total extent along the line on sight of the emitting region, that $T_{\rm R}$ as a function of $T_{\rm ex}$ and the molecular column density N can be obtained. By substituting for E_i, $g_j = 2j+1$ and A_{ji}, which is given by

$$A_{ji} = \frac{16\pi^3}{3\varepsilon_0 hc^3}\nu_{ji}^3\mu^2\frac{j}{2j+1} \tag{1.15}$$

where μ is the dipole moment of the molecule, gives

$$\tau(\nu_{ji}) = \frac{2\pi^2}{3\varepsilon_0 c}\frac{B}{kT_{\rm ex}}\nu_{ji}\mu^2 j e^{-hBi(i+1)/kT_{\rm ex}}(1-e^{-h\nu_{ji}/kT_{\rm ex}})N\phi(\nu_{ji}). \tag{1.16}$$

The broadening of molecular lines in regions of star formation is almost invariably due to the dynamics of the cloud, since the observed line widths are much larger than the intrinsic line widths and are frequently also larger than the thermal line widths (Linke & Goldsmith 1980). The line profile function is therefore determined by the cloud's velocity field. Often, a Gaussian line shape caused by turbulence is assumed, so that integrated over the whole of the line,

$$\int \tau(\nu)d\nu \simeq 1.064\tau_0\Delta\nu \simeq \tau_0\frac{\Delta V\nu_{ji}}{c}$$

where τ_0 is the line peak optical depth and ΔV the velocity FWHM, assumed to be the same for each transition. By observing successive transitions $J = k \rightarrow j$, $J = j \rightarrow i$ (where $k = j+1$), their optical depth ratios give

$$\frac{\tau_{kj}}{\tau_{ji}} = \frac{j+1}{j}\frac{[1-e^{-2hB(j+1)/kT_{\rm ex}}]}{[e^{2hBj/kT_{\rm ex}}-1]}.$$

In this way, once the line brightness ratio

$$\frac{T_{kj}}{T_{ji}} = \frac{1-e^{-\tau_{kj}}}{1-e^{-\tau_{ji}}} \tag{1.17}$$

has been determined, an estimate for $T_{\rm ex}$ can be calculated.

If the same transition in a rare isotope (for example $C^{34}S$) is observed with a known abundance ratio relative to the brighter molecule (CS), an absolute value for the optical depth can be derived, again from the line brightness ratio:

$$\frac{T_{\rm R}(CS)}{T_{\rm R}(C^{34}S)} = \frac{1-e^{\tau_{CS}}}{1-e^{-\tau_{C^{34}S}}} = \frac{1-e^{R\tau_{C^{34}S}}}{1-e^{-\tau_{C^{34}S}}}$$

where $R = X(CS)/X(C^{34}S)$.

In theory, equations 1.13 and 1.14 can be combined, assuming $T_{\rm ex} \gg T_{\rm bg}$, to derive $T_{\rm ex}$:

$$T_{\rm ex} \simeq \frac{h\nu}{k}\left[\ln\left(1+\frac{h\nu(1-e^{-\tau})}{kT_{\rm R}}\right)\right]^{-1}. \qquad (1.18)$$

However this also assumes that an accurate value for $T_{\rm R}$ can be obtained, and in practice the source structure *within* the telescope beam is generally unknown. Thus equation 1.17 gives a better estimate of a beam–averaged $T_{\rm ex}$, as long as the same beam size was used for each line. This is not as much of a problem when using rare isotopes, since the beam size will be the same for both species if the same telescope is used. Cantó, Rodríguez & Anglada (1987) discuss the uncertainties this method of LTE analysis introduces in the presence of a temperature gradient. In section 4.3 I discuss the effect of the assumption of LTE on the derivation of N using the above equations.

The CS molecule has a sufficiently high dipole moment (approximately 20 times that of CO) that it requires molecular hydrogen number densities $\gtrsim 10^{11}\,{\rm m}^{-3}$ for the levels to be populated according to the kinetic temperature. A critical density $(n_{\rm crit})_{ji} = C_{ji}(T_{\rm kin})/A_{ji}$, where C_{ji} is the collision rate for excitation from $J = j \rightarrow i$, can be defined as a measure of the density required for excitation of the level j to be above that of the background radiation field. For $T_{\rm kin} = 40\,{\rm K}$, I have used the collision rates from Green & Chapman (1978) and $\mu = 6.6 \times 10^{-30}\,{\rm Cm}$ (in equation 1.15) to tabulate values of $n_{\rm crit}$ for the lower transitions of CS (Table 1.1). The frequencies ν_{ji} are taken from Lovas (1986).

Since stars are known to form in the dense cores of molecular clouds, CS is clearly an excellent probe of the conditions pertaining to the star formation process. The density obtained from modelling particular molecular lines can be expected to be close to $n_{\rm crit}$, since this is a measure of the density needed to obtain significant emission and higher densities will serve to thermalise the populations of the higher energy levels. Snell *et al.* (1984) and Mundy *et al.* (1986) illustrate how CS and its rare isotope $C^{34}S$ can be

Table 1.1: Critical densities for CS.

Transition $j \rightarrow i$	ν_{ji} (GHz)	A_{ji} (s^{-1})	$C_{ji}(40\,K)$ ($m^{-3}\,s^{-1}$)	n_{crit} (m^{-3})
$1 \rightarrow 0$	48.991	1.78×10^{-6}	2.5×10^{-17}	7×10^{10}
$2 \rightarrow 1$	97.981	1.71×10^{-5}	3.9×10^{-17}	4×10^{11}
$3 \rightarrow 2$	146.969	6.19×10^{-5}	4.5×10^{-17}	1×10^{12}
$4 \rightarrow 3$	195.954	1.52×10^{-4}	4.7×10^{-17}	3×10^{12}
$5 \rightarrow 4$	244.936	3.04×10^{-4}	4.3×10^{-17}	7×10^{12}
$6 \rightarrow 5$	293.912	5.33×10^{-4}	4.5×10^{-17}	1×10^{13}
$7 \rightarrow 6$	342.883	8.57×10^{-4}	3.9×10^{-17}	2×10^{13}

used to examine the density profiles of molecular clouds, and have discovered that cores associated with OB star formation do not have prominent large–scale density gradients, unlike clouds forming low–mass stars (*e.g.* Loren, Sandqvist & Wootten 1983).

The 7 – 6 transition of CS and $C^{34}S$ has been used in Chapter 3 to look at warm, dense gas in NGC 2024, and in Chapter 4 the lowest two transitions in both isotopes are modelled using the above LTE equations to determine the excitation conditions of DR21(OH).

Chapter 2

B335

2.1 Introduction

B335 is an isolated dark cloud with a relatively simple structure compared with most molecular clouds. An upper limit of 400 pc has been placed on its distance by the absence of foreground stars (Bok & McCarthy 1974), although large–scale extinction measurements and its coincidence with the Lindblad ring (Tomita, Saito & Ohtani 1979; Elmegreen 1982) have led most authors to assume a distance of 250 pc, which I have also adopted. An associated compact, embedded, far–infrared/submillimetre continuum source was detected by Keene *et al.* (1983), and a low–velocity bipolar outflow was found to be centred on the FIR source by Frerking & Langer (1982) and Goldsmith *et al.* (1984), signalling the presence of low–mass star formation. The large–scale structure and dynamics of the globule have been studied in detail by Frerking, Langer & Wilson (1987), who, after detecting a blue– and red–shifted component in ^{12}CO $J = 1 - 0$ channel maps offset from the original outflow (Langer, Frerking & Wilson 1986), deduced that the globule was in fact evolved, with two outflows, rather than a young cloud still undergoing star–formation as had previously been thought. More recently, however, the over–lapping red– and blue–shifted emission has been interpreted as the result of a highly–collimated single bipolar outflow, oriented in the plane of the sky (Hirano *et al.* 1988; Cabrit, Goldsmith & Snell 1988; Moriarty-Schieven & Snell 1989). Hirano *et al.* concluded that the flow must be focussed within 0.02 pc of the driving source.

B335 also has a possible HH object in the red lobe of the outflow, detected by Hα emission (Vrba *et al.* 1986). This might be considered surprising, since one would expect HH objects to be detected preferentially in the blue lobe, but as the outflow is

nearly in the plane of the sky the column density of intervening dust and gas is likely to be similar for both the blue and red lobes. Moreover, the red lobe appears to have broken out of the edge of the cloud (Moriarty-Schieven & Snell 1989), indicating that there must be a steeper density gradient along the red lobe than the blue lobe, making it possible for us to detect optical emission from nearer to the central object in the red lobe than the blue lobe.

The FIR source at the centre of the outflow was barely resolved in a 55 arcsec beam at 360 μm by Gee *et al.* (1985), who claimed a source size of 28 ± 5 arcsec. Gee *et al.* argued that their data were consistent with a protostellar source, but were unable to resolve the accretion disk that they proposed as the source of the luminosity, and a possible driving source of the outflow.

A possible test of the model put forward by Gee *et al.* (1985) is to resolve the small–scale structure associated with the FIR source, so particular emphasis is placed on high–resolution continuum observations. Below, the results of mapping the dust emission at submillimetre wavelengths are used to try to determine the true evolutionary state of the embedded source. This work has been published by Chandler *et al.* (1990).

2.2 Observations

The submillimetre continuum observations were made with the 15 m James Clerk Maxwell Telescope (JCMT) on Mauna Kea, Hawaii, during 1988 April, August and October. Photometry was performed using the common–user ^{3}He cooled bolometer UKT14, with filters centred on 2 mm, 1.3 mm, 1.1 mm, 800 μm, 600 μm, 450 μm and 350 μm. Flux calibration was performed against Mars and Uranus, and is the most significant source of uncertainty in the photometry, due to variation in the sky transparency over the period of the observations. The photometry is shown in Table 2.1, where the total uncertainties include both the statistical and estimated calibration uncertainties.

Two over–sampled maps were made at 800 μm with a 17 arcsec beam. They were taken in an azimuth–elevation coordinate system by chopping and scanning simultaneously, producing differential maps, covering an area 105×105 arcsec, using 7.5 arcsec pixel spacing and a chop throw of 60 arcsec. They were reduced using the NOD2 software (Haslam 1974), and co–added. The pointing accuracy is estimated to be about 4 arcsec for the 800 μm maps. A map was also made at 450 μm with 3 arcsec spacing, for which the HPBW at 450 μm was measured to be 8 ± 1 arcsec from a beam map

Table 2.1: Submillimetre photometry of B335.

Wavelength	Effective freq (GHz)	Beam size (″)	Flux per beam (Jy)	Statistical uncertainty (Jy)	Total uncertainty (Jy)
2 mm	156	32	$3\sigma = 0.57$		
1.3 mm	238	21	0.64	0.03	0.07
1.1 mm	272	19	0.68	0.02	0.07
800 μm	380	17	1.88	0.03	0.28
		13	1.30	0.07	0.21
600 μm	463	19	4.0	0.3	0.85
450 μm	676	18	15.0	1.3	4.7
		8	9.8	1.1	3.1
350 μm	854	18	35	2.4	14

of Uranus. This map was produced from an evenly–spaced grid of single photometry points. The pointing was checked directly before and after the 450 μm map using K3–50, and was found to be accurate to ± 2 arcsec over that period.

2.3 Results

The 800 μm map (solid contours) is displayed in Figure 2.1 together with the CO $J = 1-0$ contours of the outflow from Hirano *et al.* (1988). The lowest contour in the continuum map is at 0.2 Jy, and the other contours are spaced at 1σ intervals of 0.2 Jy. The R.A. and Dec. axes are offsets from the position of the submillimetre source, $\alpha(1950) = 19^{\rm h}34^{\rm m}35.7^{\rm s} \pm 0.7^{\rm s}$, $\delta(1950) = 07°27'15'' \pm 10''$.

Fitting a Gaussian to the flux distribution in the 800 μm map gives a FWHM of 22 ± 2 arcsec. Approximating the actual source distribution to be Gaussian, and after deconvolving with the 17 arcsec beam, a source size of 14 ± 3 arcsec is obtained. The 1σ contour is extended north–south (the axis of symmetry of the outflow is east–west); this low–level emission appears in *both* of the two maps that have been co–added to produce the contour plot displayed in Figure 2.1. At the time that the maps were taken the angles between an R.A.–Dec. coordinate system and the local (az–el) coordinate system were approximately 20°and 55°, so any extended emission is therefore away from the chop direction (azimuth).

The high–resolution 450 μm map is shown in Figure 2.2, where the contours are at 1σ intervals of 1.1 Jy, and the peak is 9.8 Jy. This map covers the central 20 arcsec of

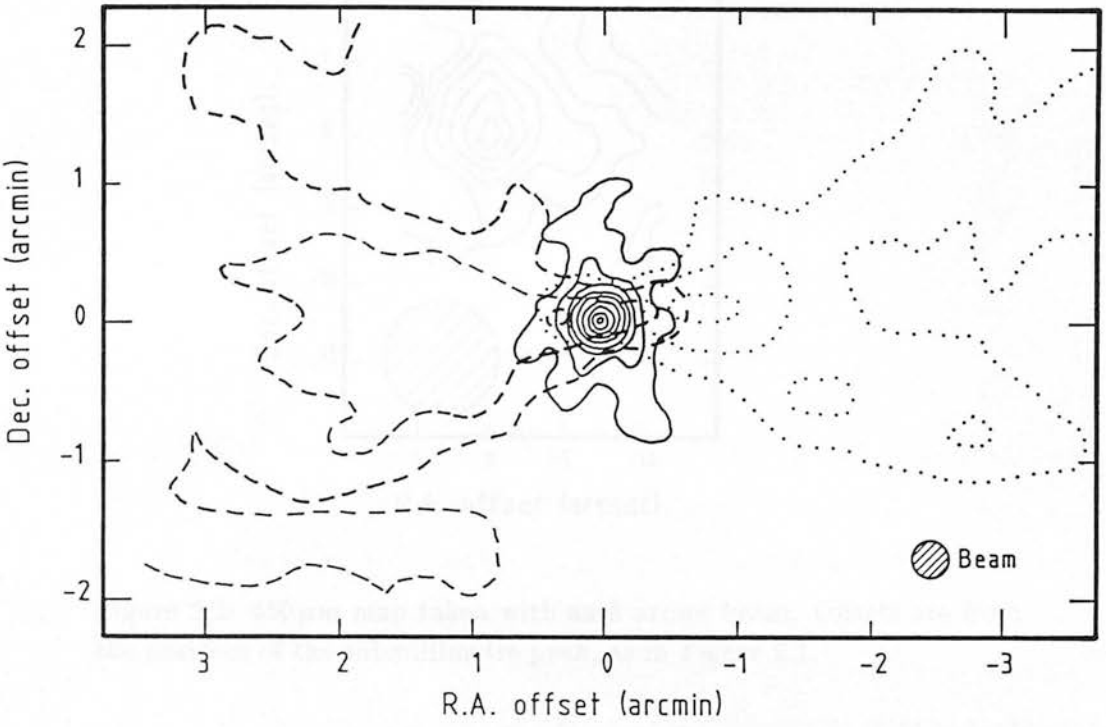

Figure 2.1: 800 μm map of B335 (solid contours) together with the high–velocity CO emission; the blue wing is represented by the dashed contours, and the red wing by the dotted contours. Positional offsets are relative to $19^h34^m35.7^s$, 07°27′15″.

the 800 μm map, and again approximating the source distribution to be Gaussian, the deconvolved source size is < 6 arcsec in right ascension and 7.5±2.0 arcsec in declination. Without fully resolving the source at several wavelengths there is not enough information to be able to model the effects of a temperature and density gradient, or the way in which the apparent source size varies as a function of frequency, so the approximation of Gaussian distributions is used bearing in mind that such gradients are likely to exist. VLA NH_3(1,1) observations, (P.E. Palmer, quoted in Davidson 1987) also indicate a core size less than 15 arcsec.

In order to compare the photometric data (Table 2.1) with earlier measurements made with larger beams, I have calculated the flux that would be obtained in a 50 arcsec Gaussian beam, by convolving the maps with suitably normalised Gaussian functions. In order to do this I have had to assume that the source distribution shown in the 800 μm map is approximately valid for all wavelengths $\lambda \geq 600\,\mu$m, and that the source

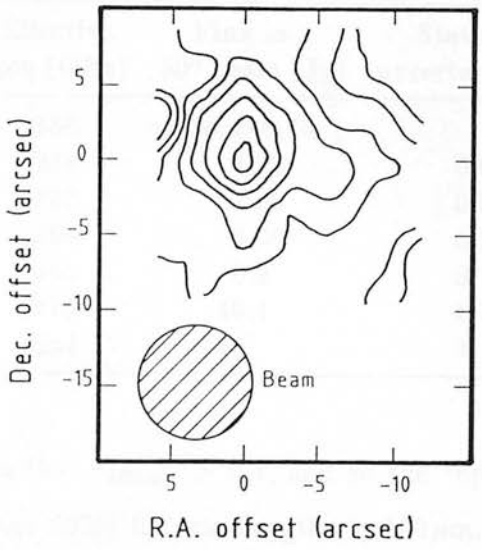

Figure 2.2: 450 μm map taken with an 8 arcsec beam. Offsets are from the position of the submillimetre peak, as in Figure 2.1.

distribution shown in the 450 μm map is approximately valid for $\lambda = 350\,\mu$m as well. There are some difficulties with this when using the 450 μm map, firstly because the diffraction–limited beam at 450 μm has non–Gaussian wings, and secondly because the map does not extend far enough to get entirely off the source. I have approximated the beam to be Gaussian and I have ignored any missed flux outside the region of the map. This results in large uncertainties in the flux in a 50 arcsec beam at 450 μm and 350 μm, but is a more reasonable estimate than would have been obtained had I assumed the same source distribution as at 800 μm. The results of this convolution are shown in Table 2.2, and are also plotted in Figure 2.3.

If a steep density gradient exists then even the longer wavelengths will contain a significant contribution from the warmer dust responsible for the 60 μm emission, so all data taken with a beam size of $\leq$ 50 arcsec (11 points, Figure 2.4), including the 60 μm point, have been used to try to obtain average parameters for the dust within the central region. If the usual assumption that the dust continuum emission is optically thin is made, a blackbody curve with $\tau \propto \nu^{\beta}$ $(1 < \beta < 2)$ does not fit the 60 μm point well (dashed line, Figure 2.4). The results for this fit are $T_{\rm dust} = 23\,$K, $\beta = 1.0$, $\Omega\tau_{450\,\mu{\rm m}} = 1 \times 10^{-10}$ where Ω is the effective solid angle of the source in steradians, and $\chi^2 = 12.6$ with 11 data points and 3 free parameters. The source size in the 450 μm

Table 2.2: Simulated fluxes in a 50 arcsec beam.

Wavelength	Effective freq (GHz)	Flux in a 50″ beam (Jy)	Statistical uncertainty (Jy)	Total uncertainty (Jy)
2 mm	156	$3\sigma = 0.76$		
1.3 mm	238	1.20	0.08	0.14
1.1 mm	272	1.39	0.07	0.16
800 μm	380	4.06	0.13	0.62
600 μm	463	8.2	0.7	1.8
450 μm	676	19.1	1.7	7.6
350 μm	854	45	3	21

map then indicates that $\tau_{450\,\mu\mathrm{m}} > 0.1$, and so the "optically–thin" approximation is only valid (to within 20%) for wavelengths $\gtrsim 100\,\mu$m. However, if the same points are fitted to a blackbody curve modified by $(1 - e^{-\tau})$ (*i.e.*, making no assumptions about the optical depth of the emission) where $\tau \propto \nu^{\beta}$, a better fit is found. This has $\chi^2 = 6.3$ with 11 data points and 4 free parameters – the temperature, the optical depth, the frequency dependence of the optical depth β, and the source size, and occurs for $T_{\mathrm{dust}} = 31\,\mathrm{K}$ (solid curve, Figure 2.4). Integrating under this curve gives a luminosity of approximately $2.6\,\mathrm{L}_{\odot}$. For this model, which assumes a uniformly bright isothermal source, the fitted parameters are $\beta = 1.6$, $\tau_{450\,\mu\mathrm{m}} = 1.7$, and a source area of 3.7 square arcsecs. The optical depth (and implied column density) and the source size derived from such a fit are complicated mean values, and are difficult to interpret relative to the observed source. A lower limit to the temperature of $T_{\mathrm{dust}} = 15\,\mathrm{K}$ is required to account for the Rayleigh–Jeans part of the spectrum including the observed emission at 350 μm.

The column and space molecular hydrogen number densities can be estimated from the dust continuum emission (Hildebrand 1983), although the gas–to–dust ratio has only been calibrated using interstellar clouds that are optically thin in the submillimetre. Using the Chicago assumptions of Hildebrand, I find that for the extreme of the uniform source model of the spectrum $N(\mathrm{H}_2) \sim 1 \times 10^{29}\,\mathrm{m}^{-2}$, $n(\mathrm{H}_2) \sim 1 \times 10^{15}\,\mathrm{m}^{-3}$, and the mass of the gas associated with the dust is $1.3\,\mathrm{M}_{\odot}$. This is in excellent agreement with the mass obtained by Keene *et al.* (1983) of $\simeq 2.5\,\mathrm{M}_{\odot}$ (who used a temperature of 15 K) since in the Rayleigh–Jeans region of the spectrum where the emission is optically thin, the flux is proportional to $M_{\mathrm{dust}} \times T_{\mathrm{dust}}$. Given that in fact a single temperature is

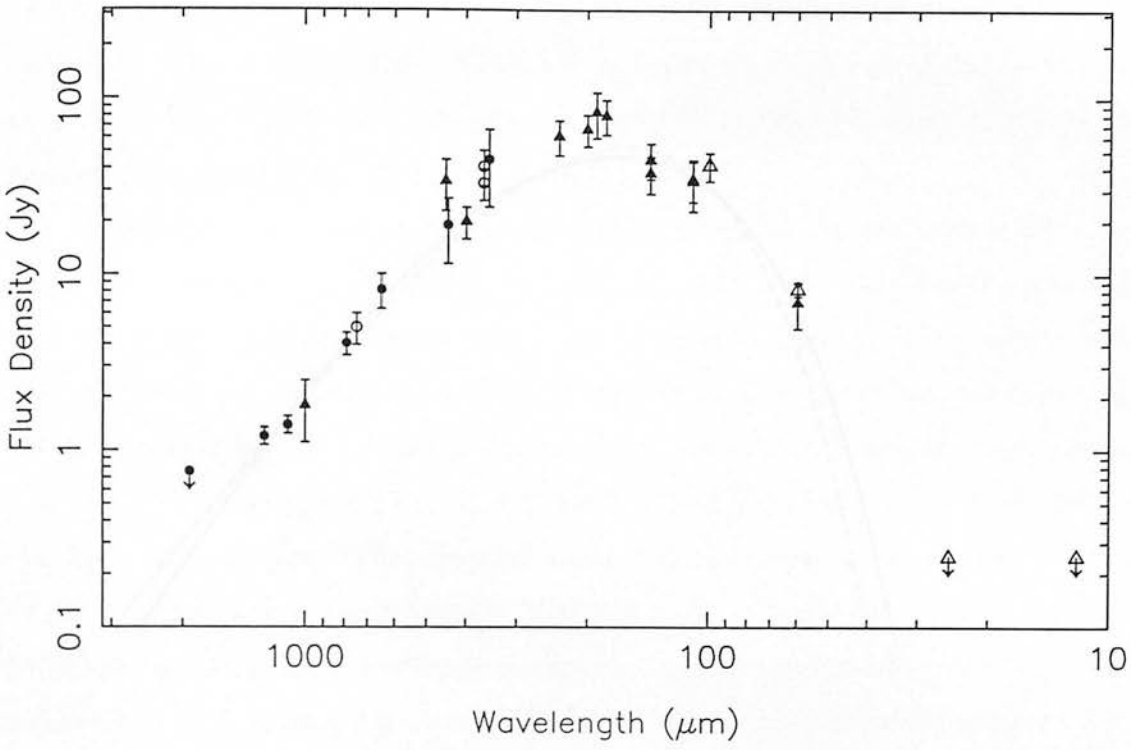

Figure 2.3: The far–infrared/submillimetre spectrum of B335. Points from this work are shown as filled circles. Other data plotted are from Keene *et al.* (1983; filled triangles), Gee *et al.* (1985; open circles) and fluxes from the IRAS *Point Source Catalogue* (open triangles).

unlikely to be a good approximation to the emitting dust, the mass derived from fitting the continuum spectrum with a single temperature is rather uncertain. However, to within the uncertainties of the calibration of the dust–to–gas ratio, these numbers indicate a core mass $M_{\rm core}$ of approximately $2\,{\rm M}_\odot$. Associating this with the source in the $450\,\mu$m map, peak values for a Gaussian distribution of $N({\rm H}_2) \simeq 1 \times 10^{28}\,{\rm m}^{-2}$ and $n({\rm H}_2) \simeq 5 \times 10^{13}\,{\rm m}^{-3}$ are obtained.

2.4 Discussion

2.4.1 The submillimetre source

The structure of the submillimetre continuum source has still not been fully resolved by the observations, but there is some evidence for an elongation north–south, perpen-

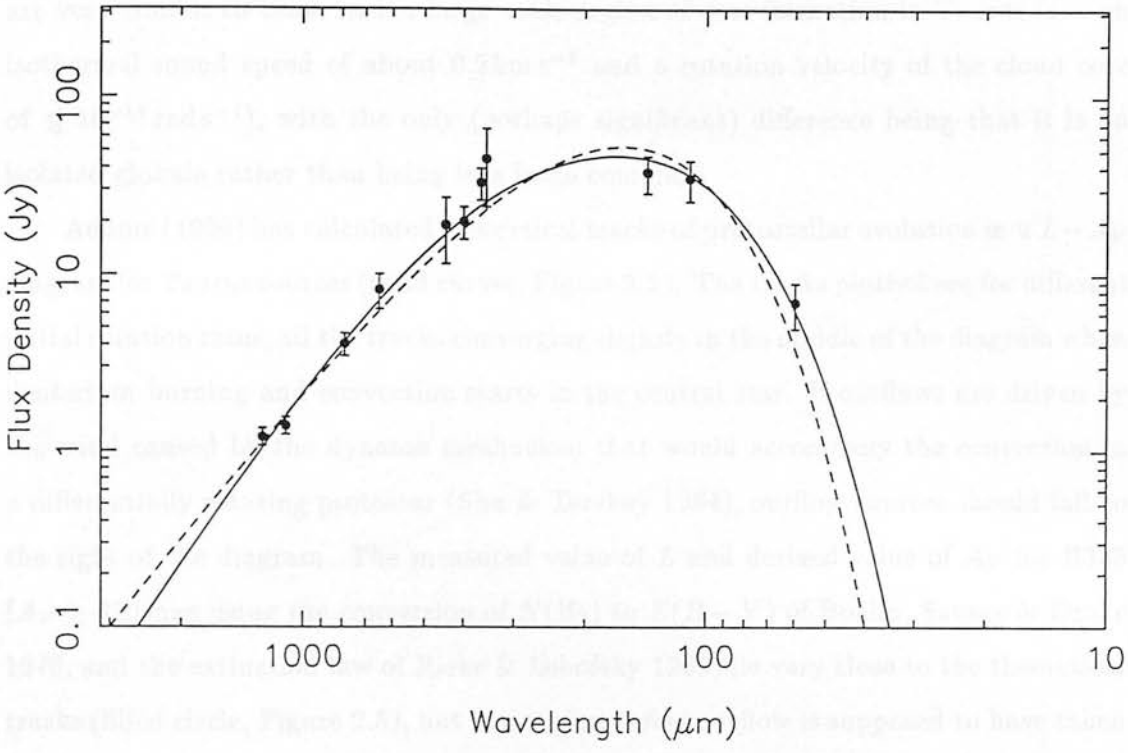

Figure 2.4: Fits to data taken with beams $\leq$ 50 arcsec. The dashed curve is the best "optically–thin" fit (see text), which has $T_{\rm dust}$ = 23 K. The solid curve is the best fit to a function $\Omega(1 - e^{-\tau})B(\nu, T)$, with $T_{\rm dust}$ = 31 K.

dicular to the axis of the outflow. The position of the source is the same as that found by Gee *et al.* (1985), which is 20 arcsec east of that given by Keene *et al.* (1983). This means that the peak in many molecular line maps ($C^{18}O$ 1 – 0, CS 3 – 2 and 2 – 1; NH_3; HC_3N) *is* coincident with the dust continuum source[1]; previously, it had been thought that the FIR source was *not* the significant HC_3N emitting region (Hasegawa *et al.* 1986), although a close association was suggested. Velocity information on very small scales is needed to establish the true relationship of the cloud core, as traced by the submillimetre continuum and molecular emission, to the central exciting object.

If one tries to classify the source in B335 according to the current models of pre–stellar evolution (*e.g.* Shu, Adams & Lizano 1987) then it has already passed the "pro-

[1]Previous $C^{18}O$ 1 – 0 observations of Walmsley & Menten (1987), which showed a $C^{18}O$ peak some 30 arcsec away from the submillimetre source, have been repeated (Menten *et al.* 1989) and now the peak is at the same position as the submillimetre source to within the errors.

tostellar" phase and is now in its "outflow" phase. This being the case, the remarkable property of this source is its low luminosity. The conditions in the surrounding cloud are very similar to those in the large–scale region of star formation in Taurus (*i.e.* an isothermal sound speed of about $0.2\,\mathrm{km\,s^{-1}}$ and a rotation velocity of the cloud core of $\lesssim 10^{-14}\,\mathrm{rad\,s^{-1}}$), with the only (perhaps significant) difference being that it is an isolated globule rather than being in a large complex.

Adams (1990) has calculated theoretical tracks of protostellar evolution in a $L - A_V$ diagram for Taurus sources (solid curves, Figure 2.5). The tracks plotted are for different initial rotation rates, all the tracks converging slightly in the middle of the diagram when deuterium burning and convection starts in the central star. If outflows are driven by the wind caused by the dynamo mechanism that would accompany the convection in a differentially rotating protostar (Shu & Terebey 1984), outflow sources should fall to the right of the diagram. The measured value of L and derived value of A_V for B335 ($A_V \gtrsim 320\,\mathrm{mag}$ using the conversion of $N(\mathrm{H_2})$ to $E(B-V)$ of Bohlin, Savage & Drake 1978, and the extinction law of Rieke & Lebofsky 1985) lie very close to the theoretical tracks (filled circle, Figure 2.5), but in a region *before* outflow is supposed to have taken place. If these tracks are correct, these results could mean that outflow is possible from objects much younger than the Shu *et al.* (1987) model expects, and the source in B335 represents an extremely early stage of protostellar evolution.

Here it is worth noting that the model applied to the theoretical tracks depends on the collapse solution since this determines the temperature and density distribution of the dust in the surrounding envelope. One of the major points to make about the distribution used in the model described above is that accretion occurs through essentially an infinitely thin disk, and that the distribution is approximately spherically symmetric except very close to the source (Terebey, Shu & Cassen 1984). This means that as long as we do not observe the central source along an outflow lobe or within about 3° of the disk plane, the extinction will be almost independent of inclination angle to within a factor of 2 (Adams 1990). The theoretical tracks in the $L - A_V$ diagram are therefore relatively insensitive to the source orientation in principle, though A_V will depend on the collapse model. Likewise, the luminosity depends on the accretion efficiency assumed, and also on the relative fractions of material accreting directly onto the protostar rather than via the accretion disk.

The core of B335 has been resolved perpendicular to the outflow axis but not parallel

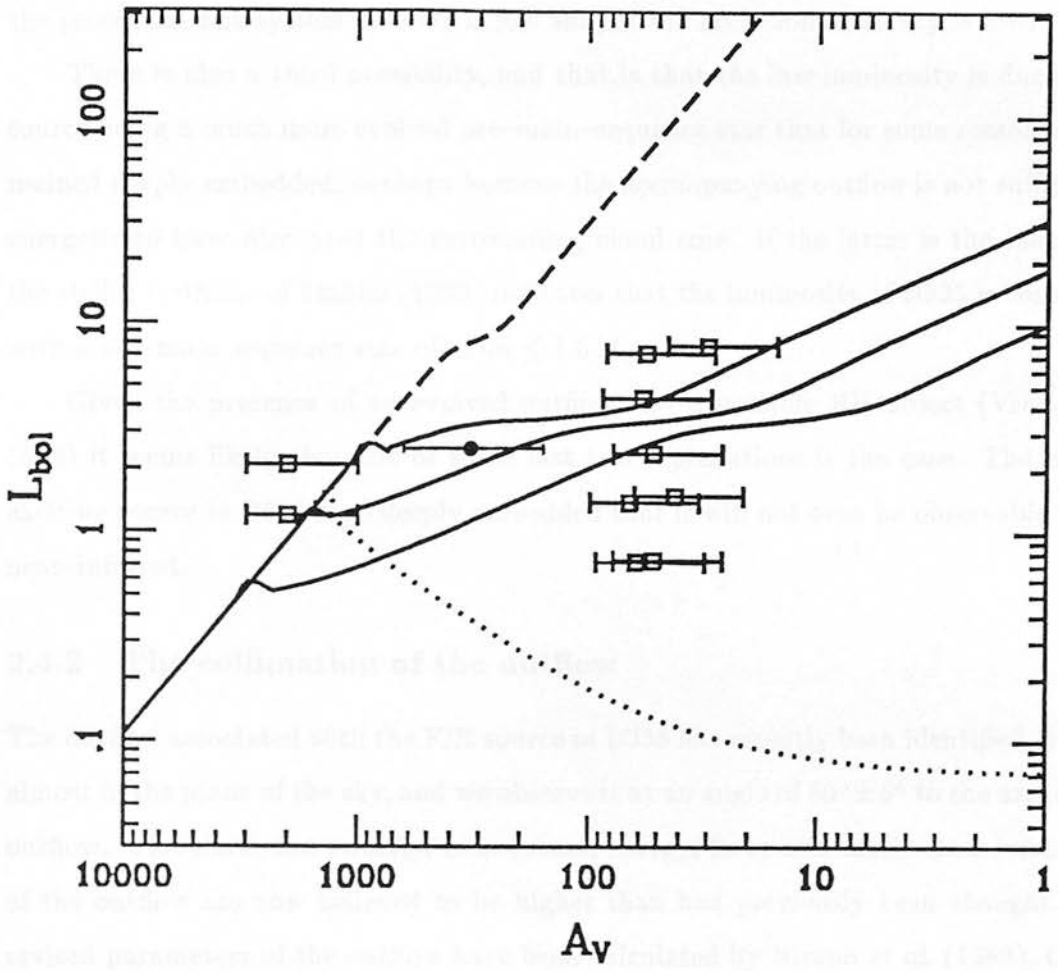

Figure 2.5: Theoretical tracks in the $L - A_V$ diagram for Taurus (from Adams, 1990). Sources that have been observed in Taurus are indicated by open squares. B335 is marked by a filled circle.

to it, suggesting that if the inclination angle of the outflow also defines the inclination angle of a disk or flattened core, the high extinction could be due the high column density of gas and dust in the disk plane, and the low luminosity could then originate from a more evolved object. This could only be the case if an accompanying disk were considerably thicker than that suggested by the theoretical modelling. However, accepting this as a possibility and allowing for a lower extinction to compare with the measured luminosity in the diagram then raises the question of why the luminosity is lower than the theoretical Taurus tracks. It is possible for a source near the beginning of its outflow phase to have a lower luminosity than that predicted by Adams, Lada & Shu

(1987) if the parameters they used for the Taurus molecular cloud are not applicable to an isolated globule such as B335. This can happen if, relative to Taurus, the mass of the protostar–disk system in B335 is low and/or the accretion efficiency is low.

There is also a third possibility, and that is that the low luminosity is due to the source being a much more evolved pre–main–sequence star that for some reason has remained deeply embedded, perhaps because the accompanying outflow is not sufficiently energetic to have disrupted the surrounding cloud core. If the latter is the case, then the stellar birthline of Stahler (1983) indicates that the luminosity of B335 is consistent with a pre–main sequence star of mass $\leq 1.5\,M_{\odot}$.

Given the presence of an evolved outflow and a possible HH object (Vrba *et al.* 1986) it seems likely that one of these last two explanations is the case. The central exciting source in B335 is so deeply embedded that it will not even be observable in the near–infrared.

2.4.2 The collimation of the outflow

The outflow associated with the FIR source in B335 has recently been identified as lying almost in the plane of the sky, and we observe it at an angle of $80° \pm 5°$ to the axis of the outflow. Therefore, the velocity, momentum, energy, force and mechanical luminosity of the outflow are now believed to be higher than had previously been thought. The revised parameters of the outflow have been calculated by Hirano *et al.* (1988), Cabrit *et al.* (1988) and Moriarty-Schieven & Snell (1989), and I have used the results of all three papers to estimate the effect of the outflow on the core, and to try to constrain models for its collimation.

I consider several models for the driving source of the outflow and the collimation mechanism. Firstly, models in which the flow is intrinsically bipolar require an anisotropic mechanism for the production of the wind. All such models require the presence of an accretion disk, the rotational energy of which is the source of the energy of the outflow. Torbett (1984) suggests that one mechanism for the production of a bipolar outflow is via the hydrodynamic ejection of material at the inner boundary of an accretion disk, producing pressure–driven winds that are intrinsically bipolar. Pudritz & Norman (1986) and Königl (1989) present arguments for hydromagnetic winds from accretion disks being the driving source of outflows. All of these models require that the stored rotational energy of the disk be greater than the energy of the outflow

in order for the disk to be able to supply the required energy to power the outflow. This assumes that the system is quasi–stationary, and will not apply to a source if we happen to observe it just at the end of its outflow phase, when the rotational energy might be expected to be less than that of the outflow. I consider several configurations for such a disk, and calculate the rotational energy that can be stored and used as an energy source for the outflow. The disks considered are as follows:

(i) A uniform rigid disk with its outer edge rotating at Keplerian velocity (break–up speed).

(ii) A disk with a Gaussian density distribution as a function of radius, with its outer edge rotating at Keplerian velocity.

(iii) A uniform Keplerian disk.

(iv) A Gaussian Keplerian disk.

(v) A ring or torus.

If the mass of the "disk" (which I identify as being the mass of the submillimetre source) is M_d, the radius of the disk is R_d (from the 450 μm map $R_d = 1.4 \times 10^{14}$ m, M_* is the mass of the central young stellar object and G is the gravitational constant, then expressions for the rotational energies of the disk can be derived. For case (i), the energy is (approximating the gravitational field of the disk throughout by $-GM_d/r$)

$$E_{rot} = 0.25 \frac{GM_d}{R_d}(M_d + M_*).$$

For case (ii), with the rigid Gaussian disk, the energy depends on the ratio $R_d/R_{1/2}$, where $R_{1/2}$ is the half width to half maximum of the Gaussian density distribution. The value obtained for the uniform rigid disk may be regarded as an upper limit to the energy of a rotating Gaussian disk. For $R_d > R_{1/2}$,

$$E_{rot} < 0.22 \frac{GM_d}{R_d}(M_d + M_*).$$

With a uniform Keplerian disk, case (iii),

$$E_{rot} = \frac{GM_d}{R_d}\left(\frac{M_d}{3} + M_*\right),$$

and for a Gaussian Keplerian disk, case (iv),

$$E_{rot} = \frac{GM_d}{R_{1/2}}(0.216M_d + 0.738M_*).$$

Finally, a ring or torus of radius R_d rotating with Keplerian velocity, case (v), has

$$E_{rot} = 0.5\frac{GM_d}{R_d}(M_d + M_*).$$

I find that with all the configurations where M_* is less than $1\,M_\odot$ the stored rotational energy of a rotating disk or torus is much less than the energy associated with the molecular outflow. The results of the calculations are presented in Table 2.3 for $M_* = 1\,M_\odot$, and I have also calculated the value of M_* that would be needed for $E_{rot} = E_{\rm outflow}$. Since there are two estimates for $E_{\rm outflow} = 1/2 M_L V_L^2$ of 7.4×10^{37} J (Hirano *et al.*) and 2.0×10^{37} J (Cabrit *et al.*; Moriarty-Schieven & Snell), I present calculations for both values of $E_{\rm outflow}$, and expect that the true value lies somewhere in between. These calculations have assumed that *all* the available rotational energy has been converted into the energy of the outflow, so the derived values of M_* may be regarded as lower limits. Almost all the models require that M_* is about $10\,M_\odot$. The low luminosity of this source (approximately $2.6\,L_\odot$) makes this highly unlikely, and so I believe that models in which the outflow is powered by a rotating accretion disk or torus are not applicable to B335.

Table 2.3: Rotational energies for disk models.

Model	E_{rot} ($M_* = 1\,M_\odot$) (10^{37} J)	M_* required for production of outflow ($M_\odot$) For $E_{\rm outflow} = 2.0 \times 10^{37}$ J [a]	For $E_{\rm outflow} = 7.4 \times 10^{37}$ J [b]
(i)	0.29	19	75
(ii)	<0.29	>19	>75
(iii)	0.64	4.6	19
(iv)	0.45	6.5	26
(v)	0.57	8.4	37

[a] Cabrit *et al.*; Moriarty-Schieven & Snell.
[b] Hirano *et al.*

The other models I consider are those in which the wind is intrinsically isotropic, and the collimation of the bipolar flow occurs because of the surrounding core structure (*e.g.* Königl 1982). I consider both momentum–driven and energy–driven models, as described below, and for each model the force on the core due to the outflowing wind must be less than or of the order of the gravitational binding force on the core for the core to be able to collimate the outflow. For a Gaussian core with HWHM of $R_{1/2}$, the gravitational binding force is

$$F_g = \frac{GM_c}{R_{1/2}^2}(0.252M_c + 1.386M_*),$$

where M_c is the mass of the cloud core. The equivalent expression for a uniform core of radius R_c is

$$F_g = \frac{GM_c}{R_c^2}(0.75M_c + 3M_*).$$

If the lobes have mass M_L, velocity V_L, and linear extent R_L, then the rate of momentum transfer to the lobes F_L is given by the momentum of the lobes $M_L V_L$, divided by the dynamical timescale R_L/V_L, so that $F_L = M_L V_L^2/R_L$. The values of F_L calculated by Hirano *et al.*, Cabrit *et al.* and Moriarty-Schieven & Snell, together with Ω_L are given in Table 2.4. There is a significant difference between the values of F_L found by Hirano *et al.* and those quoted in the other two papers, first because they derive a slightly higher velocity, secondly they use a CO abundance differing by a factor of 2, and thirdly because they did not map a large enough area to cover the entire outflow, thereby underestimating the linear extent R_L. The underestimate of R_L can be corrected for by using results from the more extended mapping of Cabrit *et al.*, which results in a reduction of F_L by a factor of 3. I use both this corrected value of F_L from Hirano *et al.*, and the numbers of Cabrit *et al.* and Moriarty-Schieven & Snell for my calculations.

Table 2.4: Core parameters for outflow models.

	Source of parameters used			
	This paper	HKNT[a]	CGS[b]	M-SS[c]
F_g (Gaussian core, $M_* = 1\,M_\odot$) (10^{21} N)	52			
F_g (uniform core, $M_* = 1\,M_\odot$) (10^{21} N)	123			
Ω_L (sr)	0.55			
F_L (10^{21} N)		5.1	1.5	2.2
F_c (Momentum driven model) (10^{21} N)		60	16	23
F_c (Energy driven model) (10^{21} N)		24	6	9

[a] Hirano *et al.*, corrected for the linear extent of the outflow as determined by Cabrit *et al.*

[b] Cabrit *et al.*

[c] Moriarty-Schieven & Snell.

The models addressed are the following (*e.g.* Davidson 1987):

(a) *Momentum driven.* The outflow is driven directly by the momentum of a stellar

wind so that the observed force required to drive the outflow is equal to the momentum flux $\dot{M}_w V_w$ of the wind within the lobe. If the stellar wind is isotropic, then the force on the core in this case is

$$F_c = \left(\frac{\Omega_c}{2\Omega_L}\right) F_L$$

where Ω_L is the solid angle subtended by one outflow lobe at the source, Ω_c is the solid angle subtended by the rest of the core ($= 4\pi - 2\Omega_L$).

(b) *Energy driven.* If the cooling time of the energetic stellar wind is longer than the dynamical timescale of the outflow then the wind inside the lobe can become pressurised and the flow can be driven by thermal pressure. The efficiency ϵ with which the wind energy is converted into the energy of the outflow lobe depends on the density of the surrounding cloud, which Dyson (1984) and Kwok & Volk (1985) calculate to be about 0.2 to 0.3. In this case the force on the core is

$$F_c = \frac{1}{\epsilon}\left(\frac{\Omega_c}{2\Omega_L}\right)\left(\frac{V_L}{V_w}\right) F_L$$

where $V_w/V_L > 1$. The value of F_c for both models is given in Table 2.4, where I have used $V_w/V_L = 10$ and $\epsilon = 0.25$. For all values of F_L I find that F_c is the same order of magnitude as F_g. One would not expect F_c to be more than a factor of a few smaller than F_g since if this was the case it would be more difficult for the wind to break through the core to form the outflow. For the extreme case of the momentum–driven model, and the upper limit to F_c derived from the Hirano *et al.* data, I find that $M_* \gtrsim 1.2\,\mathrm{M}_\odot$, which seems more reasonable than the $10\,\mathrm{M}_\odot$ required for the disk models, given its luminosity. The observed submillimetre source can, therefore, collimate the flow, and I suggest that the outflow in B335 is more likely to be due to an isotropic stellar wind that has been collimated by the surrounding cloud core than a disk wind. Cabrit *et al.* also present arguments for the collimation of the flow by the cloud core based on CS measurements of the velocity dispersion.

If the outflow is due to a stellar wind that is intrinsically anisotropic (*e.g.* Hartmann & MacGregor 1982) then the constraints on the mass of the central object are less severe, and M_* can be less than $1\,\mathrm{M}_\odot$. Indeed, an anisotropic, bipolar wind would help to explain why the core has not yet been dispersed perpendicular to the outflow axis.

2.5 Conclusions

High–resolution submillimetre continuum measurements have been made of the far–infrared source in the isolated Bok globule B335. It is resolved perpendicular to the axis of the accompanying outflow in an 8 arcsec beam, but unresolved parallel to it. These measurements have enabled us to set an upper limit on the physical size of the source, which is believed to be a very dense ($n(H_2) \gtrsim 5 \times 10^{13}\,m^{-3}$) core of dust and gas surrounding the object in the centre. Without higher resolution molecular line observations the precise relationship between the two is unknown. The position of the submillimetre continuum core coincides exactly with all the molecular line peaks. This core is found to be capable of collimating an initially isotropic wind into the observed bipolar structure.

The central object does not appear to fit the currently popular models for protostellar evolution. Its high A_V, low luminosity, and the presence of an outflow provides three possibilities: (i) that outflow is possible from protostars much younger than had previously been expected, (ii) that the source of the luminosity is a more evolved protostar with an outflow that has a much lower mass and/or accretion efficiency than has been inferred in Taurus, and the high A_V is due to the orientation of the source, or (iii) that the source is already well–evolved and is a pre–main sequence star that for some reason has remained deeply embedded.

Chapter 3

NGC 2024

3.1 Introduction

NGC 2024 (also known as Orion B, W12, G206.5–16.4) is a bright HII region in the Orion molecular cloud complex. At optical wavelengths its appearance is dominated by a dark dust lane that lies in front of the HII region, though in the near–infrared the region is found to contain more than thirty point sources coincident with the radio continuum emission (Barnes *et al.* 1989). A ridge of molecular gas appears superimposed on the dark lane, and Thronson *et al.* (1984) suggested that the two were of the same origin and that the dense molecular cloud lay in front of the HII region. However, recent observations have led to a picture for the geometry of the region in which the dense gas lies *behind* the HII (Crutcher *et al.* 1986; Mezger *et al.* 1988; Barnes *et al.* 1989). A schematic diagram of this geometry is shown in Figure 3.1. The interface between the radio HII region and the dense molecular cloud is an ionisation front, and is also the site of considerable molecular hydrogen emission (Barnes *et al.* 1989).

As part of a search for protostellar condensations *without* luminous stellar cores, *i.e.*, cold sources with dust temperatures of about 14 K whose sole heating source is the interstellar radiation field (ISRF), Mezger *et al.* (1988) mapped the molecular ridge in NGC 2024 with the IRAM 30 m telescope in 1.3 mm dust continuum. They found that the cloud contained six millimetre sources (Figure 3.2), which they interpreted as high–density ($n(\mathrm{H}) \sim 10^{14} - 10^{15}\,\mathrm{m}^{-3}$), cold ($T_{\mathrm{dust}} \simeq 16\,\mathrm{K}$), isothermal condensations, on the basis of the colour temperature derived from their high–resolution 1.3 mm mapping and lower resolution 350 μm mapping. The full continuum spectrum, which includes data taken with much bigger beams than the 11 arcsec of the 1.3 mm measurements of

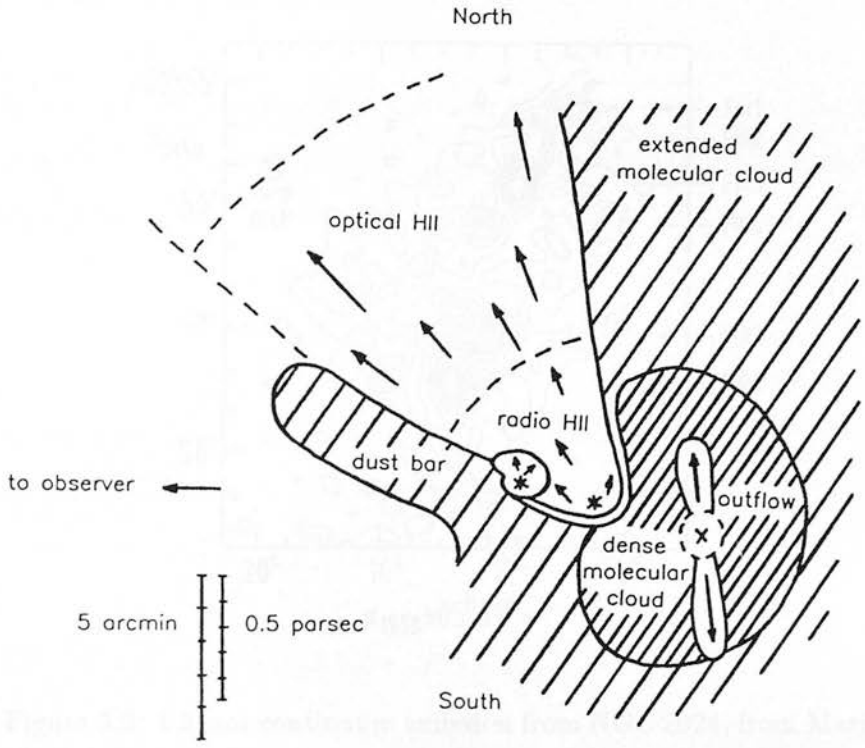

Figure 3.1: Schematic diagram showing the arrangement of features of NGC 2024 (adapted from Barnes *et al.* 1989). The physical scale bars shown are for an assumed distance of 450 pc.

Mezger *et al.*, indicates that a warm dust component of 45 K is still needed to account for the far-infrared flux between 40 and 160 μm (Thronson *et al.* 1984). Mezger *et al.* therefore proposed that the cold protostellar condensations were embedded within much warmer, less dense, gas and dust, that was perhaps heated externally by the foreground HII region. If these six cores were truly protostellar condensations they would be the first to have been detected, and therefore warrant detailed observations of the physical conditions present within them.

FIR6 is coincident with an H_2O maser (Genzel & Downes 1977), and has also recently been found to be the source of a very energetic, young outflow (Richer 1990). There is extensive, highly-collimated, high-velocity gas stretching approximately 5 arcmin north-south, but here there are conflicting results. A map made with the 14 m telescope of the Five College Radio Astronomy Observatory (FCRAO) in CO $J = 2 - 1$ (Sanders & Willner 1985) shows bipolar structure with red-shifted emission toward the

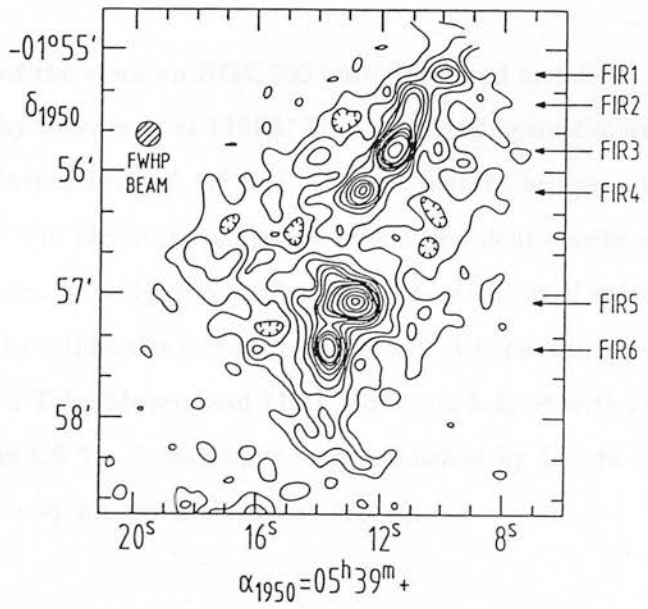

Figure 3.2: 1.3 mm continuum emission from NGC 2024, from Mezger *et al.* (1988).

south and blue–shifted emission toward the north, centred in the region of FIR5/FIR6. However, a map in the same line made with the 15 m James Clerk Maxwell Telescope (JCMT) shows no such blue–shifted emission (Richer *et al.* 1989), indicating a unipolar structure for the high–velocity gas. At the present time it is not clear which set of observations are in error. This makes identification of the exciting source of the extended outflow extremely difficult based on positional coincidence, though it seems most likely to be either FIR5 or FIR6. A highly reddened near–infrared source was found by Barnes *et al.* (1989) close to FIR5 and FIR6 which they propose as a candidate for the origin of the CO outflow, though it is not associated with either of the dense cores.

Although the presence of phenomena commonly associated with high–mass star formation shows that at least one of the millimetre cores contains a young stellar object, in disagreement with the contention of Mezger *et al.* (1988), the other five still require investigation. Consequently, CS and $C^{34}S$ $J = 7 - 6$ observations of the molecular cloud have been carried out to ascertain the excitation conditions within the cores, in an attempt to shed light on the evolutionary state of the sources, and to determine the distribution of dense molecular gas on small scales to compare with the dust continuum.

An initial search for near–infrared counterparts to the FIR sources has also been undertaken, to test the hypothesis that the remaining cores do not contain self–luminous sources.

The results of the work on NGC 2024 are presented as follows. First of all the conclusions derived by Mezger *et al.* (1988) from the existing continuum data are discussed. Then, high–resolution CS and $C^{34}S$ $J = 7 - 6$ spectra are presented and interpreted with reference to the physical conditions within the dense cores and the evolutionary state of the sources. Finally, the results of the near–infrared search for stellar objects associated with the millimetre cores are presented. All this work has been carried out in collaboration with Toby Moore, and Matt Mountain helped with the CS $7 - 6$ mapping observations. The CS $7 - 6$ data have been published by Moore *et al.* (1989), and the near–infrared data by Moore & Chandler (1989).

3.2 Existing continuum data

The interpretation by Mezger *et al.* (1988) of the 1.3 mm dust continuum data as isothermal protostellar cores requires careful consideration. Such objects represent a missing link observationally between quiescent clouds and young stellar objects that display the familiar signs of star formation such as energetic outflow and winds. The primary reason why they have remained as yet undetected is that they are extremely faint, deriving their luminosity solely from the heating of dust grains by the radiation field that permeates the Galaxy.

The appearance of isothermal protostellar condensations heated externally by the Galactic ISRF has been calculated by Mathis, Mezger & Panagia (1983). The equilibrium temperature attained by dust within a condensation is approximately 10 to 15 K, and its luminosity depends on the surface area being subjected to the radiation field. Identifying such an object unambiguously as a cold, isothermal "protostar" therefore requires a determination of the dust temperature within the core. This is only possible if high–resolution data is available for several frequencies, so that the full continuum spectrum of each source can be modelled.

The continuum data used by Mezger *et al.* are shown in Figure 3.3. They include far–infrared data taken with a 49 arcsec beam from Thronson *et al.* (1984), the 400 μm integrated flux from Hudson & Soifer (1976) observed with a 1.6 arcmin beam, a 1 mm point taken with a 3.9 arcmin beam (Chini *et al.* 1984), the 1.3 mm flux from Mezger

et al., and their 350 μm data taken with a 30 arcsec beam. A three–component model was constructed to account for the observed data, with warm dust at 45 K responsible for the shorter wavelength emission, and two cool components at 16 K invoked to fit the millimetre data. The cool dust emission was separated into that originating from the cores themselves, labelled with a 350 μm optical depth of 0.6 in Figure 3.3, and that originating from extended background emission, labelled with a 350 μm optical depth of 0.1. The dust emissivity was assumed to vary as ν^2 within their model, and the cool 16 K component dominates the emission at wavelengths longer than 350 μm.

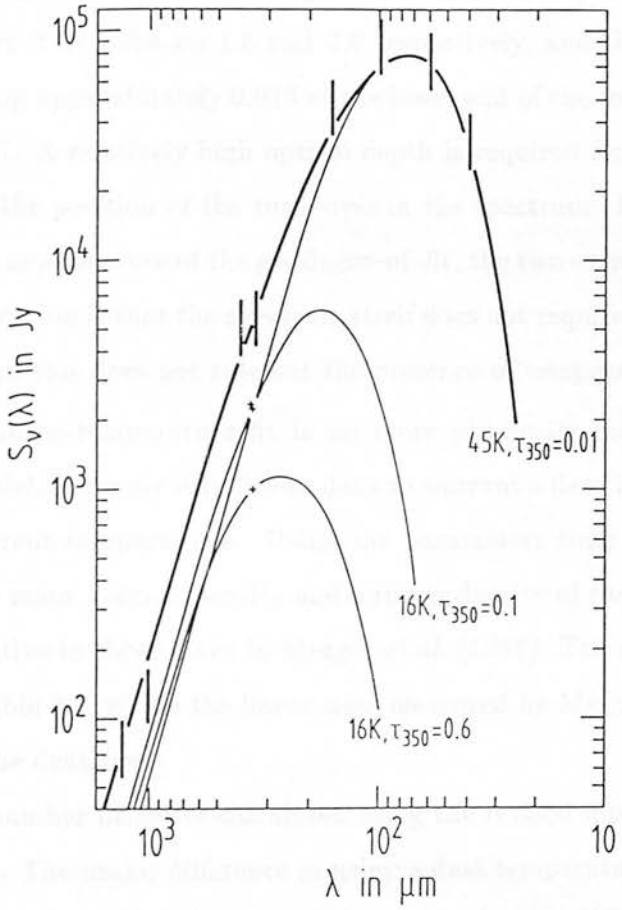

Figure 3.3: The integrated dust emission spectrum of NGC 2024 and its decomposition into three components, from Mezger *et al.* (1988).

However, the model put forward by Mezger *et al.* to account for the continuum spectrum is not unique, and there are other physical mechanisms that can make the spectral index appear less steep and enhance emission at long wavelengths than invoking

a single temperature, cool, massive dust component. There is considerable structure in the radio continuum on scales of a few arcsecs (Barnes *et al.* 1989) that could contribute to the flux at longer wavelengths, though Mezger *et al.* claim that the map shown in Figure 3.2 was not affected by free–free emission. Since the nature of temperature gradients within the dense molecular cloud is unknown without high–resolution observations at shorter wavelengths, it is perhaps more consistent to treat the eight measured integrated fluxes as originating from a single temperature dust component, and relax the constraint on the spectral index of the dust emissivity to fit the data.

Acceptable fits ($\chi^2 \lesssim 4$ with four degrees of freedom) consistent with the 30% error bars used by Mezger *et al.* can be obtained for all temperatures between 42 and 70 K. These two extremes are shown in Figure 3.4. The corresponding values of the dust emissivity index β lie between 1.6 and 2.0 respectively, and the 350 μm optical depth varies from being approximately 0.013 at the lower end of the temperature range to 0.67 for $T_{\rm dust} = 70$ K. A relatively high optical depth is required for the high temperatures, to account for the position of the turn–over in the spectrum. However, as far as using the χ^2 statistic as a measure of the goodness–of–fit, the two extremes plotted are equally valid. The indication is that the spectrum itself does not require a cold dust component, though of course this does not rule out the presence of temperature gradients.

While a single–temperature fit is no more physically reasonable than a multi–component model, there are insufficient data to warrant a detailed model including dust at several different temperatures. Using the parameters from the single–temperature fits reduces the mass, column density and number density of the cores by a factor of 5.5 on average relative to those given in Mezger *et al.* (1988). The new values for each core are listed in Table 3.1, where the linear sizes measured by Mezger *et al.* have been used to determine the densities.

The new number densities calculated using the revised dust temperatures are still extremely high. The major difference in using a dust temperature higher than the 16 K assumed by Mezger *et al.* is that the corresponding luminosity of each core implied by the observed 1.3 mm flux is larger by up to a factor of 350. If the cores have luminosities of 10^2 to 10^3 $L_\odot$ (obtained for temperatures between 42 and 70 K) rather than the low values obtained using a temperature of 16 K (which lie in the range 2 to 9 $L_\odot$ for the various cores), then internal heating sources are needed. For a dust emissivity index β of 2.0 the most luminous source is FIR4, since it has the largest linear extent and is the

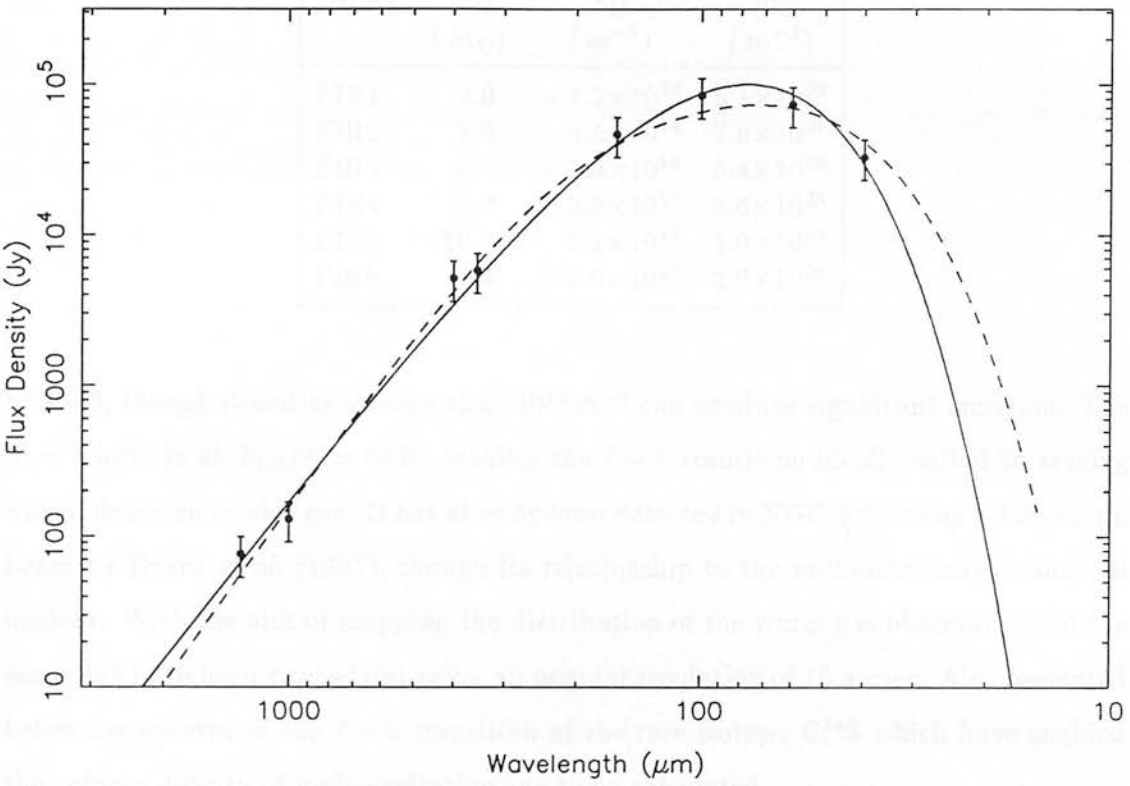

Figure 3.4: Two possible single–temperature grey body fits to the spectrum. The solid curve is for $T_{\rm dust} = 42\,{\rm K}$, and the dashed curve has $T_{\rm dust} = 70\,{\rm K}$.

most optically thin, making it possible for significantly more energy to be radiated at shorter wavelengths than for the other cores.

Clearly a single high–resolution measurement alone cannot identify whether the dense cores have embedded young stellar objects, or if they have, the nature of those sources. Further high–resolution continuum measurements, ideally at submillimetre/ far–infrared wavelengths, are needed to complete the continuum spectra and enable the dust temperature of the individual FIR sources to be determined.

3.3 CS emission

Determination of the excitation conditions of the gas within the cores FIR1–6 is obviously a crucial step towards clarifying the evolutionary state of the millimetre sources. CS $J = 7 - 6$ requires high densities of around $10^{13}\,{\rm m}^{-3}$ for the transition to be ther-

Table 3.1: Revised core properties.

Source	M_H ($M_\odot$)	n_H (m^{-3})	N_H (m^{-2})
FIR1	2.0	$> 1.7\times10^{14}$	5.1×10^{28}
FIR2	3.0	2.5×10^{14}	7.6×10^{28}
FIR3	6.7	$> 1.3\times10^{14}$	6.4×10^{28}
FIR4	5.2	3.9×10^{13}	2.6×10^{28}
FIR5	10.8	2.1×10^{14}	1.0×10^{29}
FIR6	4.3	$> 7.0\times10^{13}$	3.6×10^{28}

malised, though densities greater than $10^{12}\,m^{-3}$ can produce significant emission. The $J = 7$ level is at $E_{rot}/k = 66\,K$, making the $7 - 6$ transition ideally suited to tracing warm, dense molecular gas. It has already been detected in NGC 2024 using a 1.2 arcmin beam by Evans *et al.* (1987), though its relationship to the millimetre cores remained unclear. With the aim of mapping the distribution of the warm gas observations of the same line have been carried out using an angular resolution of 15 arcsec. Also presented below are spectra of the $7 - 6$ transition of the rare isotope $C^{34}S$ which have enabled the column density of high-excitation gas to be calculated.

3.3.1 Observations

The CS $J = 7 - 6$ transition at 342.882949 GHz was mapped with the JCMT on Mauna Kea, Hawaii, during 1988 September using a common-user 345 GHz Schottky receiver. Spectra were obtained with a 1024-channel acousto-optical spectrometer (AOS) having a channel width of 488 kHz and spectral resolution of 1 MHz. The ridge containing FIR1–6 in NGC 2024 was mapped with a 15 arcsec beam, using a regular grid, with points separated by 8 arcsec. The area was well-sampled except towards FIR1, where only two spectra were obtained further to the north. The pointing was checked at intervals of about 45 minutes against the molecular line peak in OMC1 (Masson *et al.* 1987), resulting in an rms error of 3 arcsec. The spectra were corrected for rear spillover, atmospheric and ohmic losses (Kutner & Ulich 1981), resulting in units of T_A^*. A point at an offset 30 arcmin east and 15 arcmin south was used as the reference position.

Individual spectra of CS $7 - 6$ were taken towards the positions of FIR1 to FIR6 given in Mezger *et al.* (1988) in 1990 February, together with $C^{34}S$ $7 - 6$ spectra at 337.396602 GHz of FIR2–6. The same 345 GHz receiver was used, this time combined

with an AOS having a channel width 250 kHz and spectral resolution of 330 kHz. System temperatures of around 3000 K resulted in an rms noise of 0.3 K per channel for the 30 minute integrations used for the $C^{34}S$ spectra, and 0.5 to 0.7 K for the shorter integrations for the CS spectra. The pointing was excellent, good to approximately 2 arcsec rms. The off–position used was a point 4 arcmin west. The main–beam efficiency η_{MB} was equal to 0.6 for both sets of observations.

3.3.2 Results

The result of the CS 7 – 6 mapping is presented in Figure 3.5. It shows the antenna temperature T_A^* integrated over the whole line, $\int T_A^*(V)dV$, in Figure 3.5(a); the rms noise level is approximately 2.5 K km s^{-1}. Figure 3.5(b) displays the peak value of T_A^*, where the rms noise is approximately 1.0 K. The positions of FIR1–6 are marked on the map, so that the distribution can be easily compared with that of the dust continuum in Figure 3.2.

The spectra taken towards each core are shown in Figure 3.6. A reference position located directly between FIR4 and FIR5 was observed to compare with the emission from the cores, and is marked REF in Figure 3.6(e). The results are summarised in Table 3.2, where the peak value of T_A^* is given for both lines in each source, together with the centre V_{LSR} and the full width at zero intensity.

Table 3.2: Observed CS parameters for the FIR sources.

Source	T_A^* (CS 7 – 6) (K)	T_A^* ($C^{34}S$ 7 – 6) (K)	V_{LSR} (km s^{-1})	FWZI of CS line (km s^{-1})
FIR1	7.6	–	11.0	2.6
FIR2	8.2	1.4	10.6	3.2
FIR3	9.8	1.9	11.0	3.3
FIR4	8.9	1.5	11.2	3.8
FIR5	5.8	2.0	11.7	3.6
FIR6	6.8	1.3	11.7	6.0

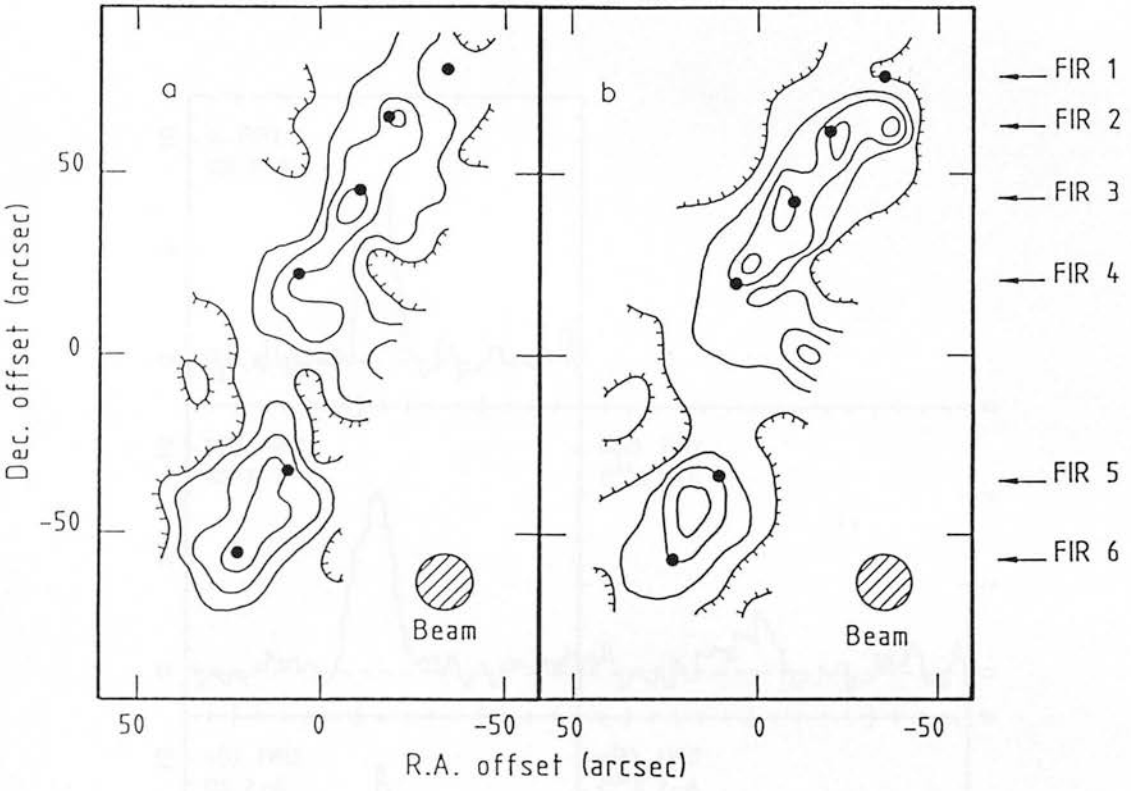

Figure 3.5: (a) Integrated CS $7-6$ emission $\int T_A^*(V)dV$ from NGC 2024. Contours are drawn at 5, 10, 15 and 20 K km s^{-1}. (b) Contours of peak T_A^* at intervals of 1.5 K, starting from a base level of 3 K. The (0,0) position in both maps is at $\alpha(1950) = 5^h39^m12.2^s$, $\delta(1950) = -1°56'30''$.

3.3.3 Discussion

3.3.3.1 Morphology and LTE analysis

The maps in Figure 3.5 show clearly that the warm molecular gas traced by the CS $7-6$ emission is localised at or very near the positions of the millimetre condensations reported by Mezger *et al.*. This indicates that there are discrete regions of heated gas associated with each of the FIR sources, except perhaps at FIR1 where the map was poorly sampled. The spectrum taken towards FIR1 shows that in fact there is significant emission at this position.

In order to obtain estimates of the optical depth in CS $7-6$ towards each source, the CS and C^{34}S line profiles (Figure 3.6) have been fitted simultaneously to a function of the form

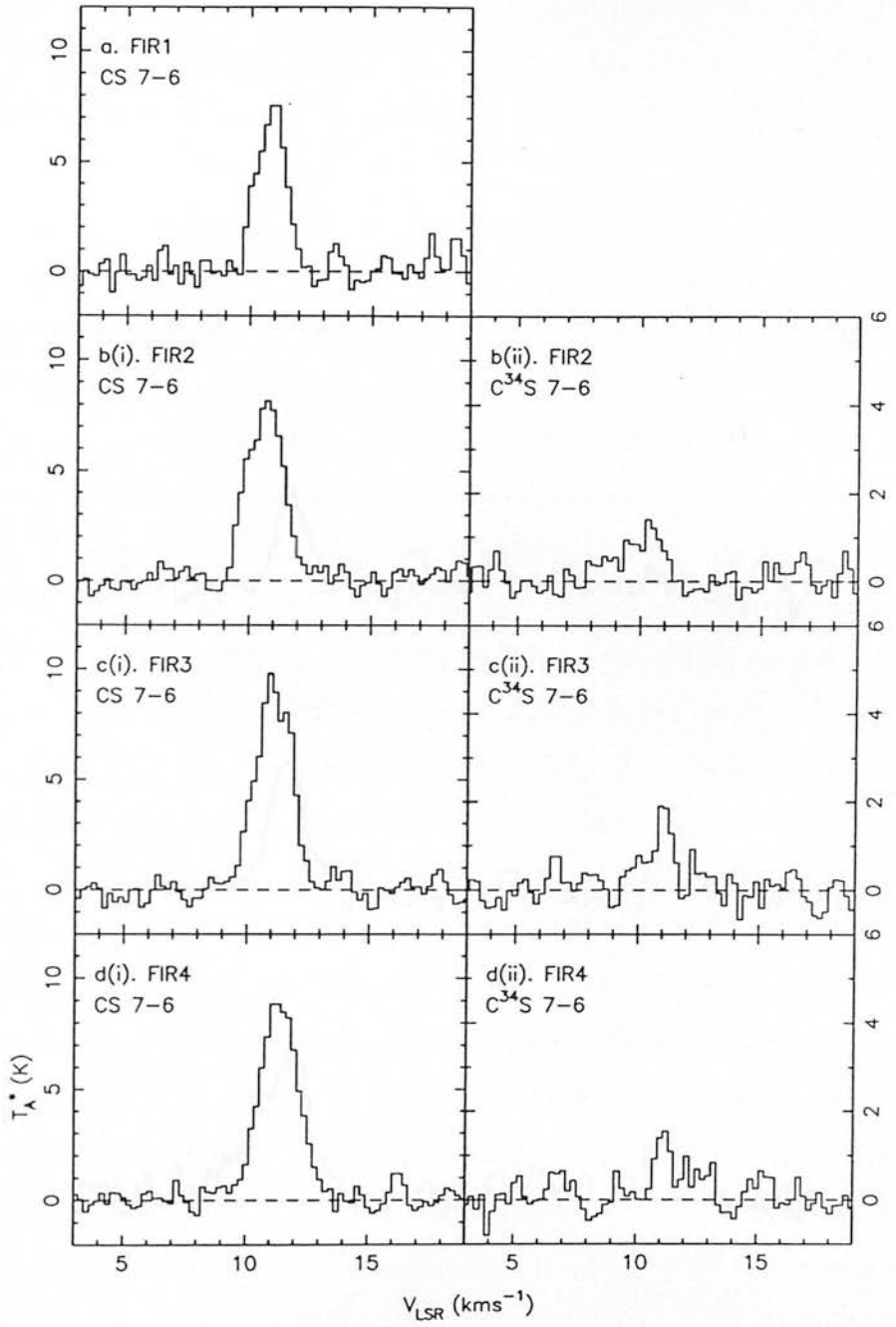

Figure 3.6: CS and $C^{34}S$ $7-6$ spectra of the cores and reference position in NGC 2024.

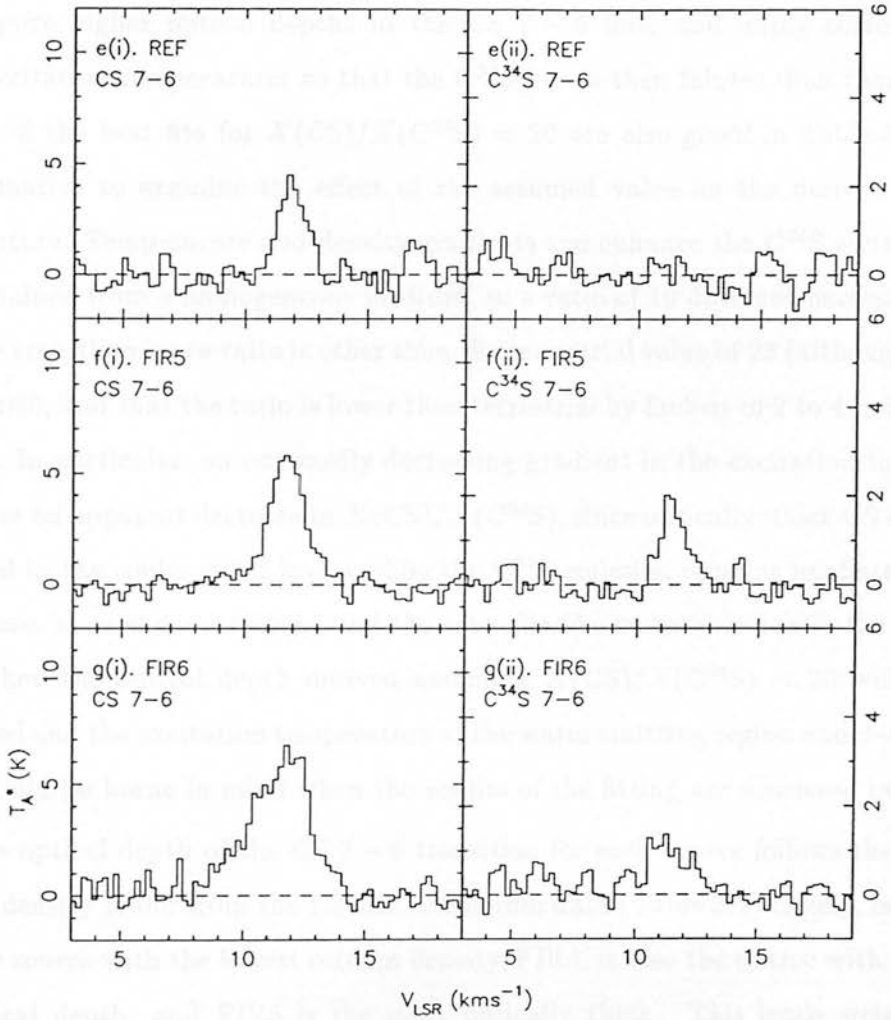
e(i). REF
CS 7–6
e(ii). REF
C34S 7–6
f(i). FIR5
CS 7–6
f(ii). FIR5
C34S 7–6
g(i). FIR6
CS 7–6
g(ii). FIR6
C34S 7–6
T_A* (K)
V_LSR (kms^-1)

$$T_A^*(V) = T_0(1 - e^{\tau(V)}) \tag{3.1}$$

with

$$\tau(V) = \tau_0 e^{-(V-V_0)^2/{V_D}^2}.$$

The optical depth as a function of velocity $\tau(V)$ is assumed to have a Gaussian distribution centred on V_0, and a dispersion V_D. The optical depth in the centre of the line τ_0 of each species is assumed to be related by $\tau_0(\mathrm{CS}) = \tau_0(\mathrm{C^{34}S})X(\mathrm{CS})/X(\mathrm{C^{34}S})$, where $X(\mathrm{CS})/X(\mathrm{C^{34}S})$ is the abundance ratio of the CS and $\mathrm{C^{34}S}$ molecules.

The line profiles for FIR2–6 are well–fitted by the function given in equation 3.1, with an abundance ratio of approximately 10. Higher values of $X(\mathrm{CS})/X(\mathrm{C^{34}S})$ than this require higher optical depths in the CS $7-6$ line, and imply correspondingly lower excitation temperatures so that the $\mathrm{C^{34}S}$ line is then fainter than that observed. Results of the best fits for $X(\mathrm{CS})/X(\mathrm{C^{34}S}) = 20$ are also given in Table 3.3 since it is informative to examine the effect of the assumed value on the derived excitation temperature. Temperature and density gradients can enhance the $\mathrm{C^{34}S}$ emission above that obtained from a homogeneous medium, so a ratio of 10 does not necessarily imply that the true abundance ratio is other than the terrestrial value of 23 (although Frerking *et al.*, 1980, find that the ratio is lower than terrestrial by factors of 2 to 4 in interstellar clouds). In particular, an outwardly decreasing gradient in the excitation temperature can cause an apparent decrease in $X(\mathrm{CS})/X(\mathrm{C^{34}S})$, since optically–thick CS emission is absorbed in the cooler outer layers while the $\mathrm{C^{34}S}$ emission remains unaffected. If this is the case, as seems most likely, and the true abundance ratio is nearer the terrestrial value, then the optical depth derived assuming $X(\mathrm{CS})/X(\mathrm{C^{34}S}) = 20$ will be over–estimated and the excitation temperature of the warm emitting region under–estimated. This should be borne in mind when the results of the fitting are discussed below.

The optical depth of the CS $7-6$ transition for each source follows the hydrogen column density found from the 1.3 mm continuum data (Table 3.1) closely, in the sense that the source with the lowest column density, FIR4, is also the source with the lowest CS optical depth, and FIR5 is the most optically thick. This lends weight to the argument that the CS $7-6$ emission originates from the FIR cores.

The excitation temperature can be calculated using equation 1.18. Numerically, for CS $7-6$, this can be written

$$T_{ex} \simeq \frac{16.5}{\ln\left(1 + \frac{16.5(1-e^{-\tau})}{T_R}\right)}.$$

Table 3.3: Fitted parameters for CS and $C^{34}S$ spectra.

Source	τ_0(CS)	V_0 ($km\,s^{-1}$)	V_D ($km\,s^{-1}$)	Peak T_A^*(CS) (K)	Peak $T_A^*(C^{34}S)$ (K)
$X(CS)/X(C^{34}S) = 10$					
FIR2	1.11	10.64	0.92	7.90	1.24
FIR3	1.01	11.09	0.91	9.14	1.38
FIR4	0.21	11.38	1.06	8.66	0.99
FIR5	2.18	11.73	0.80	5.47	1.21
FIR6	0.99	11.54	1.52	5.94	0.89
$X(CS)/X(C^{34}S) = 20$					
FIR2	2.49	10.64	0.82	7.59	0.97
FIR3	2.22	11.09	0.82	8.86	1.04
FIR4	0.97	11.39	0.97	8.79	0.67
FIR5	3.80	11.73	0.71	5.29	0.94
FIR6	1.89	11.52	1.39	5.80	0.62

The radiation brightness temperature T_R is obtained by correcting the antenna temperature T_A^* for the main-beam efficiency η_{MB}, and the source-beam coupling efficiency η_c, giving $T_R = T_A^*/\eta_{MB}\eta_c$. Since η_c depends on the (unknown) source structure within the beam, the value of T_{ex} has been calculated for two representative values of $\eta_c = 1.0$ and $\eta_c = 0.5$. The results for abundance ratios of both 10 and 20 are listed in Table 3.4.

Table 3.4: Excitation temperatures for various values of η_c.

Source	$X(CS)/X(C^{34}S) = 10$		$X(CS)/X(C^{34}S) = 20$	
	$T_{ex}(\eta_c{=}1.0)$	$T_{ex}(\eta_c{=}0.5)$	$T_{ex}(\eta_c{=}1.0)$	$T_{ex}(\eta_c{=}0.5)$
FIR1 [a]	>19.8	>32.9		
FIR2	27.0	47.0	21.0	35.2
FIR3	31.5	55.8	23.9	40.8
FIR4	87.6	167.4	31.1	55.0
FIR5	17.2	28.0	15.9	25.4
FIR6	23.0	39.2	18.4	30.3

[a] Lower limit obtained by assuming $\tau_0(CS) \gg 1$.

The difference between the excitation temperatures calculated using abundance ratios differing by a factor of 2 are surprisingly small, and for all the sources except FIR5, there is every indication that the excitation temperature is considerably higher than 16 K. An absolute lower limit has been calculated for FIR1 by assuming that

the CS emission is very optically thick, since no $C^{34}S$ data exist for this source. It seems likely that excitation temperatures of 40 to 50 K are applicable to most of the millimetre cores, similar to the single–temperature fits to the continuum spectrum, with FIR4 being particularly warm. The column density of CS molecules can be estimated by assuming LTE, so that for the $7-6$ transition the optical depth is related to $N(\mathrm{CS})$ by

$$N(\mathrm{CS}) = 4.4 \times 10^{15} \tau_0 V_\mathrm{D} T_\mathrm{ex} e^{49.4/T_\mathrm{ex}} (1 - e^{16.5/T_\mathrm{ex}})^{-1} \qquad \mathrm{m}^{-2}$$

where a Gaussian velocity distribution with velocity dispersion V_D in $\mathrm{km\,s^{-1}}$ has been assumed. Values in the range $0.9 - 3.8 \times 10^{18}\,\mathrm{m^{-2}}$ (the lowest value is for FIR4, the highest for FIR5) are obtained using the optical depths calculated for an abundance ratio of 10, while for an abundance ratio of 20 CS column densities lie between $1.5 - 6.5 \times 10^{18}\,\mathrm{m^{-2}}$. Assuming a CS fractional abundance relative to molecular hydrogen $X(\mathrm{CS})$ of 5×10^{-9} (Irvine, Goldsmith & Hjalmarson 1987) gives hydrogen column densities of 2×10^{26} to $10^{27}\,\mathrm{m^{-2}}$.

The derived excitation temperatures are similar to those found from the far–infrared continuum (Thronson *et al.* 1984), leading Mezger *et al.* to argue that the CS emission also originates from the warmer gas in front of the millimetre cores. However, in order to produce number densities of the order of the critical density for significant excitation of the $7-6$ line, the extent of the emitting regions must be less than about 1 arcsec. It is extremely unlikely that localised clumps of very high density gas should exist on the front face of the molecular cloud coincident with the FIR cores, so these data provide evidence that temperatures significantly higher than that assumed by Mezger *et al.* apply to the millimetre cores, and that they contain self–luminous embedded sources.

3.3.3.2 Individual cores

A further indication of high optical depth towards FIR5 and FIR6 is the fact that the integrated emission peaks at or near the FIR sources, whereas the peak antenna temperature does not. Optically–thick emission from the cores are more prone to self–absorption by cooler foreground material, depressing the observed peak T_A^*.

The CS $7-6$ spectrum of FIR6 is strikingly wide compared with the other sources, and its profile is the least well described by a Gaussian velocity distribution. The best explanation for the presence of such a feature is that extremely dense material is interacting with the energetic young outflow found by Richer (1990). This outflow is

still very young (its dynamical age is estimated to be 400 years), and very luminous ($L_{CO} \simeq 15\,L_{\odot}$), with a total kinetic energy of 7.0×10^{37} J. For the mass determined by the millimetre continuum observations and the velocity dispersion measured in the CS $7-6$ line, the kinetic energy of dense gas is approximately 1.1×10^{37} J. Now if the core were acting as the collimating mechanism of the outflow, and the outflow were the result of a spherically symmetric stellar wind that had broken out of the core in opposite directions, the remainder of the energy being dumped into the core itself, then the core would have considerably more kinetic energy than observed. The collimation of the outflow must therefore occur closer to the source, and the wide lines seen in CS must be the result of the high–velocity gas interacting with the surrounding medium as it emerges from the core.

This explanation would also seem to apply to the high–resolution HCO^+ interferometer map of Barnes & Crutcher (1990), though their interpretation of the observed features is much more exotic. They find HCO^+ emission at different velocities offset spatially, and invoke an expanding torus centred on FIR6 to account for the morphology of the emission. They also see a "plume" at a velocity of $15\,km\,s^{-1}$ extended north–south whose origin they deduce to be less than 8 arcsec from FIR5. It is therefore likely that the large–scale, extended outflow is related to the high–velocity dense gas traced by the HCO^+, and that both originate from an embedded source within FIR5.

FIR6 is the only source showing signs of small–scale energetic activity in the CS spectra, and a more plausible explanation for the HCO^+ morphology than the ellipse of an inclined expanding torus of Barnes & Crutcher, is the presence of high–velocity, entrained dense gas. The sense of the velocity shift of the HCO^+ is the same as that of the CO outflow, with blue–shifted emission to the northeast and red–shifted emission to the southwest. This fits in with the picture that FIR6 contains a very young stellar object that has not yet dispersed the dense cloud core.

FIR5 is on the edge of the molecular cloud immediately south of the prominent radio emission from the HII region (Barnes *et al.* 1989), and its location could be the reason for the lack of blue–shifted, high–velocity CO (Richer *et al.* 1989). The northern lobe probably expands directly into the HII region, and there is the definite possibility that the O9 star responsible for the ionisation is also embedded nearby. The high hydrogen column density of FIR5 would then explain why no near–infrared or optical counterpart has yet been identified, although it seems unusual that such a luminous source would

be embedded in the coolest FIR core, and there is no sign of a compact HII region coincident with it. Clearly near–infrared polarisation measurements are required in order to determine unambiguously which is the exciting star of the HII region.

The other source that is interesting is at the other extreme, FIR4. It has the lowest optical depth in both CS and dust continuum, and holds the most promise for the detection of an associated stellar object. The search for near–infrared sources that could be embedded within the millimetre cores is described in the following section.

3.4 Near–infrared imaging

The results of the CS and $C^{34}S$ 7 – 6 observations clearly show that the millimetre cores discovered by Mezger *et al.* (1988) are quite warm, with gas excitation temperatures higher than 20 K, and more likely to be in the region of 40 to 50 K. This requires the cores to contain hot, embedded young stellar objects as the source of the luminosity, and prompted an initial search for near–infrared counterparts to the millimetre sources. The results of the medium–sensitivity, high–spatial resolution, near–infrared continuum observations in the NGC 2024 region are presented below.

3.4.1 Observations

The observations were made as part of the Service Observing Programme at the 3.8 m U.K. Infrared Telescope (UKIRT) on Mauna Kea, Hawaii, on October 24, 1988 with the common–user near–infrared array camera IRCAM 1[1] The camera was operated at the scale of 1.24 arcsec per pixel, resulting in an area of 77 × 72 arcsec per frame. Exposures were taken without sky chopping, through broad–band filters at J (1.25 μm), H (1.65 μm) and K (2.22 μm) towards fields centred on $\alpha(1950) = 5^h39^m11.5^s$, $\delta(1950) = -1°55'47''$, and $5^h39^m13.3^s$, $-1°57'15''$. Calibration observations were carried out using the infrared standard star HD40335, assuming $J = 6.55$, $H = 6.47$ and $K = 6.45$, and the absolute calibration uncertainty is estimated to be about 10%. The dark current was subtracted from the image and sky frames, and the image frames were then flat–fielded by dividing by frames of nearby sky (at an offset of 10 arcmin east). On–source integrations of 60 seconds yielded rms noise levels per pixel at J, H and K of 0.021, 0.027 and 0.028 mJy ($(3.9, 2.9, 1.7) \times 10^{-17}$ W m^{-2} μm^{-1}) respectively. Stellar images

[1] Andy Longmore, Tim Hawarden and Tom Geballe are acknowledged for approving and performing the UKIRT Service observations. UKIRT is operated on behalf of the U.K. Science & Engineering Research Council by the Royal Observatory, Edinburgh.

have half–power widths of 1.9 arcsec in all the frames, the spatial resolution being limited by the seeing. The absolute pointing accuracy of the observations is approximately 2 arcsec.

3.4.2 Results

The J, H and K frames covering FIR1–6 are shown in Figure 3.7, where the positions of the millimetre cores are marked by crosses. The bright object off the eastern edge of the northern field is the near–infrared star NGC 2024 #2 (Grasdalen 1974). The absolute value of the background level chosen may differ between the northern and southern fields, since there is considerable diffuse emission in the region originating from dust heated by the HII region, and possibly from scattered light.

In the southern field, covering FIR5 and FIR6, no sources were detected within 6 arcsec of the 1.3 mm positions of either object. The source initially proposed as a possible origin of the extended CO outflow by Barnes *et al.* (1989), IRS 31, is just about visible in the K frame at an offset of $\Delta\alpha = 2$ arcsec, $\Delta\delta = -78$ arcsec, and is mentioned for reference only. No photometry of this source is possible because it is too close to the edge of the frame.

The near–infrared sources detected are listed in Table 3.5, with K flux densities and $H - K$ and $J - H$ colours, where available. One of the sources in the IRCAM frames, listed as source 29 in Table 3.5, has also been observed by Barnes *et al.* For comparison, they obtain values of $J = 13.5$, $H = 11.2$ and $K = 9.5$, whilst photometry from the IRCAM frames give $J = 13.3$, $H = 11.2$ and $K = 10.0$. The difference in the K magnitude is probably because the 10 arcsec aperture used by Barnes *et al.* included source 31 (Table 3.5; this is *not* the same source as IRS 31 found by Barnes *et al.*) and a considerable amount of extended emission. This list is not a complete sample of the near–infrared sources in the IRCAM frames, and therefore cannot be used to examine the luminosity function of the objects detected. A more extended survey of the region is required for that, so that the extended diffuse emission can be accurately subtracted first.

Figure 3.8 displays the area around the cores FIR4 at H and K, showing an unresolved object at 2 μm within 2 arcsec of the millimetre continuum peak. Contours are the same as for Figure 3.7. The (0,0) position, marked by a cross, is the position of the 1.3 mm peak found by Mezger *et al.*, $\alpha(1950) = 5^{\rm h}39^{\rm m}12.6^{\rm s}$, $\delta(1950) = -1°56'10''$. This

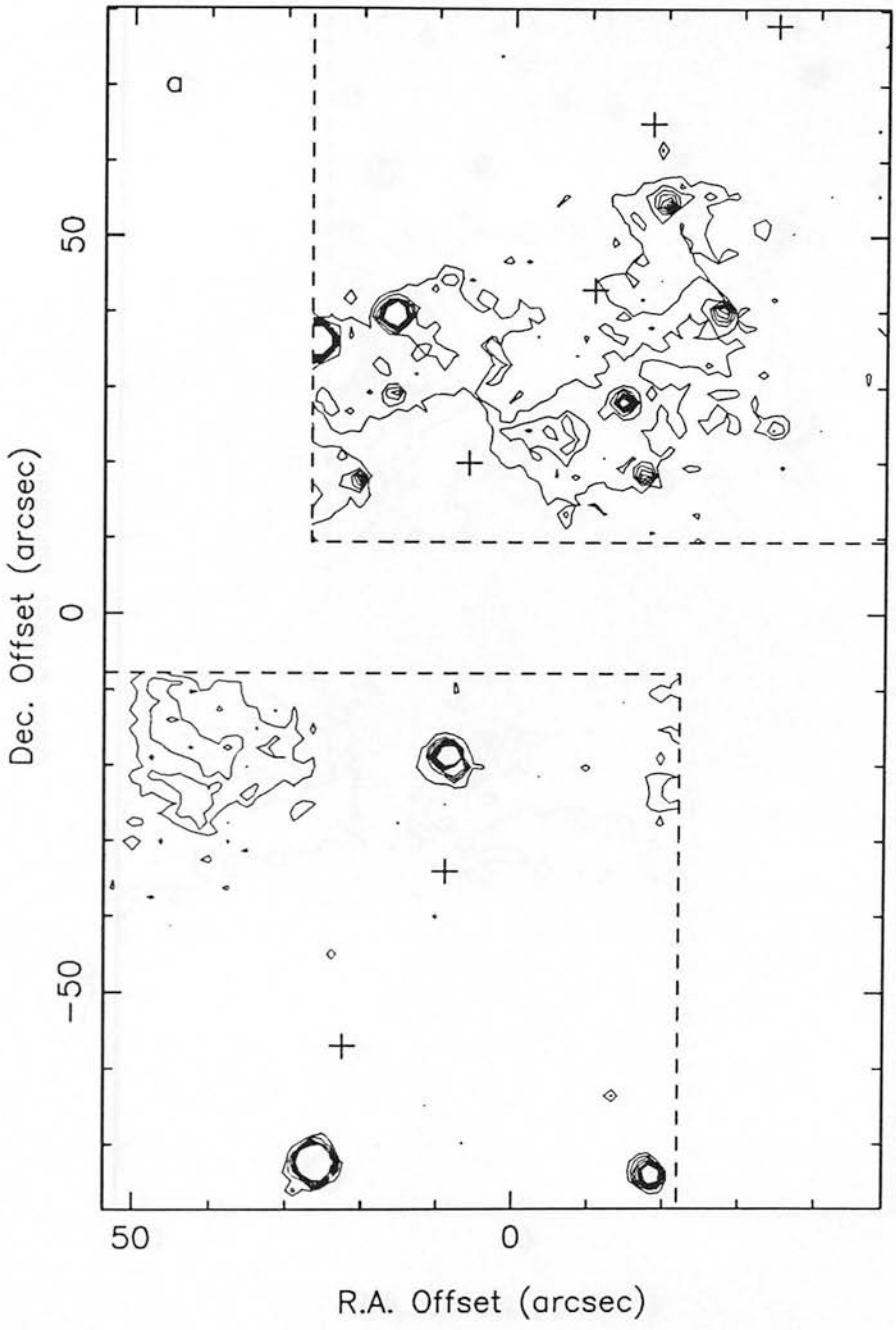

Figure 3.7: (a) J frames of NGC 2024. Contours are at 3σ intervals of 0.062 mJy per pixel above the sky background. The (0,0) position is the same as Figure 3.5.

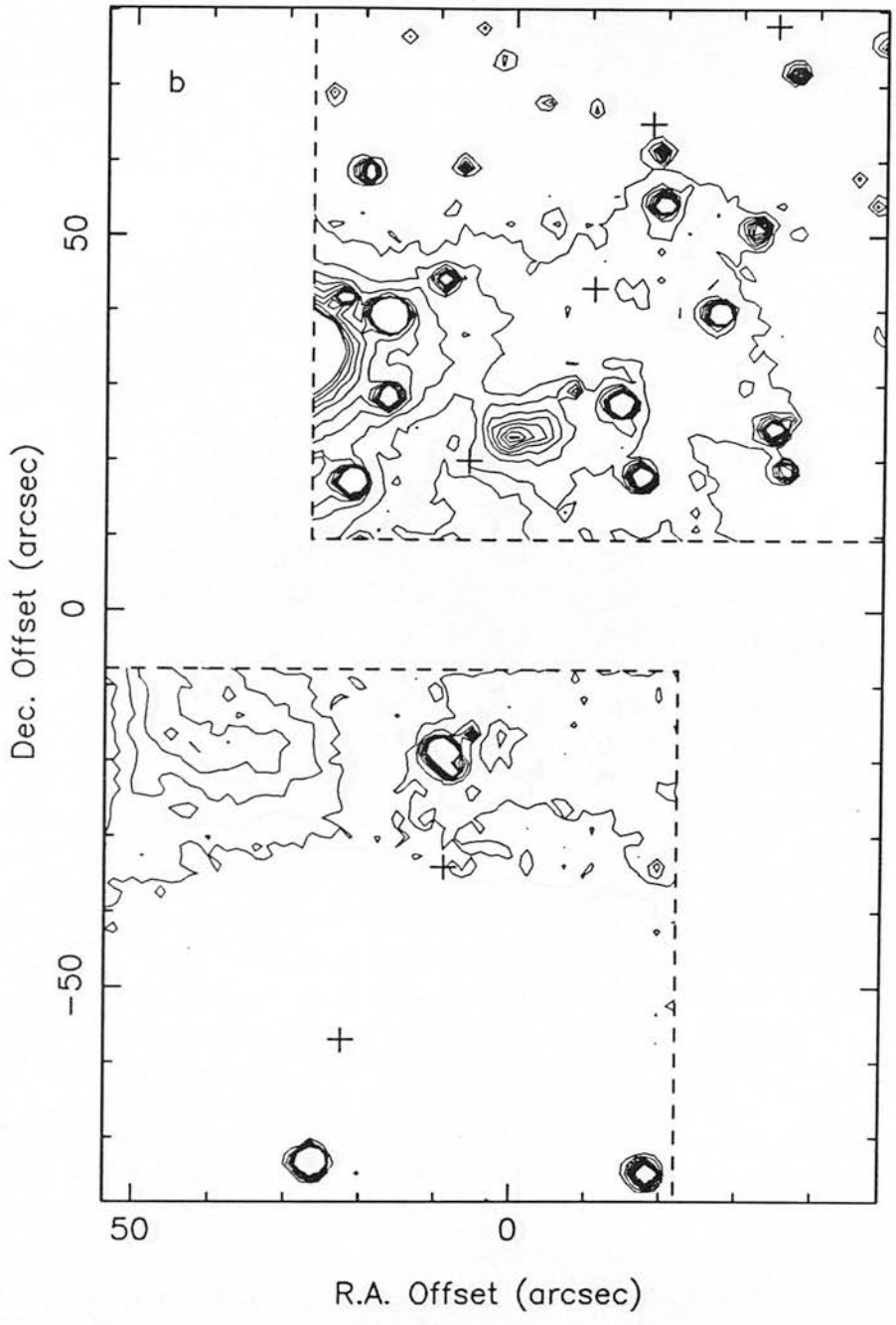

Figure 3.7: (b) H frames of NGC 2024. Contours are at 5σ intervals of 0.134 mJy per pixel above the sky background.

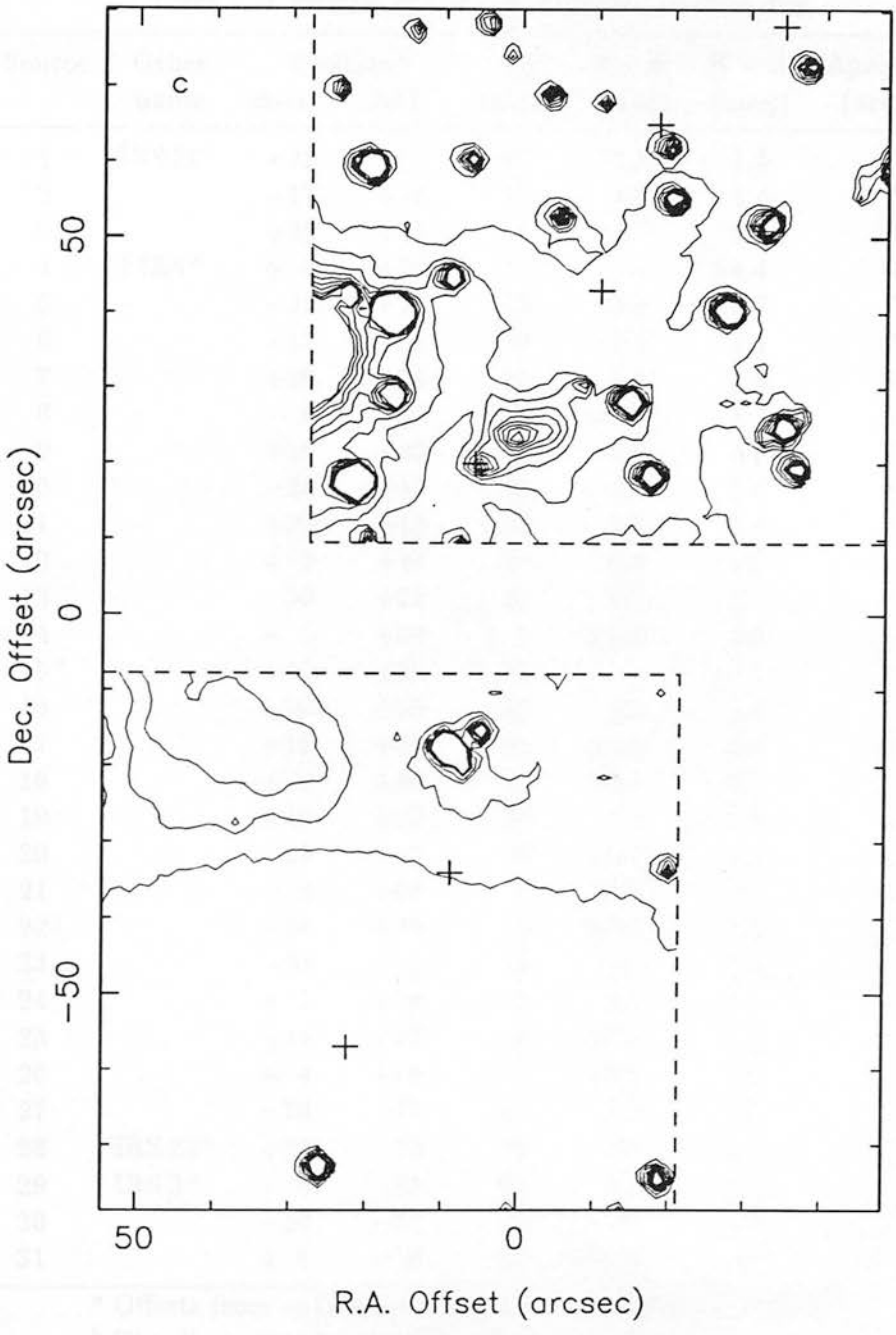

Figure 3.7: (c) K frames of NGC 2024. Contours are at 10σ intervals of 0.278 mJy per pixel above the sky background.

Table 3.5: Results of the near–infrared photometry.

Source	Other name	Position[a] $\Delta\alpha$ (″)	$\Delta\delta$ (″)	S_K (mJy)	$J-H$ (mag)	$H-K$ (mag)	Aperture[b] (arcsec)
1	IRS 20[c]	+21	+17	60	3.5	1.5	7
2		−17	+18	26	2.8	1.4	7
3		+36	+19	15	>4.7	2.3	6
4	FIR4[d]	+ 5	+20	12	–	>4.4	6
5		−35	+25	29	3.4	1.7	7
6		−15	+28	33	2.4	1.1	7
7		+16	+29	30	3.4	1.6	6
8		− 8	+30	5	>4.3	1.4	5
9		+16	+40	91	2.8	0.8	7
10		−28	+40	38	3.1	1.6	6
11		+22	+42	30	3.7	1.6	6
12		+ 9	+44	17	2.9	1.6	6
13		−33	+51	21	3.5	1.9	6
14		− 5	+52	9	>2.9	3.5	5
15[e]		−45	+55	5	–	–	5
16		−20	+55	15	2.1	1.1	5
17		+19	+59	40	>5.5	2.6	6
18		+ 6	+60	10	>4.1	2.4	5
19		−19	+62	10	2.7	1.8	5
20		−11	+67	3	>3.2	2.1	5
21		− 4	+68	7	>3.6	2.6	5
22		−24	+69	5	>3.5	2.2	5
23		−38	+72	11	3.4	1.9	5
24		+ 1	+74	3	1.5	1.4	5
25		+14	+77	4	>2.9	2.4	5
26		+ 4	+78	6	>2.9	3.0	5
27		−19	−74	15	1.5	0.6	7
28	IRS 22[c]	+26	−73	24	0.5	0.1	7
29	IRS 3[c]	+ 8	−19	65	2.1	1.2	7
30		−20	−34	5	>3.8	1.9	5
31		+ 5	−16	11	>4.0	2.6	5

[a] Offsets from $\alpha(1950) = 5^h39^m12.2^s$, $\delta(1950) = -1°56'30''$.
[b] The diameter of a circular software aperture.
[c] Barnes *et al.* (1989).
[d] Mezger *et al.* (1988).
[e] Not included in H or J frame.

source is not detected at H or at J, and photometry in a 6 arcsec circular aperture gives a K flux density of $S_K = 12\,\mathrm{mJy}$. A 3σ upper limit to the peak surface brightness of FIR4 at H gives a lower limit to the $H - K$ colour index of 4.4.

Associated with the $2\,\mu\mathrm{m}$ point source in FIR4 is a bright, compact patch of extended emission about 6×4 arcsec in size. This small nebulosity is clearly visible at H and K but was only weakly detected at J. In an elliptical aperture with a semi–major axis of 6.5 arcsec and eccentricity 0.5, $S_J = 6\,\mathrm{mJy}$, $S_H = 25\,\mathrm{mJy}$ and $S_K = 61\,\mathrm{mJy}$, with corresponding magnitudes of $J = 13.6$, $H = 11.6$ and $K = 10.1$. Therefore the colours integrated over the nebula are $J - H = 2.0$ and $H - K = 1.5$, considerably bluer than the source itself.

The extended patch of emission in all three southern frames at about $\Delta\alpha = +40''$, $\Delta\delta = -20''$ is coincident with the southern compact peak (SCP) in radio continuum found by Crutcher *et al.* (1986).

3.4.3 Discussion

The weak $2\,\mu\mathrm{m}$ point source in Figure 3.8(b) can be confidently identified with the dense core NGC 2024 FIR4. Within the pointing accuracy of the present observations, the near–infrared object is coincident with the 1.3 mm position quoted by Mezger *et al.* (1988). Also, the FIR4 candidate is the most reddened object found in either of the frames – the mean $H - K$ colour of all detected sources (Table 3.5) is 1.8, whilst for FIR4 $H - K > 4.4$. This is consistent with the model of the region described in section 3.1 which places the 1.3 mm cores in the densest part of the molecular cloud, behind the HII region. Hence these objects suffer greater extinction than the stars associated with the HII region itself, which are obscured only by the foreground dust bar. The new $2\,\mu\mathrm{m}$ source is also the only object clearly associated with localised extended emission, even though the region contains a large amount of diffuse emission associated either with NGC 2024 #2 (the very bright $2\,\mu\mathrm{m}$ star found by Grasdalen, 1974; see Figure 3.7), or with the northern compact peak (NCP) in the radio continuum (Crutcher *et al.* 1986).

The presence of near–infrared emission is a clear indication that the core possesses a hot stellar source deeply embedded within it. The cold isothermal condensations postulated by Mezger *et al.* would be completely undetectable at $2\,\mu\mathrm{m}$ and the external layers of such objects are unlikely to be heated to sufficiently high temperatures (a few $\times\,100\,\mathrm{K}$) by a diffuse radiation field. In addition, the $2\,\mu\mathrm{m}$ source is less than 2 arcsec

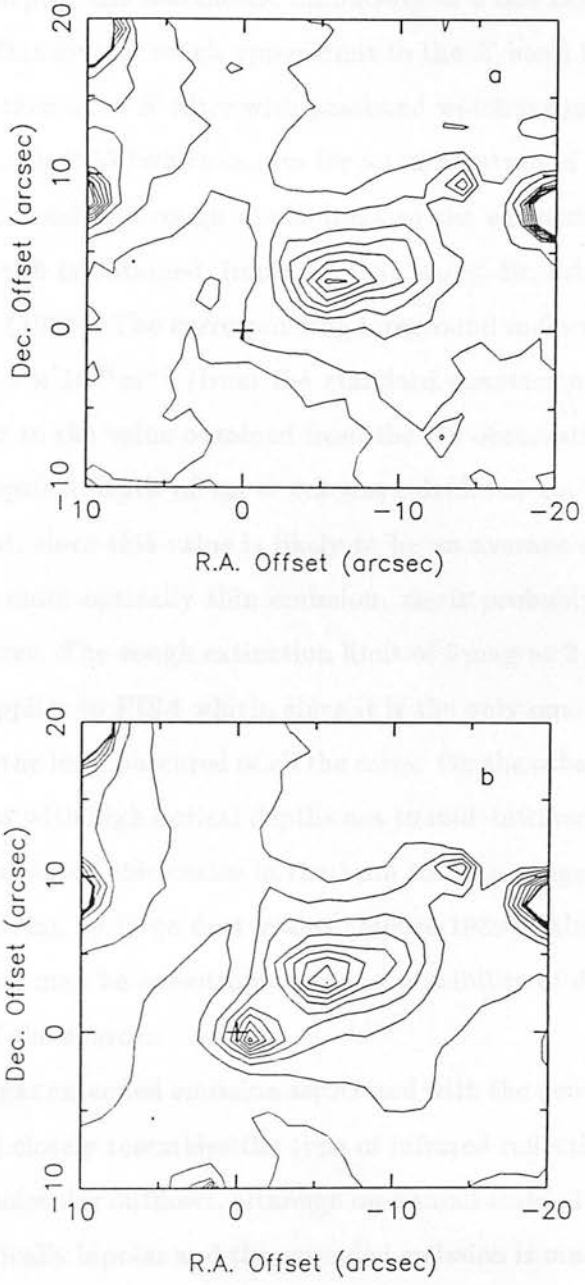

Figure 3.8: (a) 1.65 μm surface brightness around FIR4. (b) The same region at 2.22 μm. Contours are the same as for Figure 3.7.

($< 1,000$ AU at 450 pc) in size and, since the observed dimensions of the dust core are approximately 14×8 arcsec (Mezger *et al.*), it is clear that the near–infrared emission cannot be from an externally heated layer around an otherwise cold condensation.

If the observed 1.3 mm flux is combined with an estimated temperature and associated dust optical depth, the bolometric luminosity of FIR4 can be approximated to be a few $\times$ 100 $L_\odot$. This gives a rough upper limit to the K band luminosity since, for a blackbody observed through a K filter with passband width 0.4 μm, the maximum possible value of $L_K/L_{\rm bol}$ is 0.13 (which occurs for a temperature of 1670 K). Hence, from the observed K flux density, a rough upper limit to the extinction toward the source within FIR4 of $A_K \lesssim 9$ is obtained, implying that $A_V \lesssim 80$, using the extinction law of Rieke & Lebofsky (1985). The corresponding foreground molecular hydrogen column density is $N(H_2) \lesssim 8 \times 10^{26}\,{\rm m}^{-2}$ (from the standard conversion of Bohlin, Savage & Drake, 1978), similar to the value obtained from the CS observations.

A peak 60 μm optical depth of $\tau_{60} = 0.3$ was calculated by Thronson *et al.* using a 50 arcsec beam but, since this value is likely to be an average over large amounts of extended and much more optically thin emission, τ_{60} is probably much higher in the spatially compact cores. The rough extinction limit of 9 mag at 2 μm is consistent with $\tau_{60} = 0.3$ but only applies to FIR4 which, since it is the only one detected in the near–infrared, is probably the least obscured of all the cores. On the other hand, near–infrared emission from sources with high optical depths out to mid–infrared wavelengths may be enhanced by high scattering efficiencies in the 1 μm to 3 μm range and by the effects of strong forward scattering by large dust grains (Moore 1989). Also, the distribution of extinguishing material may be anisotropic and the possibility of detection may depend on the orientation of the source.

The patch of bright extended emission associated with the new near–infrared source at FIR4 (Figure 3.8) closely resembles the type of infrared reflection nebula associated with high–velocity molecular outflows, although on a small scale. The nebula is unipolar rather than symmetrically bipolar and the extended emission is much less reddened than the source, but these features are common (*e.g.* GSS30 in Ophiuchus: Castelaz *et al.*, 1985; SGS1 in NGC 1333: Castelaz *et al.*, 1986; GGD 27: Yamashita *et al.*, 1987; R Mon: Aspin *et al.*, 1988 and Yamashita *et al.*, 1989). Since such nebulae are thought to arise from photons scattered in the compressed dusty shell around a collimated outflow from the central object, it is plausible that FIR4 is generating a similar but smaller

outflow.

Comparatively un-reddened near–infrared light is scattered in the nebula towards the observer, after emerging through a region of reduced extinction, perhaps directly caused by the outflow. The scattered light may become even bluer in colour if the wavelength–dependent grain albedo falls rapidly beyond about $1\,\mu$m (as predicted by Draine & Lee, 1984). The common asymmetry of reflection nebulae is often explained as being due to (and used as evidence for) the presence of a large interstellar disk around the central source, tilted so as to obscure and redden both the source and the far lobe of the nebula. However, strong forward scattering of near–infrared radiation by large dust grains may also contribute to the almost universal suppression of the backward–directed lobe in bipolar reflection nebulae (Moore 1989).

Within FIR4 there appears to be a heavily extinguished, low to medium mass stellar object which may be producing a compact collimated outflow. This description suggests a very unevolved T Tauri star, a type of object frequently associated with massive winds and outflows throughout a considerable portion of its early development.

The current observations provide no evidence of near–infrared radiation from the other northern FIR cores. The source about 4 arcsec southwest of FIR2 (Figure 3.7) is unlikely to be a true association; the offset is twice the 1σ positional uncertainty of the present data. Although the object (source 19) is somewhat reddened ($J - H = 2.7$, $H - K = 1.8$) it is unresolved and its size and colour are not distinguishable from a number of unrelated nearby sources in the larger observed area. This object, like the other similar sources nearby, is most likely to be one of the cluster that includes the main ionising sources for the optical HII region.

Since, as observed in the millimetre continuum, FIR4 is qualitatively no different from the five other FIR cores found by Mezger *et al.*, there are two plausible conclusions that may be drawn from the detection of near–infrared emission and the inferred presence of a hot central source in only one of the four observed. It most likely that the sources that are currently undetected in the near–infrared also contain hot cores but are too deeply embedded and too faint to have been found by the present observations. Alternatively, if some or all of the undetected cores are subsequently found to be true cold protostars, it is clearly demonstrated that it is not possible to determine the nature of a young embedded source on the basis of only far–infrared and (sub)millimetre observations. In order to discount either possibility more sensitive observations are required

in the near–infrared and mid–infrared continuum, especially between 5 μm and 20 μm, where extinction is significantly reduced and where a hot dust spectrum should peak. Near–infrared polarimetry will be required to support the suggestion that the nebulosity associated with FIR4 is due to scattered light in an outflow–associated reflection nebula.

3.5 Conclusions

The high–resolution CS and $C^{34}S$ 7 – 6 observations have revealed the presence of dense, warm gas associated with the millimetre continuum sources in NGC 2024 found by Mezger *et al.* (1988). The excitation temperatures obtained from the data are considerably more than the 16 K assumed by Mezger *et al.* for the dust emission, and indicate that the sources contain intermediate luminosity (10^2 to 10^3 $L_\odot$) embedded young stellar objects. A re-analysis of existing continuum data shows that a dust temperature in the range 42 to about 70 K fits the continuum emission from the whole region well, without the need for a massive cool component to account for the long–wavelength data.

The excitation temperature of the 7 – 6 line from the most extended millimetre core, FIR5, is also the lowest, and this object is a good candidate for the source of the extended outflow that runs north–south over about 5 arcmin. A particularly wide CS 7 – 6 line is observed towards FIR6, which has recently been found to be the origin of a very young and energetic outflow (Richer 1990). This is interpreted as being the result of a high–velocity wind interacting with the surrounding cloud core, and I also suggest that this model accounts for the existing high–resolution HCO^+ data rather than the expanding torus put forward by Barnes & Crutcher (1990).

The lowest optical depth in the CS 7 – 6 line is found towards FIR4, which is consistent with the detection of 2 μm continuum emission from that source. The presence of near–infrared emission is strong evidence that the core contains a hot embedded stellar source rather than a cold protostellar condensation, as has been proposed. Accompanying the near–infrared source is a compact unipolar nebula which has the distinctive features of an infrared reflection nebula and is likely to be associated with an unevolved, collimated outflow from the central object. In the millimetre continuum, FIR4 is qualitatively no different from the other cores in NGC 2024 which were not detected in the near–infrared. Either the other cores are also hot sources but too deeply embedded to have been detected by these observations, or far–infrared and submillimetre observations

alone cannot distinguish between cold sources and deeply embedded young stars.

Chapter 4

DR21(OH)

4.1 Introduction

DR21(OH) is part of a large complex of massive star formation in the Cygnus X region of the sky. It lies 3 arcmin north of the DR21 group of compact HII regions, within the same cloud. Dickel, Dickel & Wilson (1978) proposed that the DR21 cloud ($V_{\rm LSR} = -3\,{\rm km\,s^{-1}}$) is interacting with the W75 cloud (average $V_{\rm LSR} = +9\,{\rm km\,s^{-1}}$), the latter showing a velocity gradient from $+11\,{\rm km\,s^{-1}}$ near W75N down to $+8\,{\rm km\,s^{-1}}$ southeast of DR21. Star formation is occurring along a ridge at an angle of about 40° to the Galactic plane in both clouds. The model they described is shown in Figure 4.1.

DR21(OH), although having associated masers of OH (Norris *et al.* 1982), H_2O (Genzel & Downes 1977) and CH_3OH (Batrla & Menten 1988) signifying the presence of high–mass, young stellar objects, shows no sign of radio continuum emission down to a limit of 10 mJy at 14.5 GHz (Johnston, Henkel & Wilson 1984). This fact, plus the lack of any sign of the energetic outflow or shocked molecular hydrogen such as that displayed by DR21 indicates that DR21(OH) probably contains source(s) at a younger stage of evolution.

High–resolution interferometer measurements in 1.4 mm continuum (Woody *et al.* 1989), formaldehyde $2_{11} - 2_{12}$ (Johnston *et al.* 1984) and thermal methanol emission (Batrla & Menten 1988) show structure on scales less than 10 arcsec, with two or more clumps associated with the various masers. More extensive millimetre and submillimetre mapping (Richardson, Sandell & Krisciunas 1989; Mangum, Wootten & Mundy 1989) has revealed further sources of dust continuum emission within an area of 1.5 × 1.5 arcmin, with relatively low dust temperatures (about 40 K), and molecular hydrogen

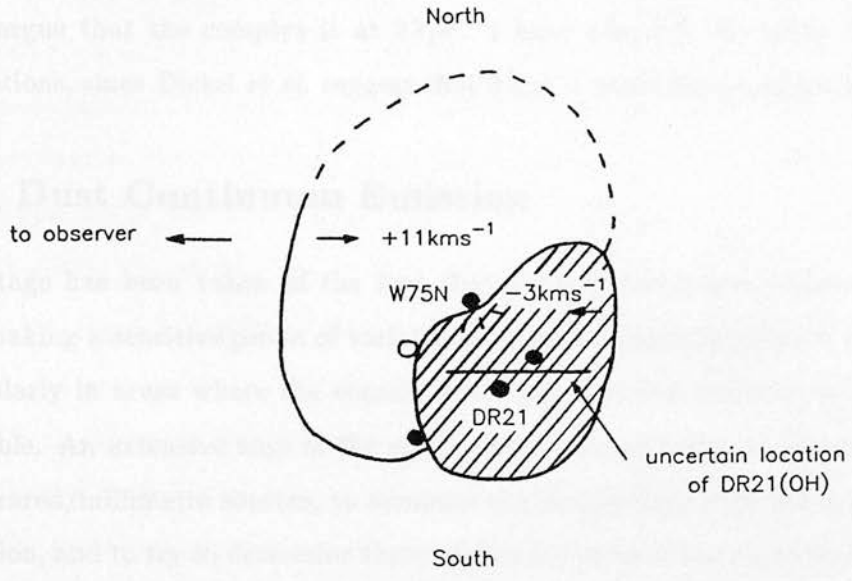

Figure 4.1: Schematic model of the DR21–W75 region put forward by Dickel *et al.* (1978). The filled circles represent regions of enhanced temperature and density as observed in CO emission, and the open circle indicates a region of increased line width.

number densities of approximately $10^{12}\,\mathrm{m}^{-3}$. A further H_2O maser source to the north of DR21(OH) (Cato *et al.* 1976; Genzel & Downes 1977) has also been found to be a source of 50 and 100 μm continuum (Harvey *et al.* 1986).

The existence of such a large number of closely associated sources clearly requires extensive, high resolution mapping, to examine the overall relationship of the various far–infrared and maser sources. Any model for the mechanism that triggered star formation in the region has to account for the observed morphology in both the W75 cloud and the DR21 cloud, so detailed mapping of the respective cloud cores is essential. The evolutionary state of the sources around DR21(OH) are as yet uncertain, though Richardson *et al.* suggested that the cores are still undergoing collapse. Below I use high resolution (11 arcsec) observations of 1.3 mm continuum emission to trace the regions of high temperature/column density of the cloud cores, for a region 5 × 5 arcmin around DR21(OH) itself and the more northern sources. I also present CS and $C^{34}S$ spectra towards DR21(OH) that reveal the kinematics of the various sources, and fit them with a simple LTE two–component model. The core contains extensive high–density gas that could be in a state of infall. My thanks go to Rolf Chini and Walter Gear for obtaining

the 1.3 mm map, and to Toby Moore and Matt Mountain for taking the CS spectra.

The distance to DR21(OH) has frequently been assumed to be 3 kpc, though Dickel *et al.* argue that the complex is at 2 kpc. I have adopted the latter distance in my calculations, since Dickel *et al.* suggest that 3 kpc is probably an upper limit.

4.2 Dust Continuum Emission

Advantage has been taken of the fact that 1.3 mm continuum emission is optically thin, making a sensitive probe of variations in (dust column density) × (temperature), particularly in areas where the contribution from free–free emission is thought to be negligible. An extensive map of the entire region is used below to identify the various far–infrared/millimetre sources, to compare the morphology with other regions of star formation, and to try to determine the evolutionary state of the embedded young stellar objects taking into account existing data.

4.2.1 Observations

The 1.3 mm continuum observations were made using the Max Planck Institut für Radioastronomie (MPIfR) ^{3}He cooled bolometer at the Nasmyth focus of the Institut de Radioastronomie Millimetrique (IRAM) 30 m telescope on Pico Veleta, Spain, in 1989 March. At this wavelength the beam size was 11 arcsec; chopping in azimuth at a frequency of 8.5 Hz was achieved using the secondary, with the beams separated by 30 arcsec. Uranus was mapped as a calibration source, assuming a brightness temperature of 99 ± 3 K, and the pointing, which was found to be repeatable to within 2 arcsec rms, was checked against Uranus and NGC 7027. The zenith opacity was monitored by sky dips, and the zenith transmission was found to be $80 - 90\%$ at 230 GHz. Mapping was performed by scanning the source in the direction of the chopper throw with a scanning velocity of 8 arcmin per minute, using a scan separation of 4 arcsec.

Three maps of 4×3 arcmin centred on $\alpha(1950) = 20^{\rm h}37^{\rm m}14.9^{\rm s}$, $\delta(1950) = 42°12'00''$ and three maps of 6×5 arcmin centred on $20^{\rm h}37^{\rm m}14.9^{\rm s}$, $42°12'30''$ were taken, together with a 3×2 arcmin map of Uranus, which was processed in an identical manner to the maps of DR21(OH) for calibration purposes.

4.2.2 Results

The six continuum maps were converted into single–beam maps using the algorithm of Emerson, Klein & Haslam (1979), transformed into celestial coordinates using the NOD2 software (Haslam 1974), and coadded. The resulting image is shown in Figure 4.2. The rms noise varies across the final map, depending on how many maps contributed to a particular point, the lowest noise (approximately 30 mJy per beam) therefore being towards DR21(OH) itself.

The emission is extended along a north–south ridge, with emission from DR21 evident just at the bottom of the region mapped. Figure 4.2 clearly shows the three sources reported by Richardson *et al.* (1989) and Mangum *et al.* (1990), and I adopt the notation used by Mangum *et al.*, namely DR21(OH)M, DR21(OH)S and DR21(OH)W. The map also reveals two much fainter sources immediately to the north of DR21(OH)M, one 39 arcsec north, DR21(OH)N1, and one 58 arcsec north, DR21(OH)N2. All five sources seem to be part of an associated group within the larger ridge. Positions of these five sources together with the three bright objects 2 arcminutes north of DR21(OH)M are given in Table 4.1.

Table 4.1: Positions of the millimetre sources near DR21(OH).

Source Name	α(1950) (^{h} ^{m} ^{s})	δ(1950) ($^\circ$ $'$ $''$)	Remarks
DR21(OH)S	20 37 14.5	42 11 25	First detected by Gear *et al.* (1988)
DR21(OH)W	20 37 12.4	42 11 45	First detected by Richardson *et al.*
DR21(OH)M	20 37 14.0	42 12 08	Woody *et al.* show it to be two sources
DR21(OH)N1	20 37 13.1	42 12 46	No previous observations
DR21(OH)N2	20 37 12.8	42 13 05	No previous observations
FIR1(H_2O)	20 37 13.4	42 13 57	Has associated H_2O maser
FIR2	20 37 15.4	42 14 19	No previous observations
FIR3(H_2O)	20 37 16.3	42 15 14	Possibly associated with H_2O maser

Obtaining integrated fluxes for all of the sources is slightly complicated by the bright diffuse emission associated with the ridge. I have therefore subtracted off a base level of 500 mJy per beam, and calculated the total flux per source accordingly. Uncertainties in the flux per beam in the map are dominated by the calibration, and are estimated to be 10% (Table 4.2). Integrated fluxes have larger uncertainties, estimated to be about 20%, because of the problems associated with determining a suitable background level.

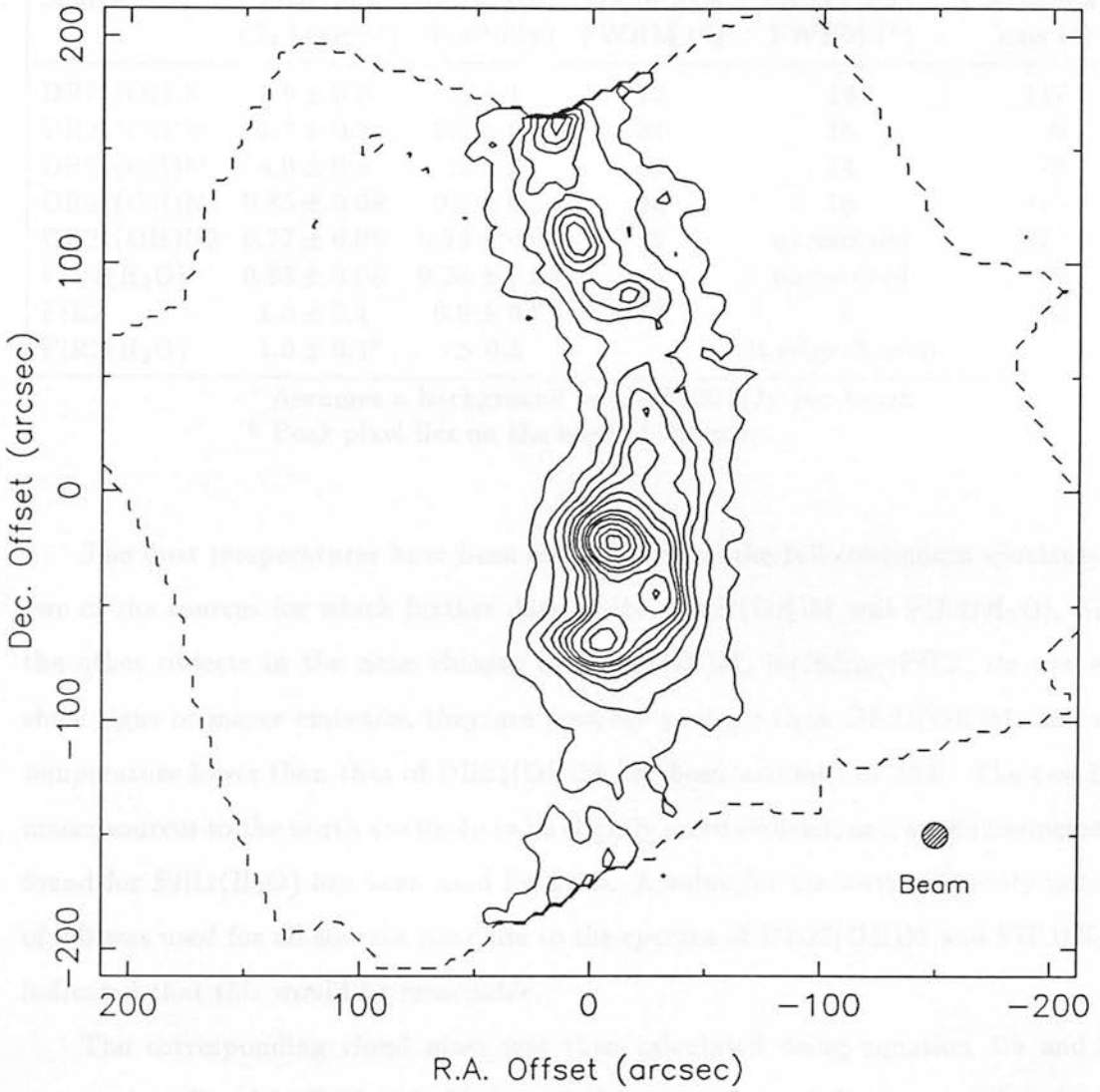

Figure 4.2: 1.3 mm continuum emission from DR21(OH); the dashed line marks the edge of the mapped area. Contours are drawn at intervals of 150 mJy per beam between 150 and 1050, 300 mJy per beam between 1050 and 1950, and then at intervals of 600 mJy per beam. Offsets are with respect to $\alpha(1950) = 20^{h}37^{m}14.9^{s}$, $\delta(1950) = 42°12'30''$.

The results are given in Table 4.2, together with deconvolved source widths along the major and minor axes assuming a Gaussian source and Gaussian beam. The position angle of the major axis is given in degrees east of north.

Table 4.2: 1.3 mm photometry and source sizes.

Source	Peak flux (Jy beam^{-1})	Integrated flux[a] (Jy)	Major axis FWHM (″)	Minor axis FWHM (″)	P.A. of major axis (°)
DR21(OH)S	1.9 ± 0.2	5 ± 1	22	14	117
DR21(OH)W	1.7 ± 0.2	2.3 ± 0.5	24	15	0
DR21(OH)M	4.0 ± 0.4	10 ± 2	18	14	79
DR21(OH)N1	0.85 ± 0.08	0.7 ± 0.1	22	18	176
DR21(OH)N2	0.77 ± 0.08	0.34 ± 0.07	15	unresolved	12
FIR1(H_2O)	0.83 ± 0.08	0.38 ± 0.08	9	unresolved	97
FIR2	1.0 ± 0.1	0.9 ± 0.2	18	9	20
FIR3(H_2O)	1.0 ± 0.1[b]	> 0.5		at edge of map	

[a] Assumes a background level of 500 mJy per beam.
[b] Peak pixel lies on the edge of the map.

The dust temperatures have been estimated from the full continuum spectrum for two of the sources for which further data exists, DR21(OH)M and FIR1(H_2O). Since the other objects in the near vicinity of DR21(OH)M, including FIR2, do not even show signs of maser emission, they are possibly younger than DR21(OH)M, and so a temperature lower than that of DR21(OH)M has been assumed of 30 K. The two H_2O maser sources to the north are likely to be slightly more evolved, and so the temperature found for FIR1(H_2O) has been used for both. A value for the dust emissivity index β of 2.0 was used for all sources since fits to the spectra of DR21(OH)M and FIR1(H_2O) indicated that this would be reasonable.

The corresponding cloud mass was then calculated using equation 1.8 and the temperature listed in Table 4.3. If $\beta = 1.0$ then the values of the mass, and molecular hydrogen column and space densities in Table 4.3 are too high by a factor (1300/400) = 3.25, since the gas–to–dust conversion used was calculated for 400 μm (Hildebrand 1983). The peak molecular hydrogen column density and space density has been calculated assuming that the mass is distributed with Gaussian geometry. The luminosity for the sources other than DR21(OH)M and FIR1(H_2O) have been estimated by assuming that a single temperature dust component is responsible for the observed 1.3 mm emission.

Table 4.3: Derived properties of the sources near DR21(OH).

Source	T_{dust} (K)	Luminosity[a] ($L_\odot$)	Mass[a] ($M_\odot$)	$N(H_2)$ peak (m^{-2})	$n(H_2)$ peak (m^{-3})
DR21(OH)S	30[b]	$\sim 2\times10^3$	660	9.3×10^{27}	1.7×10^{12}
DR21(OH)W	30[b]	$\sim 2\times10^3$	300	3.6×10^{27}	6.0×10^{11}
DR21(OH)M	40[c]	4.1×10^3	940	1.6×10^{28}	3.2×10^{12}
DR21(OH)N1	30[b]	$\sim 2\times10^3$	92	1.0×10^{27}	1.6×10^{11}
DR21(OH)N2	30[b]	$\sim 7\times10^2$	45	$> 1.4\times10^{27}$	$> 3.9\times10^{11}$
FIR1(H_2O)	65[c]	2.6×10^3	21	$> 1.1\times10^{27}$	$> 3.9\times10^{11}$
FIR2	30[b]	$\sim 1\times10^3$	120	1.3×10^{27}	3.2×10^{11}
FIR3(H_2O)	65[b]		> 27		

[a] Assumes a distance of 2 kpc.
[b] Assumed value (see text).
[c] Calculated from fitting the continuum spectrum.

4.2.3 Individual sources

4.2.3.1 DR21(OH)M

DR21(OH)M has been resolved into two continuum components by Woody *et al.* (1989) using the Owens Valley Interferometer, though it just appears slightly elongated in Figure 4.2. Figure 4.3 shows where the various components lie with respect to the 1.3 mm dust continuum and the masers.

The flux listed in Table 4.2 is plotted in Figure 4.4 together with existing photometry points from Harvey *et al.* (1986), Gear *et al.* (1988), and Richardson *et al.* (1989). The resolution used by Harvey *et al.* should have been sufficient to resolve DR21(OH)M and DR21(OH)S if there had been significant emission from the more southerly source. However no such source was found at 50 and 100 μm, so I assume that the flux they measure is mainly due to DR21(OH)M. The 800 μm flux of Richardson *et al.* lies somewhat above a smooth curve between the other points longward of 100 μm, so just the four points at 1.3 mm, 1.1 mm, 350 μm and 100 μm were fitted to a greybody function of the form $B(\nu)(1-e^{-\tau(\nu)})\Omega$, where Ω is the source solid angle and $\tau \propto \nu^\beta$. For $\beta = 2.0$, the fit is shown in Figure 4.4. The results for this fit are $T_{dust} = 40$ K, $\tau_{100\,\mu m} = 26.5$ and $\Omega = 1.14 \times 10^{-9}$ sr, with a χ^2 of 0.85. The implied optical depth at 1.3 mm is 0.16 which is high, and is necessary to give the required spectral slope at long wavelengths. Model fits with a value of β less than 2.0 failed to converge, because the temperature required to fit the slope at long wavelengths is then too high to account for the observed

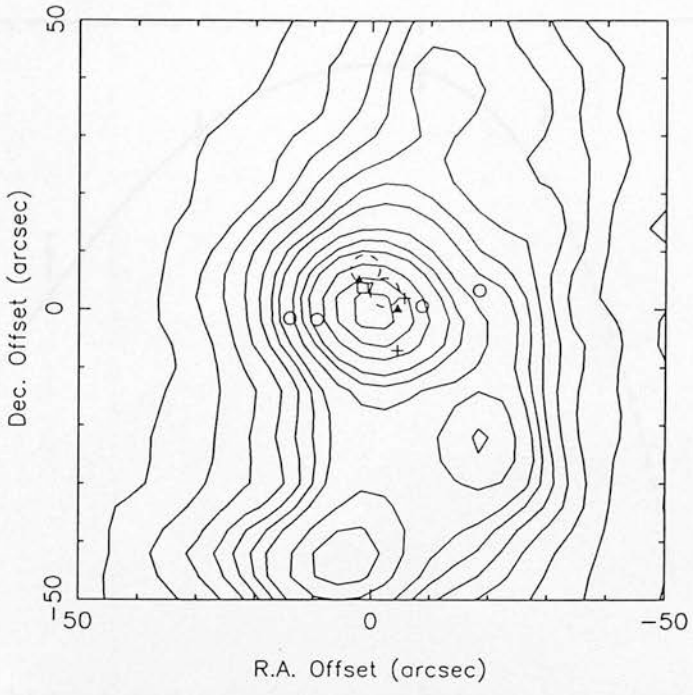

Figure 4.3: The position of features relative to DR21(OH)M. The peaks found by the interferometer (Woody *et al.* 1989) are marked by filled triangles, and the peaks in the formaldehyde emission (Johnston *et al.* 1984) are indicated by crosses. The group of OH masers (Norris *et al.* 1982) are marked by an open square, the H_2O maser positions (Genzel & Downes 1977) are marked by dashed circles and the methanol masers (Plambeck & Menten 1990) are shown as open circles.

position of the turnover in the spectrum. This model is extremely simple and takes no account of density or temperature gradients, but if they exist they will serve to broaden the spectrum without the need for such high optical depths.

The value of Ω corresponds to a source diameter of 9.6 arcsec for spherical geometry, or 6.5 arcsec FWHM for Gaussian geometry. This can be compared with the value obtained by fitting the map with a two dimensional Gaussian along the major and minor axes shown in Table 4.2. The agreement is remarkably good, and indicates that temperature gradients are relatively small over the regions responsible for the far–infrared/submillimetre emission.

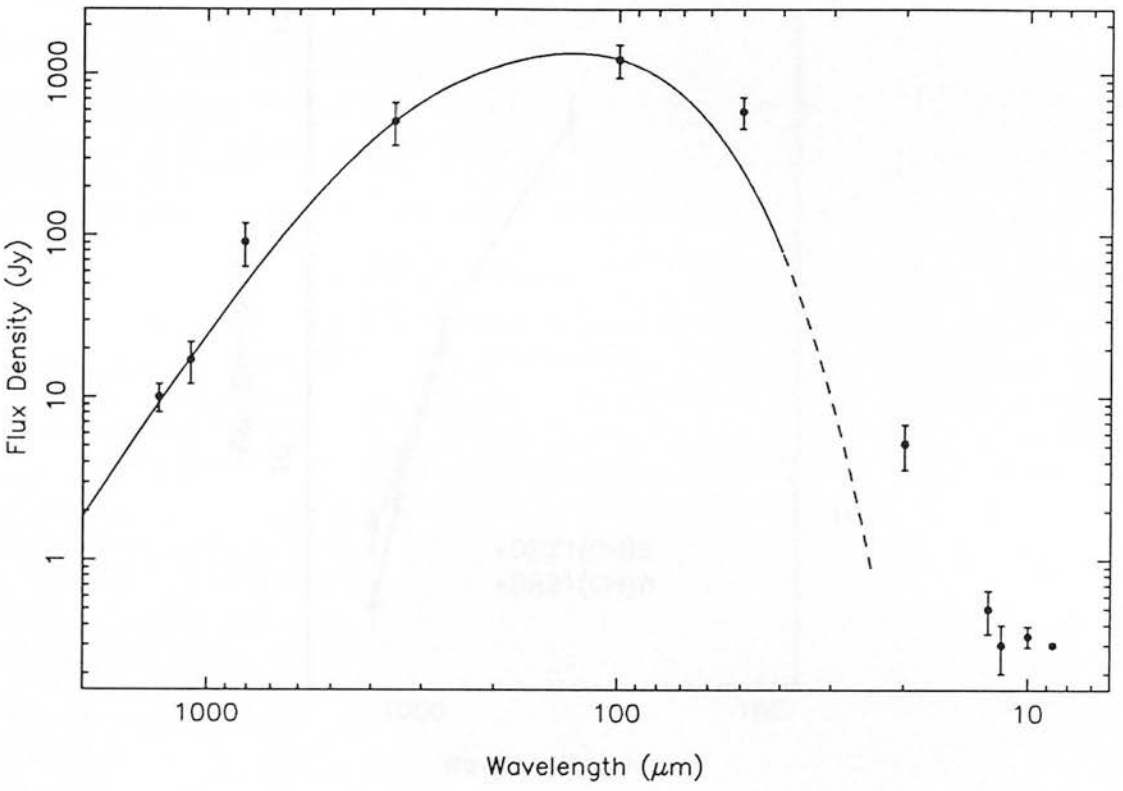

Figure 4.4: The continuum spectrum of DR21(OH)M, with a fit for $T_{\rm dust} = 40\,{\rm K}$.

4.2.3.2 DR21(OH)S and DR21(OH)W

The two bright continuum sources to the south of DR21(OH)M were first reported by Gear *et al.* (1988) and Richardson *et al.* (1989). Neither shows any sign of maser activity, and both are sites of significant thermal methanol emission (Batrla & Menten 1988). The existing photometry for both sources is plotted in Figure 4.5. A rough upper limit to the 50 and 100 μm fluxes of 600 Jy can be obtained for DR21(OH)S from the far-infrared mapping of Harvey *et al.* (1986), giving an estimated dust temperature in the range 15 to 50 K, consistent with the temperature assumed in Table 4.3.

4.2.3.3 DR21(OH)N1 and DR21(OH)N2

Two new sources that are considerably fainter than DR21(OH)M have been found immediately to the north. They are part of the same group and have core masses of

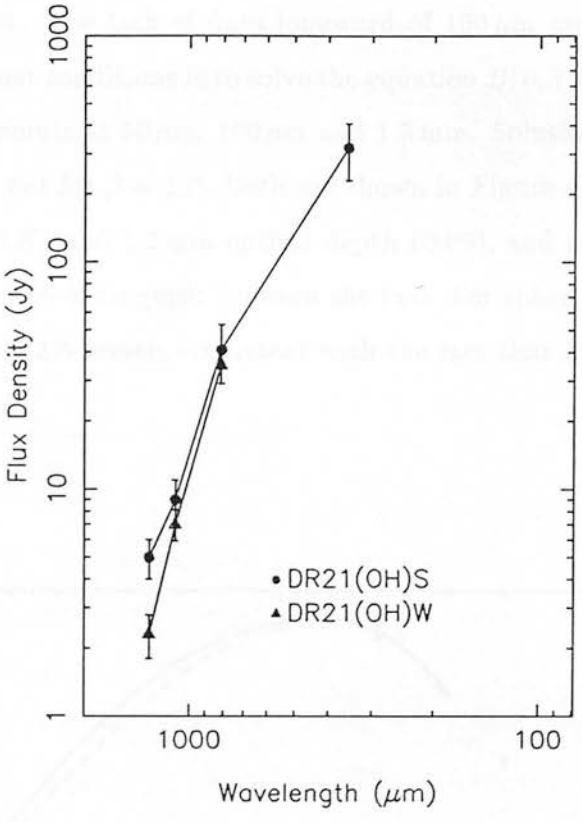

Figure 4.5: Existing photometry of DR21(OH)S and DR21(OH)W. Fluxes come from Gear *et al.* (1988), Richardson *et al.* (1989) and the present work.

$50 - 100\,M_\odot$ with the assumed temperature of 30 K, although they could be colder and correspondingly more massive. They appear to be either younger than the more southerly sources, or a site of lower–mass star formation. Either way, they clearly warrant further investigation.

4.2.3.4 FIR1(H_2O)

FIR1(H_2O) has been observed by Harvey *et al.* (1986) in the mid and far–infrared, who proposed that it is a young pre–main sequence star that is the exciting source for the H_2O maser found by Cato *et al.* (1976) and Genzel & Downes (1977). Figure 4.2 shows it to be situated near a ridge of emission extended in R.A. that could indicate the presence of another, fainter, embedded source. The 8 to 120 μm photometry of Harvey *et al.*, together with the 1.3 mm point in shown in Figure 4.6. Its spectral shape is typical

of embedded YSOs (Yorke & Shustov 1981). It has significantly more mid-infrared emission than DR21(OH)M and is detectable in the near-infrared, and is probably less deeply embedded. The lack of data longward of 100 μm means that the only way of estimating the dust conditions is to solve the equation $B(\nu,T)(1-e^{-\tau(\nu)})\Omega$ with $\tau \propto \nu^{\beta}$, using the three points at 50 μm, 100 μm and 1.3 mm. Solutions were found for $\beta = 2.0$ and $\beta = 1.5$ but not for $\beta = 1.0$. Both are shown in Figure 4.6. They give very similar temperatures (65 K) and 1.3 mm optical depth (0.06), and clearly more submillimetre points are needed to distinguish between the two. For spherical symmetry the implied source diameter is 2.5 arcsec, consistent with the fact that it was unresolved by an 11 arcsec beam.

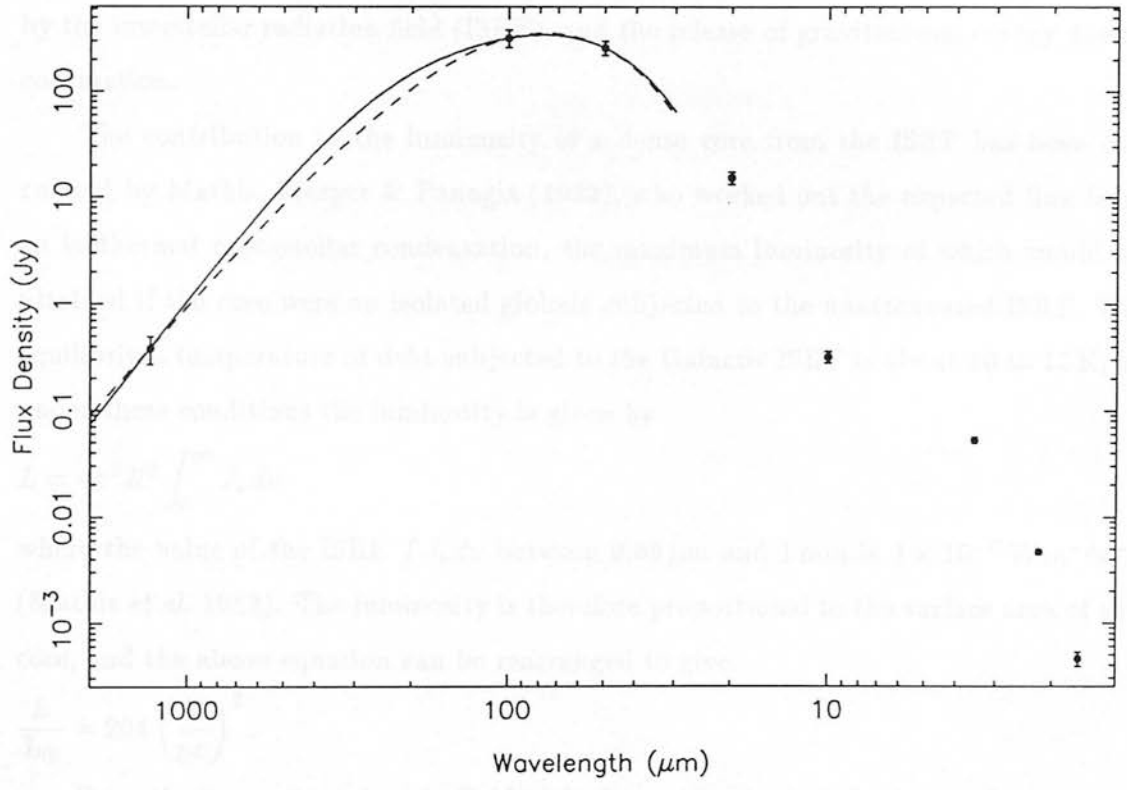

Figure 4.6: The spectrum of FIR1(H_2O) with fits for a temperature of 65 K. The solid curve has $\beta = 2$, and the dashed curve has $\beta = 1.5$.

4.2.3.5 FIR2 and FIR3(H_2O)

There have been no previous observations of FIR2, but if it were as warm as FIR1(H_2O) it would have shown up in the 50 and 100 μm maps of Harvey *et al.* (1986). FIR3(H_2O) is unfortunately on the edge of the map, which allows only lower limits to the integrated flux and mass to be estimated. A H_2O maser was found at $\alpha(1950) = 20^h37^m16.7^s$, $\delta(1950) = 42°15'15''$ by Genzel & Downes (1977) which is almost certainly associated with the observed millimetre source.

4.2.4 Discussion

4.2.4.1 Evolutionary state of the sources

To decide whether the cores contain embedded, luminous protostars or young stellar objects, I consider the possible contributions to the luminosity of the cores from heating by the interstellar radiation field (ISRF), and the release of gravitational energy due to contraction.

The contribution to the luminosity of a dense core from the ISRF has been calculated by Mathis, Mezger & Panagia (1983), who worked out the expected flux from an isothermal protostellar condensation, the maximum luminosity of which would be attained if the core were an isolated globule subjected to the unattenuated ISRF. The equilibrium temperature of dust subjected to the Galactic ISRF is about 10 to 15 K, so under these conditions the luminosity is given by

$$L = 4\pi^2 R^2 \int_0^\infty J_\nu d\nu$$

where the value of the ISRF $\int J_\nu d\nu$ between 0.09 μm and 1 mm is $2 \times 10^{-6}\,\mathrm{W\,m^{-2}s^{-1}}$ (Mathis *et al.* 1983). The luminosity is therefore proportional to the surface area of the core, and the above equation can be rearranged to give

$$\frac{L}{\mathrm{L}_\odot} = 204 \left(\frac{R}{\mathrm{pc}}\right)^2 .$$

From the linear sizes given in Table 4.2, the maximum contribution to the luminosity of a source by heating due to the ISRF is for DR21(OH)N1, where $L_{\mathrm{ISRF}} = 1.6\,\mathrm{L}_\odot$. Although the luminosities in Table 4.3 are estimated by assuming temperatures considerably higher than the dust equilibrium temperature, a similar calculation using a temperature of 12 K indicates that for DR21(OH)N1 $L_{\mathrm{ISRF}} = 0.03 L_{\mathrm{tot}}$.

The value of the ISRF can be enhanced by the close proximity of newly–formed OB field stars. The closest early–type stars to DR21(OH) are those associated with DR21,

which contains ZAMS stars between O8 and B0 (Harris 1973, corrected for a distance of 2 kpc) at a distance of nearly 2 pc to the south. If these were not still embedded within a large amount of dust (the visual extinction towards the centre of the OB cluster is more than 400 magnitudes from the results of Richardson *et al.* 1989) they would have a significant effect on the heating of the other cores. However they are far too heavily extinguished to be contributing to the luminosity of DR21(OH). I therefore conclude that any such contribution is negligible.

Now I look at the possible contribution to the luminosity from gravitational contraction. The maximum rate at which gravitational energy can be radiated away from a collapsing cloud occurs when none of the energy goes into raising the temperature of the infalling gas. This means that the collapse is isothermal, and may be a reasonable approximation for collapsing molecular clouds until they become optically–thick to infrared radiation. The cloud under consideration cannot be in free–fall since in that situation all the energy would be converted into the kinetic energy of the gas, but for simplicity imagine that its infall velocity is some fraction ϵ of the free–fall velocity, and that the remainder of the energy released by the contraction is radiated away.

Consider a spherically symmetric cloud with an initial density distribution $\rho_i(r_i)$, where i denotes the initial conditions. Conservation of the energy of a shell mass $m = 4\pi r_i^2 dr_i \rho_i(r_i)$ at radius r demands that

$$-\frac{GM(<r_i)m}{r} + \frac{1}{2}m\left(\frac{dr}{dt}\right)^2 - \int \frac{dE}{dt}dt = \text{constant}$$

where dE/dt is the luminosity of the shell due to its contraction, and $M(<r_i) = \int_0^{r_i} 4\pi r_i'^2 \rho_i(r_i')dr_i'$ is the mass within the shell. $\int (dE/dt)dt$ is therefore the total energy that has been lost by the shell due to radiation, and work done against non-gravitational forces, and the luminosity dE/dt is

$$\frac{dE}{dt} = \frac{GM(<r_i)m}{r^2}\frac{dr}{dt} + m\frac{d^2r}{dt^2}\frac{dr}{dt}.$$

If the collapse velocity is a fraction of the free–fall velocity, it is given by

$$\frac{dr}{dt} = \epsilon(2GM(<r_i))^{1/2}\left(\frac{1}{r} - \frac{1}{r_i}\right)^{1/2},$$

so that the rate at which gravitational energy is lost is

$$\frac{dE}{dt} = \epsilon(1-\epsilon^2)\sqrt{2}\frac{(GM(<r_i))^{3/2}}{r^2}m\left(\frac{1}{r} - \frac{1}{r_i}\right)^{1/2}.$$

This has a maximum for $\epsilon = 1/\sqrt{3}$. The radiated energy loss will be less than this.

To obtain the luminosity dE/dt solely as a function of time, $r(t)$ must be evaluated. This can be done by making the substitution $r = r_i \cos^2\theta$ (*e.g.* Dyson & Williams 1980), so that the time after the start of the collapse, t, is

$$t = \left(\frac{r_i^3}{2\epsilon^2 GM(<r_i)}\right)^{1/2} \left(\theta + \frac{1}{2}\sin 2\theta\right),$$

and the luminosity of the shell in terms of θ is

$$\frac{dE}{dt} = \sqrt{2}\,\epsilon(1-\epsilon^2)\,((GM(<r_i))^{3/2}\,\frac{4\pi r_i^2 dr_i \rho_i(r_i)}{r_i^{1/2}}\frac{\sin\theta}{\cos^5\theta}.$$

The simplest situation is for a cloud that is initially uniform with density ρ_0 and radius R_i, for which the expression for the total luminosity (summing over all r_i) as a function of θ (inserting the above value for ϵ) is

$$\left(\frac{dE}{dt}\right)_{\rm tot} = \frac{2\sqrt{2}}{135}\,G^{3/2}(4\pi\rho_0)^{5/2}R_i^5\frac{\sin\theta}{\cos^5\theta}.$$

Written explicitly as a function of R, the outside radius of the cloud, and $M_{\rm cloud}$, the total mass of the cloud, the luminosity is

$$\left(\frac{dE}{dt}\right)_{\rm tot} = \frac{2\sqrt{6}}{15}\,G^{3/2}\left(\frac{M_{\rm cloud}}{R}\right)^{5/2}\left(1-\frac{R}{R_i}\right)^{1/2},$$

so that for $R \ll R_i$, the luminosity is virtually independent of R_i.

The result of calculating $(dE/dt)_{\rm tot}$ as a function of t is plotted in Figure 4.7 for a cloud of $1000\,{\rm M}_\odot$ with an initial radius 1 pc. The collapse time t_c is where $r = 0$, at which point the luminosity is infinite. The luminosity is $\gtrsim 10^3\,{\rm L}_\odot$, similar to that observed (see Table 4.3) for a total of just 4000 years at the end of the collapse, less if the mass of the cloud is lower.

For the individual sources I have calculated the luminosity that we would see now from a cloud with the mass given in Table 4.3 and the linear dimension obtained from the source sizes listed in Table 4.2. The maximum contribution is found for DR21(OH)M, for which approximately 6% of the luminosity could be due to the release of gravitational energy.

This is the maximum possible contribution that gravitational contraction can make towards the luminosity, and there are several mechanisms that would tend to slow the collapse to significantly less than the free–fall velocity. Support from magnetic pressure can be significant (Mouschovias & Spitzer 1976; Tomisaka, Ikeuchi & Nakamura 1988), and wide molecular lines show that supersonic turbulence is prevalent within GMCs (*e.g.* Larson 1981). It therefore seems likely that the luminosity of the cores in DR21(OH) require the presence of embedded self–luminous sources to account for the observations, and that any such sources must be very young to have left the cloud core so apparently undisturbed by the kind of phenomena currently disrupting DR21.

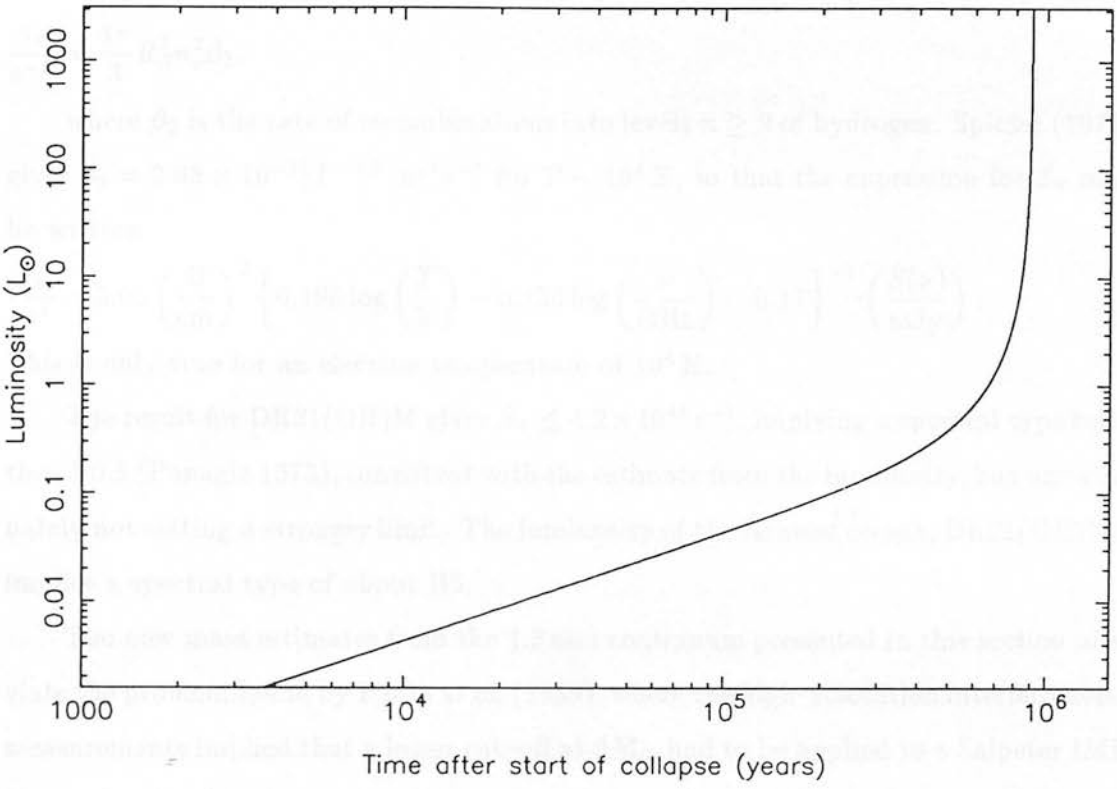

Figure 4.7: The maximum luminosity obtainable from the gravitational contraction of a cloud of $1000\,M_\odot$ with an initial radius 1 pc.

The other extreme can also be considered, whereby all the luminosity from each core is due to a single, embedded, ZAMS star. The luminosity of DR21(OH)M implies a ZAMS star of spectral type B2 or later. To work out whether the upper limit on the radio continuum emission is useful for setting an upper limit on the spectral type, I have calculated a corresponding upper limit to the expected flux of ionizing photons. To do this, I first used the expression for the absorption coefficient $\kappa(\nu)$ given in Spitzer (1978), which was originally derived by Oster (1961). The optical depth τ is then approximated by $\kappa(\nu)l$ where l is the pathlength through the source, and by using the Rayleigh–Jeans approximation, assuming small optical depth and a uniform spherical source, the following expression for the flux density $S(\nu)$ is obtained:

$$\frac{S(\nu)}{\mathrm{mJy}} = 9.77\times10^{-10}\left(\frac{n_e}{\mathrm{cm}^{-3}}\right)^2\left(\frac{T}{\mathrm{K}}\right)^{-0.5}\left(\frac{\theta_s}{\mathrm{arcsec}}\right)^3\left(\frac{D}{\mathrm{pc}}\right)\times \left\{0.195\log\left(\frac{T}{\mathrm{K}}\right)-0.130\log\left(\frac{\nu}{\mathrm{GHz}}\right)-0.17\right\}.$$

Here, n_e is the electron number density, θ_s is the source diameter, T the electron temperature and D is the distance to the source. Now, for a Strömgren sphere with radius R_S is related to the rate at which the star emits ionizing photons S_* by

$$\frac{S_*}{\mathrm{s}^{-1}} = \frac{4\pi}{3} R_S^3 n_e^2 \beta_2,$$

where β_2 is the rate of recombinations into levels $n \geq 2$ of hydrogen. Spitzer (1978) gives $\beta_2 = 2.68 \times 10^{-11} T^{-0.5}\,\mathrm{cm^3\,s^{-1}}$ for $T \sim 10^4\,\mathrm{K}$, so that the expression for S_* may be written

$$\frac{S_*}{\mathrm{s}^{-1}} = 5.05 \left(\frac{D}{\mathrm{cm}}\right)^2 \left\{0.195 \log\left(\frac{T}{\mathrm{K}}\right) - 0.130 \log\left(\frac{\nu}{\mathrm{GHz}}\right) - 0.17\right\}^{-1} \left(\frac{S(\nu)}{\mathrm{mJy}}\right).$$

This is only true for an electron temperature of $10^4\,\mathrm{K}$.

The result for DR21(OH)M gives $S_* \lesssim 4.2 \times 10^{45}\,\mathrm{s^{-1}}$, implying a spectral type later then B0.5 (Panagia 1973), consistent with the estimate from the luminosity, but unfortunately not setting a stronger limit. The luminosity of the faintest object, DR21(OH)N1, implies a spectral type of about B5.

The new mass estimates from the 1.3 mm continuum presented in this section alleviate the problem found by Padin *et al.* (1989), where the high–resolution interferometer measurements implied that a lower cut–off at $6\,\mathrm{M_\odot}$ had to be applied to a Salpeter IMF to account for their low mass–to–luminosity ratio. They clearly missed a large amount of extended emission that the single–beam mapping detected, and standard IMFs (*e.g.* Miller & Scalo 1979) can now account for the observations. For example, if the cloud had already finished forming stars and a Miller–Scalo mass function were applicable, the mass function can be normalised to fit the observed luminosity (Appendix A) so that the highest mass star present is $14.8\,\mathrm{M_\odot}$. In this case, the total mass of stars formed is $150\,\mathrm{M_\odot}$, giving a star formation efficiency of $M_{\mathrm{stars}}/(M_{\mathrm{cloud}} + M_{\mathrm{stars}}) = 0.14$. This is not unreasonable, though it seems unlikely that star formation has now finished, because the cloud core has evidently not been dispersed by active star formation.

A better explanation that accounts for the luminosity is the presence of a star with a mass slightly higher than $14.8\,\mathrm{M_\odot}$, that is responsible for the majority of the luminosity and explains the proximity of the masers. In this situation, again assuming that a Miller–Scalo IMF is appropriate at the time that star formation within the cloud has finished, the implication is that the lower–mass stars have yet to form. There is certainly no problem with finding enough material from which to make these stars.

The region has several features in common with other areas of high–mass star formation. The dense cores in the cloud are situated in an extended ridge, similar to

that found in NGC 2024 (Chapter 3) and OMC1 (Mezger, Wink & Zylka 1990). The total mass of the cloud core is $2000\,M_\odot$, comparable to the value obtained by Mezger *et al.* for OMC1 of $1700\,M_\odot$. At the distance of DR21(OH), the two cores OMC1 and OMC2 would subtend an angle of about 5 arcmin. The linear resolution is a factor of 4.4 worse, so the separation of the millimetre continuum peaks in DR21(OH) found by the Owens Valley Interferometer (Woody *et al.* 1989) are still further apart than the various sources found in the dense cores of OMC1 (Mezger *et al.*).

The comparison with Orion also illustrates the large separation of the methanol masers (Plambeck & Menten, 1990, Figure 4.3), implying that they are associated with dense clumps at considerable distances from the exciting source. This suggests the presence of an energetic outflow that is still too young to have disrupted the core significantly, and the dense methanol clumps occur at the interface between the outflowing gas and the surrounding dense medium (as Plambeck & Menten have suggested for DR21). The line of methanol masers is parallel to the large–scale DR21 outflow, as would be the case if a magnetic field threading the whole GMC were responsible for the observed orientation, or if winds preferentially break out of the cloud core perpendicular to the ridge. Any high–velocity CO would be difficult to detect first because the region is so confused by its location along a spiral arm, and secondly emission from W75 would mask any red–wing emission from DR21(OH). The upper limit to the molecular hydrogen $v = 1 - 0\ S(1)$ line flux of $6 \times 10^{-16}\,W\,m^{-2}$ (Fischer, Righini-Cohen & Simon 1980) does not rule out the presence of shocked H_2 emission, since the extinction at $2\,\mu m$ implied by the 1.3 mm data of approximately 80 mag is extremely high.

To summarise, the luminosities of the 1.3 mm continuum sources near DR21(OH) require the presence of embedded young sources. Star formation is still going on within the cloud core, and the most likely explanation for the existence of the various masers separated by such a large distance near DR21(OH)M is the presence of an outflow that is still very young, and as yet has not been detected.

4.3 CS emission

The densities found within the cores of DR21(OH) from the millimetre continuum observations above show that a molecule sensitive to high densities is required if the kinematics of the core are to be examined. The CS $1 - 0$ and $2 - 1$ transitions require densities of $(0.7 - 4) \times 10^{11}\,m^{-3}$ to be thermalised, which are clearly suitable for

DR21(OH).

4.3.1 Observations

Observations of the molecules CS and $C^{34}S$ were carried out in 1988 April using the Nobeyama Radio Observatory (NRO) 45 m telescope, Japan. The rotational transitions $J = 1 - 0$ and $J = 2 - 1$ were observed simultaneously, for each isotope, by using a polarization beam splitter to direct the two polarizations to different receivers, namely an SIS receiver for the 49 GHz transitions, and a Schottky receiver for the 98 GHz transitions. Spectra of all transitions were taken with high–resolution (37 kHz) 2048–channel acousto–optical spectrometers, resulting in total bandwidths of 40 MHz. The single sideband system temperature obtained for the SIS receiver at 49 GHz was about 300 K, and for the Schottky receiver at 98 GHz, $T_{\rm sys}$ was about 600 K. The system temperatures were corrected for rear spillover and for atmospheric and ohmic losses (Kutner & Ulich 1981). The telescope beam was approximately Gaussian with half–power widths of 36 arcsec at 49 GHz and 18 arcsec at 98 GHz, with main beam efficiencies of 0.88 and 0.52 respectively.

The CS and $C^{34}S$ emission was mapped using a grid spacing of 15 arcsec, resulting in oversampled $J = 1 - 0$ maps and undersampled $J = 2 - 1$ maps. For the CS transitions at 48.990964 GHz and 97.980968 GHz two maps were made, one with 7×7 pixels and one with 8×8 pixels, with slightly different centres. For the $C^{34}S$ transitions at 48.206956 GHz and 96.412982 GHz a 7×6 map was made with the same centre position as the 7×7 CS map. High signal to noise spectra were taken towards DR21(OH)M, DR21(OH)S and DR21(OH)W in all four lines. Pointing was checked by observing the SiO maser in NML Cyg at 43 GHz, giving a repeatability of 5 arcsec rms, apart from a correction of 10 arcsec needed for the 8×8 map. A point 2.5 arcmin east of $\alpha(1950) = 20^{\rm h}37^{\rm m}14.9^{\rm s}$, $\delta(1950) = 42°12'10''$ was used as a sky reference.

4.3.2 Results

Spectra are shown in units of main beam brightness temperature, $T_{\rm MB}$. Here, I have used the main beam brightness temperature as an approximation for $T_{\rm R}^{*}$ (in the notation of Kutner & Ulich 1981), so that to obtain the true brightness temperature distribution $T_{\rm R}$ the spectra should also be divided by the source–beam coupling efficiency, $\eta_{\rm c}$. Since $\eta_{\rm c}$ is unknown without prior knowledge of the true source distribution, I assume that

$\eta_c = 1$ in the analysis below, which will only be true for very extended sources.

The high signal–to–noise CS and $C^{34}S$ line profiles that were taken towards the three sources DR21(OH)M, DR21(OH)S and DR21(OH)W are displayed in Figure 4.8 to Figure 4.10. The profiles show considerable structure, ranging from slightly asymmetrical absorption in the CS $J = 2 - 1$ towards DR21(OH)S to deep self–absorption and asymmetric profiles even in the optically thinner transitions towards DR21(OH)M.

The map spectra, which are more noisy but which are useful for examining trends in line strengths and profiles across the source, are shown in Figure 4.11 to Figure 4.14, where the CS and $C^{34}S$ spectra have been re-sampled to $0.5\,\mathrm{km\,s^{-1}}$ and $1.0\,\mathrm{km\,s^{-1}}$ resolution respectively. Offsets are relative to the position of the 1.3 mm continuum source DR21(OH)M, $\alpha(1950) = 20^h37^m14.0^s$, $\delta(1950) = 42°12'08''$. Although the $J = 2 - 1$ maps are undersampled, the data that exist represent the best approximation to the actual brightness distribution available and so have not been smoothed for the purpose of examining the morphology. For comparison between the $2 - 1$ and $1 - 0$ lines the $2 - 1$ spectra have been smoothed to 36 arcsec resolution.

The lines are very broad, with emission extending from $V_{LSR} = -10$ to $+4\,\mathrm{km\,s^{-1}}$ over most of the map. The total integrated emission between these two velocities for each transition is shown in Figure 4.15 to Figure 4.17; the positions of the continuum sources DR21(OH)M, DR21(OH)S and DR21(OH)W are all marked by crosses in the CS $2 - 1$ map, Figure 4.16.

In order to investigate the kinematics of the various clumps within the core, the emission has been integrated over various velocity channels. These are shown in Figure 4.18 to Figure 4.20 for both of the CS transitions and $C^{34}S$ $2 - 1$. The $C^{34}S$ $1 - 0$ has insufficient signal–to–noise to provide any useful velocity information.

4.3.3 Discussion

4.3.3.1 Morphology

It is clear that the CS emission, especially the high–resolution CS $2 - 1$, corresponds very closely with the dust continuum, though the peaks of the integrated emission for the various transitions are offset by several arcseconds. This difference is unlikely to be a pointing error, since the $2 - 1$ and $1 - 0$ maps were taken simultaneously. Indeed, there appears to be a component at a velocity of $-1\,\mathrm{km\,s^{-1}}$ in the spectra towards DR21(OH)M and DR21(OH)W, especially evident in the $C^{34}S$ $2 - 1$ of DR21(OH)M

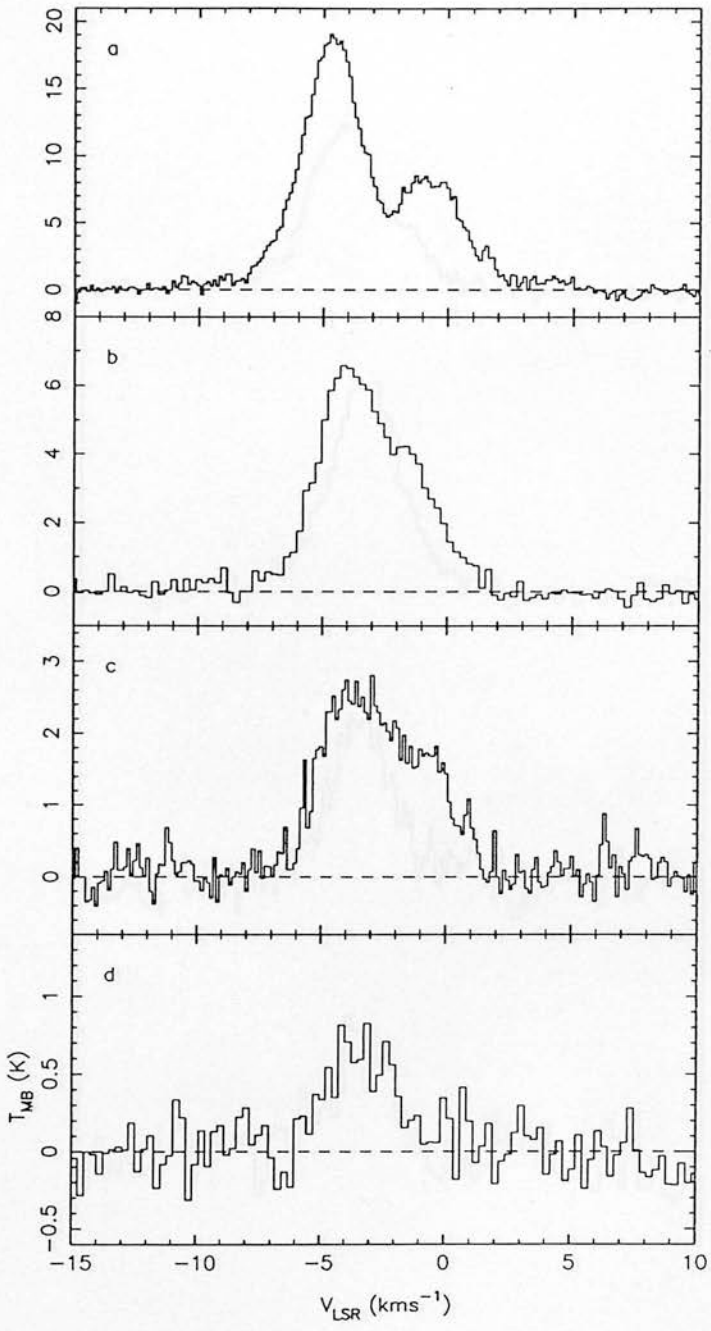

Figure 4.8: Spectra taken towards DR21(OH)M: (a) CS $2-1$ (b) CS $1-0$ (c) $C^{34}S$ $2-1$ (d) $C^{34}S$ $1-0$.

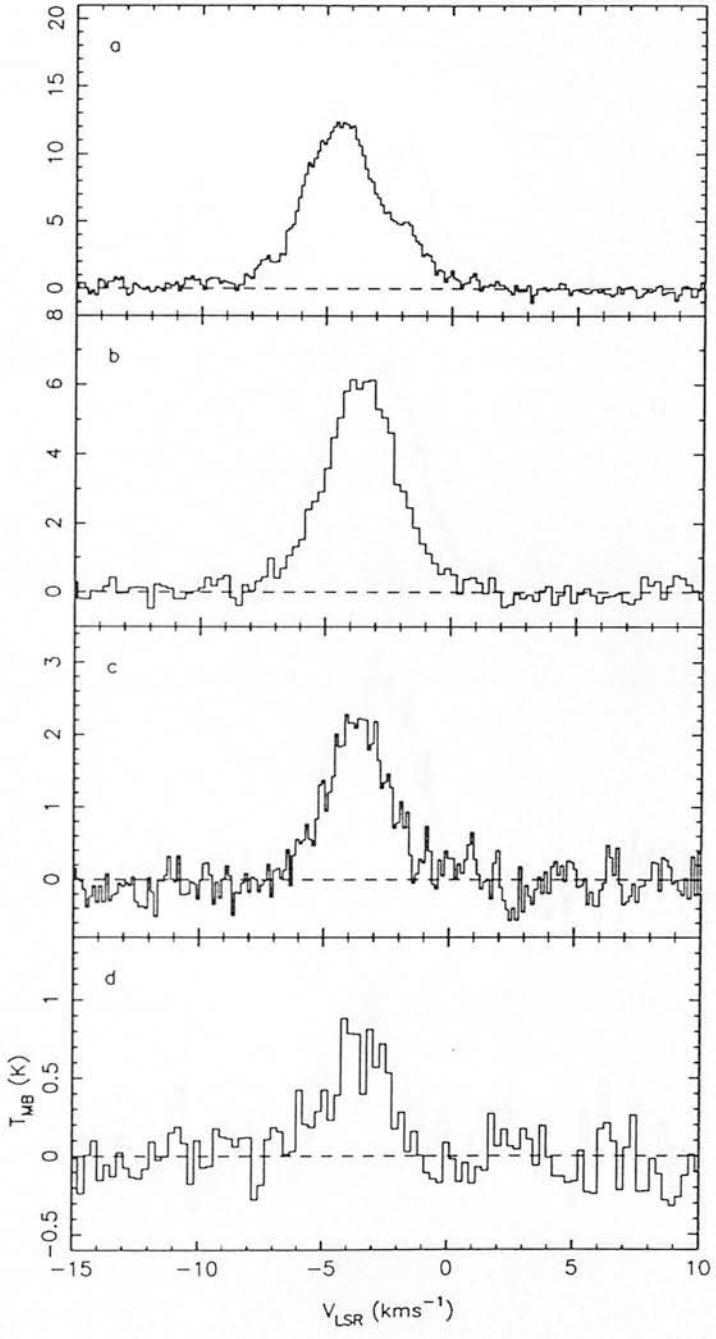

Figure 4.9: Spectra taken towards DR21(OH)S: (a) CS $2-1$ (b) CS $1-0$ (c) $C^{34}S$ $2-1$ (d) $C^{34}S$ $1-0$.

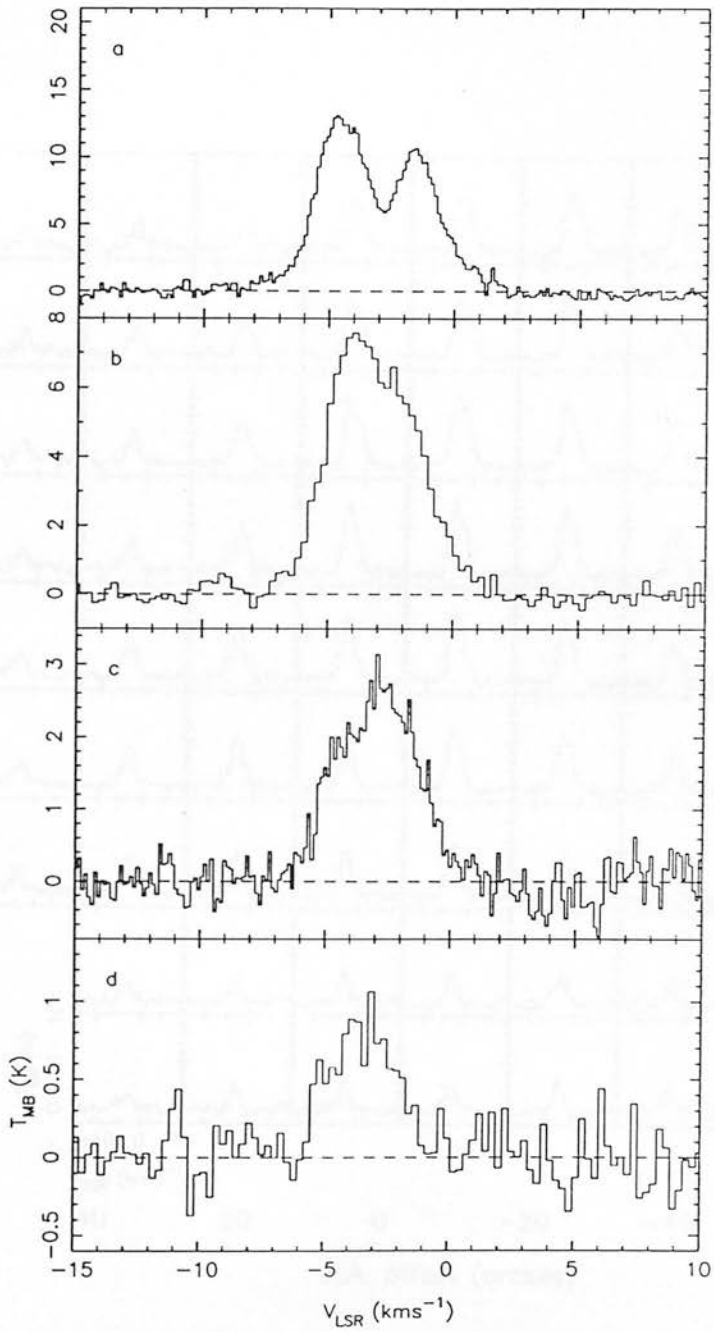

Figure 4.10: Spectra taken towards DR21(OH)W: (a) CS $2-1$ (b) CS $1-0$ (c) $C^{34}S$ $2-1$ (d) $C^{34}S$ $1-0$.

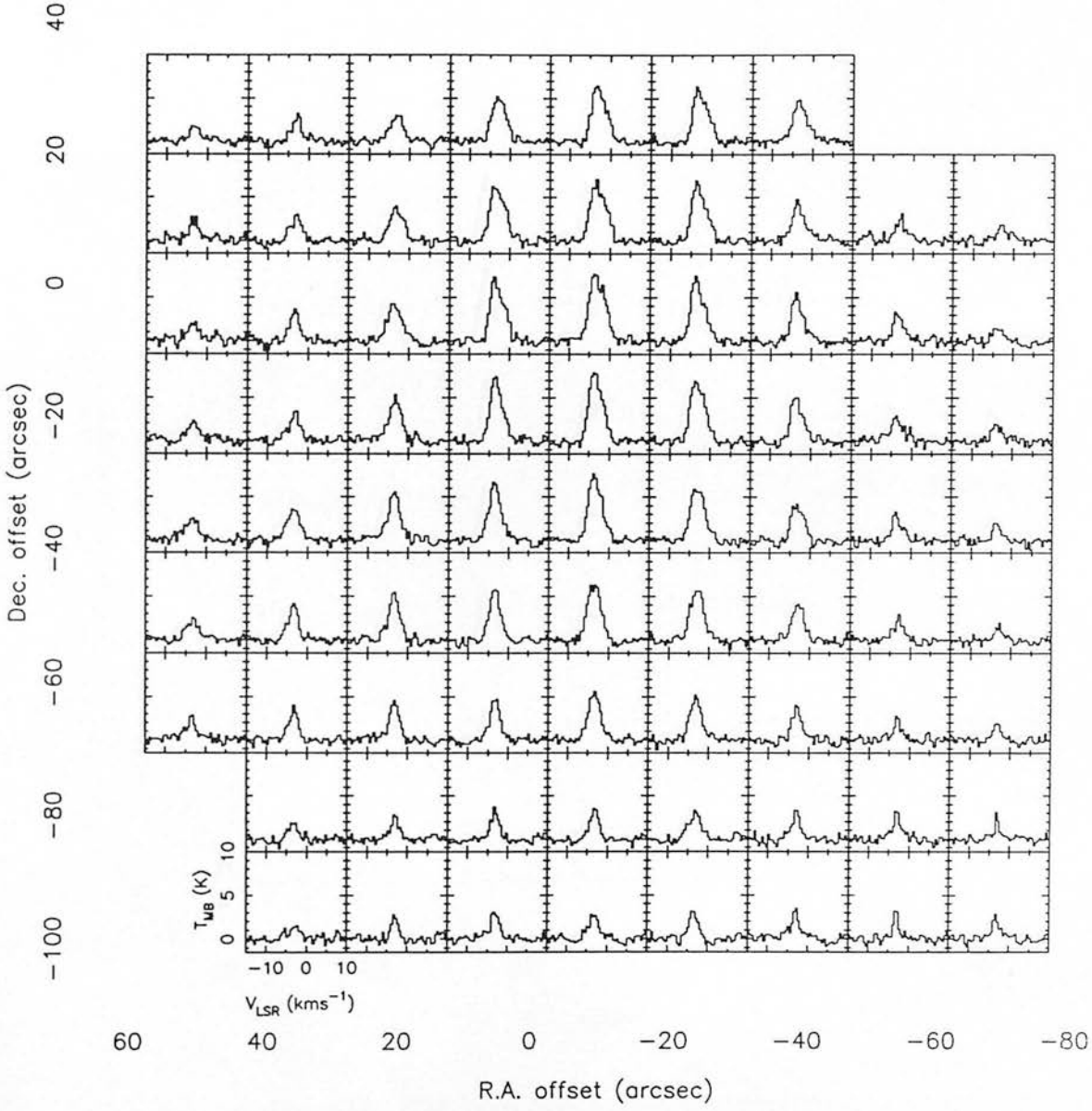

Figure 4.11: CS $1-0$ map spectra of DR21(OH).

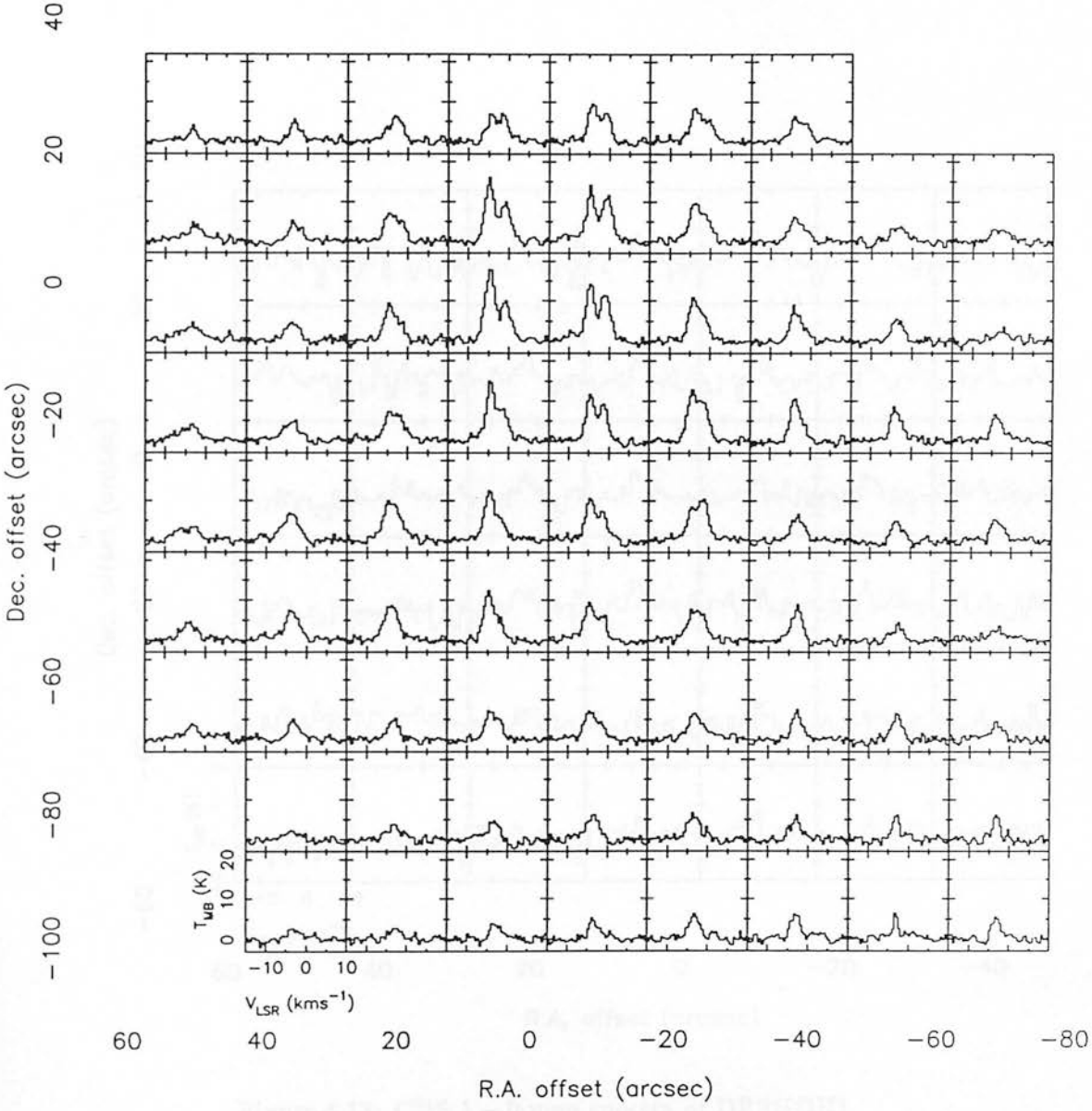

Figure 4.12: CS $2-1$ map spectra of DR21(OH).

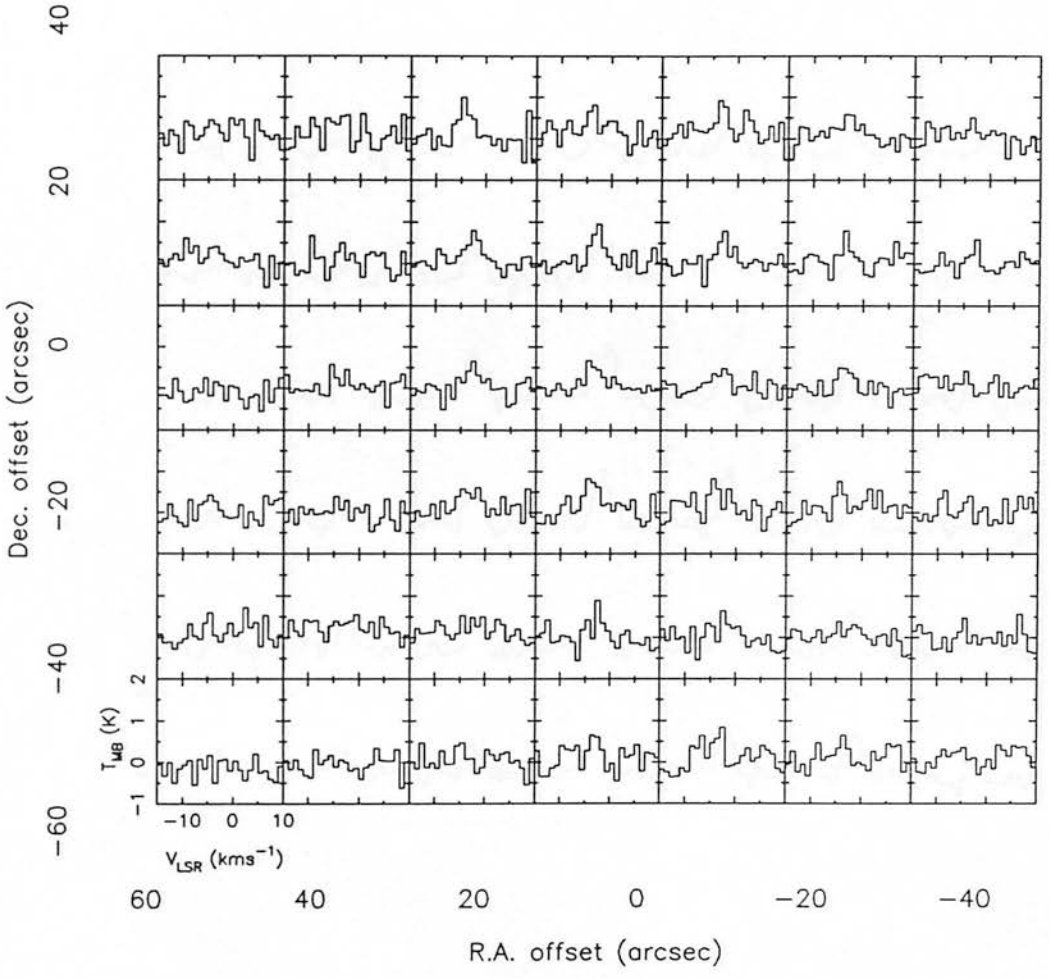

Figure 4.13: $C^{34}S$ 1 – 0 map spectra of DR21(OH).

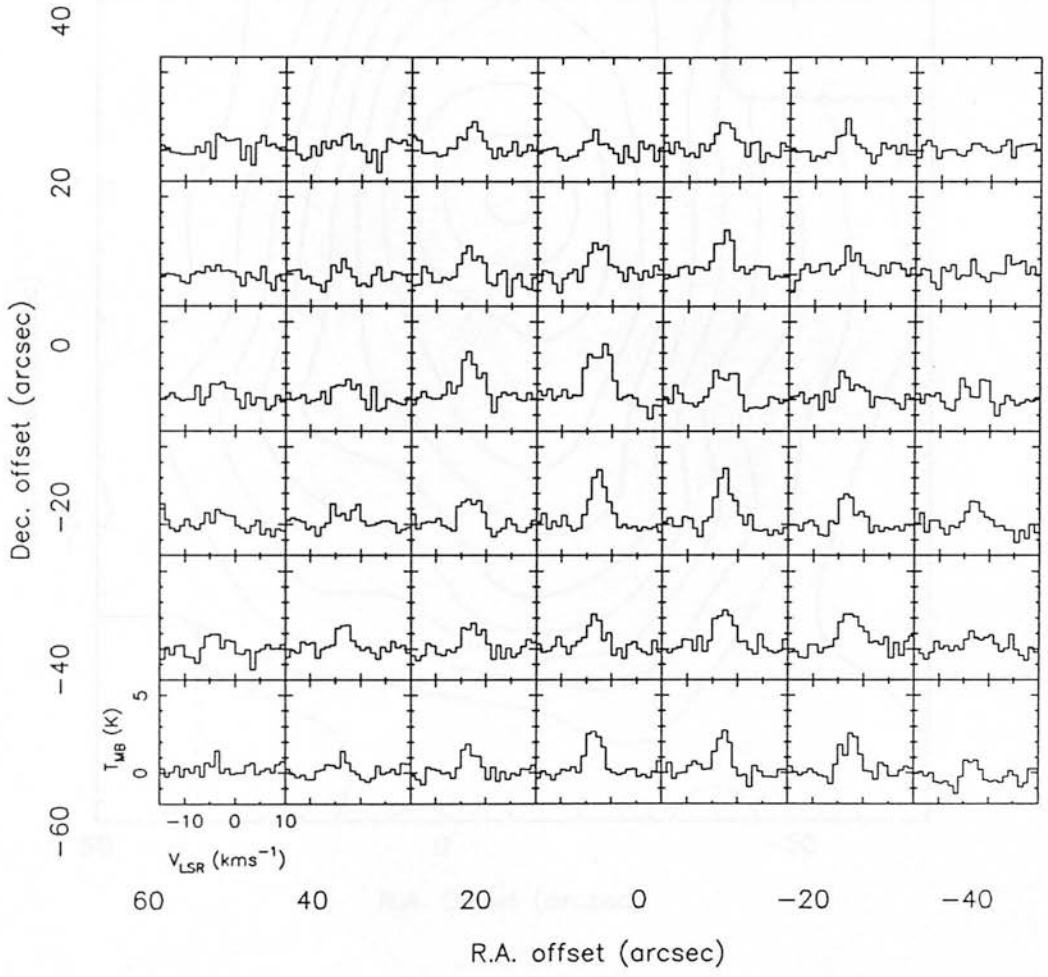

Figure 4.14: $C^{34}S$ 2 – 1 map spectra of DR21(OH).

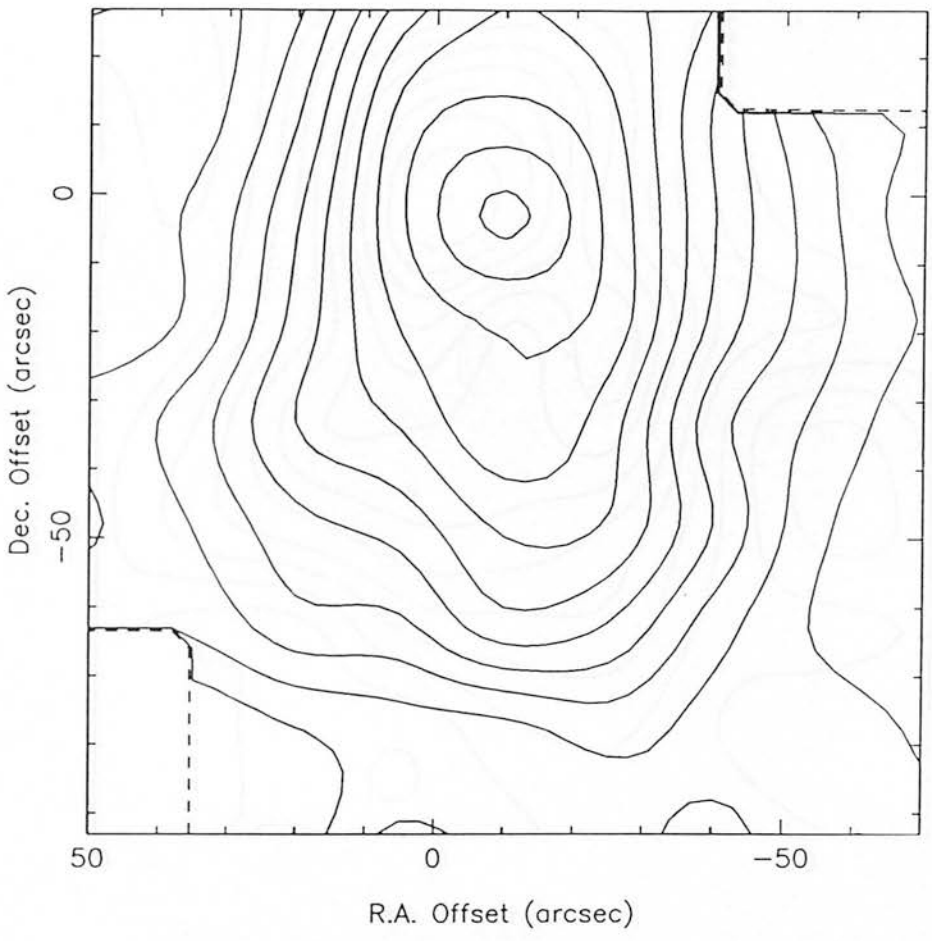

Figure 4.15: Integrated CS $1-0$ emission between $V_{\rm LSR} = -10$ and $+4\,{\rm km\,s^{-1}}$. Contours are at intervals of $3\,{\rm K\,km\,s^{-1}}$, from a base level of $6\,{\rm K\,km\,s^{-1}}$.

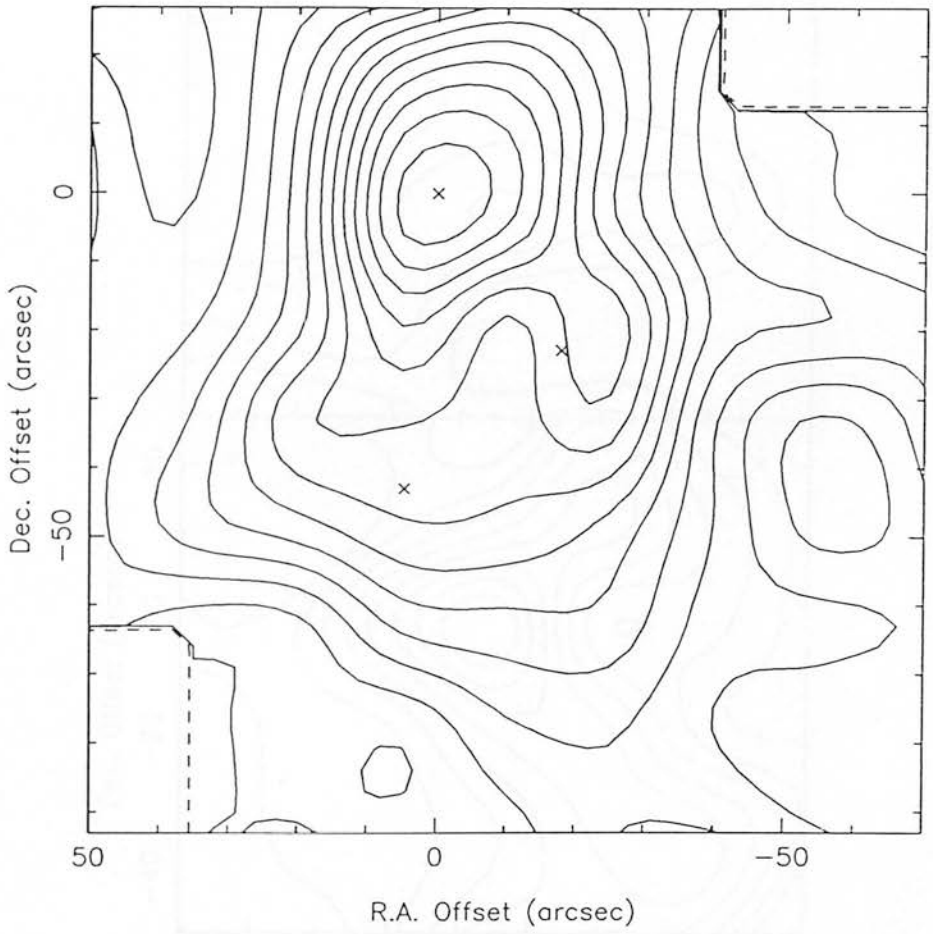

Figure 4.16: Integrated CS $2-1$ emission between $V_{\rm LSR} = -10$ and $+4\,{\rm km\,s^{-1}}$. Contours are at spacings of $6\,{\rm K\,km\,s^{-1}}$, from a base of $12\,{\rm K\,km\,s^{-1}}$.

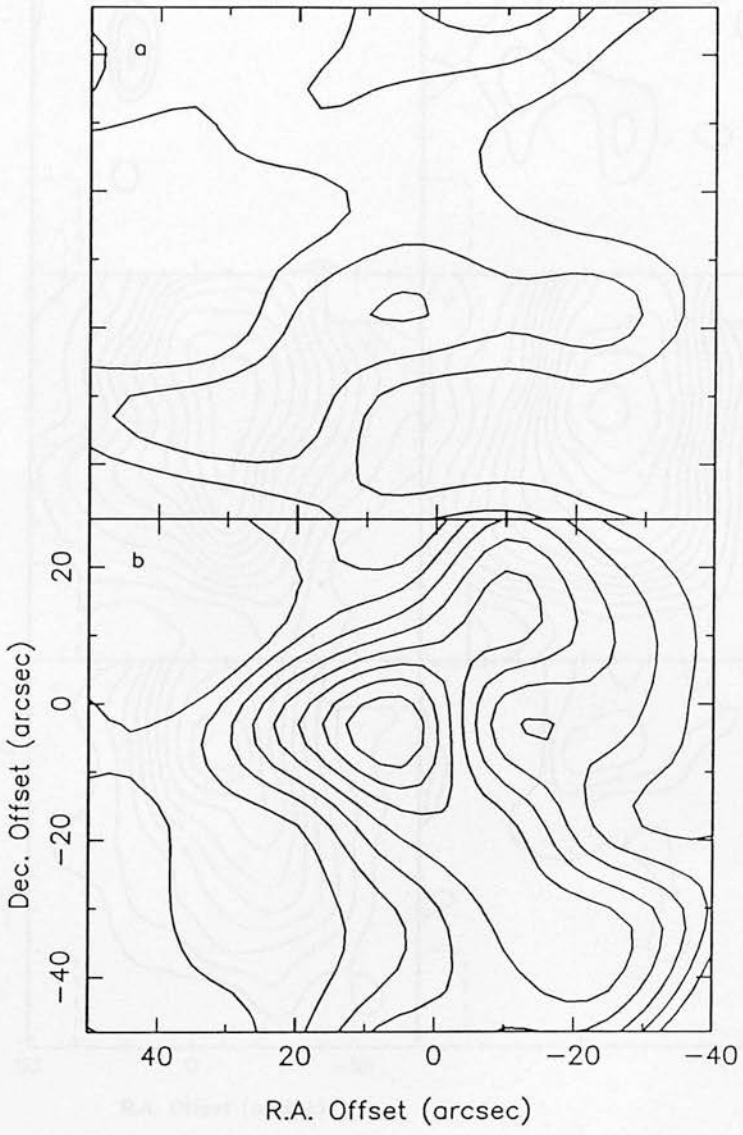

Figure 4.17: Integrated $C^{34}S$ emission between $V_{LSR} = -10$ and $+4\,km\,s^{-1}$: (a) $1-0$: contours are at $1\,K\,km\,s^{-1}$ spacing from a base of $2\,K\,km\,s^{-1}$; (b) $2-1$: contours are at $2\,K\,km\,s^{-1}$ intervals with the lowest at $4\,K\,km\,s^{-1}$.

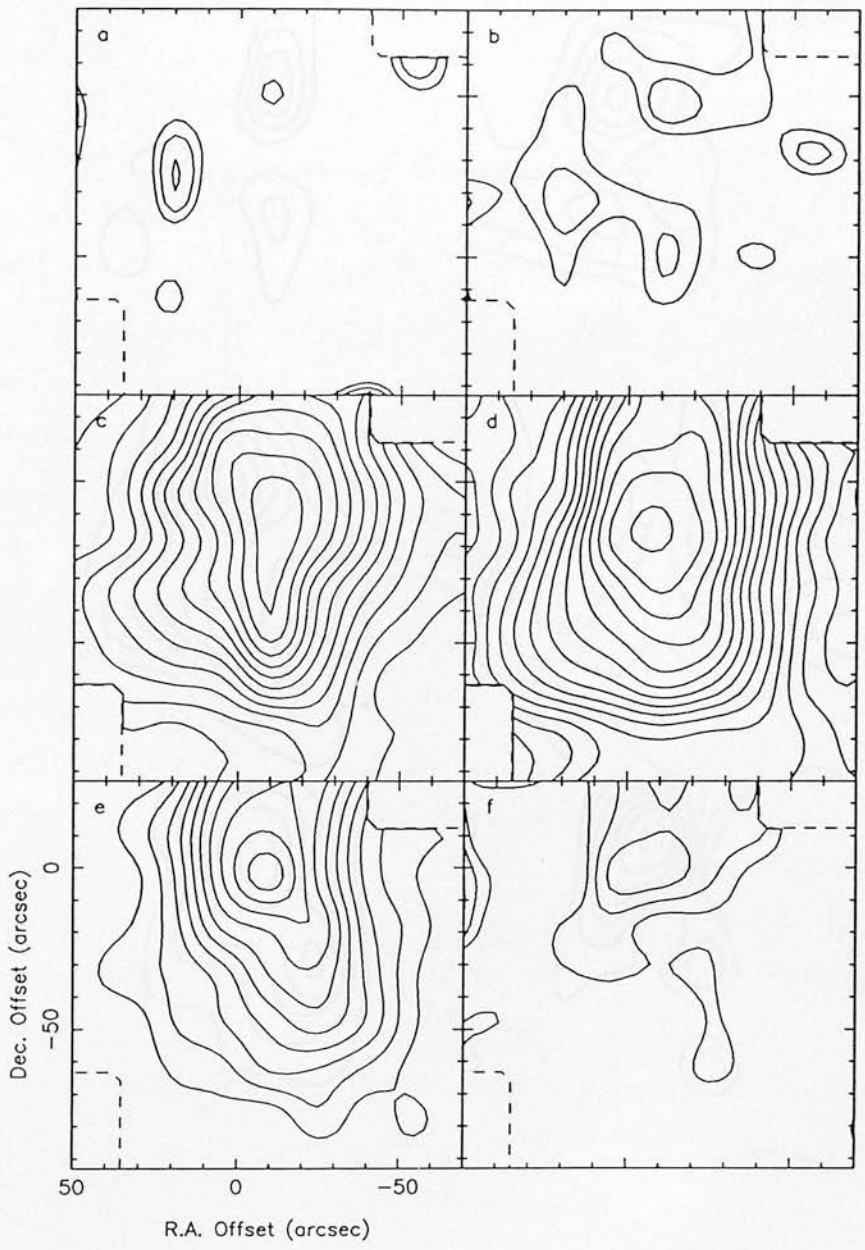

Figure 4.18: CS $1-0$ channel maps. The velocity intervals used are as follows: (a) $V_{\rm LSR} = -15$ to $-8\,{\rm km\,s^{-1}}$; (b) $V_{\rm LSR} = -8$ to $-6\,{\rm km\,s^{-1}}$; (c) -6 to $-4\,{\rm km\,s^{-1}}$; (d) -4 to $-2\,{\rm km\,s^{-1}}$; (e) -2 to $0\,{\rm km\,s^{-1}}$; (f) 0 to $4\,{\rm km\,s^{-1}}$. Figures (a), (b) and (f) have contours at $0.4\,{\rm K\,km\,s^{-1}}$ from a base of $0.8\,{\rm K\,km\,s^{-1}}$, and for Figures (c), (d) and (e) contours are at $0.8\,{\rm K\,km\,s^{-1}}$ from a base of $1.6\,{\rm K\,km\,s^{-1}}$.

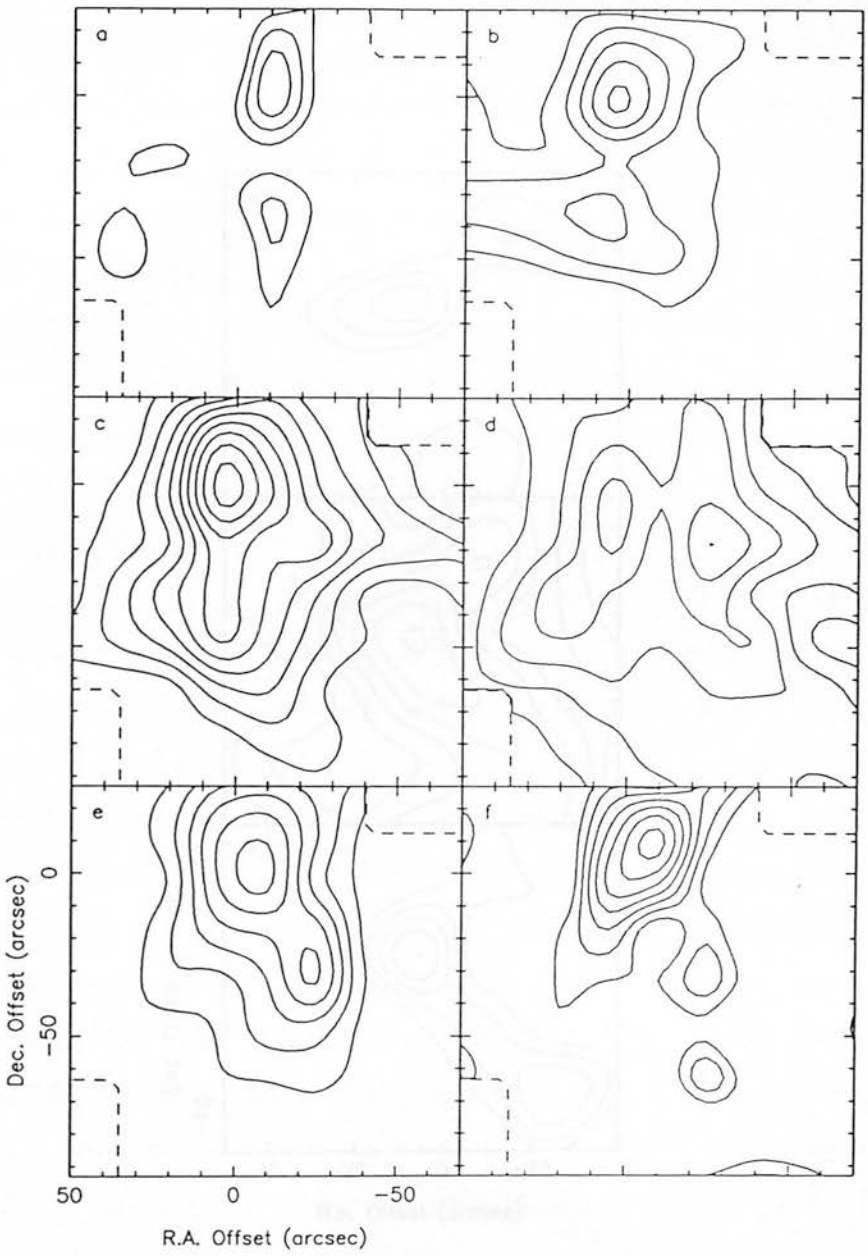

Figure 4.19: CS $2-1$ channel maps. The velocity intervals are the same as for Figure 4.18. Figures (a), (b) and (f) have contours at $1.5\,\mathrm{K\,km\,s^{-1}}$ from $3.0\,\mathrm{K\,km\,s^{-1}}$, and Figures (c), (d) and (e) has contours at $3.0\,\mathrm{K\,km\,s^{-1}}$ from a base level of $6.0\,\mathrm{K\,km\,s^{-1}}$.

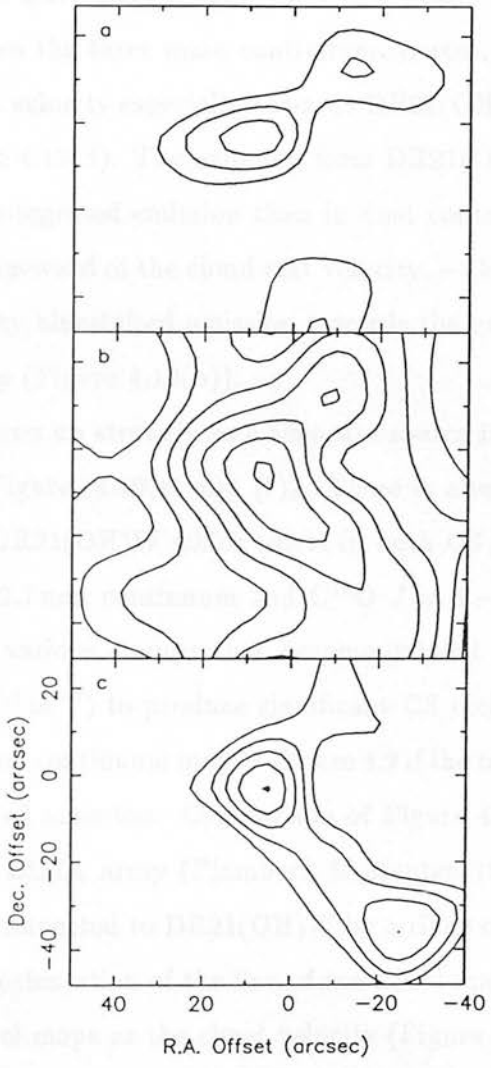

Figure 4.20: $C^{34}S$ 2 − 1 channel maps. The velocity intervals used are (a) −10 to −5 km s^{-1}; (b) −5 to −1 km s^{-1}; (c) −1 to 4 km s^{-1}. Figures (a) and (c) have contours at 0.75 K km s^{-1} from a base of 1.5 K km s^{-1}, and Figure (b) has contours spaced by 1.5 K km s^{-1} from 3.0 K km s^{-1}.

(Figure 4.8(c)), that is strikingly absent from DR21(OH)S. This component is relatively faint and presumably optically thin, and the map of the integrated intensity from the velocity channel that contains the wing emission (Figures 4.18(f) and 4.19(f)) shows that it peaks at identical positions in both transitions of CS, indicating that the slightly different positions of the peaks towards DR21(OH)M is a result of high optical depth in the self–reversed $2-1$ spectra.

Emission from DR21(OH)M dominates all the velocity channels, though at the cloud rest velocity (Figure 4.18(d)) the CS $1-0$ peaks more towards the centre of the cluster, in between the three main continuum sources. The CS $2-1$ is extremely self–absorbed at that velocity especially towards DR21(OH)M, which explains the odd morphology of Figure 4.19(d). The emission from DR21(OH)S is much less prominent in the map of total integrated emission than in dust continuum. It appears predominantly at velocities blueward of the cloud rest velocity, $-3\,\mathrm{km\,s^{-1}}$, with an indication of extended high–velocity blueshifted emission towards the east especially evident in the CS $2-1$ channel map (Figure 4.19(b)).

DR21(OH)W shows up strongly as a separate source in the red channels, between -2 and $+4\,\mathrm{km\,s^{-1}}$ (Figures 4.19(e) and (f)). There is also another red–shifted clump just to the south of DR21(OH)W which exists in both CS $2-1$ and $1-0$, and seems to be present in the 2.7 mm continuum and $C^{18}O$ $J=1-0$ of Mangum, Wootten & Mundy (1989). The various clumps that become evident at different velocities must be quite dense ($\gtrsim 10^{11}\,\mathrm{m^{-3}}$) to produce significant CS emission, and would also have counterparts in the dust continuum map in Figure 4.2 if the region were not so dominated by large–scale extended emission. Comparison of Figure 4.16 with the interferometer map made using the BIMA array (Plambeck & Menten 1990) in the same line show that DR21(OH)M is connected to DR21(OH)W by a ridge of CS $2-1$ emission roughly perpendicular to the orientation of the line of methanol masers. This also shows up in the $C^{34}S$ $2-1$ channel maps at the cloud velocity (Figure 4.20(b)) and at red–shifted velocities (Figure 4.20(c)).

There is no sign of emission from DR21(OH)S in the interferometer map (Plambeck & Menten 1990) or the $C^{34}S$ maps presented here, although it is not clear that the interferometer map extended far enough south, and the $C^{34}S$ spectra are quite noisy. However if the effect is real, it means that this core is colder than the others and that the small–scale clumping of warm gas is not significant for this source, although

emission in the $J = 1 - 0$ line of $C^{18}O$ *has* been detected (Mangum, Wootten & Mundy 1989). Either way, it is the ridge of dense gas between DR21(OH)M and DR21(OH)W that is the most striking feature revealed by the CS contour maps, together with the separation of the various clumps associated with the continuum sources into distinct velocity components.

4.3.3.2 CS spectra

The features evident in the velocity channel maps also show up clearly in the map spectra, Figure 4.11 to 4.14. Towards the east of the mapped area, the CS $2 - 1$ spectra especially show clear emission out to $-10\,\mathrm{km\,s^{-1}}$ distinctly lacking towards the west. There is little emission redward of $0\,\mathrm{km\,s^{-1}}$ except towards DR21(OH)M and DR21(OH)W. The lines are particularly broad towards DR21(OH)M, and there is a general trend for blue–wing emission towards the east and red–wing emission towards the west. This corresponds well with the trend in velocities of the methanol maser clumps found by Batrla & Menten (1988) and Plambeck & Menten (1990), and in general the LSR velocity of the OH and H_2O masers tends to decrease from about $-1\,\mathrm{km\,s^{-1}}$ to $-5\,\mathrm{km\,s^{-1}}$ with increasing R.A.

Over much of the mapped area the CS $2 - 1$ spectra show prominent asymmetric self–absorption features. The self–absorption appears at a similar velocity to the rest velocity of the cloud, and is approximately constant over a large area of the core region, indicating that the components responsible for the foreground absorption and the background emission are associated. The most likely cause is the presence of infall, where the velocity of the infalling gas is redshifted along the line of sight relative to the cloud rest velocity. The temperature and/or the density must also decrease with increasing distance from the cloud centre to result in self–reversal.

Although the presence of a foreground cloud with a velocity component towards the source can successfully reproduce the same profile, so that single spectra can easily be misinterpreted (*e.g.* Menten *et al.* 1987), this does not appear to be the case for DR21(OH). A cool foreground cloud would result in absorption in *all* the spectra that are sufficiently bright, unless it was very small and happened to coincide with the dense core, which seems unreasonable. The self–absorption peaks towards the centre of the cloud, and is virtually non-existent at offsets of ± 20 arcsec in R.A., even though the lines are still very bright. Infall can explain this behaviour, since towards the edge of the cloud

core any infalling material has its velocity almost perpendicular to the line of sight, and results in little or no red–shifted absorption. The foreground gas may still absorb at the rest velocity of the cloud, but the resulting profiles are not asymmetric. Therefore, the profiles across the DR21(OH) cloud can be explained qualitatively by infall, although they are complicated by the existence of the clumps at distinct velocities described in section 4.3.3.1.

There appears to be less self–absorption towards DR21(OH)S, which could either be because it is situated towards the front edge of the cloud where there is less foreground material, or because the emission from the source is too blue–shifted relative to the foreground for self–absorption to take place.

Comparison of the CS $2-1$ spectrum of DR21(OH)M with the interferometer measurements of Plambeck & Menten (1990, Figure 4.21), taken with a beam 10×5 arcsec at a position angle of 30°, shows that for the resolution of the $2-1$ at least, there is very little beam dilution, and $\eta_c \simeq 1$. At the cloud rest velocity of $-3\,\mathrm{km\,s^{-1}}$ the brightness temperature of the Plambeck & Menten spectrum falls to approximately zero, which could either be because the emission seen at that velocity in the NRO spectra is too large–scale to be detected by the interferometer, and all the emission from any compact sources at that velocity has been entirely absorbed by material in directly in front of DR21(OH)M, or because there is a "hole" towards DR21(OH)M, where the absorbing material is a small–scale clump coincident with the peak, that is not spatially resolved in the NRO spectra. The former explanation fits in with the picture of the outwardly–decreasing gradient in the excitation temperature necessary to produce the typical infall profiles, the latter being less believable because of the requirement of a chance coincidence. The interferometer spectrum also indicates that the *high–velocity* emission is associated with relatively small–scale structure.

4.3.3.3 LTE modelling

The cloud clearly contains a large number of individual sources embedded in separate clumps, rendering a detailed, physically reasonable, radiative transfer analysis very difficult unless one is prepared to ignore the evidence provided by high–resolution observations. However, in order to obtain an idea of the excitation conditions within the bulk of the cloud, I have approximated the CS emission by a simple two–slab model, with warm, dense gas in the background and cooler gas in the foreground at a velocity

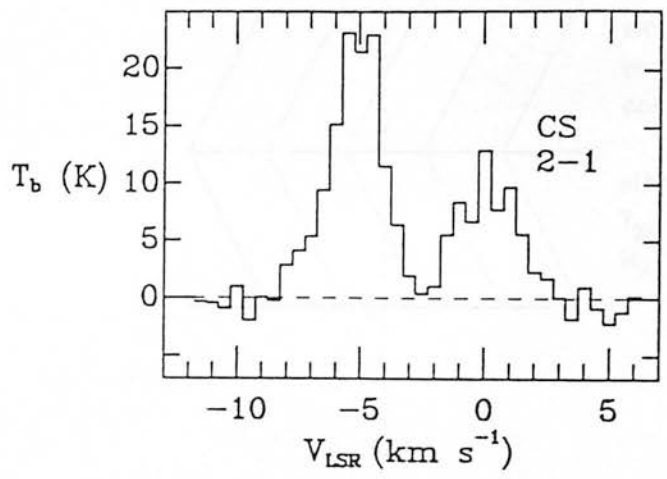

Figure 4.21: The interferometer spectrum of CS $2-1$ taken with a 10×5 arcsec beam, from Plambeck & Menten (1990).

redshifted relative to the background.

All gas was assumed to be in LTE. The geometry is shown in Figure 4.22, though for the purpose of the modelling the foreground gas is assumed to be sufficiently far away from the background gas that radiative transfer effects between the two slabs are negligible, and the background emission acts as a spatially uniform illuminating radiation field for the foreground gas at each point.

I have not taken into consideration the effect of variations in the excitation conditions as a function of position on the radiative transfer at a particular point, so that effectively each point where the CS and $C^{34}S$ profiles were measured is assumed to be independent of the surrounding points. This is a rather simplistic view, but the results of higher resolution observations show that a more detailed geometry and time consuming model was not justified.

For the purpose of the modelling, the CS and $C^{34}S$ $2-1$ spectra were smoothed to 36 arcsec resolution for comparison with the $1-0$ spectra. The results are shown in Figure 4.23 for points where data in all four transitions existed.

The line profiles towards each individual point were fitted by the function

$$T(V) = J(T_1)(1 - e^{-\tau_1})e^{-\tau_2} + J(T_2)(1 - e^{-\tau_2}), \tag{4.1}$$

where $J(T)$ has been defined in equation 1.14. The subscript '1' refers to the background

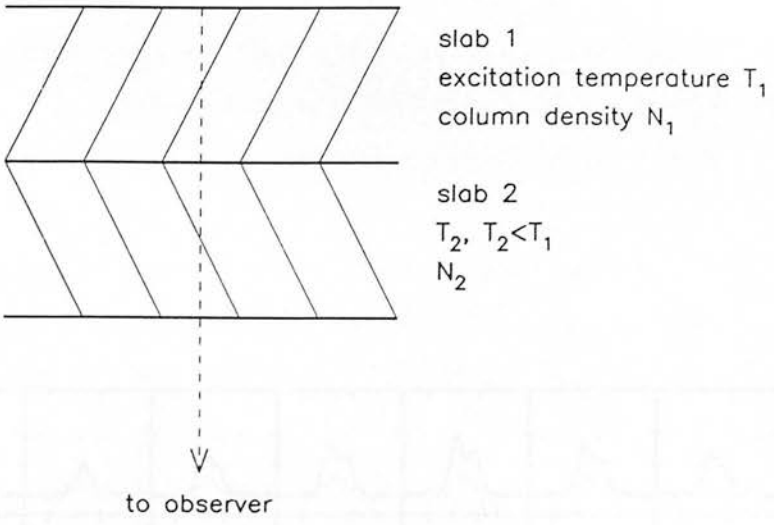

Figure 4.22: Geometry for the LTE modelling.

gas, and '2' refers to the foreground gas, as in Figure 4.22. The velocity distribution of both the foreground and background components was assumed to be Gaussian, resulting in a normalised velocity profile function

$$\phi(V) = \frac{1}{V_{\rm D}\pi^{1/2}} e^{-(V-V_0)^2/{V_{\rm D}}^2}$$

where $V_{\rm D}$ is the e^{-1} velocity dispersion and V_0 is the central LSR velocity of the distribution. This then gives, for the optical depth as a function of V for a transition with frequency ν_{ji} (see equation 1.16),

$$\tau(V) = \frac{2\pi^{3/2}}{3\varepsilon_0} \frac{B}{kT_{\rm ex}} \mu^2 j e^{-hBj(j-1)/kT_{\rm ex}} (1 - e^{-h\nu_{ji}/kT_{\rm ex}}) \frac{e^{-(V-V_0)^2/{V_{\rm D}}^2}}{V_{\rm D}} N.$$

$V_{\rm D}$ is measured in $\mathrm{m\,s^{-1}}$. Numerically this becomes

$$\tau(V) = 1.323 \times 10^{-18} \frac{B}{T_{\rm ex}} j e^{-0.048Bj(j-1)/T_{\rm ex}} (1 - e^{-0.048\nu_{ji}/T_{\rm ex}}) \frac{e^{-(V-V_0)^2/{V_{\rm D}}^2}}{V_{\rm D}} N, \qquad (4.2)$$

with $V_{\rm D}$ in $\mathrm{km\,s^{-1}}$ and ν_{ji} and B in GHz. N is the column density of the particular species in units of molecules $\mathrm{m^{-2}}$.

The functional form of $\tau(V)$ (equation 4.2) was used in equation 4.1, and the spectra at each individual point were fitted simultaneously by varying V_0, $V_{\rm D}$, $T_{\rm ex}$ and N for both the background and foreground gas, using a minimisation of χ^2 method. The rms noise,

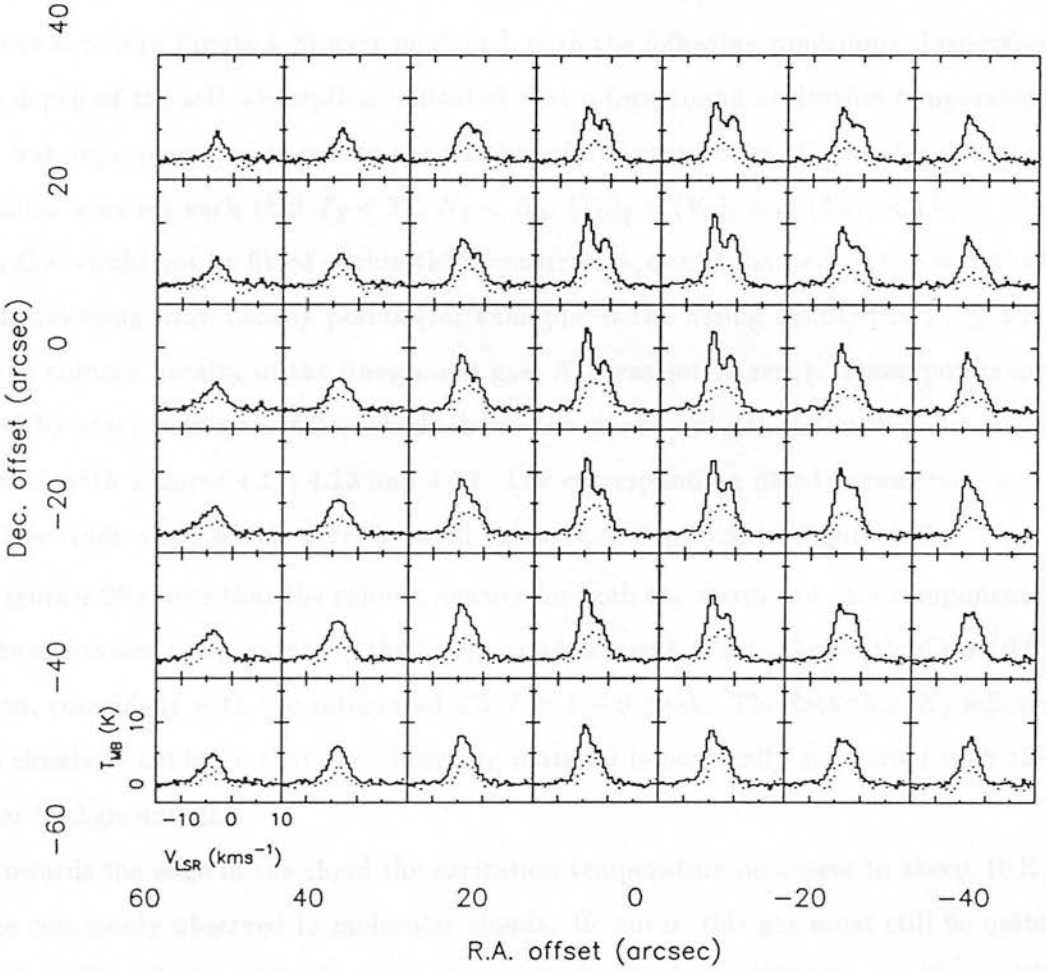

Figure 4.23: CS $2-1$ and $C^{34}S$ $2-1$ spectra smoothed to 36 arcsec resolution. The $C^{34}S$ spectra (dotted lines) have been multiplied by 2 for clarity.

measured away from the line for all the spectra, was assumed to be constant over the whole line width. The same excitation temperature was assumed for both the CS and $C^{34}S$ lines. An initial test fitting the abundance ratio $X(CS)/X(C^{34}S)$ for each position indicated that a value between 10 and 20 was appropriate, so $X(CS)/X(C^{34}S) = 15$ was used for the whole region. The terrestrial abundance ratio of S to ^{34}S is approximately 23, though Frerking *et al.* (1980) find that for interstellar clouds the ratio of CS to $C^{34}S$ can be lower than this by factors of 2 to 4.

The high signal–to–noise spectra could not be fitted because there was no way of smoothing the $2-1$ data to 36 arcsec resolution. However, all the map spectra at the positions shown in Figure 4.23 were modelled, with the following conditions. Inspection of the depth of the self–absorption indicated that a foreground excitation temperature of 5 K was appropriate, so to reduce the number of free parameters this was fixed. Other conditions were set such that $T_2 < T_1$, $N_2 < N_1$, $(V_0)_2 > (V_0)_1$ and $(V_D)_2 < (V_D)_1$. For points that could not be fitted within these constraints, one of the parameters was fixed by extrapolating from nearby points (for example, if the fitting resulted in $T_1 \leq 5\,\mathrm{K}$, then the column density of the foreground gas, N_2, was set to zero). These points are marked by stars in Figure 4.24, which shows the model spectra for each point to be compared with Figures 4.11, 4.13 and 4.23. The corresponding fitted parameters, with palm trees indicating which were assumed values, are displayed in Figure 4.25.

Figure 4.25 shows that the column density for both the warm and cool components, and the excitation temperature of the background, all peak just to the south of the (0,0) position, coincident with the integrated CS $J = 1 - 0$ peak. The fact that N_2 follows N_1 so closely is evidence that the absorbing material is physically associated with the warmer background gas.

Towards the edge of the cloud the excitation temperature decreases to about 10 K, a value commonly observed in molecular clouds. However, this gas must still be quite dense ($\gtrsim 10^{10}\,\mathrm{m}^{-3}$, though in fact it need not necessarily be in LTE) for significant CS emission. The peak excitation temperature is about 40 K, remarkably similar to that derived from the continuum spectrum. This is most likely to be a coincidence because of the uncertainties associated with calibration and beam dilution. Nevertheless, it provides confidence that the values of the other parameters found by the modelling are sensible.

The peak column density of warm CS was found to be $1.5 \times 10^{19}\,\mathrm{m}^{-2}$ which, for

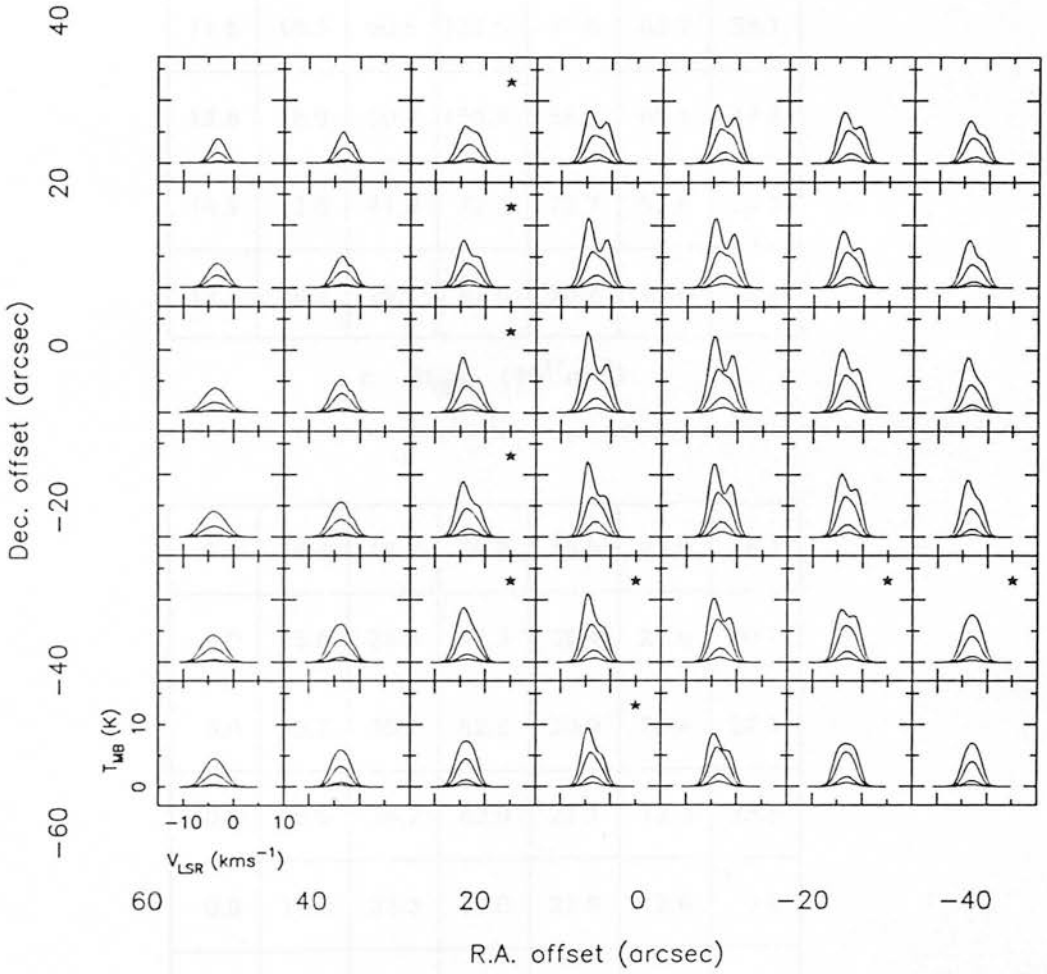

Figure 4.24: Model CS and $C^{34}S$ $2-1$ and $1-0$ spectra for DR21(OH). For all the positions, the brightest line is CS $2-1$, the second brightest CS $1-0$, the third brightest $C^{34}S$ $2-1$, and the faintest is $C^{34}S$ $1-0$. Positions marked by stars are those for which one of the model parameters had to be fixed (see text).

7.6	12.3	25.2	63.8	65.8	51.2	31.6
10.5	15.1	38.6	91.2	88.4	57.4	31.5
11.6	18.3	50.5	132.5	97.6	63.7	38.1
12.6	18.9	50.7	150.4	88.6	65.1	44.7
14.9	23.8	41.8	72.2	72.7	52.8	26.9
12.7	19.2	29.1	47.6	58.2	43.6	22.8

a. $(N_{CS})_1$ $(10^{17}m^{-2})$

0.0	6.4	16.2	39.9	28.9	22.0	16.1
0.0	5.6	28.8	42.3	35.4	21.8	20.7
0.0	5.2	35.2	52.8	30.0	22.4	22.1
0.0	5.9	34.7	62.9	27.1	17.3	23.8
0.0	11.5	23.3	38.0	22.6	12.6	† 0.0
0.0	0.0	0.0	24.6	19.2	0.0	0.0

b. $(N_{CS})_2$ $(10^{16}m^{-2})$

Figure 4.25: Fitted parameters corresponding to the spectra in Figure 4.24. (a) CS column density of the background, warm gas; (b) CS column density of the foreground, absorbing gas. Points marked by palm trees are assumed values.

−3.16	−3.09	−3.22	−2.93	−2.78	−2.74	−2.97
−3.22	−3.27	−3.24	−3.00	−2.86	−2.89	−3.09
−3.57	−3.54	−3.32	−3.00	−2.98	−3.01	−3.19
−3.86	−3.67	−3.31	−3.06	−3.10	−3.04	−3.13
−3.98	−3.69	−3.50	−3.33	−3.21	−3.00	−3.07
−3.73	−3.69	−3.78	−3.52	−3.35	−3.09	−2.95

c. $(V_0)_1$ (kms^{-1})

–	−2.22	−2.81	−2.61	−2.38	−2.06	−2.03
–	−2.25	−2.58	−2.53	−2.48	−2.17	−2.16
–	−2.22	−2.54	−2.47	−2.52	−2.34	−2.17
–	−1.87	−2.46	−2.46	−2.58	−2.49	−2.39
–	−1.43	−1.90	−2.43	−2.55	−2.66	–
–	–	–	−2.55	−2.43	–	–

d. $(V_0)_2$ (kms^{-1})

Figure 4.25: (c) The central V_{LSR} of the Gaussian velocity distribution for the background gas; (d) the same as Figure (c) for the foreground gas.

1.84	2.00	2.40	2.33	2.32	2.28	2.30
2.27	2.24	2.33	2.37	2.44	2.30	2.31
2.85	2.26	2.33	2.30	2.32	2.20	2.10
2.89	2.51	2.23	2.12	2.12	2.09	2.02
2.67	2.34	2.20	2.10	2.05	2.08	2.10
2.50	2.11	2.06	2.01	2.01	2.01	1.90

e. $(V_D)_1$ (kms^{-1})

–	0.47	1.48	1.63	1.41	1.39	1.26
–	0.51	1.48	1.53	1.44	1.38	1.33
–	0.54	†1.50	1.69	1.34	1.40	1.44
–	0.59	†1.70	1.96	1.35	1.36	1.57
–	0.91	†1.70	†1.70	1.37	†1.40	–
–	–	–	†1.40	1.42	–	–

f. $(V_D)_2$ (kms^{-1})

Figure 4.25: (e) The velocity dispersion of the warm background gas; (f) the same as Figure (e) for the foreground absorbing gas.

11.6	11.4	† 17.0	23.8	17.5	13.9	12.2
9.1	10.3	† 18.0	24.9	22.9	15.1	16.7
12.2	9.8	22.8	35.2	21.1	17.4	17.8
12.1	11.2	21.6	42.2	19.7	16.4	22.3
9.5	10.5	14.8	22.2	16.1	14.1	12.4
11.6	10.6	11.5	16.5	13.1	10.2	11.5

g. $(T_{ex})_1$ (K)

Figure 4.25: (g) The excitation temperature of the background gas.

an assumed CS fractional abundance relative to molecular hydrogen $X(\mathrm{CS})$ of 5×10^{-9} (Irvine, Goldsmith & Hjalmarson 1987) gives $\mathrm{N(H_2)} \sim 3 \times 10^{27}\,\mathrm{m^{-2}}$. The value of $X(\mathrm{CS})$ was found by Irvine *et al.* to vary by an order of magnitude from cloud to cloud, so this is highly uncertain. However the column density of molecular hydrogen derived by this method is similar to that found from the dust continuum, and results in a total mass of the area modelled of about $1800\,\mathrm{M_\odot}$. The column density of the cool CS peaks at the same position as the warm gas, though the actual values obtained are not meaningful because it is unlikely to be in LTE at a temperature of 5 K. If the gas is really at a kinetic temperature greater than 5 K as seems most likely, then the values of N_2 given in Figure 4.25(b) are too large.

The velocity width $(V_\mathrm{D})_1$ has a maximum roughly at the position of DR21(OH)M, though towards the south-eastern edge $(V_\mathrm{D})_1$ is large where the blue wings are evident in the spectra. Similarly, $(V_0)_1$ has its most blueshifted value at those points. The average value of $(V_0)_2 - (V_0)_1$, not including those points obviously dominated by wing

emission, is $0.7\,\mathrm{km\,s^{-1}}$. There is also a tendency for the value of $(V_0)_1$ to decrease from the north–west to south–east, in the same sense as the proposed velocity shear observed in W75 which could be due the interaction of the two clouds (Dickel *et al.* 1978). $(V_D)_2$ has a definite maximum towards the column density peak.

The corresponding optical depths of the warm background emission are intermediate for CS, with values towards DR21(OH)M at $V = (V_0)_1$ of $\tau(\mathrm{CS}\ 2-1) = 1.24$, $\tau(\mathrm{CS}\ 1-0) = 0.34$, $\tau(\mathrm{C^{34}S}\ 2-1) = 0.080$ and $\tau(\mathrm{C^{34}S}\ 1-0) = 0.022$. The CS emission is therefore rather sensitive to density and temperature variations.

The results of the LTE modelling therefore provides a picture that fits in well with the continuum data. Dense, warm gas and dust at a temperature of approximately 40 K is localised in the core of the GMC, with cooler material, still with rather high molecular hydrogen number densities of around $10^{10}\,\mathrm{m^{-3}}$, located at a distance of 0.44 pc from the centre. Towards the positions of DR21(OH)S and DR21(OH)W the CS excitation temperature is about 20 K, though this number is probably beam diluted. The morphology and mass of the dense gas traced by the CS emission is similar to that derived from the continuum observations (section 4.2), indicating that they are tracing the same material.

4.3.3.4 Applicability of the model

The assumption that all the gas is in LTE implies that it is all above the critical density for that transition (section 1.4) so that the excitation temperature is equal to the kinetic temperature. Since the critical density is higher for higher J transitions the lower levels become thermalised first. If the higher levels are under–populated then the partition function is bigger than the true number of available states, and for a given excitation temperature the analysis will result in an overestimate of N even if $T_{\mathrm{ex}} = T_{\mathrm{kin}}$ for the low levels. Similarly, if the lower states are not thermally populated so that T_{ex} is less than T_{kin}, N is again overestimated. For a given T_{ex} all deviations from LTE under usual cloud conditions for CS will result in an overestimate of N.

Since kinetic temperatures as low as 5 K are not seen in molecular clouds (typically $T_{\mathrm{kin}} \gtrsim 10\,\mathrm{K}$) the absorbing layer of gas in the model is not in LTE and the model results in values of N_2 that are too high. Without solving the statistical equilibrium of the level populations under the influence of both collisions and radiative processes it is difficult to tell by how much N_2 is overestimated. For the warm bulk of the gas at

an excitation temperature of 40 K the partition function for a molecule with an infinite number of levels (as has been assumed here – equation 1.12) has a value $\simeq 34$. For a three–level molecule with the $J = 0, 1, 2$ levels thermally populated with the same excitation temperature the partition function would be $\simeq 8$, so the value of N_1 derived here is no more than a factor of 4 too big as long as the lowest three levels follow the Boltzmann distribution (implying molecular hydrogen number densities $\gtrsim 10^{11}\,\mathrm{m}^{-3}$).

If, as is most likely, an inwardly increasing temperature gradient exists, Cantó, Rodríguez & Anglada (1987) showed that the excitation temperature derived will depend on the optical depth of the transitions. They investigated the relationship between the optical depth, excitation temperature and filling factor derived by assuming a single temperature (as is common in the literature), with the actual optical depth and range of excitation temperatures present in a smooth source (*i.e.* non–clumpy, so that the true filling factor $f = 1$). They show that a temperature gradient along the line of sight will produce fictitious filling factors if a single temperature is assumed, and that the temperature derived in this manner is physically unrelated to the temperatures actually present in the source and can be much larger. This happens when, in the single–temperature analysis, the optical depth ratio $\tau(2-1)/\tau(1-0)$ starts to approach the value obtained for $T_{\mathrm{ex}} = \infty$ of 4. The derived excitation temperature then exceeds any temperature actually present in the emitting region, and the corresponding filling factor then has to become very small to account for the observed brightness temperature.

The model described above inherently assumes a smooth source with $f = 1$. Since f is defined by the relation

$$T_{\mathrm{R}}^{*} = f\, J(T)\,(1 - e^{-\tau})$$

this means that for the same observed value of T_{R}^{*} the excitation temperature found in my model will be lower than that given by a single temperature derived from the line ratios. As was pointed out by Cantó *et al.* the value of f usually depends on which transition is used for the calculation, since it bears no relation to the true source structure and is introduced purely to tie in the single–temperature analysis with the observations. From the work of Cantó *et al.* it is clear that setting $f = 1$ and finding a best–fit for the excitation temperature will result in a value closer to the actual range of temperatures present over a larger range of optical depths than solving equations for the line ratios, if temperature gradients exist.

If density gradients exist then the observed emission will originate predominantly

in regions with high temperature and/or density unless the transition is significantly optically thick. Then, since the filling factor will no longer be unity, the derived excitation temperature will be an underestimate of the true peak temperature. This could well be the case for DR21(OH), but higher resolution observations are needed before the effect can be quantified.

It is useful to compare these results with those of Snell *et al.* (1984), who modelled CS and $C^{34}S$ emission from a number of dense cloud cores using a large velocity gradient (LVG) radiative transfer analysis. They found that a constant abundance ratio $X(CS)/X(C^{34}S)$ for an individual cloud could not fit their data, with variations in the ratio by about a factor of 2 necessary to fit all the positions within the cloud. This is similar to the results of the initial test of the model described in section 4.3.3.3, where the low ratio of about 10 was found to be suitable towards the centre of the cloud and a ratio of 20 fitted the outer parts.

The enhancement of emission from the rare isotope compared with CS could be caused by several effects. For example, if the filling factor is less than unity, then the optical depth of the emitting clumps is higher than that derived in the modelling, so that the $C^{34}S$ lines are brighter than expected from a terrestrial isotope ratio. Alternatively, a gradient in the excitation temperature will result in lower brightness temperatures in the CS lines if the foreground cooler medium is optically thick, whereas the $C^{34}S$ lines will not be affected. It seems clear that both of these effects are contributing to the variation in the relative brightness of the $C^{34}S$ lines in DR21(OH), and the contribution of each will only be determined by a full radiative transfer analysis with a physically reasonable cloud geometry.

To summarise, the model will produce over–estimates of the beam–averaged column density, N, though the numbers obtained will be good to within an order of magnitude. In the presence of temperature gradients, the excitation temperatures derived from the fitting are better constrained to be within the range of the actual temperatures present than solving the LTE equations just using line ratios, because the filling factor f has been assumed to be unity. The model therefore results in the best approximation to the true cloud conditions within the assumption of LTE.

4.3.3.5 Cloud equilibrium

The next stage is to determine whether the linewidths found in the CS spectra are consistent with the cloud being supported in virial equilibrium. The stability of the cloud is determined by the contributions to the various terms in the virial equation, which for a self–gravitating magnetized fluid is

$$\frac{1}{2}\frac{d^2I}{dt^2} = 2K + 3\int PdV + \Omega + \int \frac{\mathrm{B}^2}{2\mu_0}dV - \left\{ \begin{array}{c} \text{surface} \\ \text{pressure} \\ \text{term} \end{array} \right\} + \left\{ \begin{array}{c} \text{magnetic} \\ \text{tension} \\ \text{term} \end{array} \right\}.$$

I is the moment of inertia, K is the bulk kinetic energy, $\int PdV = (\gamma - 1)U$ for a perfect gas with thermal energy U and ratio of specific heat capacities γ, Ω is the gravitational potential energy and the fourth term, $\int \frac{B^2}{2\mu_0}dV$, is the magnetic energy. Contributions to the surface pressure term come from the thermal and magnetic pressure of the surrounding intercloud medium.

Initially, one can neglect the surface pressure and magnetic terms. The bulk kinetic energy K can be estimated from the velocity dispersion observed in the CS lines. This involves making the assumption that the large line widths detected are due to *support* mechanisms for the cloud core, rather than (for example) high–velocity infalling gas at the centre, and that the support is isotropic. Then, by also assuming spherical symmetry so that the three–dimensional velocity dispersion σ is equal to $\sqrt{3}\,V_{\mathrm{D}}$,

$$K = \frac{3}{2}MV_{\mathrm{D}}{}^2.$$

M is the cloud mass, which is approximately $2000\,\mathrm{M}_\odot$ from the continuum and CS data. This can be evaluated numerically using $V_{\mathrm{D}} = 2.4\,\mathrm{km\,s^{-1}}$ to give $K = 3.4 \times 10^{40}\,\mathrm{J}$. The sound speed c_{s} for gas with $T_{\mathrm{kin}} = 40\,\mathrm{K}$ is $0.4\,\mathrm{km\,s^{-1}}$, which is much smaller than the CS line widths. The thermal energy is therefore negligible compared with the bulk kinetic energy.

The gravitational potential energy Ω is given by

$$\Omega = -\frac{GM^2}{R}\frac{(3-\alpha)}{(5-2\alpha)}$$

for a cloud with radius R and density distribution $\rho \propto r^{-\alpha}$. The extent of the emission used depends on the geometry assumed. The half–power width in right ascension assuming Gaussian source and beam geometry is $\simeq 45$ arcsec in both the CS $1-0$ and $2-1$, corresponding to a diameter of 0.44 pc at a distance of 2 kpc. Alternatively if a power–law density distribution is assumed it is best to equate the radius R to the total

extent of the emission, which is approximately 60 arcsec. Both for the Gaussian cloud and for a power law with $\alpha = 2$ (predicted for the envelopes of cloud cores, *e.g.* Shu 1977) this gives $\Omega = 6 \times 10^{40}$ J.

Rotation could also provide support, though if the slight velocity shift shown in Figure 4.25(c) of about $1\,\mathrm{km\,s^{-1}}$ across a region with linear dimension of 1 pc were due to rotation, its angular velocity is significantly less than Keplerian. Therefore, the magnitude of the rotational energy is likely to be less than 10% of the turbulent energy calculated from the observed velocity dispersion of $2.4\,\mathrm{km\,s^{-1}}$.

Comparison of the terms calculated above show that within the uncertainties due to lack of knowledge about the true source geometry, the cloud is close to being in virial equilibrium. The effect of magnetic fields and external pressure have not been included, though an internal magnetic field will tend to give more support against collapse, and external pressure will tend to increase the inward acceleration of the gas. If virial equilibrium is *assumed*, the virial mass obtained by equating d^2I/dt^2 to zero is $2500\,\mathrm{M_\odot}$.

The virial theorem says nothing about the underlying nature of the high velocity dispersion, and the source of the wide molecular lines remains undetermined by this analysis. However, since the asymmetrically absorbed line profiles are most likely caused by the infalling outer parts of the cloud, the line wings in spectra towards the cloud centre could well originate very close to the embedded sources where high infall velocities are most likely to occur, and the density is sufficiently high for significant emission even from $C^{34}S$. Another possibility is that the line wings are caused by high–velocity, dense gas that has been swept up by a very young, energetic outflow.

So, the cloud core is roughly in equilibrium, on large scales at least. Deep within the centre of each core star formation is taking place, and especially in DR21(OH)M, is responsible for the wing emission from relatively high–velocity, dense gas.

4.4 Conclusions

High–resolution 1.3 mm dust continuum observations have revealed the presence of at least eight dense cores located along a ridge in the DR21 cloud. Three of these, DR21(OH)M, FIR1(H_2O) and FIR3(H_2O), are associated with H_2O masers. The dust temperatures obtained for those sources for which other data exist are 40 and 65 K (DR21(OH)M and FIR1(H_2O) respectively), the FIR sources to the north being warmer

and probably more evolved than those near DR21(OH). The presence of embedded sources is required to explain the luminosity of the cores, since contributions from the interstellar radiation field and gravitational contraction are all negligible. This is true even for the cooler cores to the south, though any such sources must still be very young for the cloud to have remained undispersed. The luminosity of DR21(OH)M is probably dominated by a single star with a mass of approximately $15\,M_{\odot}$, with the lower mass stars yet to form. This star is associated with the OH, H_2O and CH_3OH masers, and could also be heating the two millimetre continuum peaks found by the Owens Valley Interferometer (Woody *et al.* 1989).

The velocity structure of the cores around DR21(OH) have been studied by mapping the region in CS and $C^{34}S$ $2-1$ and $1-0$. The three cores, DR21(OH)M, DR21(OH)S and DR21(OH)W, all appear at slightly different velocities, with DR21(OH)W apparently connected to DR21(OH)M by a ridge of dense gas oriented perpendicular to the methanol masers (Plambeck & Menten 1990). Self-reversed line profiles are found in CS $2-1$ that can be explained by the presence of infall over the central regions. The CS and $C^{34}S$ spectra are all relatively wide, with wing emission most prominent east of DR21(OH)M. Modelling the spectra by a simple two-component geometry, with all the gas in LTE, indicates that the warm, emitting gas (with a peak excitation temperature of about 40 K) is physically associated with the cooler absorbing gas in the foreground. A typical interstellar abundance ratio $X(CS)/X(C^{34}S) = 15$ can adequately account for the brightness of the CS and $C^{34}S$ lines.

The mass of the DR21(OH) cloud (which includes DR21(OH)M, DR21(OH)S and DR21(OH)W) is about $2000\,M_{\odot}$, from both the continuum data and the CS data. It is approximately in virial equilibrium, provided the wide lines are caused by supportive turbulence rather than infalling dense gas at the centre of the cloud. However the wing emission, together with the orientation and separation of the various masers associated with DR21(OH)M, imply the presence of a very young outflow, yet to be detected, that could provide a means of support for the cloud core. Observations in a rare isotope of CO are required, since emission from ^{12}CO is too confused in this region of the sky.

Chapter 5

Conclusions

The work presented in this thesis set out to examine several areas of star formation previously believed to be the youngest of their type in the context of the current ideas outlined in Chapter 1. All of the sources have been found to be quite young, although none was found to be a "true protostar" since they have all probably already begun nuclear burning. B335 has been studied as an example of isolated, low–mass star formation, and has been used as a test of theoretical evolutionary tracks, and to examine possible outflow collimation mechanisms; NGC 2024 contains embedded, intermediate–mass cores that have been found to be at varying stages of evolution; the sources near DR21(OH) are cores of a GMC at a correspondingly higher temperature than found in the low–mass case, and are potentially the youngest high–mass objects yet discovered.

5.1 Low–mass star formation: B335

The core of the isolated globule B335 has been mapped in thermal submillimetre dust continuum emission, and has been found to be elongated perpendicular to the outflow. The emission has not been resolved by an 8 arcsec beam in the direction of the outflow axis, giving dimensions of $1900\times \leq 1500\,\mathrm{AU}$ (FWHM). The core has been found to be very dense, with molecular hydrogen number densities of $n(\mathrm{H_2}) \gtrsim 5 \times 10^{13}\,\mathrm{m^{-3}}$, and optical extinction in excess of 320 mag.

Evolutionary state The detailed modelling carried out by Shu and coworkers of the evolution of low–mass protostars has been used to try to determine the evolutionary state of the embedded source in B335. The presence of an evolved outflow whilst the luminosity of the exciting source is so low and the extinction so high presents three

possibilities:

(i) Outflow is possible from sources much younger than previously expected. This statement also implies that if the wind driving the outflow is protostellar in origin then deuterium burning cannot be the driving mechanism, and some other device for driving the protostellar mass loss must be found. Disk winds are not discounted by this argument, although the energetics of the core are not conducive to being able to drive the outflow.

(ii) The embedded source is a more evolved protostar whose low luminosity can be accounted for by invoking a lower mass and/or accretion efficiency than that assumed for the theoretical tracks in Taurus. The high extinction towards the source then has to be due to the orientation of a thick disk. The fact that B335 is an isolated globule rather than part of a large complex like Taurus could be influencing the nature of the star formation occurring there, but then the generality of the star formation theory is brought into question.

(iii) The source is a pre–main–sequence star with a suitably low luminosity that has remained embedded, with its high extinction again due to the orientation of a thick disk. The fact that the star is not yet visible could be because the outflow is not energetic enough to disperse the core.

Given the presence of an evolved outflow and a possible HH object (Vrba *et al.* 1986) it seems likely that one of the latter two explanations is the case.

Collimation of the outflow The mass ($2\,M_\odot$) and radius (about 1000 AU) of the core traced by the dust emission means that it is sufficiently gravitationally bound to be able to collimate an initially isotropic wind into the observed bipolar structure, though this doesn't rule out an intrinsically anisotropic wind. Indeed, an anisotropic, bipolar wind would help to explain why the core has not yet been dispersed perpendicular to the outflow axis. It appears that the outflow cannot be driven by a disk wind as suggested by Pudritz & Norman (1986).

Future work The submillimetre observations of B335 provide the first thermal continuum evidence for disk structure perpendicular to an outflow on circumstellar scales. Flattened, elongated structures have been detected in molecular line emission in sources such as IRAS 16923 (Mundy, Wilking & Myers 1986) and L1551 IRS5 (Sargent *et al.* 1988), but in these cases the continuum emission was unresolved. Clearly, further high–

resolution interferometric measurements of B335 at optically–thin wavelengths will be next essential step towards detecting the circumstellar disks that have been predicted by theory. As an example, a linear resolution of about 400 AU can be achieved for B335 by the Owens Valley Millimetre Wave Interferometer, sufficient to probe the structure of dust disks with dimensions of a few $\times 1000$ AU.

Detailed examination of the interaction of the outflow or protostellar wind with its surroundings will determine whether the observed core morphology of B335 can be explained by the fact that the outflow is insufficiently energetic to disperse the dense gas. Since the effects of the interaction will be most prominent close to the source, the best probe will again be interferometric observations of the high–velocity gas.

5.2 Intermediate–mass star formation: NGC 2024

The high–resolution observations in CS and $C^{34}S$ 7 – 6 showed that most, if not all, of the six dense cores, FIR1–6, discovered by Mezger *et al.* (1988) are too warm to be protostellar condensations. Significant CS 7–6 emission has been found to be associated with all of the dense cores, with excitation temperatures in the range 20 to 60 K. This is considerably higher than the temperature of 16 K suggested by Mezger *et al.*, and a re-analysis of the existing continuum data from the entire region shows that single–temperature fits in the range 42 to 70 K can also account for the observed dust spectrum. The revised mass estimates of the cores lie between 2 and 11 $M_\odot$. Luminosities of 10^2 to 10^3 $L_\odot$ are implied, which requires the presence of embedded heating sources. The evolutionary state of three of the sources have been examined in more detail:

FIR4 The lowest optical depth in the CS 7 – 6 line, and in millimetre continuum, is found towards FIR4. The results of a search for near–infrared emission associated with the cores revealed a highly reddened 2 μm source coincident with FIR4, whilst no other cores were detected. The presence of near–infrared emission is strong evidence that the core does in fact contain an embedded stellar source and is not a protostellar condensation. Also found near the 2 μm source is a compact unipolar nebula. It appears to have the features of an infrared reflection nebula, and is probably the result of an outflow from the central object having broken through the interface between the molecular cloud and the foreground HII region. Its extent from the exciting source is only 4500 AU, so it is likely to be very young.

FIR5 FIR5 is the only core that could still be cold enough to be a protostellar condensation, based on the CS observations. It is the most extended source of thermal dust emission, and the excitation temperature of the CS $7-6$ line is the lowest of all six cores. However, high–resolution HCO^+ observations led Barnes & Crutcher (1990) to suggest that FIR5 is a good candidate for the origin of the outflow that extends over 5 arcmin. In the context of the picture of star formation presented in Chapter 1, this is clearly not consistent with FIR5 being a protostellar condensation. If FIR5 *is* the source of the outflow, then its high extinction could be due to its environment, since any stellar wind can most easily evaporate into the HII region rather than dispersing the surrounding core.

FIR6 The CS $7-6$ spectrum of FIR6 is particularly wide with emission extending to $\pm 3\,\mathrm{km\,s^{-1}}$ either side of the cloud rest velocity, almost twice as broad as the emission from all the other cores. It has recently been found to be the source of a very energetic, young molecular outflow (Richer 1990), and the CS line is therefore interpreted as resulting from the interaction of a high–velocity wind with the surrounding dense core. This also seems to explain the kinematics of the existing HCO^+ data, rather than the expanding torus suggested by Barnes & Crutcher (1990).

All of the sources described above are beyond the "protostar" stage. The remaining cores, FIR1–3, may be at comparable evolutionary stages, and since they are all qualitatively similar to FIR4–6 in millimetre continuum emission and CS $7-6$, this is rather likely. The close proximity of the HII region may have triggered star formation in the ridge by driving a shock into the molecular cloud, but this does not explain why the core located closest to the ionisation front, FIR5, is also the coldest.

Future work There are several questions that remain to be answered about star formation in NGC 2024. Near–infrared polarimetry of the nebula associated with FIR4 will confirm its origin, and polarimetry of the scattered near–infrared emission just north of the ionisation front will pin down the position of the ionising source of the HII region that has not yet been identified. Mid–infrared observations of the dense cores are needed since these will reveal the distribution of hot dust, and will not be contaminated dust being heated by the foreground HII region that could be contributing to the FIR/millimetre emission. Finally, FIR6 provides the ideal opportunity of examining the interaction of a stellar wind on the dense gas in the environs of a very young outflow

source.

5.3 High–mass star formation: DR21(OH)

Of all the three sources examined in this thesis, DR21(OH) is potentially the youngest, though its larger distance makes linear resolution a problem. 1.3 mm thermal dust continuum mapping, with a resolution of 11 arcsec (0.1 pc) has shown that just north of the complex of compact HII regions DR21, lies a chain of dense cores situated in the same cloud, but with far less sign of activity compared with the more southerly sources. Bright 1.3 mm emission has been found to be associated with three maser sources, DR21(OH)M, FIR1(H_2O) and FIR3(H_2O). For those objects where other shorter wavelength data already exists, the temperature of the dust, obtained by fitting the continuum spectra by a single temperature, is around 40 to 65 K, typical of cores forming high–mass stars. The sources close to DR21(OH) are coolest and probably the youngest, though their lower temperature could also be an indication that they are sites of lower–mass star formation.

Core morphology The location of the embedded sources within the DR21 cloud is consistent with star formation taking place from the inside outwards rather than star formation being triggered externally as has been suggested for some other sources (*e.g.* Ho, Klein & Haschick 1986). DR21(OH) is also sufficiently far away from DR21 that it appears to be unaffected by the star formation going on there, implying that the origin of the dense ridge around DR21(OH) was probably independent of the activity to the south. In this respect, the morphology of the cores within the more extended GMC can be adequately explained by the model described by Mestel (1965), in which a cloud contracting under the influence of a magnetic field will form a flattened structure, with smaller fragments condensing from the collapsing cloud.

Stellar content The luminosity of the cores is sufficiently high (each core is a few $\times 10^3\,L_\odot$) that it can only be produced by embedded young stars. The possible contribution to the heating of the cores from the interstellar radiation field and the release of gravitational energy is too small to account for the observed luminosity. However, since the cloud core has remained undispersed, and there is no sign of an HII region indicative of OB stars that could disrupt the cloud, it must still be very young. It seems most likely

that to account for the presence of the OH, H_2O and CH_3OH masers associated with DR21(O)M, there is a single star with a mass of approximately $15\,M_\odot$ that accounts for the luminosity. For a Miller–Scalo IMF, this result also implies that the lower mass stars have yet to form, since star formation has clearly not yet finished within the cores, which is again consistent with the different timescales predicted by theory (*e.g.* Shu, Adams & Lizano 1987). This star could also be heating the two millimetre continuum peaks that have been found by higher resolution interferometer measurements (Woody *et al.* 1989). Unfortunately the existing upper limit on the radio continuum flux does not place a tighter upper limit on the possible spectral type of the exciting star.

Core dynamics The cores are sufficiently dense that the lower levels of CS are likely to be thermalised, so the $1-0$ and $2-1$ transitions of CS and $C^{34}S$ have been used to examine the velocity structure within the cloud. The individual clumps appear in different velocity channels, separated by approximately $5\,km\,s^{-1}$, with one of the sources immediately to the south of DR21(OH)M apparently connected to the maser source by a ridge of emission. This ridge is perpendicular to the orientation of the methanol masers (Plambeck & Menten 1990).

The CS $2-1$ profiles towards the centre of the cluster are self–reversed, and the variation of the profiles across the cloud can be explained by the presence of cooler, infalling gas along the line–of–sight. All the spectra are relatively wide, even the $C^{34}S$ lines, and wing emission is present to the east of DR21(OH)M. In order to obtain a quantitative estimate of the excitation conditions of CS, the spectra at each position has been modelled by two components, with warm background gas in LTE and cooler foreground gas, also in LTE. The results indicate that the two components are physically associated, and the warm gas has a peak excitation temperature of about 40 K at the centre. Comparing this with the dust temperature, it is apparent that the LTE assumption was justified.

The mass of the cloud core is about $2000\,M_\odot$, obtained from both the dust continuum emission and the CS data. The CS linewidths, together with the derived mass, indicate that the cloud is approximately in virial equilibrium.

Future work It appears that one of the sources of the wide CS lines, and presumably also one of the sources of turbulent support of the cloud, is the presence of an extremely young outflow. This has yet to be detected directly, since the usual method of examining

the line wings of ^{12}CO will not work because the proximity of the W75 cloud masks the emission. At present its existence can only be inferred from the wings detected by the CS mapping, and the orientation and separation of the masers associated with DR21(OH)M. To verify this suggestion will require observations in ^{13}CO that will not be so confused by high optical depth.

5.4 Future observations of protostars

It has become apparent that one of the major problems that faces the detection of protostars is that of unambiguously identifying the stage of evolution of embedded sources. Although the thermal dust emission can, in theory, be used to quantify the evolutionary phase of protostars (Adams 1990), it seems that the models are not yet at a stage of being able to explain all the observations, and that they also contain a number of unknown parameters that cannot be determined observationally.

The work presented in Chapters 2 and 3 showed that among other things, the presence of an outflow can be used to infer that the source from which it originates has passed its protostellar phase. As long as the dynamical lifetime of the outflow is assumed to be a measure of how recently the embedded source left that phase, sources with compact outflows can be taken as being the youngest outflow sources. Those sources that do not yet have outflows can then be regarded as candidate protostars. This presents a means of testing the main ideas of protostellar evolution empirically, since for low–mass objects whose accretion luminosity is a strong function of age, we might expect a strong correlation between the source luminosity and its outflow energetics, if the accretion process or a process related to the accretion phase (for example, the onset of deuterium burning) is responsible for the production of the outflow.

A detailed investigation of the luminosity and outflow energetics of low–luminosity sources, particularly in a region such as Taurus which is known to be actively forming low–mass stars, is therefore required. The best way of identifying cool, embedded objects is to use the far–infrared colours provided by the IRAS *Point Source Catalogue* (*e.g.* Emerson 1987); Heyer *et al.* (1987) have surveyed IRAS sources in Taurus by making undersampled maps using a 45 arcsec beam, but subsequent high–resolution observations (*e.g.* Terebey, Vogel & Myers 1989; Chandler *et al.* in preparation) have shown that they missed compact, high–velocity gas.

Other surveys for high–velocity gas associated with YSOs which are large enough

to enable statistical studies of the outflow phenomenon have concentrated on luminous infrared sources, with $L_* \gtrsim 40\,L_\odot$ (*e.g.* Bally & Lada 1983; Margulis, Lada & Snell 1988; Snell *et al.* 1988; Snell, Dickman & Huang 1990). They therefore represent either medium to high mass objects, or more evolved, low–mass, pre–main–sequence stars. A correlation between flow mechanical luminosity and momentum transport rate versus total bolometric luminosity of the associated infrared sources was proposed by Bally & Lada (1983), which was found to weaken if only the high luminosity sources ($\gtrsim 500\,L_\odot$) were considered. The correlation found by Bertout (1988), who examined a sample of outflow sources whose orientation could be estimated from their flow morphology, is stronger than that of Bally & Lada. This was used as evidence that the outflows associated with high–luminosity sources could be radiatively driven, although he commented that the situation is not so clear for low–luminosity sources. It is therefore important to survey low–luminosity sources for *compact*, high–velocity gas, for which a stronger correlation than found in previous surveys might be expected.

Apart from extending the existing data set to lower mass sources, such a survey could also be used to examine the earliest stages of protostellar evolution by identifying cold cores that have no associated outflow. These sources are probably so young that they have not yet reached a stage of energetic mass loss. The next stage is then to determine whether the surrounding core can unambiguously be identified to be collapsing. This can only be done using spectral line mapping, to search for the asymmetric profiles signifying the infall of molecular material. This may prove to be the hardest part of finding a protostar, since it requires high spectral and spatial resolution, high instrumental sensitivity and careful data analysis and interpretation. However the importance of such a discovery cannot be over emphasised, and the study of very early stellar evolution remains one of the most interesting, if difficult, areas of observational astronomy.

References

Adams, F.C. 1990. *Astrophys. J.*, **363**, 578.

Adams, F.C., Lada, C.J. & Shu, F.H. 1987. *Astrophys. J.*, **312**, 788.

Adams, F.C. & Shu, F.H. 1985. *Astrophys. J.*, **296**, 655.

Adams, F.C. & Shu, F.H. 1986. *Astrophys. J.*, **308**, 836.

Andriesse, C.D. 1977. *Vistas in Astronomy*, **21**, 107.

Appenzeller, I. & Mundt, R. 1989. *Astr. Astrophys. Rev.*, **1**, 291.

Arquilla, R. & Goldsmith, P.F. 1986. *Astrophys. J.*, **303**, 356.

Aspin, C., McLean, I.S., Rayner, J.T. & McCaughrean, M.J. 1988. *Astr. Astrophys.*, **197**, 242.

Bally, J. & Lada, C.J. 1983. *Astrophys. J.*, **265**, 824.

Barnes, P.J. & Crutcher, R.M. 1990. *Astrophys. J.*, **351**, 176.

Barnes, P.J., Crutcher, R.M., Bieging, J.H., Storey, J.W.V. & Willner, S.P. 1989. **342**, 883.

Barral, J.F. & Cantó, J. 1981. *Rev. Mex. Astr. Astrof.*, **5**, 101.

Batrla, W. & Menten, K.M. 1988. *Astrophys. J.*, **329**, L117.

Beckwith, S., Persson, S.E., Neugebauer, G. & Becklin, E.E. 1978. *Astrophys. J.*, **223**, 464.

Beckwith, S.V.W., Sargent, A.I., Chini, R.S. & Güsten, R. 1990. *Astron. J.*, **99**, 924.

Beichman, C.A., Myers, P.C., Emerson, J.P., Harris, S., Mathieu, R., Benson, P.J. & Jennings, R.E. 1986. *Astrophys. J.*, **307**, 337.

Benson, P.J. & Myers, P.C. 1989. *Astrophys. J. Suppl.*, **71**, 89.

Bertout, C. 1988. In: *Formation and Evolution of Low Mass Stars*, ed. A.K. Dupree and M.T.V.T. Lago (Dordrecht: Kluwer Academic Publishers), p. 45.

Bohlin, R.C., Savage, B.D. & Drake, J.F. 1978. *Astrophys. J.*, **224**, 132.

Bok, B.J. & McCarthy, C.C. 1974. *Astron. J.*, **79**, 42.

Boss, A.P. 1987. *Astrophys. J.*, **316**, 721.

Boss, A.P. & Yorke, H.W. 1990. *Astrophys. J.*, **353**, 236.

Cabrit, S. & Bertout, C. 1990. *Astrophys. J.*, **348**, 530.

Cabrit, S., Goldsmith, P.F. & Snell, R.L. 1988. *Astrophys. J.*, **334**, 196.

Calvet, N., Basri, G. & Kuhi, L.V. 1984. *Astrophys. J.*, **277**, 725.

Cantó, J., Rodríguez, L.F. & Anglada, G. 1987. *Astrophys. J.*, **321**, 877.

Casali, M.M. & Edgar, M.L. 1987. *Mon. Not. R. astr. Soc.*, **225**, 481.

Cassen, P., Shu, F.H. & Terebey, S. 1985. In: *Protostars and Planets II*, ed. D.C. Black and M.S. Matthews (University of Arizona Press), p. 448.

Castelaz, M.W., Hackwell, J.A., Grasdalen, G.L. & Gehrz, R.D. 1986. *Astrophys. J.*, **300**, 406.

Castelaz, M.W., Hackwell, J.A., Grasdalen, G.L., Gehrz, R.D. & Gullixson, C. 1985. *Astrophys. J.*, **290**, 261.

Catala, C. 1989. In: *ESO Workshop on Low Mass Star Formation and Pre-Main Sequence Objects*, ed. B. Reipurth, p. 471.

Cato, B.T., Rönnäng, B.O., Rydbeck, O.E.H., Lewin, P.T., Yngvesson, K.S., Cardiasmenos, A.G. & Shanley, J.F. 1976. *Astrophys. J.*, **208**, 87.

Chandler, C.J., Gear, W.K., Sandell, G., Hayashi, S., Duncan, W.D., Griffin, M.J. & Hazell, A.S. 1990. *Mon. Not. R. astr. Soc.*, **243**, 330.

Chini, R., Kreysa, E., Mezger, P.G. & Gemünd, H.-P. 1984. *Astr. Astrophys.*, **137**, 117.

Crutcher, R.M., Henkel, C., Wilson, T.L., Johnston, K.J. & Bieging, J.H. 1986. *Astrophys. J.*, **307**, 302.

Dame, T.M., Elmegreen, B.G., Cohen, R.S. & Thaddeus, P. 1986. *Astrophys. J.*, **305**, 892.

Davidson, J.A. 1987. *Astrophys. J.*, **315**, 602.

Dent, W.R.F., Sandell, G., Duncan, W.D. & Robson, E.I. 1989. *Mon. Not. R. astr. Soc.*, **238**, 1497.

Dickel, J.R., Dickel, H.R. & Wilson, W.J. 1978. *Astrophys. J.*, **223**, 840.

Draine, B.T. 1983. *Astrophys. J.*, *270*, 519.

Draine, B.T. 1990. In: *The Interstellar Medium in Galaxies*, ed. H.A. Thronson Jr and J.M. Shull (Dordrecht: Kluwer Academic Publishers), p. 483.

Draine, B.T. & Lee H.M. 1984. *Astrophys. J.*, **285**, 89.

Dyson, J.E. 1984. *Astrophys. Space Sci.*, **106**, 181.

Dyson, J.E. & Williams, D.A. 1980. *The Physics of the Interstellar Medium* (Manchester University Press).

Elmegreen, B. 1982. In *Submillimetre-Wave Astronomy*, ed. J. Beckman and J. Phillips (Cambridge University Press), p. 1.

Emerson, J.P. 1987. In: *Star Forming Regions, IAU Sump. 115*, ed. M. Peimbert and J. Jugaku (Dordrecht: Reidel), p. 19.

Emerson, J.P. 1988. In: *Formation and Evolution of Low Mass Stars*, ed. A.K. Dupree

and M.T.V.T. Lago (Dordrecht: Kluwer Academic Publishers), p. 21.

Emerson, D.T., Klein, U. & Haslam, C.G.T. 1979. *Astr. Astrophys.*, **76**, 92.

Evans, N.J., Mundy, L.G., Davis, J.H. & Vanden Bout, P. 1987. *Astrophys. J.*, **312**, 344.

Fischer, J., Righini-Cohen, G. & Simon, M. 1980. *Astrophys. J.*, **238**, L155.

Frerking, M.A. & Langer, W.D. 1982. *Astrophys. J.*, **256**, 523.

Frerking, M.A., Langer, W.D. & Wilson, R.W. 1987. *Astrophys. J.*, **313**, 320.

Frerking, M.A., Wilson, R.W., Linke, R.A. & Wannier, P.G. 1980. *Astrophys. J.*, **240**, 65.

Garden, R., Geballe, T.R., Gatley, I. & Nadeau, D. 1986. *Mon. Not. R. astr. Soc.*, **220**, 203.

Garden, R.P., Russell, A.P.G. & Burton, M.G. 1990. *Astrophys. J.*, **354**, 232.

Gear, W.K. 1988. In: *Millimetre and Submillimetre Astronomy*, ed. R.D. Wolstencroft and W.B. Burton (Dordrecht: Kluwer Academic Publishers), p. 307.

Gear, W.K., Chandler, C.J., Moore, T.J.T., Cunningham, C.T. & Duncan, W.D. 1988. *Mon. Not. R. astr. Soc.*, **231**, 47P.

Gee, G., Griffin, M.J., Cunningham, C.T., Emerson, J.P., Ade, P.A.R. & Caroff, L.J. 1985. *Mon. Not. R. astr. Soc.*, **215**, 15P.

Genzel, R. & Downes, D. 1977. *Astr. Astrophys. Suppl.*, **30**, 145.

Goldsmith, P.F., Snell, R.L., Hemeon-Heyer, M. & Langer, W.D. 1984. *Astrophys. J.*, **286**, 599.

Goldsmith, P.F. & Langer, W.D. 1978. *Astrophys. J.*, **222**, 881.

Grasdalen, G.L. 1974. *Astrophys. J.*, **193**, 373.

Green, S. & Chapman, S. 1978. *Astrophys. J. Suppl.*, **37**, 169.

Habing, H.J., Goss, W.M., Matthews, H.E. & Winnberg, A. 1974. *Astr. Astrophys.*, **35**, 1.

Harris, A., Townes, C.H., Matsakis, D.N. & Palmer, P. 1983. *Astrophys. J.*, **265**, L63.

Harris, S. 1973. *Mon. Not. R. astr. Soc.*, **162**, 5P.

Hartmann, L. & MacGregor, K.B. 1982. *Astrophys. J.*, **259**, 180.

Harvey, P.M., Joy, M., Lester, D.F. & Wilking, B.A. 1986. *Astrophys. J.*, **300**, 737.

Hasegawa, T.I., Hirano, H., Kameya, O., Taniguchi, Y., Tosa, M. & Takakubo, K. 1986. *Publs astr. Soc. Japan*, **38**, 379.

Haslam, C.G.T. 1974. *Astr. Astrophys. Suppl.*, **15**, 333.

Herbig, G.H. & Jones, B.F. 1981. *Astron. J.*, **86**, 1232.

Heyer, M.H., Snell, R.L., Goldsmith, P.F. & Myers, P.C. 1987. *Astrophys. J.*, **321**, 370.

Heyer, M.H., Snell, R.L., Goldsmith, P.F., Strom, S.E. & Strom, K.M. 1986. *Astrophys. J.*, **308**, 134.

Hildebrand, R.H. 1983. *Q. Jl R. astr. Soc.*, **24**, 267.

Hirano, N., Kameya, O., Nakayama, M. & Takakubo, K. 1988. *Astrophys. J.*, **327**, L69.

Ho, P.T.P. & Haschick, A.D. 1986. *Astrophys. J.*, **304**, 501.

Ho, P.T.P., Klein, R.I. & Haschick, A.D. 1986. *Astrophys. J.*, **305**, 714.

Hudson, H.S. & Soifer, B.T. 1976. *Astrophys. J.*, **206**, 100.

Iben, I. 1965. *Astrophys. J.*, **141**, 993.

Irvine, W.M., Goldsmith, P.F. & Hjalmarson, Å. 1987. In *Interstellar Processes*, ed. D.J. Hollenbach and H.A. Thronson Jr (Dordrecht: Reidel), p. 561.

Johnston, K.J., Henkel, C. & Wilson, T.L. 1984. *Astrophys. J.*, **285**, L85.

Kaifu, N., Suzuki, S., Hasegawa, T., Morimoto, M., Inatani, J., Nagane, K., Miyazawa, K., Chikada, Y., Kanzawa, T. & Akabane, K. 1984. *Astr. Astrophys.*, **134**, 7.

Keene, J., Davidson, J.A., Harper, D.A., Hildebrand, R.H., Jaffe, D.F., Loewenstein, R.F., Low., F.J. & Pernic, R. 1983. *Astrophys. J.*, **274**, L43.

Königl, A. 1982. *Astrophys. J.*, **261**, 115.

Königl, A. 1989. *Astrophys. J.*, **342**, 208.

Kutner, M.L. & Ulich, B.L. 1981. *Astrophys. J.*, **250**, 341.

Kwok, S. & Volk, K. 1985. *Astrophys. J.*, **299**, 191.

Lada, C.J. 1985. *Ann. Rev. Astr. Ap.*, **23**, 267.

Lane, A.P. & Bally, J. 1986. *Astrophys. J.*, **310**, 820.

Langer, W.D., Frerking, M.A. & Wilson, R.W. 1986. *Astrophys. J.*, 306, L29.

Larson, R.B. 1981. *Mon. Not. R. astr. Soc.*, **194**, 809.

Leung, C.M. 1978. *Astrophys. J.*, **225**, 427.

Leung, C.M. & Brown, R.L. 1977. *Astrophys. J.*, **214**, L73.

Linke, R.A. & Goldsmith, P.F. 1980. *Astrophys. J.*, **235**, 437.

Lizano, S., Heiles, C., Rodríguez, L.F.. Koo, B.-C., Shu, F.H., Hasegawa, T., Hayashi, S. & Mirabel, I.F. 1988. *Astrophys. J.*, **328**, 763.

Lizano, S. & Shu, F.H. 1987. In: *NATO/ASI Physical Processes in Interstellar Clouds*, ed. M. Scholer (Dordrecht: Reidel), p. 173.

Lizano, S. & Shu, F.H. 1989. *Astrophys. J.*, **342**, 834.

Loren, R.B., Sandqvist, A. & Wootten, A. 1983. *Astrophys. J.*, **270**, 620.

Lovas, F.J. 1986. *J. Phys. Chem. Ref. Data*, **15**, 251.

Mangum, J.G., Wootten, A. & Mundy, L.G. 1989. *NRAO preprint.*

Mangum, J.G., Wootten, A. & Mundy, L.G. 1990. In: *Submillimetre Astronomy*, ed. G.D. Watt and A.S. Webster (Dordrecht: Kluwer Academic Publishers), p. 185.

Margulis, M., Lada, C.J. & Snell, R.L. 1988. *Astrophys. J.*, **333**, 316.

Masson, C.R., Lo, K.Y., Phillips, T.G., Sargent, A.I., Scoville, N.Z. & Woody, D.P. 1987. *Astrophys. J.*, **319**, 446.

Mathis, J.S., Mezger, P.G. & Panagia, N. 1983. *Astr. Astrophys.*, **128**, 212.

McKee, C.F. 1989. *Astrophys. J.*, **345**, 782.

Menten, K.M., Harju, J., Olano, C.A. & Walmsley, C.M. 1989. *Astr. Astrophys.*, **223**, 258.

Menten, K.M., Serabyn, E., Güsten, R. & Wilson, T.L. 1987. *Astr. Astrophys.*, **177**, L57.

Mestel, L. 1965. *Q. Jl R. astr. Soc.*, **6**, 265.

Mezger, P.G., Chini, R., Kreysa, E., Wink, J.E. & Salter, C.J. 1988. *Astr. Astrophys.*, **191**, 44.

Mezger, P.G., Wink, J.E. & Zylka, R. 1990. *Astr. Astrophys.*, **228**, 95.

Miller, G.E. & Scalo, J.M. 1979. *Astrophys. J. Suppl.*, **41**, 513.

Montmerle, T., Koch-Miramond, L., Falgarone, E. & Grindlay, J.E. 1983. *Astrophys. J.*, **269**, 182.

Moore, T.J.T. 1989. *Ph.D. Thesis*, University of Edinburgh.

Moore, T.J.T. & Chandler, C.J. 1989. *Mon. Not. R. astr. Soc.*, **241**, 19P.

Moore, T.J.T., Chandler, C.J., Gear, W.K. & Mountain, C.M. 1989. *Mon. Not. R. astr. Soc.*, **237**, 1P.

Moriarty-Schieven, G.H. & Snell, R.L. 1989. *Astrophys. J.*, **338**, 952.

Mouschovias, T. Ch. & Paleologou, E.V. 1986. *Astrophys. J.*, **308**, 781.

Mouschovias, T. Ch. & Spitzer, L. 1976. *Astrophys. J.*, **210**, 326.

Mundt, R. & Fried, J.W. 1983. *Astrophys. J.*, **274**, L83.

Mundy, L.G., Snell, R.L., Evans, N.J., Goldsmith, P.F. & Bally, J. 1986. *Astrophys. J.*, **306**, 670.

Mundy, L.G., Wilking, B.A. & Myers, S.T. 1986. *Astrophys. J.*, **311**, L75.

Myers, P.C. & Benson, P.J. 1983. *Astrophys. J.*, **266**, 309.

Myers, P.C., Dame, T.M., Thaddeus, P., Cohen, R.S., Silverberg, R.F., Dwek, E. & Hauser, M.G. 1986. *Astrophys. J.*, **301**, 398.

Myers, P.C. & Goodman, A.A. 1988. *Astrophys. J.*, **329**, 392.

Norris, R.P., Booth, R.S., Diamond, P.J. & Porter, N.D. 1982. *Mon. Not. R. astr. Soc.*, **201**, 191.

Oster, L. 1961. *Rev. Mod. Phys.*, **33**, 525.

Padin, S., Sargent, A.I., Mundy, L.G., Scoville, N.Z., Woody, D.P., Leighton, R.B., Masson, C.R., Scott, S.L., Seling, T.V., Stapelfeldt, K.R. & Terebey, S. 1989. *Astrophys. J.*, **337**, L45.

Palla, F. 1990. In: *Fragmentation of Molecular Clouds and Star Formation, IAU Symp. 147*, ed. E. Falgarone (Dordrecht: Reidel), in press.

Palla, F. & Stahler, S.W. 1990. *Astrophys. J.*, **360**, L47.

Panagia, N. 1973. *Astron. J.*, **78**, 929.

Plambeck, R.L. & Menten, K.M. 1990. *Astrophys. J.*, in press.

Pudritz, R.E. & Norman, C.A. 1986. *Astrophys. J.*, **301**, 571.

Ray, T.P., Poetzel, R., Solf, J. & Mundt, R. 1990. *Astrophys. J.*, **357**, L45.

Reid, M.J. & Moran, J.M. 1981. *Ann. Rev. Astr. Ap.*, **19**, 231.

Richardson, K.J., Sandell, G. & Krisciunas, K. 1989. *Astr. Astrophys.*, **224**, 199.

Richer, J.S., 1990. *Mon. Not. R. astr. Soc.*, **245**, 24P.

Richer, J.S., Hills, R.E., Padman, R. & Russell, A.P.G. 1989. *Mon. Not. R. astr. Soc.*, **241**, 231.

Rieke, G.H. & Lebofsky, M.J. 1985. *Astrophys. J.*, **288**, 618.

Sanders, D.B. & Willner, S.P. 1985. *Astrophys. J.*, **293**, L39.

Sargent, A.I. & Beckwith, S. 1987. *Astrophys. J.*, **323**, 294.

Sargent, A.I., Beckwith, S., Keene, J. & Masson, C. 1988. *Astrophys. J.*, **333**, 936.

Scoville, N.Z. & Good, J.C. 1989. *Astrophys. J.*, **339**, 149.

Scoville, N.Z. & Kwan, J. 1976. *Astrophys. J.*, **206**, 718.

Shu, F.H. 1977. *Astrophys. J.*, **214**, 488.

Shu, F.H., Adams, F.C. & Lizano, S. 1987. *Ann. Rev. Astr. Ap.*, **25**, 23.

Shu, F.H. & Terebey, S. 1984. In: *Cool Stars, Stellar Systems, and the Sun*, ed. S. Baliunas and L. Hartmann (Berlin: Springer-Verlag), p. 78.

Shu, F.H., Lizano, S., Ruden, S.P. & Najita, J. 1988. *Astrophys. J.*, **328**, L19.

Snell, R.L., Dickman, R.L. & Huang, Y.-L. 1990. *Astrophys. J.*, **352**, 139.

Snell, R.L., Huang, Y.-L., Dickman, R.L. & Claussen, M.J. 1988. *Astrophys. J.*, 325, 853.

Snell, R.L. & Loren, R.B. 1977. *Astrophys. J.*, **211**, 122.

Snell, R.L., Loren, R.B. & Plambeck, R.L. 1980. *Astrophys. J.*, *239*, L17.

Snell, R.L., Mundy, L.G., Goldsmith, P.F., Evans, N.J. & Erickson, N.R. 1984. *Astrophys. J.*, **276**, 625.

Solomon, P.M., Sanders, D.B. & Rivolo, A.R. 1985. *Astrophys. J.*, **292**, L19.

Spitzer, L. 1978. *Physical Processes in the Interstellar Medium* (New York: Wiley & Sons).

Stahler, S.W. 1983. *Astrophys. J.*, **274**, 822.

Terebey, S., Shu, F.H. & Cassen, P. 1984. *Astrophys. J.*, **286**, 529.

Terebey, S., Vogel, S.N. & Myers, P.C. 1989. *Astrophys. J.*, **340**, 472.

Thronson, H.A., Lada, C.J., Schwartz, P.R., Smith, H.A., Smith, J., Glaccum, W., Harper, D.A. & Loewenstein, R.F. 1984. *Astrophys. J.*, **280**, 154.

Tielens, A.G.G.M. & Allamandola, L.J. 1987. In: *Interstellar Processes*, ed. D.J. Hollenbach and H.A. Thronson Jr (Dordrecht: Reidel) p. 397.

Tomisaka, K., Ikeuchi, S. & Nakamura, T. 1988. *Astrophys. J.*, **335**, 239.

Tomita, Y., Saito, T. & Ohtani, H. 1979. *Publs astr. Soc. Japan*, **31**, 407.

Torbett, M.V. 1984. *Astrophys. J.*, **278**, 318.

Townes, C.H. & Schawlow, A.L. 1955. *Microwave Spectroscopy* (New York: McGraw-Hill).

Troland, T.H. & Heiles, C. 1986. *Astrophys. J.*, **301**, 339.

Uchida, Y. & Shibata, K. 1985. *Publs astr. Soc. Japan*, **37**, 515.

Vrba, F.J., Luginbuhl, C.B., Strom, S.E., Strom, K.M. & Heyer, M.K. 1986. *Astron. J.*, **92**, 633.

Walmsley, C.M. & Menten, K.M. 1987. *Astr. Astrophys.*, **179**, 231.

Wolfire, M.G. & Cassinelli, J.P. 1986. *Astrophys. J.*, **310**, 207.

Wolfire, M.G. & Churchwell, E. 1987. *Astrophys. J.*, **315**, 315.

Woody, D.P., Scott, S.L., Scoville, N.Z., Mundy, L.G., Sargent, A.I., Padin, S., Tinney, C.G. & Wilson, C.D. 1989. *Astrophys. J.*, **337**, L41.

Yamashita, T., Sato, S., Nagata, T., Gatley, I., Hayashi, S.S. & Fukui, Y. 1989. *Astrophys. J.*, **336**, 832.

Yamashita, T., Sato, S., Tamura, M., Suzuki, H., Takano, T., Mountain, C.M., Moore,

T.J.T., Gatley, I. & Hough, J.H. 1987. *Publs astr. Soc. Japan*, **39**, 809.

Yorke, H.W. & Shustov, B.M. 1981. *Astr. Astrophys.*, **98**, 125.

Zheng, X.W., Ho, P.T.P., Reid, M.J. & Schneps, M.H. 1985. *Astrophys. J.*, **293**, 522.

Appendix A

The stellar content of DR21(OH)

The functional form of the IMF given by Miller & Scalo (1979) is used below to estimate the mass of main–sequence stars in DR21(OH) that can account for the observed luminosity. I have used the three–segmented power–law fit to the number of stars per unit mass,

$$n(M) = k\, D_0 M^{D_1},$$

which for M in units of $\mathrm{M}_\odot$ has with $D_0 = 42$, $D_1 = -1.4$ for $0.1 \leq M/\mathrm{M}_\odot \leq 1$, $D_0 = 42$, $D_1 = -2.5$ for $1 \leq M/\mathrm{M}_\odot \leq 10$, and $D_0 = 240$, $D_1 = -3.3$ for $10 \leq M/\mathrm{M}_\odot$. k is a suitable normalisation constant.

For a given normalisation, the mass of the highest mass star likely to be present, M_u, will be

$$\int_{M_1}^{M_0} M n(M) dM = M_u$$

where the mass M_1 is defined by the criterion

$$\int_{M_1}^{M_0} n(M) dM = 1$$

and M_0 is the upper mass limit of the IMF, taken to be $62\,\mathrm{M}_\odot$ by Miller & Scalo (1979). The quantitative analysis for DR21(OH) below shows that setting $M_0 = \infty$ makes a negligible difference to the final result because of the limit on the number of high–mass stars set by the observed luminosity. The next highest mass star is then defined by

$$\int_{M_2}^{M_1} n(M) dM = 1$$

and its mass is $\int_{M_2}^{M_1} M n(M) dM$. The total mass of stars present can then be found by summing all the stars, assuming the lowest mass star present is $0.1\,\mathrm{M}_\odot$:

$$M_{\rm stars} = \sum_l \int_{M_{l+1}}^{M_l} Mn(M)dM = \int_{0.1}^{M_0} Mn(M)dM.$$

The luminosity of this ensemble of stars can be found by approximating $(L/\mathrm{L}_\odot) = (M/\mathrm{M}_\odot)^3$ over the entire mass range (Allen 1955), giving

$$L_{\rm observed} = \sum_l \left(\int_{M_{l+1}}^{M_l} Mn(M)dM \right)^3 .$$

The observed luminosity of DR21(OH)M can then be used to determine the normalisation and hence the value of M_u if the distribution of stellar masses is drawn from such a function. The equations were solved iteratively, and a value of $M_u = 14.8\,\mathrm{M}_\odot$ was found for $L_{\rm observed} = 4100\,\mathrm{L}_\odot$. Higher values of M_u resulted in all of the luminosity being produced by a small number of high to medium mass stars, with no low–mass stars yet formed. Lower values of M_u did not produce sufficient luminosity. This value of M_u may be compared with the upper limit obtained if *all* the luminosity is produced be a single high–mass star, which is $16\,\mathrm{M}_\odot$.

Appendix B

Published papers

Copies of the following papers are included here:

Chandler, C.J., Gear, W.K., Sandell, G., Hayashi, S., Duncan, W.D., Griffin, M.J. & Hazell, A.S. 1990. "B335: protostar or embedded pre–main–sequence star?" *Mon. Not. R. astr. Soc.*, **243**, 330.

Moore, T.J.T., Chandler, C.J., Gear, W.K. & Mountain, C.M. 1989. "CS ($J = 7 - 6$) from heated gas near the embedded sources in NGC 2024," *Mon. Not. R. astr. Soc.*, **237**, 1P.

Moore, T.J.T. & Chandler, C.J. 1989. "Near–infrared observations of NGC 2024: identification of a 2-μm source within a dense core," *Mon. Not. R. astr. Soc.*, **241**, 19P.

Gear, W.K., Chandler, C.J., Moore, T.J.T., Cunningham, C.T. & Duncan, W.D. 1988. "Submillimetre observations reveal that DR21(OH) is a double source," *Mon. Not. R. astr. Soc.*, **231**, 47P.

Mon. Not. R. astr. Soc. (1990) **243**, 330–335

B335: protostar or embedded pre-main-sequence star?

C. J. Chandler
Department of Astronomy, University of Edinburgh, Blackford Hill, Edinburgh EH9 3HJ

W. K. Gear
Royal Observatory, Blackford Hill, Edinburgh EH9 3HJ

G. Sandell, S. Hayashi and W. D. Duncan
Joint Astronomy Centre, 665 Komohana Street, Hilo, Hawaii 96720, USA

M. J. Griffin and A. S. Hazell
Department of Physics, Queen Mary College, Mile End Road, London E1 4NS

Accepted 1989 September 14. Received 1989 August 31; in original form 1988 December 19

SUMMARY

High-resolution submillimetre continuum observations of the far-infrared source in the isolated Bok globule B335 have been made using the JCMT. The continuum source is resolved perpendicular to the axis of the accompanying outflow in an 8 arcsec beam, but unresolved parallel to it. We conclude that it is a very dense $[n(H_2) \gtrsim 5 \times 10^{13}\ m^{-3}]$ core of dust and gas surrounding a central protostellar or pre-main-sequence object. We find that this core is able to collimate an initially isotropic wind into its observed bipolar structure. The central object does not appear to fit the currently popular models for protostellar evolution, because of its high A_V, low luminosity, and the presence of an outflow. We propose three alternatives to explain these features: (i) outflow is possible from protostars much younger than had previously been expected; (ii) the luminosity source is a more evolved protostar with an outflow, that has unusually low mass and/or accretion efficiency, and the high A_V is due to the orientation of the source, or (iii) the source is already well-evolved and is a pre-main-sequence star that, for some reason, has remained deeply embedded.

1 INTRODUCTION

B335 is an isolated dark cloud with a relatively simple structure compared with most molecular clouds. An upper limit of 400 pc has been placed on its distance by the absence of foreground stars (Bok & McCarthy 1974), although large-scale extinction measurements and its coincidence with the Lindblad ring (Tomita, Saito & Ohtani 1979; Elmegreen 1982) have led most authors to use a distance of 250 pc, which we have also adopted. An associated compact, embedded, far-infrared/submillimetre continuum source was detected by Keene *et al.* (1983), and a low-velocity bipolar outflow was found to be centred on the far-infrared (FIR) source by Frerking & Langer (1982) and Goldsmith, Snell & Hemeon-Heyer (1984). The large-scale structure and dynamics of the globule have been studied in detail by Frerking, Langer & Wilson (1987), who, after detecting a blue- and red-shifted component in ^{12}CO $J = 1 - 0$ channel maps offset from the original outflow (Langer, Frerking & Wilson 1986), deduced that the globule was in fact evolved, with two outflows, rather than a young cloud still undergoing star-formation as had previously been thought. More recently, however, the overlapping red- and blue-shifted emission has been interpreted as the result of a highly-collimated single bipolar outflow, oriented in the plane of the sky (Hirano *et al.* 1988; Cabrit, Goldsmith & Snell 1988; Moriarty-Schieven & Snell 1989). Hirano *et al.* (1988) concluded that the flow must be focused within 0.02 pc of the driving source.

B335 also has a possible Herbig–Haro (HH) object in the red lobe of the outflow, detected by Hα emission (Vrba *et al.* 1986). This might be considered surprising, since one would expect HH objects to be detected preferentially in the blue lobe, but as the outflow is nearly in the plane of the sky the column density of intervening dust and gas is likely to be similar for both the blue and red lobes. Moreover, the red lobe appears to have broken out of the edge of the cloud (Moriarty-Schieven & Snell 1989), indicating that there must

be a steeper density gradient along the red lobe than the blue lobe, making it possible for us to detect optical emission from nearer to the central object in the red lobe than the blue lobe.

The FIR source at the centre of the outflow was barely resolved in a 55 arcsec beam at 360 μm by Gee *et al.* (1985), who claimed a source size of 28 ± 5 arcsec. Gee *et al.* (1985) argued that their data were consistent with a protostellar source, but were unable to resolve the accretion disc that they proposed as the source of the luminosity, and a possible driving source of the outflow. In order to try to test their model by resolving small-scale structure associated with the FIR source, we have made high-resolution submillimetre continuum observations, in an attempt to determine the evolutionary state of this interesting object.

2 OBSERVATIONS

The observations were made with the 15-m James Clerk Maxwell Telescope (JCMT) on Mauna Kea, Hawaii, during 1988 April, August and October. Photometry was performed using the common-user ^{3}He cooled bolometer UKT14, with filters centred on 2 mm, 1.3 mm, 1.1 mm, 800 μm, 600 μm, 450 μm and 350 μm. Flux calibration was performed against Mars and Uranus, and is the most significant source of uncertainty in the photometry, due to variation in the sky transparency over the period of the observations. The photometry is shown in Table 1, where the total uncertainties include both the statistical and estimated calibration uncertainties. Two over-sampled maps were made at 800 μm with a 17 arcsec beam. They were taken in an azimuth elevation coordinate system by chopping and scanning simultaneously, producing differential maps, covering an area 105×105 arcsec, using 7.5 arcsec pixel spacing and a chop throw of 60 arcsec. They were reduced using the NOD2 software (Haslam 1974), and co-added. The pointing accuracy is estimated to be ~ 4 arcsec for the 800 μm maps. A map was also made at 450 μm with 3 arcsec spacing, for which the HPBW at 450 μm was measured to be 8 ± 1 arcsec from a beam map of Uranus. This map was produced from an evenly-spaced grid of single photometry points. The pointing was checked directly before and after the 450 μm map using K3-50, and was found to be accurate to ± 2 arcsec over that period.

Table 1. Submillimetre photometry.

Wavelength	Effective freq (GHz)	Beam size (″)	Flux per beam (Jy)	Statistical uncertainty (Jy)	Total uncertainty (Jy)
2 mm	156	32	$3\sigma = 0.57$		
1.3 mm	238	21	0.64	0.03	0.07
1.1 mm	272	19	0.68	0.02	0.07
800 μm	380	17	1.88	0.03	0.28
		13	1.30	0.07	0.21
600 μm	463	19	4.0	0.3	0.85
450 μm	676	18	15.0	1.3	4.7
		8	9.8	1.1	3.1
350 μm	854	18	35	2.4	14

3 RESULTS

The 800 μm map is displayed in Fig. 1 together with the CO $J=1-0$ contours of the outflow from Hirano *et al.* (1988, hereafter HKNT). The contours in the continuum map are at 1σ intervals of 0.2 Jy, and fitting a Gaussian to the flux distribution gives a FWHM of 22 ± 2 arcsec. Approximating the actual source distribution to be Gaussian, and after deconvolving with our 17 arcsec beam, we obtain a source size of 14 ± 3 arcsec. The 1σ contour is extended north–south (the axis of symmetry of the outflow is east–west); this low-level emission appears in *both* of the two maps that have been co-added to produce the contour plot displayed in Fig. 1. At the time that the maps were taken the angles between an RA–Dec. coordinate system and the local (az–el) coordinate system were $\sim 20°$ and $\sim 55°$, so any extended emission is therefore away from the chop direction (azimuth).

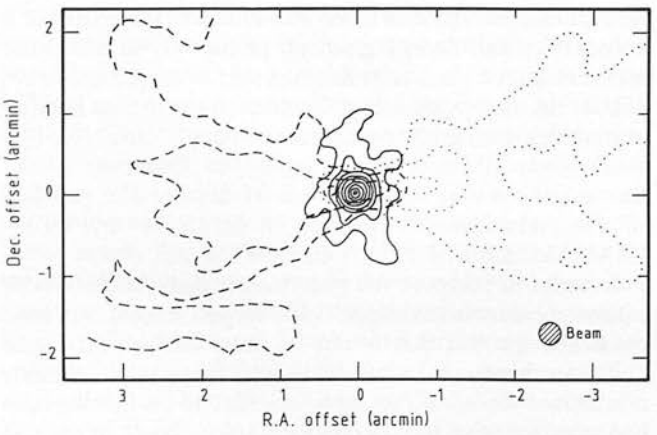

Figure 1. 800 μm map of B335 taken with a 17 arcsec beam (solid contours), together with CO $J=1-0$ contours from HKNT (the blue wing is represented by the dashed contours, and the red wing by the dotted contours). The lowest contour in the continuum map is at 0.2 Jy, and the contour interval is at 1σ spacing of 0.2 Jy. The RA and Dec. axes are offsets from the position of the submillimetre source, $\alpha(1950) = 19^h34^m35.7^s \pm 0.7^s$, $\delta(1950) = 07°27'15'' \pm 10''$.

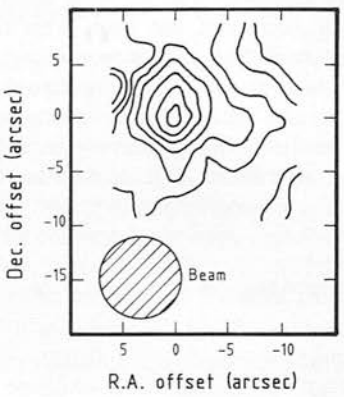

Figure 2. 450 μm map taken with an 8 arcsec beam. The lowest contour is at 1.1 Jy, and the contour interval is at 1σ intervals of 1.1 Jy. The RA and Dec. axes are offsets from the position of the submillimetre peak, as in Fig. 1.

The high-resolution 450 μm map is shown in Fig. 2, where the contours are at 1σ intervals of 1.1 Jy, and the peak is 9.8 Jy. This map covers the central 20 arcsec of the 800 μm map, and again approximating the source distribution to be Gaussian, the deconvolved source size is <6 arcsec in right ascension and 7.5 ± 2.0 arcsec in declination. Without fully resolving the source at several wavelengths we do not

have enough information to be able to model the effects of a temperature and density gradient, or the way in which the apparent source size varies as a function of frequency, so we will use the approximation of Gaussian distributions bearing in mind that such gradients are likely to exist. VLA $NH_3(1,1)$ observations (P. E. Palmer, quoted in Davidson 1987) also indicate a core size less than 15 arcsec. The position of the submillimetre source in B335 is $\alpha(1950) = 19^h34^m35.7^s \pm 0.7^s$, $\delta(1950) = 07°27'15'' \pm 10''$.

In order to compare the photometric data (Table 1) with earlier measurements made with larger beams, we have calculated the flux that would be obtained in a 50 arcsec Gaussian beam, by convolving the maps with suitably normalized Gaussian functions. In order to do this we have had to assume that the source distribution shown in the 800 μm map is approximately valid for all wavelengths $\lambda \geq 600$ μm, and that the source distribution shown in the 450 μm map is approximately valid for $\lambda = 350$ μm as well. There are some difficulties with this when using the 450 μm map, first because the diffraction-limited beam at 450 μm has non-Gaussian wings, and secondly because we did not map far enough to get entirely off the source. We have approximated the beam to be Gaussian and we have ignored any missed flux outside the region of the map. This results in large uncertainties in the flux in a 50 arcsec beam at 450 and 350 μm, but is a more reasonable estimate than would have been obtained had we assumed the same source distribution as at 800 μm. The results of this re-beaming are shown in Table 2. They are also plotted in Fig. 3, together with previous measurements from Keene *et al.* (1983), Gee *et al.* (1985) and fluxes from the IRAS *Point Source Catalog.*

Table 2. Simulated fluxes in a 50 arcsec beam.

Wavelength	Effective freq (GHz)	Flux in a 50″ beam (Jy)	Statistical uncertainty (Jy)	Total uncertainty (Jy)
2 mm	156	$3\sigma = 0.76$		
1.3 mm	238	1.20	0.08	0.14
1.1 mm	272	1.39	0.07	0.16
800 μm	380	4.06	0.13	0.62
600 μm	463	8.2	0.7	1.8
450 μm	676	19.1	1.7	7.6
350 μm	854	45	3	21

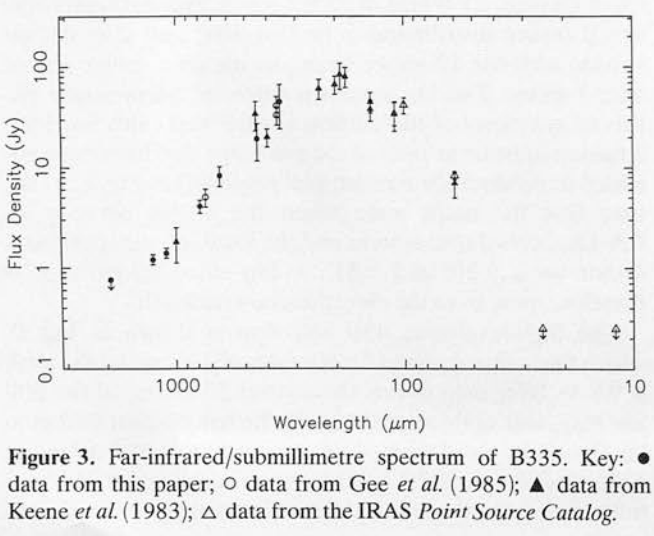

Figure 3. Far-infrared/submillimetre spectrum of B335. Key: ● data from this paper; ○ data from Gee *et al.* (1985); ▲ data from Keene *et al.* (1983); △ data from the IRAS *Point Source Catalog.*

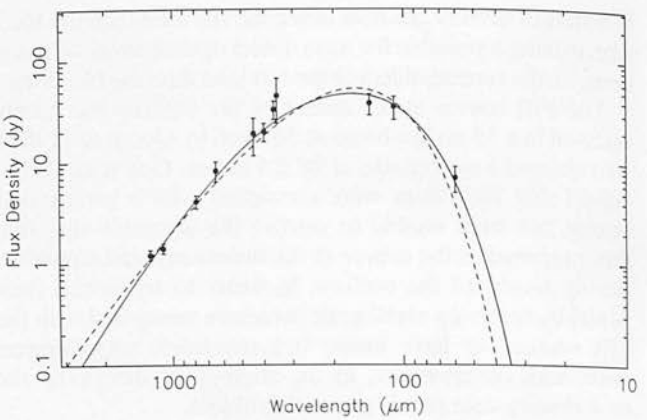

Figure 4. Data taken with beams ≤50 arcsec, together with the best optically thin fit $\Omega\tau B_\nu(23\ \mathrm{K})$, where $\tau \propto \nu^{1.0}$ (dashed line) and the best 'optically thick' fit $\Omega B_\nu(31\ \mathrm{K})(1-e^{-\tau})$, where $\tau \propto \nu^{1.6}$ (solid line).

If a steep density gradient exists then even the longer wavelengths will contain a significant contribution from the warmer dust responsible for the 60 μm emission, so all data taken with a beam size of ≤50 arcsec (11 points, Fig. 4), including the 60 μm point, have been used to try to obtain average parameters for the dust within the central region. If the usual assumption that the dust continuum emission is optically thin is made, a blackbody curve with $\tau \propto \nu^\beta$ $(1 < \beta < 2)$ does not fit the 60 μm point well (the best optically thin fit is the dashed line in Fig. 4). The results for this fit are $T = 23$ K, $\beta = 1.0$, $\Omega\tau_{450\,\mu m} = 1 \times 10^{-10}$ where Ω is the effective solid angle of the source in steradians, and $\chi^2 = 12.6$ with 11 data points and 3 free parameters. The source size in the 450 μm map then indicates that $\tau_{450\,\mu m} > 0.1$, and so the 'optimally thin' approximation is only valid (to within 20 per cent) for wavelengths $\gtrsim 100$ μm. However, if the same points are fitted to a blackbody curve modified by $(1-e^{-\tau})$ (i.e. making no assumptions about the optical depth of the emission) where $\tau \propto \nu^\beta$, we find a better fit ($\chi^2 = 6.3$ with 11 data points and 4 free parameters – the temperature, the optical depth, the frequency dependence of the optical depth β, and the source size), which is for $T = 31$ K (solid curve, Fig. 4). Integrating under this curve gives a luminosity of $\sim 2.6 L_\odot$. Within this model, which assumes a uniformly bright isothermal source, we find $\beta = 1.6$, $\tau_{450\,\mu m} = 1.7$, and a source area of 3.7 square arcsec. The optical depth (and implied column density) and the source size derived from such a fit are complicated mean values, and are difficult to interpret relative to the observed source. A lower limit to the temperature of $T = 15$ K is required to account for the Rayleigh–Jeans part of the spectrum including the observed emission at 350 μm.

The column and space molecular hydrogen number densities can be estimated from the dust continuum emission (Hildebrand 1983), although the gas-to-dust ratio has only been calibrated using interstellar clouds that are optically thin in the submillimetre. Using the Chicago assumptions of Hildebrand, we find that, for the extreme of our uniform source model of the spectrum, $N(H_2) \sim 1 \times 10^{29}$ m^{-2}, $n(H_2) \sim 1 \times 10^{15}$ m^{-3}, and the mass of the gas associated with the dust is $\sim 1.3 M_\odot$. This is in excellent agreement with the

mass obtained by Keene *et al.* (1983) of $\simeq 2.5 M_{\odot}$ (who used a temperature of 15 K) since, in the Rayleigh–Jeans region of the spectrum where the emission is optically thin, the flux is proportional to $M_{\rm dust} \times T_{\rm dust}$. Given that in fact a single temperature is unlikely to be a good approximation to the emitting dust, the mass derived from fitting the continuum spectrum with a single temperature is rather uncertain. However, to within the uncertainties of the calibration of the dust-to-gas ratio, these numbers indicate a core mass $M_{\rm core} \sim 2 M_{\odot}$. Associating this with the source in the 450 μm map, we find actual lower limits to peak values of $N(\mathrm{H_2}) \gtrsim 1 \times 10^{28}\ \mathrm{m^{-2}}$ and $n(\mathrm{H_2}) \gtrsim 5 \times 10^{13}\ \mathrm{m^{-3}}$.

4 DISCUSSION

4.1 The submillimetre source

The structure of the submillimetre continuum source has still not been fully resolved by our observations, but there is some evidence for an elongation NS, perpendicular to the axis of the outflow. The position of the source is the same as that found by Gee *et al.* (1985), which is 20 arcsec east of that given by Keene *et al.* (1983). This means that the peak in many molecular line maps (CS $J=2-1$; NH_3; HC_3N) *is* coincident with the dust continuum source; previously, it had been thought that the FIR source was *not* the significant HC_3N emitting region (Hasegawa *et al.* 1986), although a close association was suggested. One notable exception to the observed proximity between submillimetre emission and molecular line emission is the $C^{18}O$ peak (Walmsley & Menten 1987), which is ~ 30 arcsec away from the FIR source. This may be due to optical depth effects or pointing uncertainty, but within the specified pointing errors of both our observations and those of Walmsley & Menten, it seems that the $C^{18}O$ emission does not trace the same molecular gas as the dust continuum and other 'high-density' molecular line tracers. Velocity information on very small scales is needed to establish the true relationship of the cloud core, as traced by the submillimetre continuum and molecular emission, to the central exciting object.

If we try to classify the source in B335 according to the current models of pre-stellar evolution (e.g. Shu, Adams & Lizano 1987) then it has already passed the 'protostellar' phase and is now in its 'outflow' phase. This being the case, the remarkable property of this source is its low luminosity. The conditions in the surrounding cloud are very similar to those in the large-scale region of star formation in Taurus (i.e. an isothermal sound speed of ~ 0.2 km s^{-1} and rotation velocity of the cloud core of $\lesssim 10^{-14}$ rad s^{-1}), for which Adams (1989) has plotted theoretical tracks of protostellar evolution in a L–$A_{\rm V}$ diagram. Our measured value of L and derived value of $A_{\rm V}$ lie very close to the theoretical track, but in a region *before* outflow is supposed to have taken place. If these tracks are correct, then our results could mean that outflow is possible from objects much younger than the Shu *et al.* (1987) model expects, and the source in B335 represents an extremely early stage of protostellar evolution.

On the other hand, if B335 is not a young protostar, then the low luminosity and high extinction must be explained by some other reason. If the inclination angle of the outflow also defines the inclination angle of a disc or flattened core, then the anomalously high extinction could be due to the high column density of gas and dust in the disc plane, and the low luminosity could then be due to a more evolved object. It is possible for a source near the beginning of its outflow phase to have a lower luminosity than that predicted by Adams, Lada & Shu (1987) if the parameters they used for the Taurus molecular cloud are not applicable to an isolated globule such as B335, so that relative to Taurus the mass of the protostar-disc system is low and/or the accretion efficiency is low. Another possibility is that the source is much more evolved and is already well down its Hayashi track, but for some reason has remained deeply embedded, perhaps because the outflow is not energetic enough to have disrupted the surrounding cloud. If the latter is the case, then the stellar birthline of Stahler (1983) indicates that the luminosity of B335 is consistent with a pre-main-sequence star of mass $\leq 1.5 M_{\odot}$. The central exciting source in B335 is so deeply embedded [$A_{\rm V} \gtrsim 320$ mag using the conversion of $N(\mathrm{H_2})$ to $E(B-V)$ of Bohlin, Savage & Drake (1978) and the extinction law of Rieke & Lebofsky (1985)] that it will not even be observable in the near-infrared.

4.2 The relationship between the submillimetre source and the molecular outflow

The outflow associated with the FIR source in B335 has recently been identified as lying almost in the plane of the sky, and we observe it at an angle of $80° \pm 5°$ to the axis of the outflow. Therefore, the velocity, momentum, energy, force and mechanical luminosity of the outflow are now believed to be higher than had previously been thought. The revised parameters of the outflow have been calculated by HKNT, Cabrit *et al.* (1988, hereafter CGS) and Moriarty-Schieven & Snell (1989, hereafter M-SS), and we have used the results of all three papers to estimate the effect of the outflow on the core, and to try to constrain models for its collimation.

We consider several models for the driving source of the outflow and the collimation mechanism. First, models in which the flow is intrinsically bipolar require an anisotropic mechanism for the production of the wind. All such models require the presence of an accretion disc, the rotational energy of which is the source of the energy of the outflow. Torbett (1984) suggests that one mechanism for the production of a bipolar outflow is via the hydrodynamic ejection of material at the inner boundary of an accretion disc, producing pressure-driven winds that are intrinsically bipolar. Pudritz & Norman (1986) and Königl (1989) present arguments for hydromagnetic winds from accretion discs being the driving source of outflows. All of these models will require that the stored rotational energy of the disc be greater than the energy of the outflow in order for the disc to be able to supply the required energy to power the outflow. This assumes that we are considering a quasi-stationary system, and will not apply to a source if we happen to observe it just at the end of its outflow phase, when we might expect the rotational energy to be less than that of the outflow. As an example we consider a uniform Keplerian disc, and calculate the rotational energy that can be stored and used as an energy source for the outflow.

If the mass of the 'disc' (which we identify as being the mass of the submillimetre source) is $M_{\rm d}$, the radius of the disc is $R_{\rm d}$ (from the 450 μm map $R_{\rm d} = 1.4 \times 10^{14}$ m), M_* is the mass of the central young stellar object and G is the

Mon. Not. R. astr. Soc. (1990) **243**, 336–348

Carbon stars with silicate dust shells – I. Carbon stars with enhanced ^{13}C (J stars)

T. Lloyd Evans
South African Astronomical Observatory, PO Box 9, Observatory 7935, South Africa

Accepted 1989 September 15. Received 1989 September 13; in original form 1989 May 2

SUMMARY

New optical observations show that three southern carbon stars with silicate dust shells are J stars, in addition to two already known from the northern hemisphere. Four more J stars have similar red *IRAS* colours although infrared spectra are lacking. A review of published data suggests that all the carbon stars with silicate shells may be J stars. These dust shells are all very red and must be optically thick, yet the carbon stars are not conspicuously reddened at optical wavelengths. The infrared sources are not very variable, although the probability is high that a companion of such red colour would be a variable of large amplitude. It is suggested that material expelled from the carbon star, starting while it still had an oxygen-rich envelope, has accumulated in a disc around a hypothetical companion. The properties of J stars with silicate dust shells are consistent with this suggestion, while the unusual feature of the infrared sources are accounted for.

1 INTRODUCTION

The *IRAS* mission of 1983 provided spectra of approximately 4000 stars with dust shells (*IRAS* Science Team 1986) and most of those with diagnostic spectral features may be classified as O-rich (silicate features: Woolf & Ney 1969; Forrest, Gillett & Stein 1975) or C-rich (SiC emission: Treffers & Cohen 1974). The great majority of these *IRAS* spectral classifications are in agreement with the classification of the photospheric spectrum of the star at visible wavelengths but a few have the 'wrong' type of infrared spectrum for their visible-light spectrum. Carbon stars with silicate features in their infrared spectra present a challenge to current theories of stellar evolution and have been studied by several workers (Little-Marenin 1986; Willems & de Jong 1986, 1988; Nakada *et al.* 1987; Little-Marenin, Benson & Dickinson 1988; Deguchi *et al.* 1988; Chan & Kwok 1988; Vardya 1989a). The principal hypotheses suggested are:

(i) these stars are binaries in which the shell belongs to an M-type companion (Little-Marenin 1986), and

(ii) the stars are observed in a brief evolutionary stage after conversion from an M to a carbon star but before the oxygen-rich circumstellar shell of the former has had time to dissipate (Willems & de Jong 1986, 1988).

An especially striking result is that the two best-studied stars of this type are ^{13}C-rich carbon stars or J stars (Willems & de Jong 1986). This has led to the development of an alternative to the widely accepted M→S→C sequence of evolution on the asymptotic giant branch (Willems & de Jong 1988; Chan & Kwok 1988).

Few of the 20 carbon stars with silicate shells identified in the literature have been studied in detail, and initial examination of the data suggested that several had been included in error. Additionally, the *IRAS* LRS spectra (*IRAS* Science Team 1986) of the well-established examples are not typical of optically observable stars with silicate spectra. All have very strong, and in one case unusually broad, 9.7 μm emission superimposed on rather flat continua; the [12]–[25] colours are redder than those of most red variables found in the *General Catalogue of Variable Stars* (Kholopov *et al.* 1985). All these stars, as well as five additional examples which were noticed, have been re-examined to see whether their inclusion in the list of carbon stars with silicate shells is justified (Section 2). The *IRAS* data for the surviving examples are examined to place these stars in the context of stars with silicate shells in general (Section 3). Optical spectroscopy of three possible southern examples is used to check the association of silicate shells with ^{13}C-rich carbon stars (Section 4). An expanded list of ^{13}C-rich carbon stars has been compared with the *IRAS* catalogue to search for additional examples of such stars (Section 5). Finally, the available data are discussed in terms of possible models (Section 6).

2 Reclassification of LRS spectra

The Low Resolution Spectra obtained with the *IRAS* satellite were classified on a two-digit scheme, in which the digits were assigned by computer to characterize the overall shape of the spectrum and to give quantitative information on the

Mon. Not. R. astr. Soc. (1989) **237,** *Short Communication,* 1P–6P

CS($J=7-6$) from heated gas near the embedded sources in NGC 2024

T. J. T. Moore and C. J. Chandler *Department of Astronomy, University of Edinburgh, Blackford Hill, Edinburgh EH9 3HJ*

W. K. Gear and C. M. Mountain *Royal Observatory, Blackford Hill, Edinburgh EH9 3HJ*

Accepted 1988 November 21. Received 1988 November 3

Summary. CS ($J=7-6$) observations of NGC 2024, at 15-arcsec resolution, show strong emission closely associated with the recently identified submillimetre continuum sources. Significant excitation of this line indicates the presence of localized regions of dense, heated molecular gas and implies that the continuum peaks contain heavily-obscured luminous stellar cores. A lower limit of 28 K is obtained for the line excitation temperature from the observed line strengths. A re-analysis of existing continuum data predicts an effective dust temperature of $T_d=47$ K over the whole region. Lower limits of $\sim 3\times10^{26}$ m^{-2} are derived for the column density of heated molecular hydrogen toward each continuum source, assuming $T_{ex}=T_d$ and optically thin lines. There is some evidence for significant optical thickness in $J=7-6$ toward at least two of the sources.

1 Introduction

In a recent paper, Mezger *et al.* (1988) (hereafter M88) presented high-resolution maps of the 1300-μm dust emission from the cloud core region of NGC 2024 and reported six new sources, previously undetected by far-infrared and low-resolution molecular line studies. By using a three-component model of the 12-μm to 1300-μm continuum, these new objects were interpreted as high-density ($n_H\sim10^{14}$–10^{15} m^{-3}), cold ($T_d\sim16$ K), isothermal condensations without luminous stellar cores, i.e. true protostars.

The time-scale for the isothermal phase of protostar development (e.g. Nakano 1985) is likely to be significantly shorter than the sound-crossing time of the cloud ($\sim10^6$ yr). The presence of six sources in roughly the same evolutionary state thus implies simultaneous formation, presumably by contraction and fragmentation of the entire cloud. To find out more about the evolutionary state of the new sources and the physical conditions in their vicinity, we have observed the region at 15-arcsec resolution in the $J=7-6$ transition of CS (detected in a large beam by Evans *et al.* 1987), mapping the distribution of warm gas and determining its relationship to the submillimetre cores.

2 Observations and results

The observations were made with the 15-m James Clerk Maxwell Telescope (JCMT) on Mauna Kea, Hawaii, during the nights of 1988 September 8–11, with the common-user, 345 GHz Schottky receiver and a 1024-channel AOS backend. Fully sampling with an 8-arcsec regular grid, we have mapped an area containing all six FIR sources identified by M88 and covering most of the dark cloud core region. The beam size at 343 GHz was 15 arcsec. The results are shown as maps of integrated antenna temperature (T_A^*) in Fig. 1(a)and peak T_A^* in Fig. 1(b). It should be noted that the portion of the map covering the northernmost continuum source, FIR 1, is not well sampled. Only two data points were obtained to the north of this object.

The values of peak T_A^* toward each of the M88 sources covered by Fig. 1 are listed in Table 1. For conversion to the T_R^* scale, the forward scattering efficiency is $\eta_{fss} = 0.8$. Total on-source integration time per point was 60–90 s, yielding mean rms noise levels of 1.2 K per 488-kHz channel. The 1σ noise in Fig. 1(a) is 0.3 K kms^{-1}. Calibration was done via an internal rotating hot load. Absolute pointing was checked at intervals of about 45 min against the molecular line peak in OMC-1 (Masson *et al.* 1987) and the rms error was less than 3 arcsec throughout.

3 Discussion

3.1 THE WARM MOLECULAR GAS

Fig. 1 shows clearly that the warm molecular gas traced by CS($J=7-6$) ($J=7$ is at $E/k=66$ K above the ground state) is localized at or very near the positions of the submillimetre condensations reported by M88. This implies that there are discrete regions of heated gas associated with each of FIR 2–6, and hence that there are probably self-luminous heating sources within each core. A relatively advanced state of evolution in FIR 6 is also inferred by its close proximity to the origin of an extensive bipolar molecular outflow (Sanders & Willner

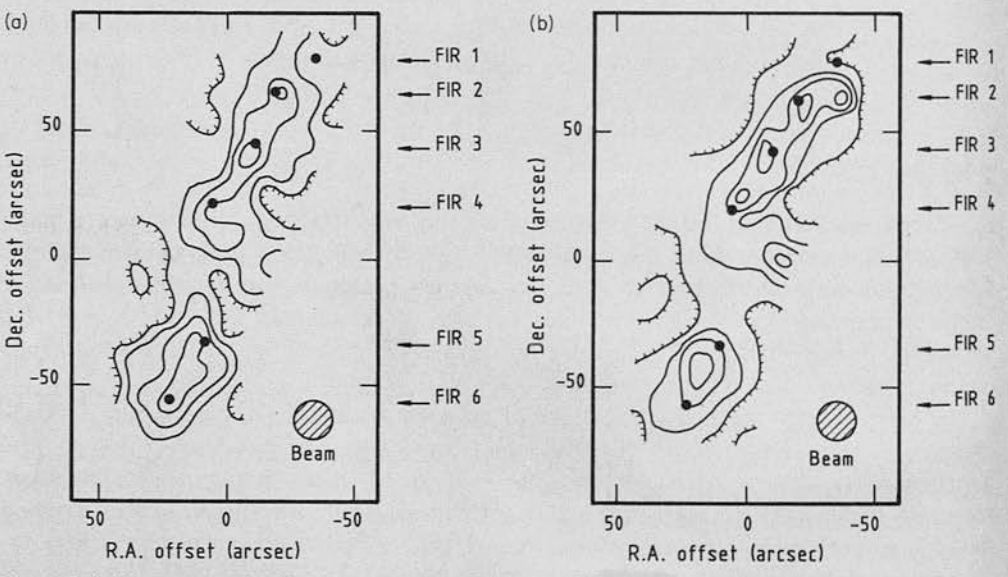

Figure 1. (a) Integrated CS($J=7-6$) emission ($\int T_A^*(V)\,dV$) in NGC 2024. Contours are drawn at 5, 10, 15 and 20 K km s^{-1}. The 1σ noise level is around 0.3 K km s^{-1}. The offset centre is $5^h39^m12\overset{s}{.}2 - 1°56'30''$ (1950). (b) Contours of peak T_A^* at intervals of 1.5 K from 3 K. The mean 1σ noise level is ~0.8 K.

Table 1. Observed and derived parameters toward FIR sources.

source	peak T_A^* /K	$\int T_A^*(V)dV$ /Kkms^{-1}	T_{ex}^c /K	N_{7-6}^{CS} /$10^{17}m^{-2}$	V_0 /kms^{-1}	m^d (1300 μm) / $M_\odot$
FIR 1	2.9	6.0	13.9	0.9	8.2	1.9
FIR 2	7.9[a]	20.2[a]	27.2	3.1	8.0	2.0
FIR 3	8.4[a]	21.8[a]	28.5	3.3	10.0	6.5
FIR 4	8.1[a]	16.8[b]	27.7	2.5	8.3	4.9
FIR 5	5.8	20.0[a]	21.7	3.0	9.3	10.5
FIR 6	6.1	22.3	22.5	3.4	11.2	4.3

[a]Value from nearest peak (Fig. 1) if within one beam radius. [b]Values from peak T_A^* position. [c]Lower limit for high optical depth and filling factor (see text). [d]Hydrogen masses from M88, adjusted for $T_d = 47$ K, $\beta = 1.60$.

1985) and an H_2O maser (Genzel & Downes 1977), the latter being frequently associated with energetic outflow sources. The only continuum source without a nearby peak in T_A^* or $\int T_A^*(V)\,dV$ is the faintest (at 1300 μm) and most northern object, FIR 1. This may indicate a lack of warm gas at this position, but the map is not well-sampled in this area and further observations may be required of this object.

A lower limit to the effective line excitation temperature (T_{ex}) can be estimated from the LTE formula for radiation temperature:

$$T_R = \frac{h\nu}{k}[(e^{h\nu/kT_{ex}} - 1)^{-1} - (e^{h\nu/2.7k} - 1)^{-1}] \times (1 - e^{-\tau}),$$

which means that for CS($J = 7-6$):

$$T_{ex} \simeq \frac{16.5}{\ln[1 + 16.5(1 - e^{-\tau})/T_R]}.$$

T_R can be derived from $T_R = T_R^*/\eta_c$, where η_c is the source coupling efficiency and contains the beam filling factor f. Since the true value of f is very uncertain, assuming a value for η_c of 0.5 provides a reliable lower limit of $T_{ex} \geq 28$ K towards the line peak near FIR 3, the equality holding where the transition optical depth is large and f is close to unity. $T_{ex} \geq 28$ K is thus consistent with the average 60/100 μm colour temperature of 45 K calculated by Thronson *et al.* (1984), but not with the dust temperature of 16 K inferred by M88 for the submillimetre cores.

Evans *et al.* (1987), observing in a 73-arcsec beam, find $T_R(7-6)/T_R(6-5) \simeq 0.7 \pm 0.2$. If the optical depth in the lines is low this implies a value for T_{ex} of 25^{+15}_{-10} K. The optically thin, high-temperature limit to the line ratio is 1.36, so a low value (< 1) can be explained by: (i) cool optically thin gas; (ii) a steep, inward-increasing temperature gradient in hot ($T_{ex} \gg 50$ K), optically thick gas; (iii) a steep, outwardly increasing temperature gradient in cool ($T_{ex} < 50$ K), optically thick gas or (iv) dilution in the large beam. The latter possibility is the most likely, especially if the $J = 6-5$ emission is more extended than the $J = 7-6$. The value of T_{ex} derived from the line ratio therefore serves as a lower limit to the effective value for the compact FIR sources. Since the critical density of the $J = 7-6$ transition is $n_{crit} \simeq 2 \times 10^{13}\,m^{-3}$, it is likely that the gas and dust are thermally well coupled where this line is detectable. We therefore find

it reasonable to assume that $T_d \simeq T_{ex}$ and adopt $T_{ex} = 47$ K from the dust temperature obtained below. This value implies optical depths of $\tau_{7-6} \simeq 0.7$ from the measured line strengths, if no self absorption is present.

The LTE formula for the CS column density producing the $J = 7 - 6$ line is:

$$N^{CS}_{7-6}(\mathrm{m}^{-2}) = 1.79 \times 10^{15} \times (1 - e^{-16.5/T_{ex}})^{-1} \times \frac{1}{\eta_c \eta_{fss}} \int T^*_A(V)\, dV.$$

This produces values in the range $(2.5\text{–}3.4) \times 10^{17}\,\mathrm{m}^{-2}$ for FIR 2–6 and total molecular hydrogen column density estimates of $(2.5\text{–}3.4) \times 10^{26}\,\mathrm{m}^{-2}$ (see Table 1), assuming a relative CS abundance of 10^{-9} (Snell *et al.* 1984) and a filling factor of unity. In order to produce space densities of order n_{crit} for significant excitation of optically thin $J = 7 - 6$, the linear extent of the emitting regions must be as small as $\sim 10^{13}$ m. However, if the line is significantly optically thick, the density need not be as high as n_{crit} since radiative trapping maintains the level population above the collisional excitation rate. Evans *et al.* (1987) obtained beam-averaged densities of around $10^{12}\,\mathrm{m}^{-3}$ by modelling the radiative transfer in the LVG approximation. If these densities are appropriate to the compact sources, τ_{7-6} may be as high as 10. If this is the case, then $T_{ex} = 28$ K must apply to the cooler outer layers of the emitting gas in the cores.

While the line emission from the northern part of the cloud (associated with FIR 1–4) is essentially unresolved (Fig. 1), the southern emission around FIR 5 and 6 seems to be slightly larger than the beam. A relatively large source size and low derived H_2 column density therefore implies either a low CS abundance or high optical depth in the line. There is some evidence for high τ_{7-6} toward FIR 5 and 6 in the comparison of integrated T^*_A (Fig. 1a), which peaks on or close to the continuum in each case, and peak T^*_A, which does not. This may be caused by self-absorption in the line emission toward the source positions; self-reversal in the foreground material is likely to affect an optically thick emission line. High line optical depths mean that N_{H_2} is under-estimated by a factor $\tau/(1 - e^{-\tau})$ and self-reversal produces under-estimates of T_{ex} when derived from the peak line temperature.

3.2 THE (SUB)MILLIMETRE CONTINUUM

M88 fitted a three-component greybody to the available continuum data for NGC 2024, setting the dust emissivity exponent at $\beta = 2.0$. In the resulting model the integrated emission at 350 μm and beyond is dominated by a large 16 K component. All the warm dust is assumed to be in a diffuse envelope surrounding cold cloud cores, contributing little to the mass and column density. Adopting a value for T_d as low as 16 K for the discrete sources implies large submillimetre optical depths, H_2 column densities and masses; however, the model adopted by M88 for the flux density distribution is not unique. If the constraint that the dust emissivity be proportional to $\nu^{2.0}$ is lifted, it is possible to obtain a very good fit (reduced $\chi^2 = 0.4$) to the same data using a simple, single-temperature model, parameterized by $T_d = 47$ K, $\beta = 1.60$ and a 350-μm optical depth of 0.06 (Fig. 2).

Since NGC 2024 contains visible hot stars, a large blister H II region and an extended CO outflow, it is evident that the disruptive formation of, and heating by massive stars has been occurring for a considerable period of time. It is likely, therefore, that warm gas and dust will have pervaded the entire region. In addition, cloud cores in regions of massive star formation are observed to be considerably warmer ($T \sim 40$ K) than those forming exclusively low-mass stars (see Shu, Adams & Lizano 1987 for a review). Since no spectral data are available for the individual FIR objects, we can only model source-averaged parameters from the integrated emission across the whole cloud. A single-temperature model, while not being any more of a unique physical description, is less subject to detailed ambiguities than a multi-component fit.

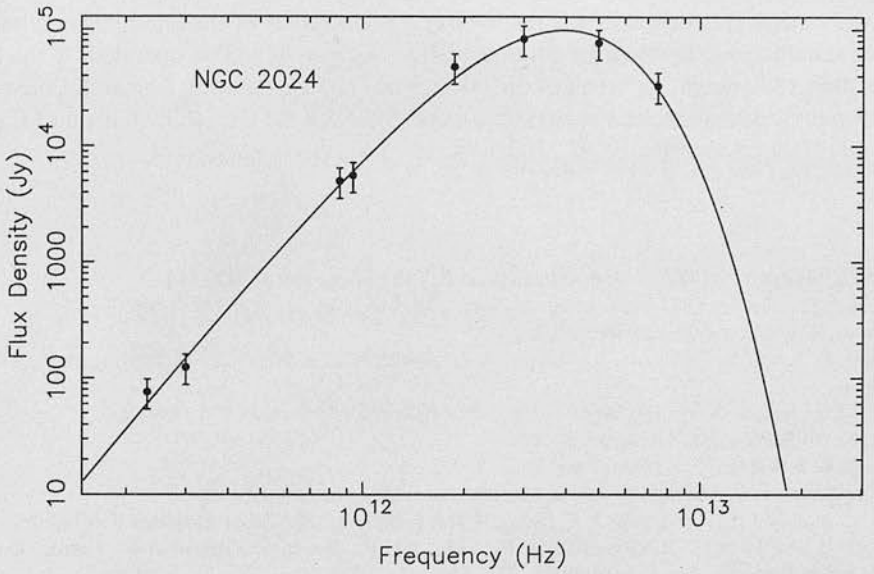

Figure 2. Single-temperature greybody fit to the integrated flux density distribution of NGC 2024. The fit parameters are $T_d = 47$ K, $\beta = 1.60$, $\tau_{350\,\mu m} = 0.06$. The data points are from Mezger *et al.* (1988) (M88). Related χ^2 for the fit is 0.4.

Using the dust-to-gas conversion from Hildebrand (1983), a 47 K single-temperature model with $\beta = 1.6$ reduces the optical depths and hydrogen column densities, derived by M88 from their 1300 μm and 350 μm data, by factors of 5.9 and 8.2, respectively (see Table 1). M88, assuming $T_d = 16$ K, find hydrogen column densities in the extended emission up to six times larger than derived from previous molecular observations (especially Snell *et al.* 1984). This discrepancy, interpreted as a decrease in molecular abundances and an increase in dust cross-section in cold, dense regions, is virtually eliminated by adopting a dust temperature near 50 K.

Further observations (e.g. in other high-excitation lines of CS and high-resolution submillimetre continuum mapping) would help to fill in the unknowns encountered above, especially the uncertain line optical depths, effective excitation temperatures and the variation in temperature and density conditions between the embedded FIR sources.

4 Conclusions

We have mapped the cloud core region of NGC 2024 in the $J = 7 - 6$ line of CS. Strong emission, closely associated with five out of the six known millimetre continuum sources, indicates localized regions of heated dense gas. Consequently, the compact continuum cores are likely to contain self-luminous heating sources and be in a rather more advanced evolutionary state than previously thought. A lower limit of 28 K is obtained for the CS($J = 7 - 6$) excitation temperature from the observed line strengths. A re-analysis of existing continuum data predicts an effective dust temperature of $T_d = 47$ K over the whole region. Lower limits of $\sim 3 \times 10^{26}$ m^{-2} are derived for the molecular hydrogen column density toward five continuum sources, assuming $T_{ex} = T_d$ and optically thin lines. There is some evidence for significant optical depth in $J = 7 - 6$ toward at least two of the sources.

Acknowledgments

Thanks are due to Saeko Hayashi and Takuya Yamashita for discussing the observations with us, and to Charles Cordell for excellent help during the observing run. Rachael Padman and

Richard Prestage are acknowledged for provision and support of the line reduction package SPECX and Marjorie Fretwell for producing the diagrams. JCMT is operated by the Royal Observatory, Edinburgh, on behalf of the UK Science and Engineering Research Council, the Netherlands Organisation for Pure Research and the National Research Council of Canada. TJTM and CJC acknowledge SERC studentships.

References

Evans, N. J., Mundy, L. G., Dais, J. H. & Vanden Bout, P., 1987. *Astrophys. J.*, **312,** 344.
Genzel, R. & Downes, D., 1977. *Astr. Astrophys. Suppl.*, **30,** 145.
Hildebrand, R., 1983. *Q. Jl R. astr. Soc.*, **24,** 267.
Masson, C. R., Lo, K. Y., Phillips, T. G., Sargent, A. I., Scoville, N. Z. & Woody, D. P., 1987. *Astrophys. J.*, **319,** 446.
Mezger, P. G., Chini, R., Kreysa, E., Wink, J. E. & Salter, C. J., 1988. *Astr. Astrophys.*, **191,** 44.
Nakano, T., 1985. *Publs astr. Soc. Japan*, **37,** 69.
Sanders, D. B. & Willner, S. P., 1985. *Astrophys. J.*, **293,** L39.
Shu, F. H., Adams, F. C. & Lizano, S., 1987. *Ann. Rev. Astr. Astrophys.*, **25,** 23.
Snell, R. L., Mundy, L. G., Goldsmith, P. F., Evans, N. J. & Erickson, N. R., 1984. *Astrophys. J.*, **276,** 625.
Thronson, H. A., Lada, C. J., Schwartz, P. R., Smith, H. A., Smith, J., Glaccum, W., Harper, D. A. & Loewenstein, P. F., 1984. *Astrophys. J.*, **280,** 154.

Mon. Not. R. astr. Soc. (1989) **241**, *Short Communication*, 19P–24P

Near-infrared observations of NGC 2024: identification of a 2-μm source within a dense core

T. J. T. Moore *Physics Department, Queen Mary College, London University, Mile End Road, London E1 4NS*

C. J. Chandler *Department of Astronomy, Edinburgh University, Blackford Hill, Edinburgh EH9 3HJ*

Accepted 1989 August 21. Received 1989 August 11

Summary. We have detected a 2-μm continuum source within one of the six dense cores in NGC 2024 found by Mezger *et al.* and interpreted as cold, isothermal protostars. The new source is highly reddened ($H-K \geq 3.8$) and quite faint ($S_K = 8.3 \times 10^{-15}$ Wm^{-2} μm^{-1}) and provides clear evidence that at least one of these cores contains a hot, embedded young star. Accompanying the point-like near-infrared source is a compact unipolar nebula which has features common to the infrared reflection nebulae associated with outflows from young sources.

1 Introduction

Six dense cores (FIR1–6) were found in NGC 2024 by Mezger *et al.* (1988; hereafter M88), from high-resolution observations in the 1.3-mm continuum, and identified as cold (~ 16 K) protostellar condensations. Recent observations in CS ($J=7-6$), however, have shown that the dense ($\sim 10^{13}$ m^{-3}) molecular gas associated with these cores is warm ($\gtrsim 30$ K, Moore *et al.* 1989), indicating the presence of a source of heat, but not ruling out the external heating of cold cores by radiation from the large, optical H II region. This paper presents the results of near-infrared continuum observations in the NGC 2024 region at medium sensitivity and with high spatial resolution, undertaken as a search for evidence of hot, embedded stellar sources within the millimetre-continuum cores.

2 Observations

The observations were made on behalf of the authors as part of the Service Observing Programme at the 3.8-m UK Infrared Telescope (UKIRT) on Mauna Kea, Hawaii, on 1988 October 24 with the common-user near-infrared array camera IRCAM 1. The camera was operated at the scale of 1.24 arcsec per pixel, giving coverage of a 77×72 arcsec^2 area on the sky. Exposures were taken, without sky chopping, through broad-band filters at J(1.25 μm), H(1.65 μm) and K(2.2 μm) towards $05^h39^m11^s.5$, $-01°55'47''$ (1950). Calibration

observations were made using the infrared flux standard HD 40335, assuming $J = 6.55$ mag, $H = 6.47$ mag and $K = 6.45$ mag. The absolute calibration accuracy is estimated as approximately 10 per cent. After subtraction of the dark current from the image frames, pixel-to-pixel response variations were divided out using flat-field frames of nearby sky (at offset +10 arcmin in RA). 60 s on-source integrations yielded rms noise levels $(4.8, 3.3, 1.8) \times 10^{-17}$ $\mathrm{Wm^{-2}\ \mu m^{-1}}$ (0.025, 0.030, 0.029 mJy) per pixel at J, H and K, respectively. The spatial resolution of the observations is seeing-limited, stellar images having half-power sizes of ~2.2 arcsec at all three wavelengths. The absolute pointing accuracy of the observations is approximately 2 arcsec.

3 Results

Fig. 1 shows a 2.2-μm surface brightness map of the field around the northern group of 1.3-mm cores, FIR1–4. The sources detected in this frame are listed in Table 1, with K flux densities plus $H-K$ and $J-H$ colours, where available. Fig. 2 displays the area around the core FIR4 at K and H, showing an unresolved 2-μm object within 2 arcsec of the millimetre-continuum peak. This source is not detected at H or at J. Photometry in a 5-arcsec circular aperture gives a K flux density of $S_K = 8.3 \times 10^{-15}$ $\mathrm{Wm^{-2}\ \mu m^{-1}}$, taking a base level in the surrounding diffuse emission at 3.7×10^{-16} $\mathrm{Wm^{-2}\ \mu m^{-1}}$ per pixel. A 3σ upper limit to the peak surface brightness of FIR4 at H gives a lower limit to the $H-K$ colour index of ≥ 3.8 mag.

Associated with the 2-μm point source in FIR4 is a bright, compact patch of extended emission about 6×4 arcsec in size. This small nebulosity is clearly visible at H and K but was only weakly detected at J. In a 10-arcsec aperture, the mean colours in the nebula are $J-H = 1.8$ mag and $H-K = 1.3$ mag, considerably bluer than the source itself.

4 Discussion

The weak 2-μm point source in Fig. 2(a) can be confidently identified with the dense core NGC 2024 FIR4. Within the pointing accuracy of the present observations, the near-infrared

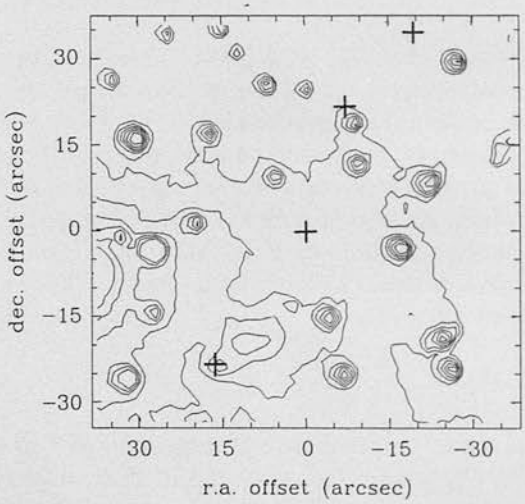

Figure 1. 2.2-μm continuum in the northern region of NGC 2024. The surface brightness contours are at (3.0, 4.7, 7.5, 11.9, 18.9 and 30.0) $\times 10^{-16}$ $\mathrm{Wm^{-2}\ \mu m^{-1}}$ per 1.24-arcsec pixel. The offset centre is $05^h39^m11\overset{s}{.}5$, $-01°55'47''$ (1950). The spatial resolution is seeing-limited at 2.2 arcsec. The bright object off the eastern edge of the field is the near-infrared star NGC 2024 #2 (Grasdalen 1974). The positions of the 1.3-mm peaks (M88) are marked by crosses.

Table 1. Results of 1- to 2-μm photometry.

Object	Offset[a] /arcsec		S_K /Wm^{-2} μm^{-1}	H–K /mag	J–H /mag	Aperture /arcsec
1	+32,	−26	3.5×10^{-14}	1.7	4.3	5
2	−7,	−25	1.6×10^{-14}	1.4	2.9	5
3	−26,	−24	9.7×10^{-15}	2.2	3.3	5
FIR-4	+15,	−24	8.3×10^{-15}	3.8*	–	5
5	−25,	−19	1.6×10^{-14}	1.6	3.1	5
6	−5,	−15	1.6×10^{-14}	1.1	2.7	5
7	+26,	−14	1.2×10^{-14}	1.1	2.8	5
8	+1,	−12	1.4×10^{-15}	1.4	2.6*	5
9	+26,	−4	3.7×10^{-14}	0.5	2.7	5
10	−17,	−2	2.1×10^{-14}	1.4	3.4	5
11	+32,	−1	7.0×10^{-15}	1.5	3.5*	3
12	+19,	+1	9.8×10^{-15}	1.6	2.8	5
13	−24,	+9	1.3×10^{-14}	1.7	3.6	5
14	+5,	+10	5.8×10^{-15}	3.1	1.6*	5
15[b]	−35,	+12	5.8×10^{-15}	–	–	5
16	−10,	+12	8.5×10^{-15}	0.8	2.3	5
17	+30,	+16	2.3×10^{-14}	2.4	3.5*	5
18	+16,	+17	5.3×10^{-15}	2.5	2.8*	5
19	−10,	+19	5.8×10^{-15}	1.7	2.3	5
20	−1,	+25	2.5×10^{-15}	2.0	2.0*	5
21	+6,	+26	4.5×10^{-15}	2.4	2.3*	5
22	+33,	+26	2.7×10^{-15}	1.8	2.3*	5
23	−29,	+30	7.2×10^{-15}	1.8	3.3*	5
24	+11,	+31	1.7×10^{-15}	1.6	1.7	5
25	+24,	+35	1.7×10^{-15}	2.3	1.7*	5
26	+14,	+36	2.5×10^{-15}	2.4	1.9*	4

[a]Offset from $05^h35^m11\overset{s}{.}5$, $-01°55'47''$ (1950) in Fig. 1.
[b]Not included in *H* or *J* frame.
*3σ lower limit.

object is coincident with the 1.3-mm position quoted by M88. Further, although the density of near-infrared sources in the region is large and the probability of a chance association relatively high, the FIR4 candidate is considerably more reddened than any other object found nearby. The mean $H-K$ colour of all detected sources (Table 1) is 1.7 mag, with a standard deviation of 0.6 mag. The observed lower limit to the $H-K$ colour of FIR4 is thus already more than 3σ larger than the mean. This is consistent with the most favoured physical model of the region (Thronson *et al.* 1984; Crutcher *et al.* 1986; M88) which places the 1.3-mm cores in the densest part of the molecular cloud, behind the H II region. Hence these objects suffer greater extinction than the stars associated with the H II region itself, which are obscured only by the

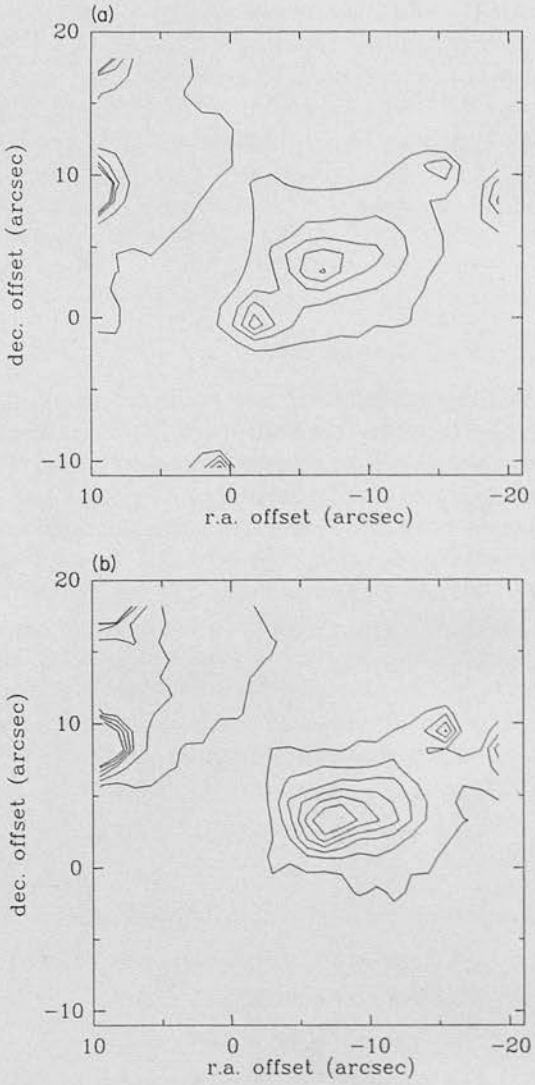

Figure 2. (a) 2.2-μm surface brightness around FIR4. The contours are drawn at (6.0, 9.0, 12.0, 15.0 and 18.0)$\times 10^{-16}$ Wm^{-2} μm^{-1} per 1.24-arcsec pixel. The offset centre is the position of the 1.3-mm continuum peak FIR4 found by M88: $05^{h}39^{m}12\overset{s}{.}6$, $-01°56'10''$ (1950). The spatial resolution is seeing-limited at 2.2 arcsec. (b) The same region at 1.65 μm. Contours are at (3.5, 5.0, 6.5, 8.0, 9.5 and 11.0)$\times 10^{-16}$ Wm^{-2} μm^{-1} per pixel.

foreground cloud (seen as a dark lane in optical photographs; see, for example, Balick 1976). The new 2-μm source is also the only object clearly associated with localized extended emission, even though the region contains a large amount of diffuse emission associated either with NGC 2024 #2 (the very bright 2-μm star found by Grasdalen 1974; see Fig. 1), or with the compact H II condensation 'NCP' (Crutcher *et al.* 1986).

The presence of near-infrared emission from an otherwise apparently cold cloud core is a clear indication that the core in fact possesses a hot stellar source deeply embedded within it. The cold ($\sim$16 K) isothermal condensations postulated by M88 would be completely undetectable at 2 μm and the external layers of such objects are unlikely to be heated to sufficiently high temperatures (a few$\times$100 K) by a diffuse radiation field. In addition, the 2-μm

source is <2 arcsec (<1000 AU at 450 pc) in size and, since the observed dimensions of the dust core are approximately 8×4 arcsec (M88), it is clear that the near-infrared emission cannot be from an externally heated layer around an otherwise cold condensation.

Since the total core mass is only $\sim5M_{\odot}$ (Moore *et al.* 1989), the bolometric luminosity of an embedded stellar source is unlikely to be larger than a few $\times\,100L_{\odot}$. This gives a rough upper limit to the K-band luminosity since, for a blackbody observed through a K filter with passband width 0.4 μm, $L_K/L_{\rm bol}$ must be $\lesssim0.13$. Hence, from the observed K flux density, we obtain a rough upper limit to the extinction toward the source within FIR4 of $A_K\lesssim9$ mag, which implies $A_V\lesssim80$ mag, using the extinction law of Rieke & Lebofsky (1985). The corresponding foreground molecular hydrogen column density is $N(\mathrm{H_2})\lesssim7.5\times10^{26}$ m^{-2} (from the standard conversion of Bohlin, Savage & Drake 1978), which is roughly consistent with the total line-of-sight value obtained by Moore *et al.* (1989) for FIR4 and with the extinction derived by Snell *et al.* (1984).

The 8.4-μm map by Grasdalen (1974) and the mid- and far-infrared observations of Thronson *et al.* (1984) show no sign of mid-infrared counterparts to the 1.3-mm sources. M88 have suggested that this lack demands that a low-temperature mass component, traced only by the (sub)millimetre continuum, dominates in the six dense cores. However, the core sizes obtained by M88 indicate that dust temperatures $\gtrsim50$ K would be required for 3σ detections of optically thick sources in the 40-μm and 60-μm maps of Thronson *et al.* and $\gtrsim40$ K to be detected at 100 μm. In other words, even relatively warm dust condensations would have escaped detection.

A peak 60-μm optical depth of $\tau_{60}=0.3$ was calculated by Thronson *et al.* (1984) using a 50-arcsec beam but, since this value is likely to be an average over large amounts of extended and much more optically thin emission, τ_{60} is probably much higher in the spatially compact cores. Our rough extinction limit of 9 mag at 2 μm is consistent with $\tau_{60}=0.3$ but only applies to FIR4 which, since it is the only one detected in the near-infrared, is probably the least obscured of all the cores. On the other hand, near-infrared emission from sources with high optical depths out to mid-infrared wavelengths may be enhanced by high scattering efficiencies in the 1-μm to 3-μm range and by the effects of strong forward scattering by large dust grains (Moore 1989). Also, the distribution of extinguishing material may be anisotropic, and the possibility of detection may depend on the orientation of the source.

The patch of bright extended emission associated with the new near-infrared source of FIR4 (Fig. 2) closely resembles the type of infrared reflection nebula associated with high-velocity molecular outflows, although on a small scale. The nebula is unipolar rather than symmetrically bipolar and the extended emission is much less reddened than the source, but these features are common (e.g. GSS30 in Ophiuchus, Castelaz *et al.* 1985; SGS1 in NGC 1333, Castelaz *et al.* 1986; GGD27, Yamashita *et al.* 1987; R Mon, Aspin *et al.* 1988 & Yamashita *et al.* 1989). Since such nebulae are thought to arise from photons scattered in the compressed dusty shell around a collimated outflow from the central object, it is plausible that FIR4 is generating a similar but smaller outflow.

Comparatively unreddened near-infrared light is scattered in such nebulae towards the observer, after emerging through a region of reduced extinction, perhaps directly caused by the outflow. The scattered light may become even bluer in colour if the wavelength-dependent grain albedo falls rapidly beyond ~1 μm (as predicted by Draine & Lee 1984). The common asymmetry of reflection nebulae is often explained as being due to (and used as evidence for) the presence of a large interstellar disc around the central source, tilted so as to obscure and redden both the source and the far lobe of the nebula. Strong forward scattering of near-infrared radiation by large dust grains may also contribute to the almost universal suppression of the backward-directed lobe in bipolar reflection nebulae (Moore 1989).

Within FIR4 there appears to be a heavily extinguished, low-mass stellar object which may be producing a compact collimated outflow. This description suggests a very unevolved T-Tauri star, a type of object frequently associated with massive winds and outflows throughout much of its early development.

The current observations provide no evidence of near-infrared radiation from the other northern FIR cores. The source ~4 arcsec south-west of FIR2 (Fig. 1) is unlikely to be a true association; the offset is twice the 1σ positional uncertainty of the present data. Although the object is somewhat reddened ($J-H=2.3$, $H-K=1.7$), it is unresolved and its size and colour are not distinguishable from a number of unrelated nearby sources in the larger observed area. This object, like the other similar sources nearby, is most likely to be one of the cluster that includes the main ionizing sources for the optical H II region.

Since, as observed in the millimetre continuum, FIR4 is qualitatively no different from the five other FIR cores found by M88, there are two plausible conclusions which may be drawn from the detection of near-infrared emission and the inferred presence of a hot central source in only one of the four observed. We consider it most likely that the sources which are currently undetected in the near-infrared also contain hot cores, but are too deeply embedded and too faint to have been found by the present observations. Alternatively, if some or all of the undetected cores are subsequently found to be true cold protostars, it is clearly demonstrated that it is not possible to determine the nature of a young embedded source on the basis of only far-infrared and (sub)millimetre observations. In order to discount either possibility, more sensitive observations are required in the near-infrared and mid-infrared continuum, especially between 5 and 20 μm, where extinction is significantly reduced and where a hot dust spectrum should peak. Near-infrared polarimetry will be required to support our postulation that the nebulosity associated with FIR4 is due to scattered light in an outflow-associated reflection nebula.

Acknowledgments

We thank Andy Longmore, Tim Hawarden and Tom Geballe for approving and performing the UKIRT Service observations. UKIRT is operated on behalf of the UK Science & Engineering Research Council by the Royal Observatory, Edinburgh. CJC acknowledges the support of a SERC Studentship.

References

Aspin, C., McLean, I. S., Rayner, J. T. & McCaughrean, M. J., 1988. *Astr. Astrophys.*, **197,** 242.
Balick, B., 1976. *Astrophys. J.*, **208,** 75.
Bohlin, R. C., Savage, B. D. & Drake, J. F., 1978. *Astrophys. J.*, **224,** 132.
Castelaz, M. W., Hackwell, J. A., Grasdalen, G. L., Gehrz, R. D. & Gullixson, C., 1985. *Astrophys. J.*, **290,** 261.
Castelaz, M. W., Hackwell, J. A., Grasdalen, G. L. & Gehrz, R. D., 1986. *Astrophys. J.*, **300,** 406.
Crutcher, R. M., Henkel, C., Wilson, T. L., Johnson, K. J. & Bieging, J. H., 1986. *Astrophys. J.*, **307,** 302.
Draine, B. T. & Lee, H. M., 1984. *Astrophys. J.*, **285,** 89.
Grasdalen, G. L., 1974. *Astrophys. J.*, **193,** 373.
Mezger, P. G., Chini, R., Kreysa, E., Wink, J. E. & Salter, C. J., 1988. *Astr. Astrophys.*, **191,** 44.
Moore, T. J. T., 1989. *PhD thesis,* Edinburgh University.
Moore, T. J. T., Chandler, C. J., Gear, W. K. & Mountain, C. M., 1989. *Mon. Not. R. astr. Soc.*, **237,** 1P.
Rieke, G. H. & Lebofsky, M. J., 1985. *Astrophys. J.*, **288,** 618.
Snell, R. L., Mundy, L. G., Goldsmith, P. F., Evans, N. J. & Erickson, N. R., 1984. *Astrophys. J.*, **276,** 625.
Thronson, H. A., Lada, C. J., Schwartz, P. R., Smith, H. A., Smith, J., Glaccum, W., Harper, D. A. & Lowenstein, R. F., 1984. *Astrophys. J.*, **280,** 154.
Yamashita, T., Sato, S., Tamura, M., Suzuki, H., Takano, T., Mountain, C. M., Moore, T. J. T., Gatley, I. & Hough, J. H., 1987. *Publs astr. Soc. Japan,* **39,** 809.
Yamashita, T., Sato, S., Nagata, T., Gatley, I., Hayashi, S. S. & Fukui, Y., 1989. *Astrophys. J.*, **336,** 832.

Mon. Not. R. astr. Soc. (1988) **231**, *Short Communication*, 47P–54P

Submillimetre observations reveal that DR21 (OH) is a double source

W. K. Gear *Royal Observatory, Blackford Hill, Edinburgh EH9 3HJ*
C. J. Chandler and T. J. T. Moore *Astronomy Department, Edinburgh University, Blackford Hill, Edinburgh EH9 3HJ*
C. T. Cunningham *Rutherford Appleton Laboratory, Chilton OX11 0QX*
W. D. Duncan *Joint Astronomy Centre, 665 Komohana Street, Hilo Hawaii 96720, USA*

Accepted 1988 January 13. Received 1988 January 12

Summary. We have scanned the region around the OH maser source DR21 (OH) with a 20-arcsec beam at a wavelength of 350 μm and discovered a hitherto unknown double structure, with two peaks of roughly equal mass separated by 40 arcsec (0.1 pc) in declination. The northernmost peak is coincident with the OH maser position and the centroid of the far-infrared emission, while the southern source has not previously been found at any wavelength. Both sources are extremely dense and deeply embedded, with optical depths of order unity even in the far-infrared. The southern source may be one of the densest molecular cores yet found, and is a candidate protostar. These results confirm that OB star formation can occur deep within molecular clouds, and not just at their edges.

1 Introduction

The DR21/W75 complex in the Cygnus-X region has been extensively studied in molecular lines (e.g. Dickel, Dickel & Wilson 1978; Richardson *et al.* 1986a) and far-infrared continuum (e.g. Harvey *et al.* 1986). Dickel *et al.* conclude that it consists of two colliding clouds, the DR21 cloud with a velocity of $-3\,\mathrm{km\,s^{-1}}$ and the W75 cloud with a velocity of $11\,\mathrm{km\,s^{-1}}$. There are several extensive regions of star formation, namely DR21, DR21 (OH), W75N and a region to the north of DR21 (OH) close to an H_2O maser position. Detailed observations have concentrated on DR21 and the northern maser source, while DR21 (OH) has been relatively neglected.

The DR21 (OH) position has also been referred to in the literature as W75-S and W75 (OH), but Dickel *et al.* conclude that it is part of the $-3\,\mathrm{km\,s^{-1}}$ DR21 cloud rather than the $11\,\mathrm{km\,s^{-1}}$ W75 cloud, so we shall use the name DR21 (OH). We observed this source as part of a programme of observations of dense molecular cores at 350 μm (Cunningham *et al.* 1984; Cunningham, Griffin & Gee, in preparation; Gear *et al.* 1986; Richardson *et al.* 1986b). Submillimetre continuum

observations are an excellent tracer of the column density in such regions (Hildebrand 1983) since the emission is almost always optically thin and, on the long-wavelength side of the thermal spectrum, is not sensitive to temperature variations, unlike far-infrared observations.

It is a remarkable fact that, for the small number of dense molecular cores for which submillimetre continuum maps are available, a previously unknown cool dense protostellar condensation has been found in almost every case (Keene, Hildebrand & Whitcomb 1982; Gezari 1982; Jaffe *et al.* 1983, 1984; Cunningham *et al.* 1984, and in preparation). In this paper we present a high-resolution scan at 350 μm through DR21 (OH) which reveals a double structure which had remained previously undiscovered despite the region having been mapped with similar resolution in the far-infrared (Harvey *et al.* 1986). Despite the uncertain temperature of the two sources, it is clear that they are amongst the densest such cores so far discovered.

2 Observations

Preliminary observations revealing the double structure of DR21 (OH) were made during daylight observing in 1986 April. More detailed observations confirming this result were made during night-time observing in 1986 July. All observations were made using the common-user submillimetre photometer UKT14 on the United Kingdom Infrared Telescope on Mauna Kea, Hawaii. Calibration was performed against Jupiter and Saturn.

The aperture was 21 mm corresponding to a beamsize of 20 arcsec, measured against Mars. These are the first published observations with such a small beam at 350 μm. First, we made a fully sampled scan of the DR21 (OH) region in the north–south direction. At distances of 90 arcsec north and south the emission becomes contaminated by the contributions from the H_2O maser source and DR21 respectively (see Rieke *et al.* 1973; Harvey *et al.* 1986). We then made east–west scans at the positions of the two peaks found in the declination scan. The pointing uncertainty in these scans was approximately 2 arcsec.

3 Results

The results of our north–south scan photometry are given in Table 1 and displayed in Fig. 1. The uncertainties quoted for all fluxes are statistical, and we estimate the absolute uncertainty in the

Table 1. 350 μm declination scan through DR21 (OH).

Dec. offset	Flux (Jy)
+70	48±9
+60	51±11
+50	75±8
+40	101±3
+30	115±6
+20	203±6
+10	434±13
0	500±12
−10	368±6
−20	238±8
−30	288±6
−40	318±6
−50	201±4
−60	102±5
−70	57±6
−80	45±3
−90	29±6
−100	36±4

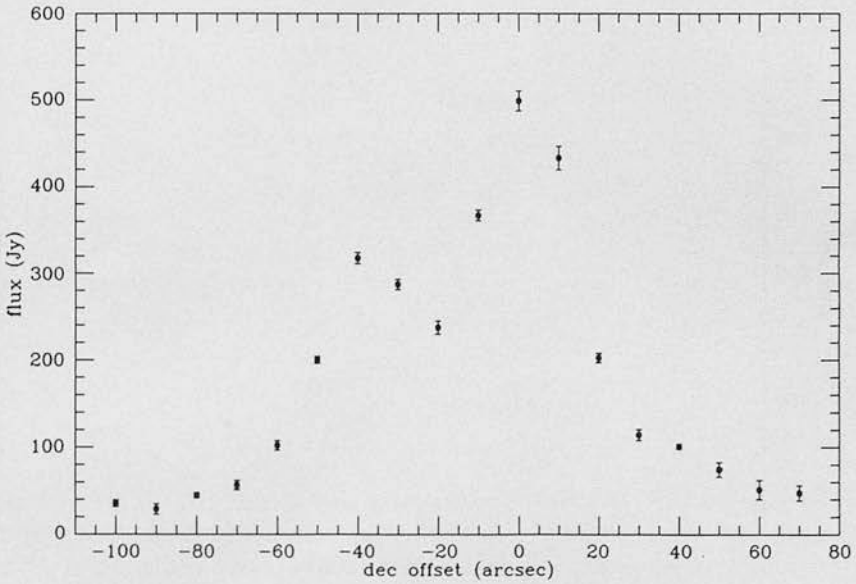

Figure 1. A declination scan through the DR21 (OH) region, revealing a clear double structure.

calibration to be approximately 20 per cent. The positions are given as declination offsets from the map centre which was at RA=20^{h}37^{m}14^s.9, Dec.=+42° 12′ 10″ (1950). It is clear that the emission is not symmetric and that there is an extension to the south with a secondary peak at around −40 arcsec.

In order to separate the contributions of the two peaks we first used a non-linear least-squares fitting programme (Bevington 1969) to fit the four points at +20, +10, 0 and −10 assuming

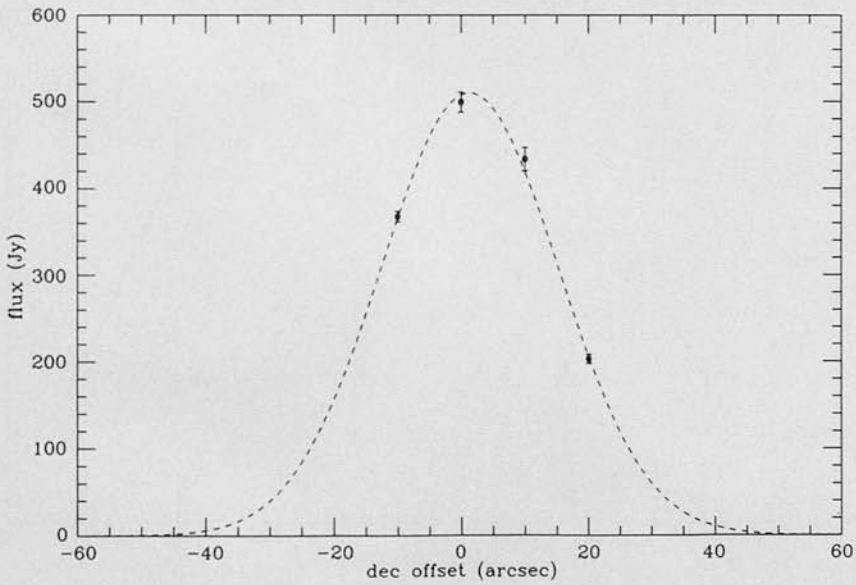

Figure 2. Best fit to the four points defining the DR21 (OH) peak, shown as a broken line. The fit is a Gaussian of FWHM 33 arcsec, which after deconvolving the beamwidth of 20 arcsec, gives a source size of 26 arcsec.

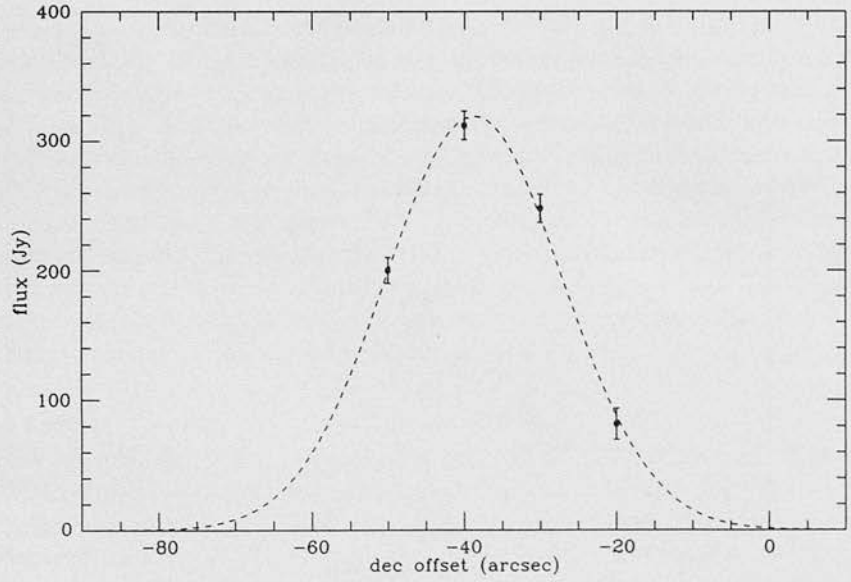

Figure 3. The best fit to the points defining the southern peak which were obtained by subtracting the fit shown in Fig. 2 from the fluxes given in Table 1. The fit is a Gaussian of FWHM 27 arcsec, which after deconvolving the beamwidth of 20 arcsec, gives a source size of 19 arcsec.

Gaussian source and beam distributions, and allowing the peak flux, position and FWHM as free parameters. The resulting best fit is shown in Fig. 2. The fitted FWHM gives a source width, after deconvolving the beamwidth, of 26±1 arcsec and a fitted peak flux of 510±10 Jy. This fit was then subtracted from the fluxes at −50, −40, −30 and −10 and the resultant derived fluxes fitted. This

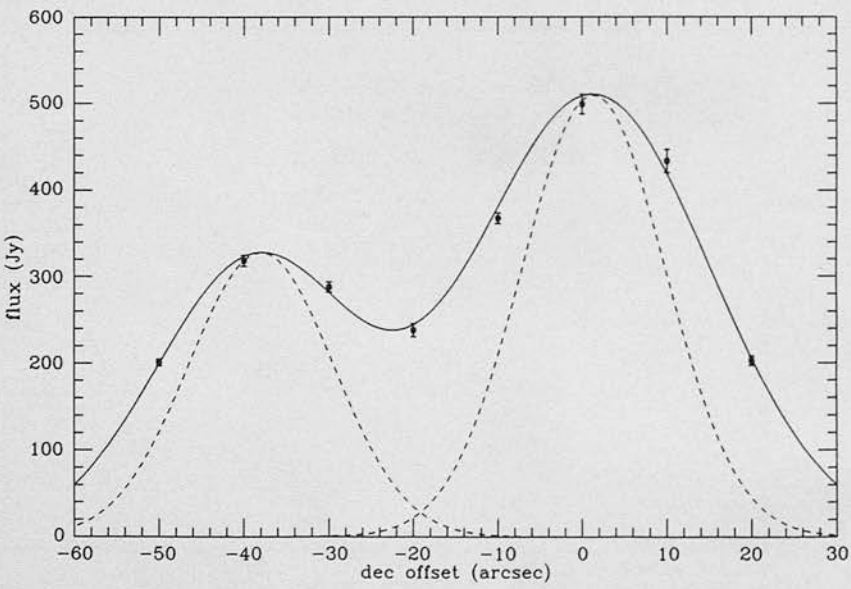

Figure 4. The full declination scan through the DR21 (OH) region, together with the sum of our two best fits shown by a solid line. The broken lines indicate the telescope beam, plotted at the position of the two peaks.

Table 2. RA scan at declination offset 0.

Offset	Flux (Jy)
−50	65±20
−40	103±7
−30	189±25
−20	347±4
−10	458±9
0	397±16
+10	230±13
+20	73±15
+30	45±21
+40	5±24
+50	36±10

fit is shown in Fig. 3. The best fit gave a peak flux of 320±10 Jy and a source width, after deconvolving the beam, of 19±3 arcsec. In Fig. 4 we show the whole scan through the source, with the dark line being the sum of the two fits and the broken lines indicating the beamwidth, plotted at the positions of the two peaks. We have clearly obtained a good fit to the scan.

The results for the east–west scan at a declination offset of 0 are given in Table 2. A fit was made to the points at RA offsets −30, −20, −10, 0, +10, +20. The resultant best fit, shown in Fig. 5, gave a source width, after deconvolving the beam, of 31±1 arcsec. The results for the east–west scan at a declination offset of −40 are given in Table 3. The best fit to the points at −30, −20, −10, 0, +10, +20 and +30 is shown in Fig. 6. The fitted source size, after deconvolving the beam is 41±8 arcsec.

Based on the RA and Dec. scans, the best-fit positions are $20^h37^m14\overset{s}{.}2$, +42° 12′ 11″ for the DR21 (OH) maser source and $20^h37^m14\overset{s}{.}6$, +42° 11′ 31″ for the newly discovered southern source.

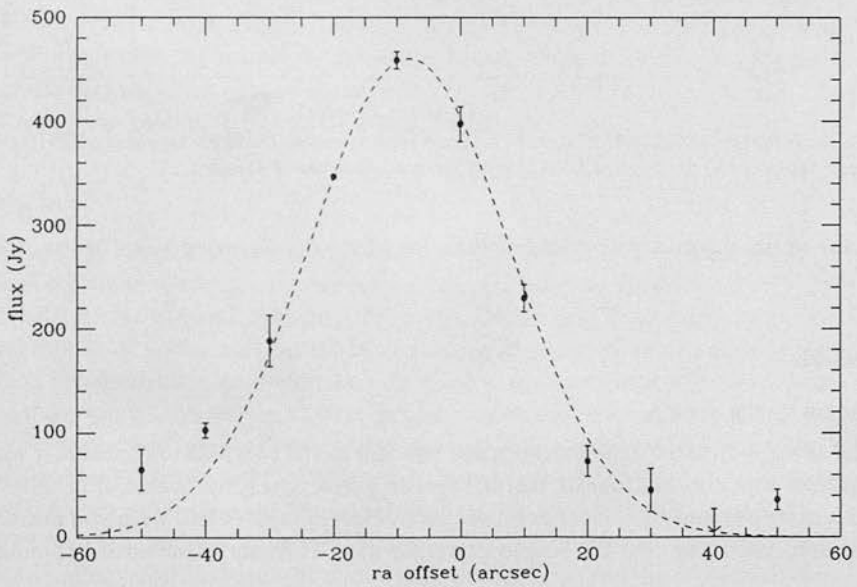

Figure 5. The best fit to the RA scan through the DR21 (OH) position. The fit is a Gaussian of FWHM 37 arcsec, which after deconvolving the beamwidth of 20 arcsec gives a source size of 31 arcsec.

Table 3. RA scan at declination −40.

Offset	Flux (Jy)
−50	62±28
−40	104±12
−30	142±23
−20	235±16
−10	306±31
0	360±14
+10	256±19
+20	171±22
+30	88±10
+40	34±32
+50	34±26

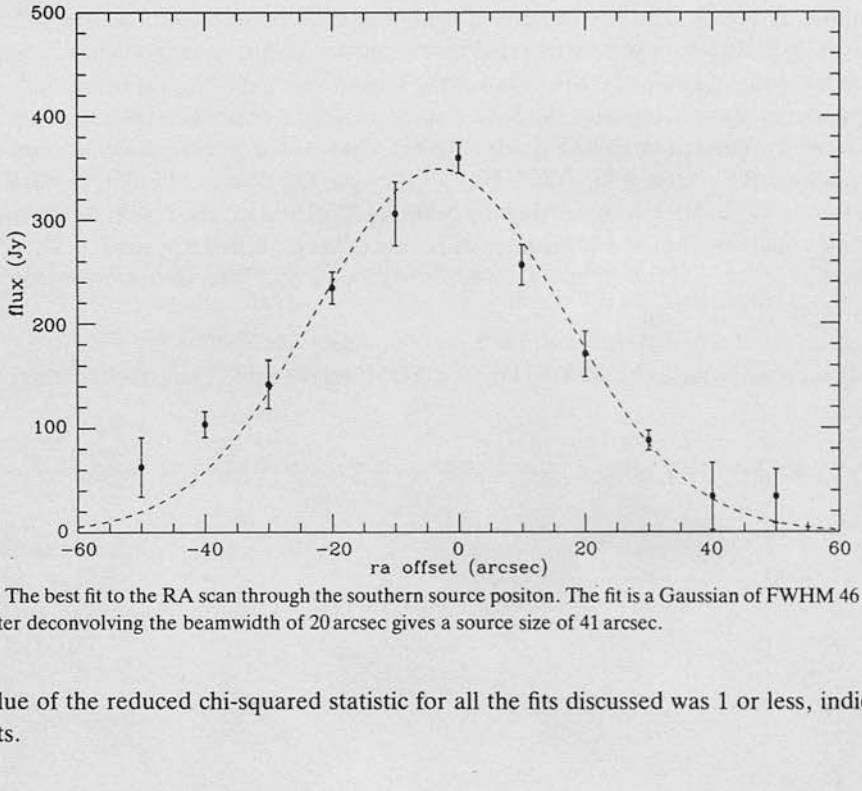

Figure 6. The best fit to the RA scan through the southern source positon. The fit is a Gaussian of FWHM 46 arcsec, which after deconvolving the beamwidth of 20 arcsec gives a source size of 41 arcsec.

The value of the reduced chi-squared statistic for all the fits discussed was 1 or less, indicating good fits.

4 Discussion

4.1 THE OH MASER SOURCE

The best-fitting position for the northern and stronger of the two peaks is coincident within the uncertainties with the position of the OH maser source given by Dickel *et al.* (1978). The centroids of the 50- and 100-μm maps presented by Harvey *et al.* (1986) were also identical with this position, indicating that the source powering the OH maser is the most luminous in the region.

Harvey *et al.* derive a temperature of 36 K for this source, assuming a λ^{-1} dust emissivity law, and using this value and the size derived in Section 3 we find a 350-μm optical depth for the central

position of 0.24. This is much higher than typical values for regions of star formation (e.g. Cunningham 1982; Jaffe *et al.* 1984) and is comparable with the dense condensation we have previously discovered at W51 (main) (Cunningham *et al.* 1984). Using a value of A_V/τ_{350} of 4700 (Gear *et al.* 1986) this corresponds to a visual extinction of 1100 mag! This explains why the strongest near-infrared source in this region is at W75 IRS1 (Garden *et al.* 1986); the extinction at the maser position is simply too great, even in the near-infrared. In fact this source will have an optical depth of unity even at 100 μm. Note that this high extinction could result in an underestimate of the temperature by several degrees.

Using the relations between τ_{350} and hydrogen column density derived by Hildebrand (1983) from the results of Whitcomb *et al.* (1981), but modified for Gaussian geometry (Gee 1987), we find a peak column density $N(H+H_2)=1.2\times10^{24}$ cm^{-2} and, assuming a distance of 3 kpc, a local peak density of $n(H+H_2)=8.6\times10^5$ cm^{-3}. The total derived mass for this source is $5.0\times10^3 M_\odot$.

4.2 THE SOUTHERN SOURCE

The southern, weaker source does not show up at all on the 50- and 100-μm maps of Harvey *et al.* (1986), and it must therefore be considerably cooler than the maser source, but without more spectral information we are unable to constrain its temperature. We can nevertheless still set useful lower limits on its density and mass. Assuming $T<30$ K we find a lower limit to the optical depth at 350 μm of 0.23 and to the column density $N(H+H_2)$ of 1.1×10^{24} cm^{-2}, corresponding to $A_V>1100$ mag. The lower limit to the local density is approximately 10^6 cm^{-3}, making this souce one of the densest cloud cores yet found. If the temperature of this source is significantly cooler than 30 K it will in fact be optically thick even at 350 μm. Provided the 350-μm emission is not optically thick, the derived mass is only linearly dependent on its temperature; for $T<30$ K we estimate $M>10^4 M_\odot$.

We also note that, unlike the maser source position, this source is considerably elongated in the east–west direction; this may indicate a disc-like structure, or alternatively observations at even higher resolution may reveal a further subdivision into more than one source.

It is clear that further observations of this extremely interesting source are required in both submillimetre continuum, with even higher spatial resolution, and in molecular line tracers which may be able to probe the extremely dense conditions which appear to be found there. Such observations may also shed light on the evolutionary status of this source, which is certainly cool enough and dense enough to be a candidate accreting protostar.

5 Conclusions

The remarkable success of submillimetre continuum observations in discovering previously unknown cool dense condensations has been noted previously by Jaffe *et al.* (1984). DR21 (OH) joins the list of NGC 6334I (Gezari 1982), W3, OMC1 and S255 (Jaffe *et al.* 1984), W51 (Cunningham *et al.* 1984) and Sgr B2 (Cunningham *et al.*, in preparation) which have been mapped in the submillimetre continuum and all of which have been found to contain closely-spaced condensations. As Jaffe *et al.* have pointed out, the submillimetre optical depths of these regions also imply that they are deeply embedded within their parent clouds, rather than forming at the edges. Our results for DR21 (OH) in this paper confirm this conclusion, and the two sources are among the most deeply embedded condensations yet found.

The DR21 region appears to be particularly active in forming stars, with the condensations discovered in this paper and also the cool young source further to the north first discovered at 1 mm by Werner *et al.* (1975) and coincident with an H_2O maser. Further investigations of these regions are required, in particular high spatial resolution submillimetre observations at more than

one wavelength are essential for determining the temperature and luminosity of the two sources. In order to investigate fully the structure and evolutionary status in the DR21 (OH)–south source, measurements in both continuum and molecular lines will be required at even higher spatial resolution.

Acknowledgments

The UKIRT is operated by the Royal Observatory, Edinburgh on behalf of the SERC. TJTM and CJC acknowledge the support of SERC studentships. We thank Pat Roche and Matt Mountain for useful discussions and Ian Robson for encouragement.

References

Bevington, P. R., 1969. *Data Reduction and Error Analysis for the Physical Sciences,* McGraw-Hill, New York.
Cunningham, C. T., 1982. *PhD thesis,* University of London.
Cunningham, C. T., Griffin, M. J., Gee, G., Ade, P. A. R. & Nolt, I. G., 1984. *Mon. Not. R. astr. Soc.,* **210,** 891.
Dickel, J. R., Dickel, H. R. & Wilson, W. J., 1978. *Astrophys. J.,* **223,** 840.
Garden, R., Geballe, T. R., Gatley, I. & Nadeau, D., 1986. *Mon. Not. R. astr. Soc.,* **220,** 203.
Gear, W. K., Gee, G., Robson, E. I., Ade, P. A. R. & Duncan, W. D., 1986. *Mon. Not. R. astr. Soc.,* **219,** 835.
Gee, G., 1987. *PhD thesis,* University of London.
Gezari, D. Y., 1982. *Astrophys. J.,* **259,** L29.
Harvey, P. M., Joy, M., Lester, D. F. & Wilking, B. A., 1986. *Astrophys. J.,* **300,** 737.
Hildebrand, R. H., 1983. *Q. Jl. R. astr. Soc.,* **24,** 267.
Jaffe, D. T., Hildebrand, R. H., Keene, J. & Whitcomb, S. E., 1983. *Astrophys. J.,* **273,** L89.
Jaffe, D. T., Davidson, J. A., Dragovan, M. & Hildebrand, R. H., 1984. *Astrophys. J.,* **284,** 637.
Keene, J., Hildebrand, R. H. & Whitcomb, S. E., 1982. *Astrophys. J.,* **252,** L11.
Richardson, K. J., White, G. J., Phillips, J. P. & Avery, L. W., 1986a. *Mon. Not. R. astr. Soc.,* **219,** 167.
Richardson, K. J., White, G. J., Gee, G., Griffin, M. J., Cunningham, C. T., Ade, P. A. R. & Avery, L. W., 1986b. *Mon. Not. R. astr. Soc.,* **216,** 713.
Rieke, G. H., Harper, D. A., Low, F. J. & Armstrong, K. R., 1973. *Astrophys. J.,* **183,** L67.
Werner, M. W., Elias, J. H., Gezari, D. Y., Hauser, M. G. & Westbrook, W. E., 1975. *Astrophys. J.,* **199,** L185.
Whitcomb, S. E., Gatley, I., Hildebrand, R. H., Keen, J., Sellgren, K. & Werner, M. W., 1981. *Astrophys. J.,* **246,** 416.